IMPERIAL COLLEGE LONDON

Selective Gene Expression in Hydrogel Suspended *Escherichia coli* through Optogenetics by Spatiotemporally Controlled Light for the Purposes of Additive Manufacturing

Borut Lampret

Thesis submitted for the degree of
Doctor of Philosophy

Faculty of Natural Sciences
Department of Chemistry

Faculty of Engineering
Dyson School of Design Engineering

London, 2022

Statement of Originality

I hereby state that this thesis and all the work therein is a result of my own work and research except where explicitly stated otherwise in the text and all due references have been provided on all literature and resources. This work has also not been submitted for any other degree or professional qualification at Imperial College London or any other institution.

Copyright Statement

The copyright of this thesis rests with the author. Unless otherwise indicated, its contents are licensed under a Creative Commons Attribution-Non Commercial 4.0 International Licence (CC BY-NC).

Under this licence, you may copy and redistribute the material in any medium or format. You may also create and distribute modified versions of the work. This is on the condition that: you credit the author and do not use it, or any derivative works, for a commercial purpose.

When reusing or sharing this work, ensure you make the licence terms clear to others by naming the licence and linking to the licence text. Where a work has been adapted, you should indicate that the work has been changed and describe those changes.

Please seek permission from the copyright holder for uses of this work that are not included in this licence or permitted under UK Copyright Law.

Acknowledgements

The road to a PhD is long and arduous especially when cut in half by a global pandemic. As with most things, any endeavour is made worse or better by people around you. I am glad to say that in my case it was the latter. I would like to thank my supervisor Dr. Connor Myant for all his support and his ability to lift your spirits in conversations about your work. Of course, I need to thank our AM group Jiwoo, Usman, Shiya, Mohanad, Livia, Freddie, Ali and Esperanza, for their support and for humoring my curiosity about their work. I would also like to thank Andreas and my second supervisor professor Guy-Bart Stan for their assistance with the biological side of my work. Finally, I would like to acknowledge my family and my parents for being there and for letting me know that no matter what I would always have a place to go back to.

Abstract

Advances in the ability to manipulate genetic material have enabled the utilization of microbes in production of both biological and synthetic materials. However, the vast majority of these materials are not suitable for additive manufacturing. While there have been significant advances in the field of bioprinting, significant effort is required to develop the so called bioinks, which support both the printing process and the encapsulated cells' survivability. To combat these challenges, the work in this thesis investigates a novel method of additive manufacturing, which can employ microbial cell factories suspended in hydrogel and optogenetics to selectively deposit the desired biological or synthetic material in a three-dimensional volume.

Genetically engineered *Escherichia coli* that produces CcaSR, a synthetic light response system, was used in order to establish spatially selective gene expression. A custom designed system was built to house the hydrogel suspended *E. coli* and to provide and shape the green and red light used to interact with the cells. A series of experiments were carried out to confirm localized gene expression within the hydrogel build volume and to test and confirm the behaviour of the CcaSR system. To enable the process of additive manufacturing, a series of spatiotemporal illumination procedures were developed and their behaviour investigated. A select illumination procedure was then employed in inducing gene expression in a nontrivial three-dimensional object confirming the viability of the proposed method for the purposes of additive manufacturing.

Contents

1 Introduction 15
1.1 Introduction 15
1.2 Research Objective 16
1.3 Thesis Outline 17

2 Literature Review 20
2.1 Microbial Cell Factories 21
2.2 Bioprinting 22
2.3 Advanced Vat Photopolymerization Methods 25
2.4 Biological light response systems 28
2.5 Optogenetic Model 30
2.6 Parameter Values of CcaSR in *E. coli* 33
2.7 Summary 34

3 Equipment, Materials and Methods 35
3.1 Sample Preparation 36
3.1.1 Culture Preparation 36
3.1.2 Hydrogel Culture Preparation 36
3.2 Mechanical Apparatus 38
3.3 Optical Apparatus 40
3.3.1 Green Laser Optical System 41
3.3.2 Red Laser Optical System 44
3.3.3 Localized Volume through Light Overlap 45
3.3.4 Optical Power Measurement Equipment 46
3.3.5 Intensity Profile Measurement Equipment 47
3.4 Control and Communication Apparatus 48
3.5 Experiment Execution 51
3.6 Data Collection 52
3.6.1 Physical Slicing of Hydrogel 52
3.6.2 Gene Expression Imaging 54
3.6.3 Image Processing 56
3.6.4 Experiment Simulation Methods 61

4 Equipment Characterisation . . . 63
4.1 Cell Population Growth . . . 64
4.2 Light Attenuation . . . 68
4.3 Light Intensity Profile . . . 70
4.3.1 Incident Beam Profiles . . . 70
4.3.2 Scattered Beam Profiles . . . 73

5 Localized Steady-State Gene Expression . . . 76
5.1 Steady-State Solution . . . 77
5.2 Results . . . 78
5.2.1 Scope of Green Light Influence . . . 80
5.2.2 Scope of Red Light Influence . . . 86
5.3 Parameter Estimations . . . 90
5.3.1 Error Estimates . . . 91
5.3.2 Red Light Leakage Estimation . . . 93
5.3.3 Estimation of the Ratio between the Maximum and Background Gene Expression . . . 95
5.4 Conclusion . . . 100

6 Gene Expression under Discontinuous Illumination . . . 101
6.1 Single Illumination . . . 102
6.1.1 Hill Function Approximation . . . 102
6.1.2 Deactivation Procedure Model . . . 103
6.1.3 Experiments' Illumination Procedure . . . 109
6.1.4 Results . . . 110
6.2 Periodic Illumination . . . 114
6.2.1 Periodic Illumination Model . . . 114
6.2.2 Experiments' Illumination Procedure . . . 118
6.2.3 Results . . . 119
6.3 Conclusion . . . 123

7 Gene Expression in Multiple Voxels . . . 126
7.1 Voxel Arrangements . . . 127
7.2 Alternating Illumination . . . 127
7.2.1 Horizontal Arrangement . . . 128
7.2.2 Vertical Arrangement . . . 135
7.2.3 Diagonal Arrangement . . . 143
7.2.4 Discussion . . . 149
7.3 Illumination for Concurrent Gene Expression . . . 150
7.3.1 Horizontal Arrangement . . . 150

7.3.2 Vertical Arrangement . . . 158
7.3.3 Diagonal Arrangement . . . 164
7.3.4 Discussion . . . 171
7.4 Illumination for Separate Gene Expression . . . 173
7.4.1 Discussion . . . 185
7.5 Conclusion . . . 186

8 Gene Expression in 3D Geometry . . . 190
8.1 Spatial and Temporal Slicing . . . 191
8.2 Double Helix . . . 195
8.2.1 Illumination . . . 195
8.2.2 Print Results . . . 197
8.3 Conclusion . . . 200

9 Conclusions and Future Work . . . 201
9.1 Conclusions . . . 201
9.2 Future work . . . 205

Bibliography . . . 206

List of figures

1.1 Results Chapters Progression Flow Chart 19

2.1 Bioprinting Methods 22
2.2 Dual Wavelength Vat Photopolymerization Method 27
2.3 Volumetric Vat Photopolymerization Method 29

3.1 3D Printing Equipment 35
3.2 Hydrogel Culture Filled Cuvette 37
3.3 Hydrogel Culture Preparation Flow Chart 37
3.4 Mechanical Apparatus 38
3.5 Axes of the Translation System 39
3.6 Incubation Chamber 39
3.7 Optical Apparatus 40
3.8 Green Laser System Fibre Launch 41
3.9 Green Laser System Focusing Optics 43
3.10 Red Laser Optical System 44
3.11 Green and Red Light Overlap 45
3.12 Optical Power Measurement Equipment 46
3.13 Intensity Profile Measurement Camera 47
3.14 Experiment Execution Flow Chart 52
3.15 Slicing Jig 53
3.16 Slicing Steps 54
3.17 Interference Pattern and Edge Reflections on Images of Hydrogel Slices 55
3.18 Image Ready Slices 56
3.19 Image Processing Steps 57
3.20 Summed Slices Image Regions 58
3.21 Average Value Calculation 60
3.22 Simulation Grid for Single Beam 61
3.23 Simulation Grid for Two Beams 62

4.1 Cell Growth Curves 65
4.2 Cell Growth Curves Best Fit Estimates 67
4.3 Transmission of Hydrogel Culture Filled Cuvette 69

4.4 Green Beam Intensity Profile . . . 71
4.5 Red Light Intensity Profile . . . 72
4.6 Exiting Green Beam Intensity Profile . . . 74
4.7 Exiting Red Light Intensity Profile . . . 75

5.1 Grid of Images of Summed Fluorescence from Steady-State Experiments 79
5.2 Grid of Plots of Normalized Average Fluorescence Values of Columns Parallel to Green Beam Path . . . 81
5.3 Normalized Steady-State Hill Function Graphs for Different Green Light Intensity Profiles . . . 82
5.4 Time Dependant Behaviour of Active-State Photoreceptor Fraction and Normalized Integrated Total Gene Expression . . . 84
5.5 Comparison between Simulated Gene Expression and Normalized Average Fluorescence Values of Columns Parallel to Beam Path . . . 86
5.6 Grid of Plots of Normalized Average Fluorescence Values on the Green Beam Path . . . 87
5.7 Background Contrasted Fluorescence Images of Two Experiments with Deactivated Initial Active-State Photoreceptor Population . . . 89
5.8 Fit of Ratio Between voxel Gene Expression and Suppressed Region Gene Expression in Steady-State Experiments . . . 94
5.9 Best Fit Estimates of Contrast in Steady-State Experiments . . . 97
5.10 Grid of Contrasted Images of Steady-State Gene Expression Measurements . . . 99

6.1 Hill Function and Its Approximation versus Proportion of Active-State Photoreceptors . . . 102
6.2 Response of Fraction of Active-State Photoreceptors and Gene Expression Rate to Different Single Voxel Illumination Strategies . . . 107
6.3 Comparison of Gene Expression Rate in Response to Different Single Voxel Illumination Strategies. . . . 108
6.4 Illumination Procedure for a Four Voxel Single Illumination Experiment 109
6.5 Measurements and Simulations of a Four Voxel Single Illumination Experiment without Red Light Illumination . . . 110
6.6 Raw Image of Fluorescence of Individual Slices From the Hybrid Initial Illumination Experiment . . . 111
6.7 Measurements and Simulations of a Four Voxel Single Illumination Experiment . . . 112
6.8 Response of Fraction of Active-State Photoreceptors and Gene Expression Rate to Periodic Single Voxel Illumination . . . 117

6.9 Illumination Procedure for a Four Voxel Periodic Illumination Experiment with Four Periods 118
6.10 Measurements and Simulations of a Four Voxel Periodic Illumination Experiment without Red Light Illumination 120
6.11 Illumination Procedure for a Four Voxel Periodic Illumination Experiment with One Period 121
6.12 Measurements and Simulations of a Four Voxel Periodic Illumination Experiment 122
6.13 Fit of Ratio Between voxel Gene Expression and Suppressed Region Gene Expression in Steady-State Experiments, Updated 124
6.14 Best Fit Estimates of Contrast in Steady-State Experiments, Updated 125

7.1 Arrangements of Two Voxels in a Plane 127
7.2 Response of Gene Expression Rate and Total Gene Expression in Horizontally Arranged Voxels to Alternating Illumination 130
7.3 Alternating Illumination Procedure for an Experiment of Two Voxels in Horizontal Arrangement 131
7.4 Simulations of Gene Expression in Two Voxels in Horizontal Arrangement Subjected to Alternating Illumination 132
7.5 Measurement of Fluorescence of Two Voxels in Horizontal Arrangement Subjected to Alternating Illumination 133
7.6 Distinguishability and Homogeneity as a Function of η for Voxels in Vertical Arrangement Subjected to Alternating Illumination 137
7.7 Response of Gene Expression Rate and Total Gene Expression in Vertically Arranged Voxels to Alternating Illumination 138
7.8 Alternating Illumination Procedure for an Experiment of Two Voxels in Vertical Arrangement 139
7.9 Simulations of Gene Expression in Two Voxels in Vertical Arrangement Subjected to Alternating Illumination 140
7.10 Measurement of Fluorescence of Two Voxels in Vertical Arrangement Subjected to Alternating Illumination 142
7.11 Response of Gene Expression Rate and Total Gene Expression in Diagonally Arranged Voxels to Alternating Illumination 145
7.12 Alternating Illumination Procedure for an Experiment of Two Voxels in Horizontal Arrangement 146
7.13 Simulations of Gene Expression in Two Voxels in Diagonal Arrangement Subjected to Alternating Illumination 147
7.14 Measurement of an Experiment of Two Voxels in Diagonal Arrangement Subjected to Alternating Illumination 148

7.15 Response of Gene Expression Rate and Total Gene Expression in Horizontally Arranged Voxels to Illumination for Concurrent Gene Expression . . . 153
7.16 Concurrent Gene Expression Illumination Procedure for an Experiment of Two Voxels in Horizontal Arrangement . . . 154
7.17 Simulations of Gene Expression in Two Voxels in Horizontal Arrangement Subjected to Concurrent Gene Expression Illumination . . . 154
7.18 Measurement of an Experiment of Two Voxels in Horizontal Arrangement Subjected to Concurrent Gene Expression Illumination . . . 156
7.19 Response of Gene Expression Rate and Total Gene Expression in Vertically Arranged Voxels to Illumination for Concurrent Gene Expression 160
7.20 Concurrent Gene Expression Illumination Procedure for an Experiment of Two Voxels in Vertical Arrangement . . . 161
7.21 Simulations of Gene Expression in Two Voxels in Vertical Arrangement Subjected to Concurrent Gene Expression Illumination . . . 162
7.22 Measurement of an Experiment of Two Voxels in Vertical Arrangement Subjected to Concurrent Gene Expression Illumination . . . 163
7.23 Response of Gene Expression Rate and Total Gene Expression in Diagonally Arranged Voxels to Illumination for Concurrent Gene Expression . . . 167
7.24 Concurrent Gene Expression Illumination Procedure for an Experiment of Two Voxels in Diagonal Arrangement . . . 168
7.25 Simulations of Gene Expression in Two Voxels in Diagonal Arrangement Subjected to Concurrent Gene Expression Illumination . . . 168
7.26 Simulation of Gene Expression in Two Voxels in Diagonal Arrangement Subjected to Concurrent Gene Expression Illumination as a Function of Z Coordinate . . . 170
7.27 Measurement of an Experiment of Two Voxels in Diagonal Arrangement Subjected to Concurrent Gene Expression Illumination . . . 171
7.28 Response of Gene Expression Rate and Total Gene Expression in All Voxel Arrangements to Illumination for Separate Gene Expression . . 175
7.29 Separate Gene Expression Illumination Procedure for Experiments of Two Voxels in All Arrangements . . . 178
7.30 Simulations of Gene Expression in Two Voxels in All Arrangements Subjected to Separate Gene Expression Illumination . . . 179
7.31 Measurement of an Experiment of Two Voxels in Horizontal Arrangement Subjected to Separate Gene Expression Illumination . . . 181
7.32 Measurement of an Experiment of Two Voxels in Vertical Arrangement Subjected to Separate Gene Expression Illumination . . . 182

7.33 Measurement of an Experiment of Two Voxels in Diagonal Arrangement Subjected to Separate Gene Expression Illumination 183
7.34 Response of Gene Expression Rate and Total Gene Expression in Horizontal Voxel Arrangements to All Illumination Procedures 186
7.35 Response of Gene Expression Rate and Total Gene Expression in Vertical Voxel Arrangements to All Illumination Procedures 187
7.36 Response of Gene Expression Rate and Total Gene Expression in Diagonal Voxel Arrangements to All Illumination Procedures 188

8.1 Schematic of Spatial Slicing, Examples of Z-slices and X-slices 192
8.2 Normalized Exponentially Growing Cell Density Segmented into Temporal Slices 194
8.3 Schematic Representation of the Red and Green Light Intensity Profiles Overlap Used During the Double Helix Print 196
8.4 Normalized Incident Intensities Used during the Print of Double Helix 196
8.5 Simulation of Gene Expression in Double Helix Print 197
8.6 Fluorescence Image of Slices from the Double Helix Print 198
8.7 Reconstruction of a Double Helix from the Fluorescence Image of Slices 199

List of Tables

2.1 Optogenetic Model Parameter Values 33

4.1 Estimated Parameters of the Growth Curves 67
4.2 Interface Attenuation Measurements 68
4.3 Transmission and Attenuation of Hydrogel Culture Filled Cuvette . . 69

5.1 Average Background Fluorescence Values 88
5.2 Estimates of Red Light Leakage 95
5.3 Parameter Estimates from the Best Fit of Maximum Contrast in Steady-State Experiments 98

6.1 Estimates of Red Light Leakage, Updated 124
6.2 Parameter Estimates from the Best Fit of Maximum Contrast in Steady-State Experiments, Updated 125

7.1 Gene Expression at Points of Interest of Simulation and Measurement of Two Voxels in Horizontal Arrangement Subjected to Alternating Illumination 134
7.2 Gene Expression at Points of Interest of Simulation and Measurement of Two Voxels in Vertical Arrangement Subjected to Alternating Illumination 141
7.3 Gene Expression at Points of Interest of Simulation and Measurement of Two Voxels in Diagonal Arrangement Subjected to Alternating Illumination 149
7.4 Gene Expression at Points of Interest of Simulation and Measurement of Two Voxels in Horizontal Arrangement Subjected to Concurrent Gene Expression Illumination 157
7.5 Gene Expression at Points of Interest of Simulation and Measurement of Two Voxels in Vertical Arrangement Subjected to Concurrent Gene Expression Illumination 164
7.6 Gene Expression at Points of Interest of Simulation and Measurement of Two Voxels in Diagonal Arrangement Subjected to Concurrent Gene Expression Illumination 172

7.7 Durations of Illumination Steps for Separate Gene Expression Illumination Procedure for All Voxel Arrangements Achieving $\eta_{min} - p_2$ . . 176
7.8 Durations of Illumination Steps for Separate Gene Expression Illumination Experiments for All Voxel Arrangements 178
7.9 Gene Expression at Points of Interest of Simulations and Measurements of Two Voxels in All Arrangements Subjected to Separate Gene Expression Illumination 184

Chapter 1

Introduction

1.1 Introduction

In nature there exists a vast and diverse amount of biological materials i.e. chemical compounds which are produced by living organisms. Utilization of these materials is an attractive proposition given the different chemical, physical and biological properties they possess. In addition, these materials can also provide more sustainable, environmentally friendlier or even cost effective alternatives and as such have gained even more interest in recent years.

With the advent of cheaper and more reliable gene editing techniques [1] interest in the so-called microbial cell factories has only grown. Some notable examples of production of biological materials with interesting physical properties are spider silk [2] and microbial cellulose [3]. Then there is the production of biodegradable plastic such as polyhydroxybutyrate (PHB) [4] or the production of calcium carbonate [5] and even nacre inspired composite materials [6]. Bacteria have also been used to convert chitin to chitosan [7] and fibrinogen to fibrin [8]. There is also interest in generating biofilms that can be used for sensing, energy generation, energy storage and self repair [9].

While the aforementioned production of biological materials has been shown in bulk, research into deposition of said materials into a three-dimensional (3D) geometry has been lacking. Research in 3D bioprinting is focused on deposition of cells themselves and their viability or the deposition of biological material that has been previously prepared in bulk and can then be populated by cells. The main 3D bioprinting techniques used are extrusion based, laser-assisted, inkjet and stereolithography [10, 11]. Each have their own advantages and disadvantages. The main issues with these techniques tend to be the physical properties of the bioink and the addition of initiators, both of which can affect printability and cell viability [12]. When it comes to deposition of biological materials via cell production, additives

that are present in such bioinks could also adversely affect the biological material itself. As such, they would need to be further specialized not only to accommodate the printing process and the producing bacteria, but also the produced biological material. Some of these challenges could be overcome by employing a completely different method.

1.2 Research Objective

Only recently have there been attempts to utilize microbial cell factories to produce some biological material in 3D geometry. An object is 3D-printed using direct ink writing, which is then left to incubate whereupon new material is being produced by the bacteria present in the bioink [13, 14]. This approach has mostly been limited to direct ink writing; however, methods that use light activation have been employed for a similar goal in two dimensions (2D) [15]. Said methods rely on light to selectively activate specific gene expression in cells populating a thin sheet of medium. However, stereolithography has been used to generate biofilms in 3D [16].

The aim of the work in this thesis is to develop a novel method of 3D printing that utilizes microbial cell factories activated through optogenetics and achieves the following objectives:

- printing of support structures is not required regardless of object geometry,
- localized gene expression at an arbitrary position within a build volume enabling 3D object generation
- the ability to generate an object without adhering to stacking of 2D planes,
- the method can facilitate object generation from multiple or composite materials.

The chosen approach to realize these objectives is to use a hydrogel populated by cells, where the cells are engineered to respond to light and activate a specific metabolic pathway. The hydrogel fills the entire build volume and provides both food and support for cells and support for the material produced by the cells. The cells used are engineered to produce photoreceptors, which are activated by green light and deactivated by red light. These active photoreceptors then initiate gene expression of the desired gene, which ultimately results in the specified material production.

The research presented in this thesis investigates the ability of a given geometry of illumination to achieve localized gene expression and the spatiotemporal requirements of said illumination that will lead to gene expression in an arbitrary 3D geometry.

1.3 Thesis Outline

Chapter 2 – Review of literature pertaining to the scope of biological materials and bacteria that have been engineered to produce a desired material. The chapter also includes a general outline of existing 3D bioprinting technologies and some novel light based non-bio 3D printing methods.

Chapter 3 – Description of the materials and methods used to prepare the hydrogel sample and bacteria contained therein. Followed by the description of the equipment used to generate localized illumination at an arbitrary position. Lastly, the chapter describes experiment execution, data collection methods and simulation methods.

Chapter 4 – Measurements conducted to determine the optical properties of both the illuminating light and the bacteria containing hydrogel sample. The chapter also includes measurements of the cell population growth.

Chapter 5 – Measurements of gene expression within the bacteria populated hydrogel subjected to constant illumination. These measurements verify the ability of the system to enable localized gene expression. They were further used to determine the relative amount of the gene-expression-deactivating red light that is present within the volume where gene expression is to occur. Lastly, the measurements were used to determine the ratio between the maximum possible induced gene expression and the background gene expression.

Chapter 6 – Measurements of localized gene expression within the bacteria populated hydrogel subjected to short single illumination period and separately to periodic illumination over the course of an experiment. These measurements were used to verify the persistence of the active state of photoreceptors and that gene expression is independent of the frequency of illumination provided that the degree of photoreceptor activation is maintained. Furthermore, these measurements, along with simulations, were used to qualitatively determine the forward and reverse photoconversion rates, which were then compared to the values previously reported.

Chapter 7 – Measurements of gene expression in three different arrangements of two voxels within a plane subjected to three different illumination procedures. Each illumination procedure is determined based off of a solution of the optogenetic model for the particular arrangement and conditions. The results of the experiments were then used to determine the best approach to illuminate the build volume in order to achieve localized gene expression in multiple locations and to further validate the predictive power of the optogenetic model.

Chapter 8 – Introduction to spatial and temporal slicing, which can be used with the investigated method. The slicing relies on the employed illumination procedure and geometry of illumination. Said slicing and illumination procedure were then used to achieve gene expression in the shape of a double helix.

Chapter 9 – A summary of conclusions reached in the thesis and suggested future work, which aims to improve and expand the current capabilities of the system and methods used.

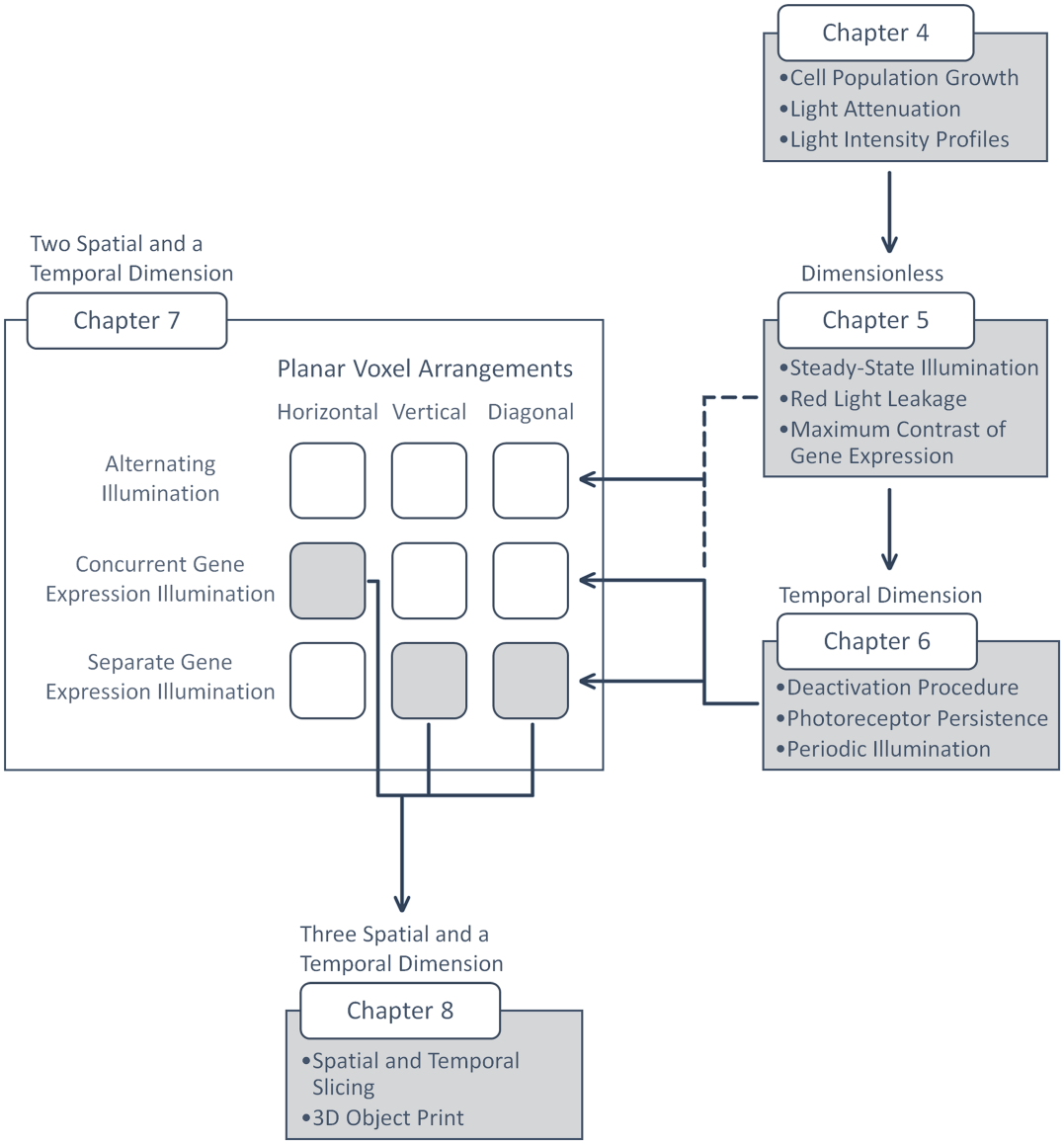


Figure 1.1: *Flow chart depicting progression of results chapters from dimensionless steady-state gene expression in Chapter 5 to three-dimensional gene expression requiring temporal considerations in Chapter 8.*

Chapter 2

Literature Review

Literature Review looks at current knowledge and technology pertaining to bioprinting. Microbial cell factories are reviewed, as these are organisms that have been genetically engineered to produce various biological materials and are as such great candidates to expand the pool of materials in 3D printing. Established bioprinting methods are described along with advanced vat photopolymerization methods to provide context and contrast to the proposed method investigated in this work. Finally, biological light response systems are introduced as the way to control gene expression in cells. Behaviour of a light response system, CcaSR, is further described, as it is the basis for selective control utilized by the proposed method.

2.1 Microbial Cell Factories

A microbial cell factory refers to microbial cells that are used as a type of manufacturing facility, whose metabolic processes were bioengineered to increase the yield of the resulting metabolites [17]. The products in these factories are not necessarily native to the original microbial cells. Biopharmaceuticals (hormones, enzymes, antibiotics, vitamins, and vaccines), polymers, monomers, high-value compounds, and other bioproducts are routinely produced in large quantities using microorganisms. Advances in the ability to manipulate genetic material and construct metabolic pathways [18, 19] has made it possible to easily turn microbes into microbial cell factories. Consequently, many different expression systems have been exploited to make useful nonmicrobial metabolites.

One of the most often used host organism for creating cell factories that produce useful chemical compounds is *Escherichia coli*. It is a genuine industrial asset thanks to its quick growth in low salt media, its compatibility with inexpensive substrates, the existing knowledge of its physiology and genetics, the simplicity of its genetic manipulation, its cost-effectiveness, its easily scaled-up processes, and its capacity to collect heterologous proteins up to 50% of its dry cell weight [20]. As an example, *E. coli* is used to generate almost 30% of authorised protein-based biopharmaceutical products [21].

Even though using *E. coli* as a host for the production of a number of industrial products has many advantages, it cannot be regarded as *the* choice for the production of heterologous proteins. One of the reasons is it tends to accumulate proteins within the cell, which makes extraction more difficult. This is why some microbes such as *Bacillus subtilis* offer better performance when it comes to protein secretion and are as such a better option in some applications [22]. Besides *E. coli* and *B. subtilis*, there have been numerous other microbes that have been used as cell factories. Most of these include *Lactococcus lactis*, *Corynebacterium glutamicum*, *Pseudomonas putida*, *Saccharomyces cerevisiae*, *Pichia pastoris*, *Hansenula polymorpha*, *Yarrowia lipolytica* and Cyanobacteria [17].

The pool of various chemical compounds, which can be produced by the aforementioned cell factories, is vast. However, cell factories were engineered to produce these compounds mainly due to their chemical, medical or biological properties. With the improvement of bioprinting techniques alongside the need for sustainable and environmentally friendly materials, interest in developing microbial cell factories, which produce materials with favourable physical properties, has grown. A major portion of bioprinting involving living cells is still focused around tissue engineering and medical applications [23]. However, there has been research into utilizing microbial cells for living building materials by exploiting biomineralization [5, 6, 24, 25].

There is also significant research being done in utilizing microbial cells for environmentally friendly materials such as polyhydroxyalkanoates (PHA) [26], PHB [4], microbial cellulose [3] and even spider silk [2]. Furthermore, there has been research into engineered living materials, which exhibit properties generally found only in nature such as self-assembly from raw materials, precise morphology control, self-repair and the ability to sense and respond to the environment [9, 11, 27].

2.2 Bioprinting

Additive manufacturing also known as 3D printing is defined as a process where material is added and joined together to form 3D objects, usually layer by layer (ISO/ASTM 52900). This is in contrast to subtractive and formative manufacturing where material is either removed or moulded into shape. The main distinction between bioprinting and regular 3D printing is the use of biological cells. Bioprinting utilizes the so-called bioinks which refers to biomaterials or biological materials that can be loaded with cells. Generally, bioprinting can be done using bioinks that are loaded with cells, bioinks alone where the resulting object is populated by cells, or by deposition of cells alone [28]. As bioinks are designed to facilitate cells, bioprinters must generally ensure or operate in a sterile environment to prevent contamination. Furthermore, bioprinters have to control the temperature and humidity within the build volume either to maintain cell viability or bioink fidelity [29]. The main goals of bioprinting tend to be tissue engineering and medical applications [30].

There are three main 3D printing methods used in bioprinting: material extrusion, material jetting and vat photopolymerization (Figure 2.1). Material extrusion based bioprinting is sometimes also referred to as pressure assisted bioprinting [31], robotic dispensing [32], direct-write bioprinting [33] or simply microextrusion bioprinting [10]. Material jetting methods in bioprinting are further divided into two main categories inkjet bioprinting and laser-assisted bioprinting.

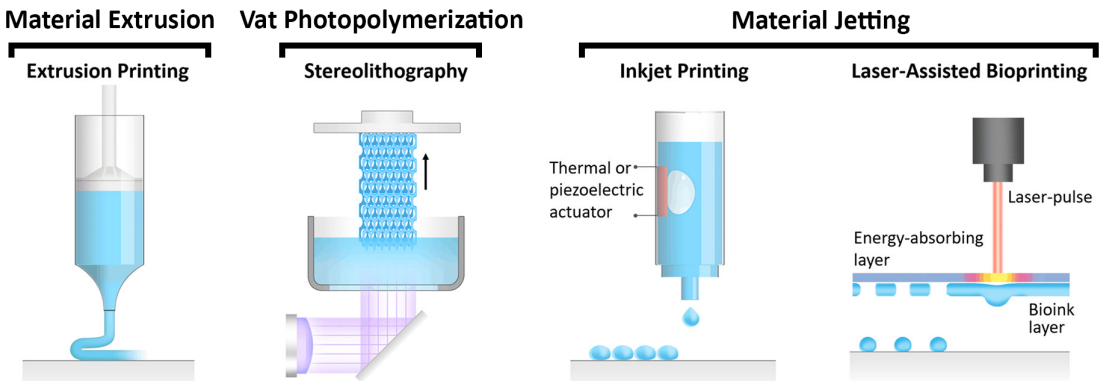


Figure 2.1: *Illustration of the three main methods split into four using the naming conventions still in use by the bioprinting community. Image is adapted from Bendell et al. [34].*

Material Extrusion Based Bioprinting

The basic principle of material extrusion based bioprinting is as the name suggests extrusion of a bioink through a nozzle onto a print bed. Most often the bioink is loaded into a syringe, which is then inserted or attached to a print head. The print head is then controlled by a computer to selectively deposit the bioink onto the print bed. After completing each individual layer the print head moves up by a given amount and continues depositing the bioink in the new layer on top of the previous one. The process continues until the object is printed.

Extrusion is achieved by exerting pressure on the bioink within the syringe. This is achieved either by a pneumatic [35] or a mechanical system [36]. The mechanical system can be further divided into one with a piston or one with a screw. Due to the nature of extrusion, rheological properties of bioinks used in extrusion based bioprinting are very important. Bioinks suitable for extrusion are generally more viscous and preferably exhibit shear thinning properties [37, 38]. In order to maintain the shape of the printed 3D structure, they also require sufficient stiffness. Once deposited, bioink stiffness can be increased through physical such as ionic, stereocomplex and thermal; chemical or photochemical crosslinking [32, 39]. Beside material properties, the parameters of extrusion such as nozzle or needle diameter, print speed, material flow rate, and layer height also affect the fidelity of the print.

The main advantages of extrusion based printing are generally the range of usable materials, high and homogeneous cell load, and room temperature processing. Extrusion based bioprinters are also not too expensive. However, these bioprinters tend to be slow and offer relatively low resolution. Furthermore, cell viability after the print can be quite low [31].

Inkjet Bioprinting

Inkjet-based bioprinting is based on the material jetting printing method used by desktop inkjet printers. It is a non-contact printing technique, which selectively sprays picoliter droplets of bioink on a hydrogel substrate or culture plate. Based on the droplet actuation mechanism, the usual techniques are divided into thermal and acoustic [40]. Thermal techniques force the bioink out of a nozzle and onto the surface by generating a bubble through heating. To produce a pulsed pressure, the localised temperature in the bioink is increased to hundreds of degrees in a few microseconds, which does not necessarily affect the viability of cells [41]. However, droplets generated this way tend not to be very ordered and can vary in size. Also, nozzle blockages are common, which further affects the quality of the print. Unlike the thermal technique, the acoustic approach does not generate heat and produces droplets with a pressure pulse from a piezoelectric actuator. Droplets of bioink

produced by this method tend to be ordered and more evenly sized [42]. It has been shown that the viability of mammalian cells deposited via piezoelectric technique can be greater than 90% [42].

As material jetting involves generation of droplets, the bioink has to be in liquid form during deposition and must form a solid structure afterwards. This has been solved by additives that crosslink through chemical, pH or photochemical mechanism [43]. However, these additives can negatively impact the properties of the bioink both in terms of material and cell viability. Also, to maintain the liquid nature of the bioink the concentration of cells has to be low enough to avoid clogging and excessive shear stress. On the other hand, inkjet technology is widely available and relatively cheap, offering high printing speeds and high resolution [31].

Laser-assisted Bioprinting

In laser-assisted bioprinting a laser is used to deposit bioinks onto a substrate. The three main components of such a bioprinter are a pulsed laser, a ribbon, and a receiving substrate. The ribbon is made of transparent glass coated with a thin metal film, which is also covered with liquid bioink. When the ribbon is illuminated by the focused pulsed laser beam, each pulse locally heats up the metal film creating a vapour bubble on the other side in the bioink. This bubble causes the non-vaporized bioink to be ejected onto the substrate [44]. The substrate is a biopolymer or cell culture medium, which facilitates cell adhesion and growth [31]. The object is thus printed a droplet-by-droplet format in a similar manner to inkjet bioprinting. Unlike inkjet bioprinting, the bioink is not limited to low viscosity. This method has been shown to print with hydrogels, cells, proteins and even ceramic materials [45]. However, certain bioinks have to include a crosslinker in order to stabilize the deposited layers, which facilitates 3D printing. Beyond material availability this method also offers high resolution, precise deposition, medium print speed and high cell viability. On the other hand, bioprinters using this method tend to be expensive, as they include a pulsed laser [31].

Vat Photopolymerization Based Bioprinting

Vat photopolymerization based bioprinting has often been referred to as stereolithography (SLA), a 3D printing technique where liquid polymer is photopolymerized using a laser that draws out each individual layer of the 3D object. However, in bioprinting stereolithography tends to refer to methods that work akin to digital light processing (DLP) or masked stereolithography (MSLA) [16, 30, 31]. Regardless, in vat photopolymerization based bioprinting the bioink is photosensitive and is solidified layer by layer by projection of an image. As bioprinting is derived from

regular 3D printing, UV light is used for bioink polymerisation. However, due to concerns of damage to cells, bioinks that polymerize under visible light have been developed [46]. Vat photopolymerization based bioprinting offers high resolution, high accuracy, and high cell viability. Due to projection of the entire layer, this technique is also fast. Furthermore, the commercial availability of light projectors has made these bioprinters relatively cheap [31]. However, stereolithography based bioprinting was not as utilized as the other three methods [46], which means that a large library of photopolymers that can be used in a bioink [31] has yet to be developed. The main issue in this effort tends to be high cytotoxicity of photoinitiators [47].

2.3 Advanced Vat Photopolymerization Methods

Vat photopolymerization is a process where liquid photopolymer in a vat is selectively cured by light-activated polymerization (ISO/ASTM 52900). Photopolymers in their simplest form consist of a monomer or oligomer and a photoinitiator. The role of the photoinitiator is to drive polymerisation upon light illumination of a specific range of wavelengths. While photopolymerization can be done without a photoinitiator [48], in the context of 3D printing this is generally not the case. Most photopolymers are made more complex, as additional additives are used to further augment their chemical, physical or optical properties.

Conventional vat photopolymerization in 3D printing is achieved by illuminating a thin layer of polymer at the surface of the vat. The initial polymerized layer is adhered to and supported by the print bed. Any subsequent layers are still polymerized at the surface of the vat; however, the print bed has since been vertically moved by one layer height. This accommodates the newly polymerized layer, which now attaches to the previous layer. The process is then continued until the full object is printed. This layering process can be done from top to bottom or from bottom to top. When layering is done from top to bottom the print bed with the object is gradually submerged into the vat so that polymerization can occur at the photopolymer-air interface on top of the vat. In bottom to top layering the print bed with the object is lifted out of the vat. In this case polymerization occurs at the photopolymer-window interface on the bottom of the vat. The window is transparent, allowing the light to polymerize the layer. The object is then raised to detach the polymerized layer from the window and lowered back into position for the next layer.

There are two ways of generating images that will cause polymerization of any given flat layer on the surface of the vat. One is by tracing a laser beam over an area in the shape of the layer to be polymerized and the other is by projecting an image of the layer. Vat photopolymerization 3D printing that utilizes the former

is referred to as stereolithography (SLA), while there are a couple of methods that utilize the latter. These are split into two categories based on the delivery of light. Digital light processing (DLP) 3D printers deliver the image via a projector, whereas masked stereolithography (MSLA) 3D printers filter incoming light using a mask, which is generated by a liquid crystal display (LCD).

Further expanding on this concept there are methods such as continuous liquid interface production (CLIP), which implements a thin dead zone at the surface of the vat [49]. The dead zone prevents polymerization by containing a sufficiently high concentration of oxygen. Photopolymerization thus occurs right below the surface, which allows the layering of the object to be virtually continuous as opposed to step-like. The implementation of the dead zone has also been achieved by adding photoinhibitors to the photopolymer [50]. In this case polymerisation is prevented by illuminating the vat with light that activates the photoinhibitor. The wavelength is different to the light that activates polymerization and is sufficiently attenuated so that only a thin dead zone is generated.

Dual Wavelength Vat Photopolymerization

Dual wavelength vat photopolymerization can be split into two different processes in the way light interacts with the photopolymer. In one process, polymerization occurs only when both colours of light are present. In the the other process, polymerization occurs in the presence of one colour and is actively suppressed in the presence of the other colour of light. These properties are achieved with the use of specific photoinitiators and/or photoinhibitors. Dual wavelength vat photopolymerization can thus be used to achieve photopolymerization of an object within the vat as opposed to surface or near surface photopolymerization.

A photoinitiator requiring two colours of light to activate polymerisation for the purpose of 3D printing has been developed more than 30 years ago [51]. However, only very recently have Regehly et al. [52] and Hahn et al. [53] demonstrated a working 3D printing method utilizing such a photoinitiator. Regehly used a photoinitiator that can be excited into its intermediate state at wavelengths of 400 nm or less and into its active state at wavelengths between 450 nm and 700 nm. Hahn, on the other hand, used a photoinitiator, which can be excited into its intermediate and active state at visible wavelengths from 350 nm to 450 nm and from 600 nm to 800 nm respectively. However, both photoinitiators aim to satisfy the same three conditions: exciting from one state to the other can be done only by using one colour of light, the intermediate state decays quickly in the absence of exciting light, and light attenuation of photoinitiator is relatively low [53]. The second condition is crucial to prevent unwanted polymerization when activating light is shone through the volume where the photoinitiator was previously excited into its intermediate state.

The third condition is required to allow for sufficient light to span the interior of the build volume. The method of generating the 3D object is the same in both cases (Figure 2.2). A sheet of light is used to illuminate the build volume and generates a thin layer within which the photoinitiator is brought to its intermediate state. Selective polymerisation is then achieved by projecting an image perpendicularly to the thin layer in the wavelength of light that activates the photoinitiator. The thin layer is then continuously translated and the projected image changed to generate the full object. As the object is suspended in the build volume, there is no need to print any support material as it is common with other methods.

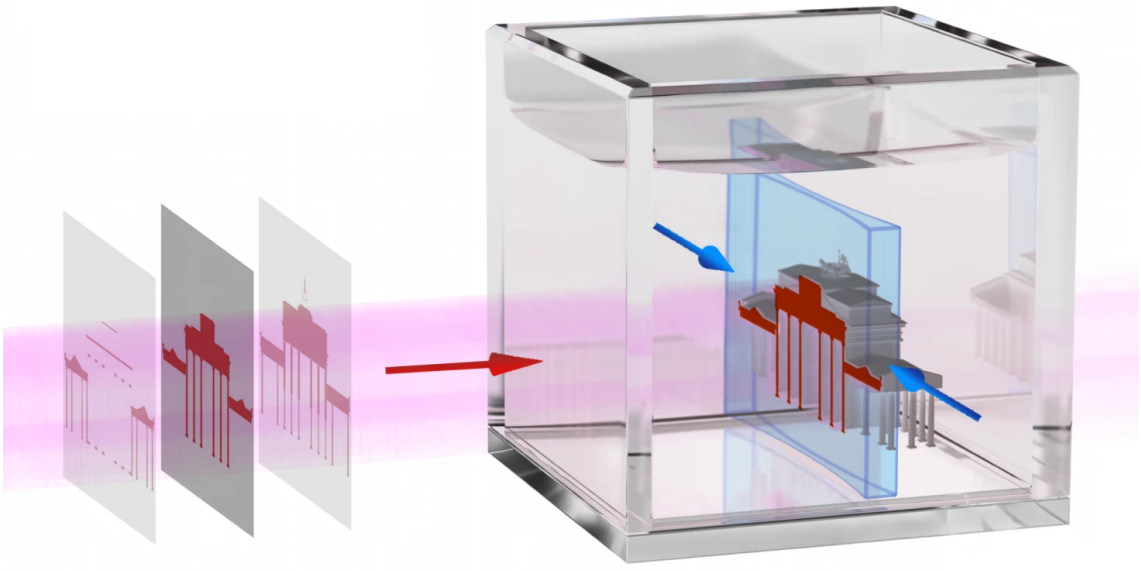


Figure 2.2: *Vat photopolymerization method utilizing two colours of light to initiate polymerization. Blue arrows indicate a thin layer of light, which brings the photoinitiator to its intermediate state, and the red arrow indicates the incoming light that finally activates the photoinitiator and causes polymerisation. Image is adapted from Regehly et al. [52].*

Photoinitiator and photoinhibitor activated by separate colours were used in 2009 to achieve subdiffraction photolithography [54]. Only fairly recently has this use been adapted for 3D printing. As with the other method, the photoinitiator and photoinhibitor must be activated by different wavelengths and their absorption spectra should not overlap at wavelengths used. Thus one wavelength activates polymerisation and the other suppresses it. The principles of object generations, on the other hand, are inverted. Li et al. [55] have demonstrated a layer by layer approach where the active layer is not illuminated by the suppressing light. Whereas the rest of the volume is illuminated by the suppressing light parallel to the active layer. The layer is then polymerized by projecting its image with the activating wavelength perpendicularly to the suppressing light. By translating the gap in the suppressing illumination and changing the layer image the entire object is poly-

merized. Van der Laan et al. [56] demonstrated the use of a photoinitiator and photoinhibitor system by generating a 3D object through general confinement instead. In their case two images of the object were projected perpendicularly to each other within the build volume. The volume represented by the intersection of the column of activating light and the column of the negative of suppressing light is polymerized, which generates a free standing object. The geometry of printable objects in this case is quite limited.

Volumetric Vat Photopolymerization

Volumetric vat photopolymerization refers to methods where the entire object is polymerized at once. To some extent work done by Van der Laan [56] could be characterized as such. However, a much superior method has been developed by Kelly et al. [57] by employing tomographic reconstruction (Figure 2.3). The method is essentially a reverse of a computed tomography scan (CT scan). A cylindrical vat representing the build volume is filled with a photopolymer and immersed into a larger rectangular vat, which is filled with a refractive index matching fluid. Index matching is used to prevent the refraction of light, which would distort the projected image used to polymerize the object. As the inner vat is rotated, the projected image changes to match the object as viewed from that direction. The distribution of intensity in each image is such that it corresponds to the thickness of the object as its viewed from that direction. By fine tuning the intensity of the incident light the object suddenly appears in the build volume after one full rotation as the threshold for polymerization is reached everywhere at the same time. As with other methods that generate objects suspended in the build volume, printing support is not needed. Likewise, the attenuation of the photopolymer should be adequate in order for incident light to span the entire build volume. From the premise of its operation this approach is poised to be the fastest 3D printing method of all. Volumetric vat photopolymerization has also been successfully utilized by Bernal et al. [58, 59] to print objects using bioink laden with cells. The resulting objects had a high cell viability of 85% and greater.

2.4 Biological light response systems

Almost all living organisms can detect and respond to light. Light response systems typically consist of a sensor, which responds to light and a response-regulator [60]. In the world of plants, bacteria and even fungi there are two classes of light response systems: phytochromes and cyanobacteriochromes (CBCR). Phytochromes are sensitive to red and far red light and can be found in all three groups. On

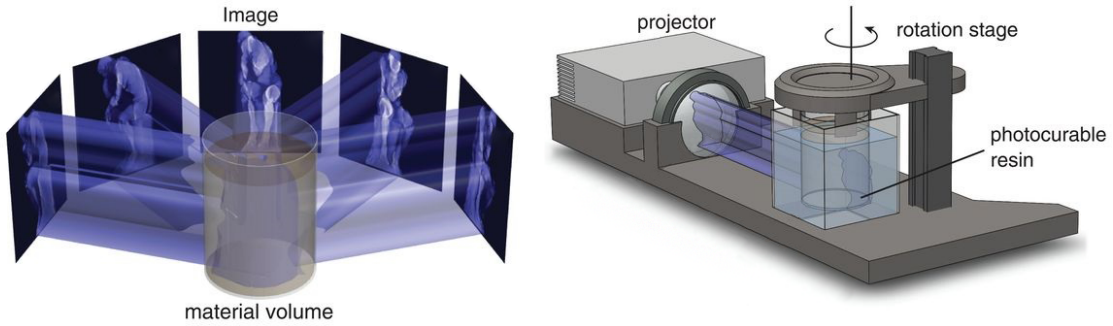


Figure 2.3: *Volumetric vat photopolymerization method utilizing tomographic reconstruction. Left, illustration of individual images of the object from the respective angle, modulated by the required intensity distribution. Right, representation of the 3D printer. Image is adapted from Kelly et al. [57].*

the other hand, cyanobacteriochromes can only be found in cyanobacteria and can respond to a wider range of wavelengths [61]. The light sensor in CBCRs includes a domain, which allows chromophore incorporation and proper photoconversion. The most common chromophores present in CBCRs are phycoviolobilin (PVB), phycocyanobilin (PCB), phytochromobilin (PΦB), and biliverdin (BV) [62]. In general, chromophores determine the sensing wavelengths. The response regulator in light response systems is a protein that can elicit a change in a cell in response to changes in its environment. Commonly these regulators are transcription factors and once activated initiate transcription of the corresponding gene. These components can be individually altered or switched out for different components to generate new light response systems. A few of these artificial light response systems include CcaSR, Cph8-OmpR and YF1-FixJ [63, 64, 65].

Of particular interest is the CcaSR light response system. CcaSR is a two-component signal transduction system that can be activated by green light and deactivated by red light. CcaS is the light sensor and CcaR is a transcription factor that acts as the response regulator. Under green light CcaS undergoes phosphorylation and switches to a red light absorbing conformation. In this state it is able to phosphorylate CcaR. Once phosphorylated, CcaR binds to the $P_{cpcG2-172}$ promoter, where it activates transcription of the gene of interest. By incorporating this system in *E. coli*, precisely controlled gene expression can be achieved through green and red light manipulation [66]. Olson et al. [67] have performed a detailed characterisation of the CcaSR system in *E. coli*, which importantly included the determination of the forward and reverse photoconversion rate of CcaS for the entire visible spectrum. Furthermore, they verified their measurements against an optogenetic model, which includes light interaction and gene expression. Initial versions of CcaSR were improved on by Ong and Tabor [68] to increase the dynamic range of gene expression. They named it CcaSR v3.0, which is the system used in this work.

2.5 Optogenetic Model

An optogenetic model describing the CcaSR two-component system's interaction with different light wavelengths and intensities implemented by Olson [67] is derived here. The CcaS component of the light response system will be referred to as the photoreceptor from now on. In order to quantify the effects of various wavelengths of light on gene expression the model includes two rate equations for ground-state and active-state photoreceptor populations:

$$\frac{dS_g}{dt} = k_{growth}S + (k_2 + k_{dark})S_a - k_1 S_g \tag{2.1}$$

$$\frac{dS_a}{dt} = k_1 S_g - (k_2 + k_{dark})S_a \tag{2.2}$$

where $S = S_g + S_a$, S_g and S_a are the total, ground-state and active-state photoreceptor populations respectively, k_{growth} is the rate at which new photoreceptors are being produced, k_{dark} is the dark reversion rate at which an active-state photoreceptor spontaneously reverts to ground-state, k_1 is the forward photoconversion rate at which light converts ground-state photoreceptor to the active-state and k_2 is the reverse photoconversion rate at which light converts the active-state photoreceptors back to ground-state. The total photoreceptor population is proportional to the cell population and as the cells grow they produce new ground-state photoreceptors. As the growth of the cell population depends on the number of cells, so does the change in number of photoreceptors depend on the number of photoreceptors. The growth rate k_{growth} of ground-state photoreceptors is thus the same as the growth rate of cells. The dark reversion rate k_{dark} for CcaSR was reported to be negligible [67, 69] and can be set to zero. The forward and reverse photoconversion rates both k_1 and k_2 depend on intensity of light and its wavelength: $k_i = I\hat{k}_i(\lambda)$ where I is the light intensity and $\hat{k}_i(\lambda)$ is the photoconversion rate per unit of light intensity at wavelength λ.

Equations (2.1) and (2.2) can be combined into a rate equation for the fraction of active-state photoreceptors compared to the total photoreceptor population $\eta(t) = \frac{S_a(t)}{S(t)}$:

$$\frac{d\eta(t)}{dt} = k_1 - \left(k_1 + k_2 + k_{growth}\right)\eta(t)\,. \tag{2.3}$$

Provided that k_1, k_2 and k_{growth} are constant on the time interval of integration, then (2.3) has the following solution:

$$\eta(t) = \eta_0 + \left(\frac{k_1}{k_{sum}} - \eta_0\right)\left(1 - e^{-k_{sum}t}\right) \tag{2.4}$$

where η_0 is the initial fraction of active-state photoreceptors and k_{sum} equals the

sum of all rates $k_{sum} = k_1 + k_2 + k_{growth}$. According to the above solution, the steady-state fraction of active-state photoreceptors is equal to the ratio between the forward photoconversion rate and the sum of all rates $\frac{k_1}{k_{sum}}$. In other words the steady-state fraction equals the fraction of the intensity of the activating light intensity versus the sum of intensities of the activating and deactivating light and the growth rate of cells.

If the photoreceptors are left in the dark ($k_1 = k_2 = 0$), then the steady-state fraction of the active-state photoreceptors is zero and it is approached exponentially with the growth rate of cells (Equation (2.5)). This is in accordance with the fact that as the cells grow new ground-state photoreceptors are being produced and over time the active-state photoreceptors become more and more diluted.

$$\eta(t) = \eta_0 e^{-k_{growth}t} \tag{2.5}$$

If the photoreceptors are illuminated with only the activating light ($k_2 = 0$), then the steady-state fraction of the active-state photoreceptors depends on the intensity of light when compared to rate of growth. If the cell population was constant the steady-state fraction would equal 100% regardless of the activating light's intensity, only affecting the rate of exponential decay (Equation (2.6)). However, as the cells grow the steady-state fraction of active-state photoreceptors is never 100% due to constant addition of ground-state photoreceptors. The activating light has to be intense enough to overcome the growth rate of cells to achieve a sufficiently high fraction of active-state photoreceptors.

$$\eta(t) = 1 - e^{-k_1 t}, \qquad \eta_0 = 0,\ k_{growth} = 0 \tag{2.6}$$

If the photoreceptors are illuminated only by the deactivating light ($k_1 = 0$), then the steady-state fraction of the active-state photoreceptors is zero. In this case the deactivating light's intensity only affects the rate at which the initial fraction of active-state photoreceptors decays to zero (Equation (2.7)).

$$\eta(t) = \eta_0 e^{-(k_2 + k_{growth})t} \tag{2.7}$$

Note that when a near zero fraction of active-state photoreceptors is required, it is more efficient to turn the activating light off rather than to increase the intensity of the deactivating light, as the reverse photoconversion rate k_2 would need to be a significant multiple of the forward photoconversion rate k_1.

The Hill function that depends on the ratio between the active-state and ground-state photoreceptors was used by Olson to connect the fraction of active-state photoreceptors to the gene expression rate of the target gene of the CcaSR system:

$$k_{ex}(t) = b + a\frac{R^n(t-\tau)}{K^n + R^n(t-\tau)} = b + a\,h(t) \tag{2.8}$$

where b is the minimum gene expression rate or the background, a is the maximum expression rate induced by the active-state photoreceptors, n is the Hill coefficient, $R = S_a/S_g = \eta/(1-\eta)$ is the ratio between active-state and ground-state photoreceptors, half-maximum parameter, K, is the ratio S_a/S_g at which induced expression is at 50% and τ is the delay between the change of the state of photoreceptors and the change in gene expression rate. $h(t)$ is the normalized Hill function, which will be referred to as only the Hill function. The gene expression rate (Equation (2.8)) encompasses all steps between active-state photoreceptors and protein production. These steps include histidine kinase autophosphorylation, phosphotransfer, response regulator dimerization, DNA binding, promoter activation, and protein production.

To determine the total gene expression density, which is the cumulative gene expression per volume after a given amount of time, the gene expression rate in each individual cell is multiplied by the number density of cells:

$$\frac{dg(t)}{dt} = k_{ex}(t)\rho_{cells}(t) \tag{2.9}$$

where g is the total gene expression density and ρ_{cells} is the number density of cells. If $k_{ex}(t)$ is constant and the growth rate of cells is exponential then the solution is also exponential:

$$g(t) = \frac{k_{ex}}{k_{growth}}\rho_0\left(e^{k_{growth}t} - 1\right), \qquad g(0) = 0 \tag{2.10}$$

where ρ_0 is the initial cell number density.

If gene expression rate and cell population are constant the solution to (2.9) is a linear function of time. However, gene expression during the lag phase of cell growth, where the population is largely constant, is very limited. Although cells can divide and maintain a constant population in the stationary phase, their metabolism is not necessarily the same as in the exponential phase. This suggests that parameters a and b in this formulation of (2.8) have to depend on the metabolism of the cell. Equation (2.9) with constant a and b is thus only valid during the early exponential phase where the death rate of cells can be neglected. The equations could be expanded to include the entire growth cycle of cells by introducing time dependant parameters a and b, and a cell death rate.

2.6 Parameter Values of CcaSR in *E. coli*

Flow cytometry measurements on *E. coli* with the CcaSR v2.0 light response system grown in a liquid medium were performed by Olson [67]. *E. coli* with the CcaSR v2.0 was exposed to light under different illumination protocols, which provided information about the specific photoconversion rates $\hat{k}_1$ and $\hat{k}_2$. Reported values for these rates are shown in Table 2.1 along with the results for the Hill parameter, n, half-maximum parameter, K, and growth rate, k_{growth}. Measurements of these parameters for the CcaSR v3.0 were preformed by Ong and Tabor [68]; however, while they do not report the values for $\hat{k}_1$ and $\hat{k}_2$ directly, they performed a time-varying measurement comparing the response of both versions of CcaSR to green 520 nm and red 660 nm light. The measurements showed statistically similar results, which suggest that the photoconversion rates are the same in both versions of CcaSR.

The parameter values of the optogenetic model used in this work are listed in Table 2.1. The reported values a and b were not used, as they are expected to differ due to a different protein production and a different metabolism – the bacteria here were suspended in hydrogel in anaerobic conditions.

Table 2.1: *Parameter values used in the optogenetic model and values reported by Olson [67] and Ong and Tabor [68]. The value of K for CcaSR v3.0 was reported in terms of photon flux, the value shown below was calculated by comparing it to the measurement of K for CcaSR v2.0 from the same report under the assumption that the growth rate [70] and $\hat{k}_1$ [68] were the same. The MEFL units are molecules of equivalent fluorescein. Units of the photoconversion rates are the conversion rate per photon flux.*

Parameter	CcaSR v2.0 [67]	CcaSR v3.0 [68]	Values Used	Units
a	9.7 ± 0.1	15.74 ± 0.53	1	10^4 MEFL
b	0.165 ± 0.002	0.0267 ± 0.0027	0	10^4 MEFL
K	0.319	0.43 ± 0.03*	0.43	–
n	2.11 ± 0.02	2.74 ± 0.04	2.7	–
k_{growth}	1.85 ± 0.01	–	0.96	$10^{-2} min^{-1}$
$\hat{k}_1(516\ nm)$	10.7 ± 0.5	–	10.7	$10^{-3} \frac{1}{min} \frac{m^2 s}{\mu mol}$
$\hat{k}_2(657\ nm)$	4.6 ± 0.3	–	4.6	$10^{-3} \frac{1}{min} \frac{m^2 s}{\mu mol}$

2.7 Summary

The widespread use and active research into microbial cell factories greatly compliments the development of a 3D printing method that utilizes said microbes to generate objects. The wide variety of biological and synthetic materials available in this way may seriously compete with materials that are available to conventional 3D printing. While 3D bioprinting methods have seen steady improvements in both bioink and resolution in all three main categories of material extrusion, material jetting and vat photopolymerization, there has yet been a method that exploits microbes in their ideal environment without the need for other potentially toxic additives. Advanced vat photopolymerization methods have been developed where objects can be printed without support within the build volume and even volumetrically. However, when used for bioprinting, the bioinks also require photoinitiators and potentially other additives to facilitate the printing process. It is in contrast to these methods that the method investigated in this work was proposed. The method is made possible with a detailed characterisation of a light response system, CcaSR, which allows for controlled gene expression through illumination of different colours of light. Importantly, the knowledge of the relevant parameters allows the employment of an optogenetic model, which is instrumental in determining the distribution of gene expression as a result of illumination.

Chapter 3

Equipment, Materials and Methods

Equipment, Materials and Methods provides a description of the materials and methods used to prepare the bacterial culture and the hydrogel, the custom designed 3D printing equipment, the experimental procedure, experiment data collection methods and experiment simulation methods. The 3D printing equipment is split into the mechanical apparatus, which provides mechanical support and facilitates three-dimensional movement; the optical apparatus, which generates and shapes the laser beams and maintains their optical power; and the control and communication apparatus, which synchronizes the mechanical and optical apparatus and provides an interface to the user. Figure 3.1 shows a render of the 3D printing equipment consisting of all three apparatuses, excluding the desktop computer.

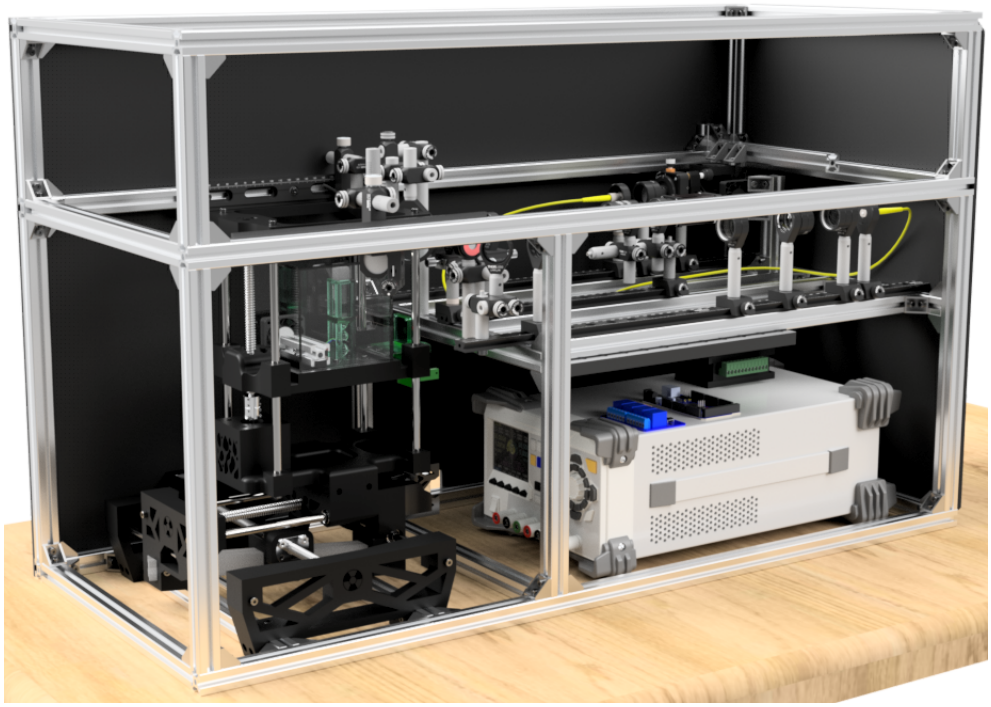


Figure 3.1: *Render of the 3D printing equipment used for experiments.*

3.1 Sample Preparation

3.1.1 Culture Preparation

Culture preparation was carried out by Andreas Hadjimitsis. The bacteria used in all experiments in this work are TOP10 *E. coli* (OneShot, Thermo Fisher Scientific). They were chemically transformed, according to the manufacturer's protocol, with two plasmids – pNO286-3 (Plasmid #107746, Addgene) and pSR58.6 (Plasmid #63176, Addgene). pSR58.6 was modified where the *sfgfp* gene was replaced by the *tdFast2* gene using start-stop assembly [71]. The transformed bacteria were plated on a clean LB-agar (MILLER, Sigma Aldrich) petri dish with two antbiotics – chloramphenicol (CAS 56-75-7, C0378, Sigma Aldrich) and spectinomycin (CAS 22189-32-8, vS4014, Sigma Aldrich). A single colony from the petri dish was grown for half a day and then mixed with a 1:1 glycerol and water solution, which was then stored at $-80°C$. These cells were then streaked on a petri dish to be used in culture sample preparation.

The culture samples were prepared by growing bacteria from a single petri dish colony. This was done by adding 4 ml of M9x1 medium to a culture tube. The M9x1 medium consists of distilled water, 11.3 g/l M9 minimal salts (MP Biomedicals), 2 g/l casamino acids (MP Biomedicals), 0.25 g/l thiamine hydrochloride (CAS 67-03-8, T4625, Sigma Aldrich), 2 mM $MgSO_4$ (Sigma Aldrich), 0.1 mM $CaCl_2$ (Sigma Aldrich) and 8 g/l glucose (Sigma Aldrich). The two antibiotics were also used in preparation. Chloramphenicol was dissolved in ethanol with a concentration of 34 $\mu g/ml$ and spectinomycin was dissolved in double distilled water with a concentration of 100 $\mu g/ml$. 4 μl of both were added to the medium, ensuring only cells with plasmids would be able to proliferate. Following that, the cells were scraped from the petri dish and added to the medium. The culture tube was then capped, wrapped in aluminium foil and placed into a shaking incubator at $37°C$ for about half a day.

3.1.2 Hydrogel Culture Preparation

Hydrogel culture preparation was supported by Andreas Hadjimitsis. Hydrogel culture was prepared by first measuring the optical density at 700 nm (OD_{700}) of the culture sample that was left to incubate. The OD_{700} was measured in a spectrophotometer (WPA Biowave II, Biochrom) using a polystyrene (PS) cuvette (Cuvette Macro Square - Kartell, Better Equipped Educational Supplies). The baseline used was the M9x1 medium. The measured $OD_{700} \in [1.5, 2]$ determined the volume of the culture sample that was used to prepare the hydrogel culture with an OD_{700} of 0.005. This OD_{700} equates to cell number density of $2.25 \times 10^4 \pm 4 \times 10^3$ cells μl^{-1},

which was determined using the microspheres method [72].

Secondly, M9x2 medium was pipetted into a falcon tube – 2 *ml* for each cuvette to be filled with hydrogel culture. Both antibiotics were added in a 1:1000 ratio in comparison to the total hydrogel culture volume. To enable imaging of the protein produced by the bacteria, fluorogenic ligand HMBR (^{TF}Lime, The Twinkle Factory) was added, which binds to tdFAST2. 250 *nmol* of the fluorogenic ligand was dissolved in 50 μl of Dimethyl sulfoxide (DMSO) and then added to the solution in a 1:2000 volume ratio compared to the total hydrogel culture volume.



Figure 3.2: *Render of hydrogel culture filled cuvette.*

Finally, 2% (w/v) agarose (CAS 39346-81-1, A4018, Sigma Aldrich) hydrogel was heated up to 60°C and mixed with the previously prepared medium solution in a 1:1 volume ratio. Before the mixture cooled down, 4 *ml* was pipetted into a cuvette as a control sample. A small volume (determined by the OD_{700}) of the culture sample was added to the remaining mixture forming the hydrogel culture with a target cell number density equivalent to OD_{700} of 0.005. Lastly, 4 *ml* of the prepared hydrogel culture was pipetted into each cuvette (Figure 3.2). The hydrogel culture filed cuvettes were stored by being wrapped in aluminium foil and placed in a refrigerator at 4°C. The hydrogel culture preparation is summed up in Figure 3.3.

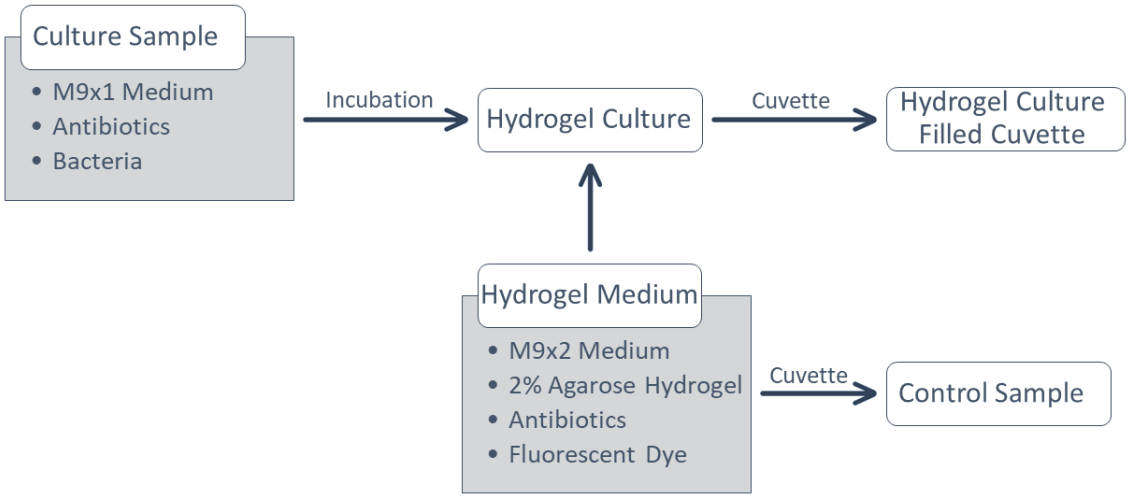


Figure 3.3: *Flow chart depicting stages of hydrogel culture preparation.*

3.2 Mechanical Apparatus

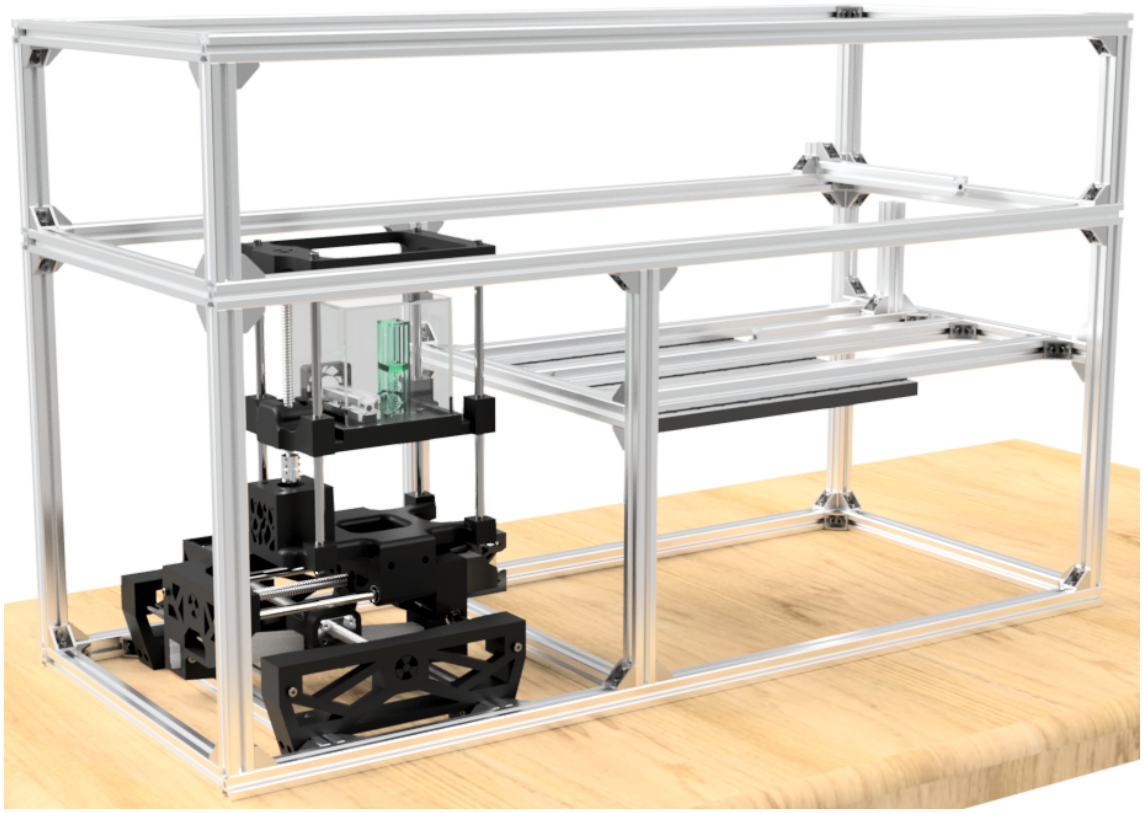


Figure 3.4: *Render of the mechanical apparatus – the translation system and the main support structure.*

The mechanical apparatus consists of the translation system and the main support structure made from aluminium profiles, which physically joins the optical apparatus and the translation system (Figure 3.4). The translation system further divides into three translation stages and an incubation chamber.

The translation stages are positioned orthogonally to each other, each actuating along its respective coordinate axis – X, Y and Z (Figure 3.5). The translation stages consist of:

- plastic support structures,
- a ball nut and a ball threaded screw (AluFlex),
- tapped 8 *mm* steel guide rods (Misumi), and
- a nema 17 stepper motor (FL42STH47-1206A).

The plastic support structures were custom designed in Fusion 360 (Autodesk) and 3D-printed with PLA using a material extrusion (MEX) 3D printer (LulzBot TAZ 6, Fargo Additive Manufacturing Equipment 3D). The plastic support structures

connect the three stages through the ball threaded screw, the ball nut and the steel guide rods. Furthermore, they connect the translation system to the main support structure, fix the incubation chamber to the Z-translation stage and house the motors. The ball threaded screw is fixed to the motor with a shaft coupler on one side and a ball bearing on the other side. The ball threaded screw with the ball nut ensure a smooth transition from motor rotation to linear actuation. This motion is facilitated by the steel guide rods, which are bolted to the plastic support structure.



Figure 3.5: *Render of the individual axes of the translation system and the accompanying support structure.*

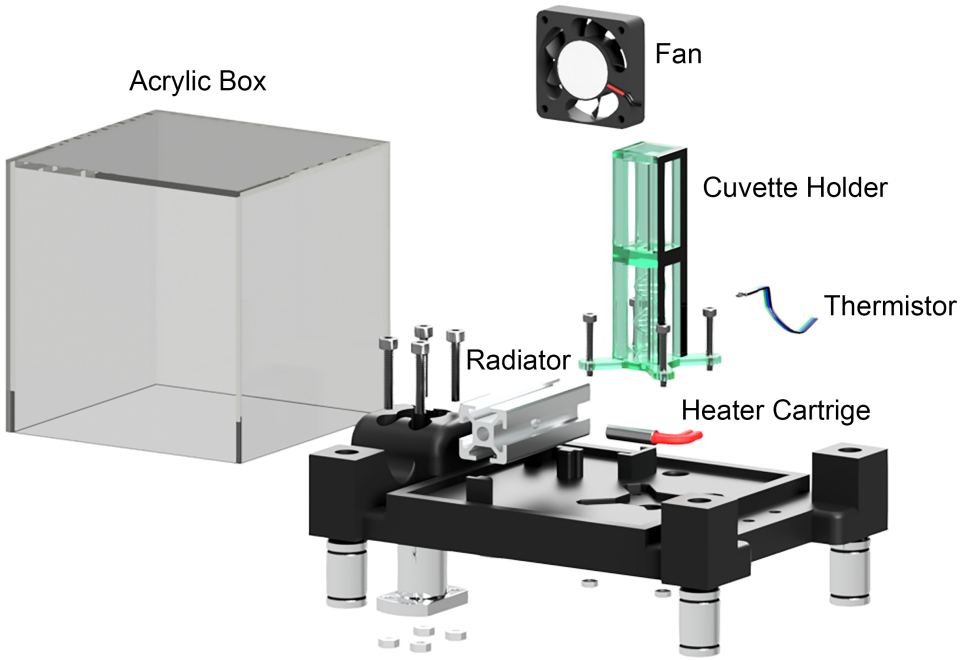


Figure 3.6: *Exploded view of the incubation chamber.*

The incubation chamber (Figure 3.6) facilitates temperature control and houses a cuvette within which is the build volume. The cuvette has interior dimensions of $1 \times 1 \times 3$ cm that represent the usable build volume. The walls of the cuvette are 1 mm thick. The exterior of the incubation chamber consists of a plastic platform covered by a transparent acrylic box. The plastic platform is mounted directly onto the Z-translation stage ball nut and the corresponding steel guide rods. The interior of the incubation chamber consist of a custom designed cuvette holder printed by a material jetting 3D printer (Objet500, Stratasys), an NTC thermistor (MF52D-103f-3950), a fan (FH4010SH) and a heater cartridge (salvaged from a LulzBot TAZ 6 hotend) inserted in a heat sink. The heat sink is an aluminium profile cut to size with a hole drilled in the centre to accommodate the heater cartridge. The heat sink and air circulation help maintain a more even temperature distribution within the chamber.

3.3 Optical Apparatus

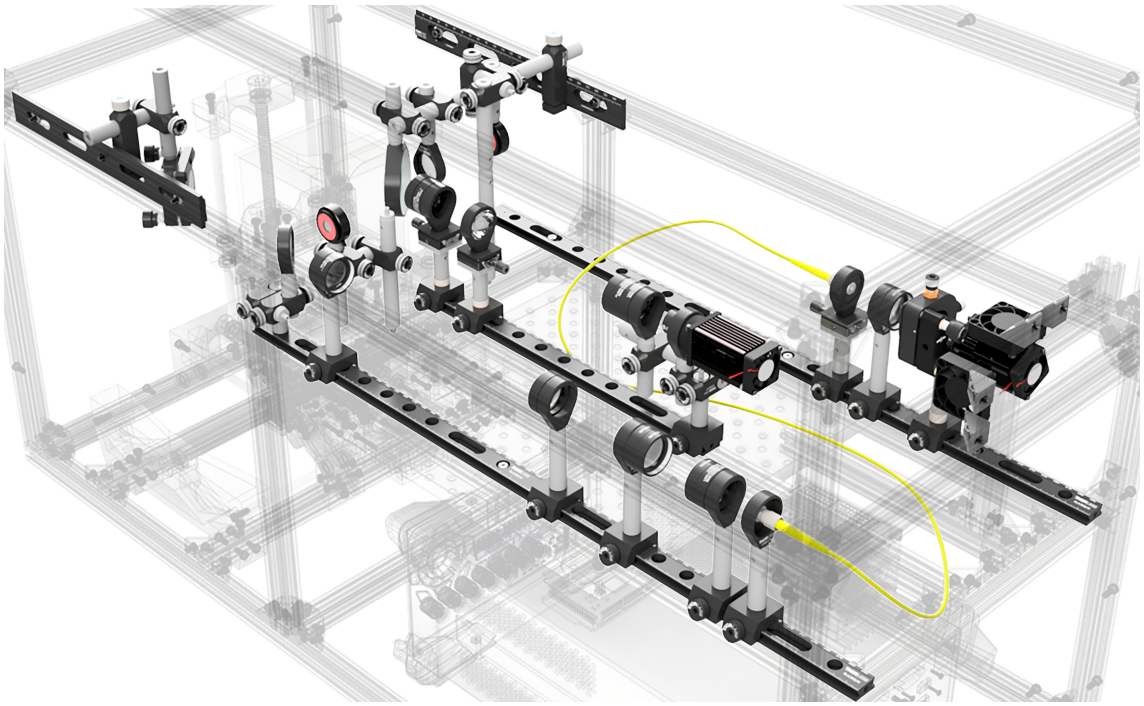


Figure 3.7: *Render of the optical apparatus.*

The optical apparatus consists of the green 515 nm and red 650 nm laser optical systems (Figure 3.7) and the optical power measurement equipment. The systems are mounted directly to the aluminium profiles of the main support structure but are otherwise separate. Black panels (Foamex, KJN Automation) were fixed to the exterior of the main support structure to block any ambient light from interfering with the experimental process.

3.3.1 Green Laser Optical System

The green 515 ± 5 nm light was generated by a 50 mW green diode laser (OFL299, OdicForce). The laser beam was focused and coupled into a single mode fibre optic cable (P1-405B-FC-1, Thorlabs). The beam emitted by the fibre optic cable was then transported and focused by a series of lenses and a mirror to the build volume.

The measured initial optical power output of the laser is 33.0 ± 0.5 mW, which stabilizes at 43.5 ± 0.5 mW. The optical power and the intensity profile of the beam produced by this laser are sensitive to temperature. A varying intensity profile significantly alters coupling efficiency of the laser beam into a fibre optic cable. A lower and more stable temperature is maintained with a heat sink and a fan that are part of the laser. To avoid shaking produced by the laser's fan, it was stopped. Instead, two additional fans were mounted to the main support structure and directed towards the heat sink but were otherwise physically separate (Figure 3.8).

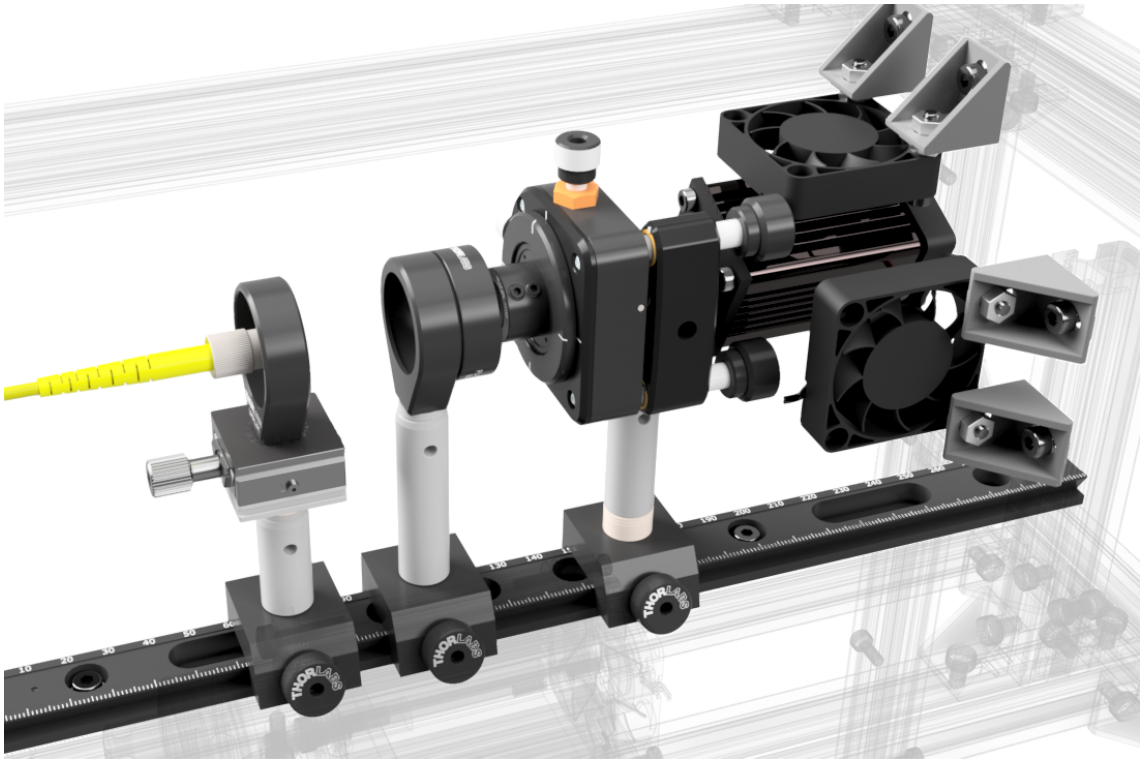


Figure 3.8: *Render of the green laser fibre launch.*

The light intensity profile of the green laser when focused is elliptic and non-homogeneous. A better light intensity profile was obtained by coupling the laser into a single mode fibre optic cable shown in Figure 3.8, which resulted in a near Gaussian light beam at the output. The diameter of the beam exiting the laser is 4 mm and the mode field diameter of the fibre optic cable is 2.5 - 3.4 μm. The beam was focused into the fibre optic cable by a spherical lens with the focal length of 40 mm (LA4306-ML, Thorlabs). Proper alignment and consequently good coupling

was enabled by mounting the laser to a 5-axis kinematic optic mount (K5X1, Thorlabs). An adapter, that allowed fixing the laser into a mounting adapter (AD11F, Thorlabs) screwed into the kinematic optic mount, was custom designed and printed using the MEX 3D printer. The kinematic optic mount allows translation in the plane perpendicular to the optical path, pitch and yaw angle adjustments. The kinematic optic mount, the lens mount (LMR1/M, Thorlabs) and the fibre optic cable mount (SM1FC and LMR1/M, Thorlabs) were attached to optical posts (TR50/M, Thorlabs) and dovetail rail carriers (RC1, Thorlabs). These assemblies were then placed on a dovetail rail (RLA300/M, Thorlabs), which ensures some alignment and allows rough movements. The fibre optic cable mount was also placed on a single-axis translation stage (DT12/M, Thorlabs), which allows finer adjustments along the optical path. The coupling efficiency achieved with these components and fine tuning was approximately 10%.

The near Gaussian beam exiting the fibre optic cable was focused using a series of lenses to a spot within the build volume. The build volume is approximately 20 *cm* from the position of the last lens on the optical path and the target beam waist diameter was 1 *mm*. Parameters to satisfy these conditions were determined by using the ABCD matrix analysis for a Gaussian beam. Two conditions require two varying parameters, which were chosen to be two distances between the lenses. To determine these distances, three ideal lenses were used in the ABCD matrix analysis and the ray transfer matrix $\boldsymbol{M}$ of such a system is then:

$$\boldsymbol{M} = \begin{bmatrix} A & B \\ C & D \end{bmatrix} = \boldsymbol{T}_4\boldsymbol{L}_3\boldsymbol{T}_3\boldsymbol{L}_2\boldsymbol{T}_2\boldsymbol{L}_1\boldsymbol{T}_1, \tag{3.1}$$

where $\boldsymbol{T}_i$ are ray transfer matrices of free space and $\boldsymbol{L}_i$ are ray transfer matrices of lenses. By choosing three lenses and fixing other parameters except the two distances between the lenses, the following system of equations can be numerically solved, provided that a solution for the distances exist:

$$BD + ACz_{R_1} = 0, \tag{3.2}$$

$$w_{02}^2 n_2 = \frac{w_{01}^2 n_1}{AD - BC}\left(A^2 + \frac{B^2}{z_{R_1}^2}\right), \tag{3.3}$$

where w_{01} is the beam waist radius of the incoming beam, w_{02} is the beam waist radius of the outgoing beam, n_1 is the refractive index at the input, n_2 is the refractive index at the output and z_{R_1} is the Rayleigh length of the incoming beam.

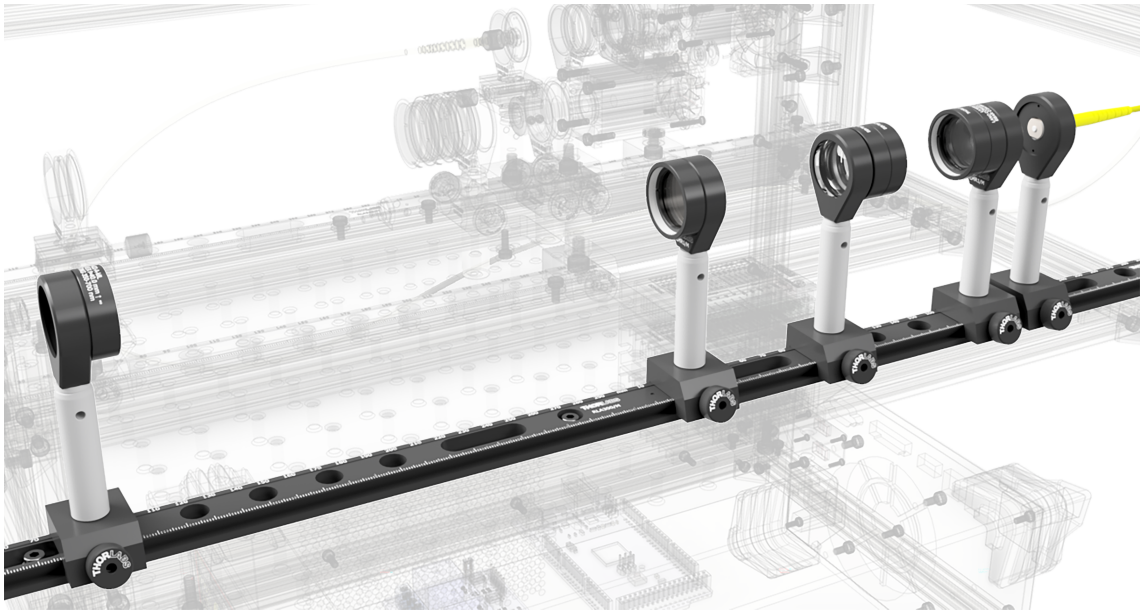


Figure 3.9: *Render of the lenses focusing the green beam exiting the optic fibre cable. The optical element second from the right is a polarizer, which is part of the optical power measurement equipment (Chapter 3.3.4)*

The solutions of the system of equations above were used as a rough guide for the real optical system. Following the solutions of (3.2) and (3.3) five lenses were chosen. Two lenses with a focal length of 75 mm (LA4725-ML, Thorlabs) with a fixed distance between them were placed after the optic fibre cable, collimating the exiting beam. Next in the optical path another lens with a focal length of 75 mm was used, followed at a fixed distance by a lens with a focal length of -75 mm (LC4513-A, Thorlabs). The last lens in the optical path used has a focal length of 40 mm (LA4306-ML, Thorlabs). All lenses were mounted on lens mounts, optical posts and dovetail rail carriers and put on a dovetail rail, allowing the lenses to be properly spaced apart (Figure 3.9).

The beam produced by the system had a beam diameter of nearly 1 mm at the center of the build volume. The position of the last lens was slightly corrected to further tune the system, which brought the beam diameter closer to 1 mm. However, adjustment of the position of a single lens affects the focus position and the beam waist diameter. Adjusting the beam diameter shifted the focus position beyond the build volume, resulting in a converging beam within the build volume. The divergence angle θ and the Rayleigh length z_R of a beam with a beam waist diameter of approximately 1 mm are small and large respectively. The beam was thus convergent with a diameter of 1.15 ± 0.05 mm at the entry point of the build volume and 1.05 ± 0.05 mm at the exit. A mirror (BB1-E02, Thorlabs) was used to deliver the beam to the build volume at a 90 deg angle relative to initial optical path. This mirror was also used to align the beam with the X-translation stage and maintain a perpendicular position relative to the build volume.

3.3.2 Red Laser Optical System

The red 650 ± 5 nm light was generated by a 200 mW red diode laser (OFL384-V2, OdicForce). The beam has a flat-top shaped intensity profile, which was collimated by an adjustable built-in collimating lens to 4 mm in diameter. The measured optical power output of the laser was 170 ± 2 mW.

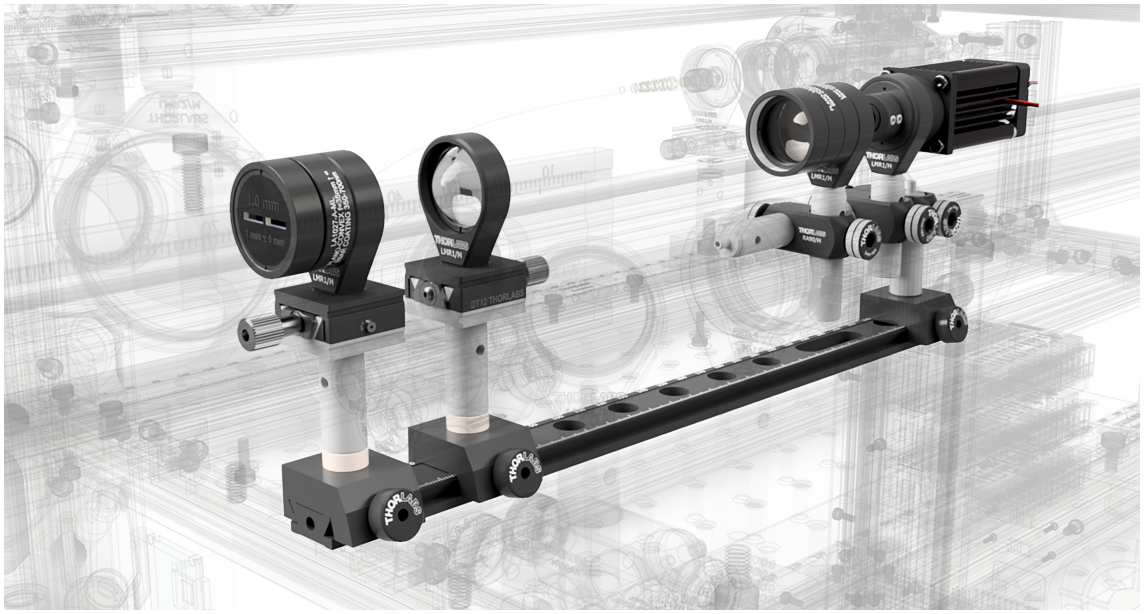


Figure 3.10: *Render of the red laser optical system. The beam shaping black screen with two slots is shown mounted on the leftmost post.*

The laser was mounted on a custom designed and MEX 3D-printed adapter that fits into another mounting adapter (AD16F, Thorlabs) that screws into a lens mount. The entire assembly was attached to an optical post and a dovetail rail carrier. The beam was expanded and collimated by a set of four lenses. The first two lenses with focal lengths of 75 mm (LA4725-ML, Thorlabs) and 40 mm (LA4306-ML from Thorlabs) were mounted on a lens mount, which was in turn attached to the optical post, that supports the laser assembly, via two optical posts and two 90° angle post clamps (RA90/M, Thorlabs). These two lenses were used to expand the beam to 2 cm in diameter, which was then collimated using the next two lenses. The first lens is an aspherical collimating lens with a focal length of 16 mm (ACL25416U-A, Thorlabs), followed by a lens with a focal length of 35 mm (LA4052-ML from Thorlabs). Both lenses were mounted, via a lens mount, on a translation stage (DT12/M, Thorlabs), which allows fine movement. The translation stages were attached to two separate optical posts and dovetail rail carriers, which were placed on the same dovetail rail as the laser assembly. The collimated beam was masked by a screen placed right after the last lens on the optical path. It was slotted into a lens tube (SM1L05, Thorlabs), which was screwed to the lens tube of the last lens.

The screen is a circular disc with two collinear slots positioned around the center (Figure 3.10), it generates a band of light with gap in the middle. The position of the last two lenses was finely adjusted so that the projected image of the screen was about double the size of the build volume at its centre at ≈ 13 *cm* away from the screen.

The optical paths of the green and red laser optical systems are roughly at the same height and intersect at the centre of the build volume. Discrepancy between the positions of the two optical paths was corrected by fine adjustments of the mirror on the green laser's optical path. The adjustments were such as to achieve the best orthogonality between both optical paths and the build volume in all directions.

3.3.3 Localized Volume through Light Overlap

A core requirement of three dimensional additive manufacturing is a volume localized in all three dimensions. It represents the smallest unit of the manufacturing process and its resolution.

The build volume in the experimental setup is filled with the hydrogel culture contained by a cuvette. It is homogeneous in all directions and remains mechanically unaltered throughout the experimental process. As such, the build volume does not provide any degree of localization. Localization was instead achieved with light distribution and its interaction with the medium – the photoreceptors.

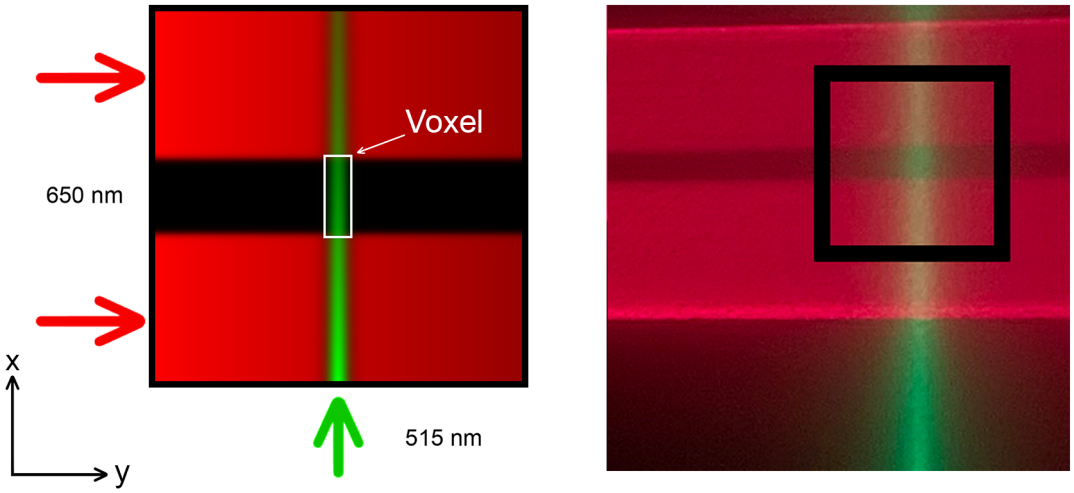


Figure 3.11: *Schematic and a picture of the green and red light overlap in the X-Y plane. The picture was taken in-situ by filling the area with fog. The alignments of the cuvette and the directions of incoming light are all perpendicular within* 1° *to* 3°*. In the Z-direction (not shown) the green light beam is positioned at the centre of the red light. The black square in the picture represents the* $12\ mm \times 12\ mm$ *cross section and* $1\ mm$ *thick walls of a cuvette.*

When green light illuminates the build volume it activates the photoreceptors in the cells along its entire optical path forming a localized volume in the shape of an *infinite* cylinder providing localization in two dimensions. The last dimension is constrained by a band of red light with a gap in the middle. The overlap of the two beams is shown in Figure 3.11. The volume where only green light is present within the build volume is the only location where gene expression is desired. This localized volume will be referred to as the voxel. The volume where green light enters and exits the voxel is overlapped by red light, which inhibits gene expression. This interaction of light with the photoreceptors allows the creation of the localized volume.

3.3.4 Optical Power Measurement Equipment

The red and the green lasers' average optical power output was controlled by means of TTL modulation and in situ optical power measurements, measured by two optical power meters (PM16-120 and PM16-121, Thorlabs). In both optical systems the beams were split using a beam splitter, before entering the incubation chamber (Figure 3.12).

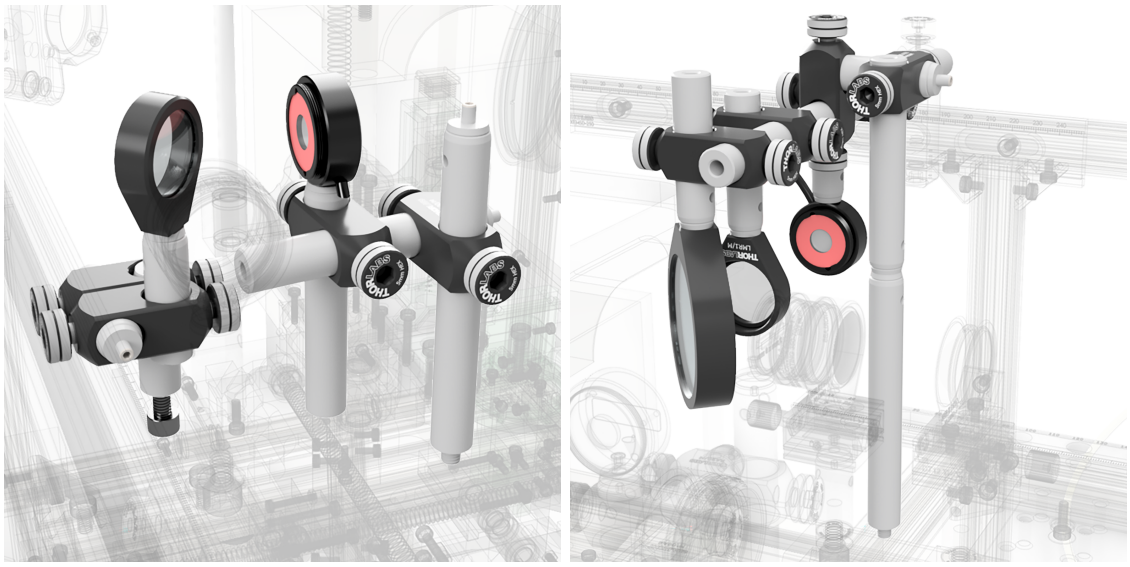


Figure 3.12: *Render of the optical power measurement equipment for the green (left) and red beam (right).*

The green laser beam was split using a 50:50 beam splitter (EBS1, Thorlabs), designed to reflect half the light towards the optical power meter. The red beam was split using a 70:30 beam splitter (EBP2, Thorlabs), designed to reflect 30% of light to the other optical power meter. Due to the size and shape of the red beam, it was focused using a lens with a focal length of 75 *mm* (LA4725-ML, Thorlabs) onto the

meter. The majority of the red light was directed towards the incubation chamber due to larger surface area when compared to the green beam. The intensity of the red light beam was much lower at the same power and it was expected to be the bottleneck for the time dependent experiments.

The split ratios of both beam splitters is rated for unpolarized light and the light produced by the lasers is polarized to some degree affecting the ratio of split light. The polarization of the laser beams also changes with temperature. Knowledge of the ratio of split light is required for accurate measurements of incident optical power, therefore a polarizer was introduced into both optical paths. The orientation of the polarizer in the red laser optical system was such that the proportion of light reflected towards the optical power meter was 18.0% and the remaining 82.0% was transmitted towards the incubation chamber. The polarizer absorbed ≈10% of red light in this orientation. The orientation of the polarizer in the green laser optical system was such that 49.4% of light was reflected towards the optical power meter and 50.6% of light was transmitted. The polarizer absorbed ≈25% of green light in this orientation. When the red laser was operated at 22% power or lower the optical output changed drastically; the polarization changed direction and became power dependant.

3.3.5 Intensity Profile Measurement Equipment

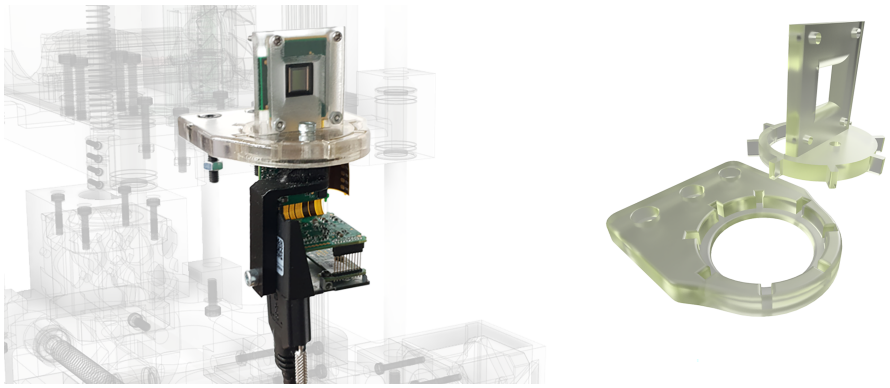


Figure 3.13: *Picture of the disassembled camera mounted on a custom designed adapter (left) and a render of the adapter (right).*

Intensity profiles of the green and red light beams were measured using a monochrome CMOS camera (MER-500-14U3M-L, Daheng Imaging). The camera was disassembled to expose the sensor and attached to a material jetting 3D-printed adapter, which was fixed to the platform of the incubation chamber (Figure 3.13). The adapter rotates enabling the imaging of both intensity profiles at the position of the build volume. A custom program was written in python 3.7.2, which allowed

real time imaging of the beam profiles and enabling real time adjustments of lens positions in order to obtain the desired intensity profile. The program can utilise the translations system to image the intensity profiles in a grid, allowing imaging of an area greater than the sensor's dimensions. This system was also used in aligning the green beam parallel to the X-axis of the translation system.

3.4 Control and Communication Apparatus

The apparatus is controlled by a microcontroller (ELEGOO MEGA 2560 R3, Elegoo) and a desktop computer. The microcontroller directly controls the stepper motors, the lasers' TTL modulation, and regulates the temperature inside the incubation chamber. The desktop computer was used to send G-code commands to the microcontroller, which then executes them. It also controls the power supply (DP832A, Rigol) for the lasers and reads the power from the optical power meters.

Microcontroller

The microcontroller is running a custom written program in Arduino programming language. It runs in a continuous loop executing four main tasks:

- Listening for and receiving G-code commands from the desktop computer and sending reports back.
- Executing received instructions.
- Maintaining the optical power feedback loop.
- Continuously reading and maintaining set temperature of the incubation chamber and sending continuous status updates to the desktop computer.

The main set of instructions sent to the microcontroller, known as G-code commands, are G0, G1 and G4, which dictate the movement of the translation system.

- G0 – linear movement with lasers off.
- G1 – linear movement with at least one active laser.
- G4 – dwell for a duration with or without active lasers.

Each of these commands is supplemented by additional parameters. The microcontroller maintains the state of the apparatus, thus requiring that instructions provide only parameters whose values have changed. These parameters are the individual X, Y and Z coordinates, movement speed, duration of dwell, and lasers' modulation duty cycles.

The main set of instructions is supplemented by instructions that manage the secondary aspects of the printing process:

- M17, M18 – turn the motors on or off.
- M141 – set the maximum and minimum temperature within the incubation chamber.
- M230 – wait until the maximum set temperature is reached.
- G28 – move to the home position.
- M2 – end of program.

An example of a G-code program is shown in listing 3.1.

Listing 3.1: *Short G-code program instructing single voxel illumination. In line 2 the program sets the incubation temperature range between* $36.7°C$ *and* $37.2°C$*. Line 4 instructs a* 20 *minute wait period. From line 5 to 8 the area around the voxel at heights of* 14.5 mm *and* 15.5 mm *is to be illuminated for* 5 *minutes with red light with a power of* 0.5 mW*. Line 9 instructs movement to the voxel position with a speed of* 3 mm/s*, followed by a* 150 *minute illumination with green light with a power of* 1 μW *and red light with a power of* 0.2 mW*. The program concludes with instructions to move to the home position, turn off the motors and end the program.*

```
1  M17
2  M141 T37.2 t36.7
3  M230
4  G4 S1200000
5  G1 Z−14.500 L10.0 L20.5
6  G4 S300000
7  G1 Z−15.500
8  G4 S300000
9  G0 X5.000 Y5.000 Z−15.000 F3
10 G4 S9000000 L10.001 L20.2
11 G28
12 M18
13 M2
```

The stepper motors were controlled by the microcontroller through three motor drivers (TB6600). The motor drivers require three binary voltage signal inputs for the power on/off, direction and step. The current output and step fraction on all motor drivers was set to 1 A and 1/32 respectively. Each step fraction occurs when the microcontroller switches from low to high voltage state on the step signal pin of the motor driver.

Similarly, the microcontroller sends step pulses with a frequency of 200 Hz to individual drivers that control the lasers. The duty cycle of the pulses determines the average optical power output of the lasers. The information about the duty cycle for each laser is sent by the desktop computer every 0.25 seconds, provided that the lasers' power requires adjustment.

The incubation chamber temperature is controlled entirely by the microcontroller. Temperature is measured through the voltage drop on the NTC thermistor in reference to a 10 $k\Omega$ resistor, which is used to determine the thermistor's resistance. Steinhart–Hart equation is then used to calculate the temperature. If the temperature in the incubation chamber is below the minimum set temperature the microcontroller switches on the relays that switch on the power of the fan and the heater cartridge. Conversely, the heater cartridge relay is switched off, if the temperature rises above the maximum set temperature.

Every half a second the microcontroller sends an update to the desktop computer containing the temperature of the incubation chamber and either the time left to wait until the end of the current dwell or the progress of the current movement.

Desktop Computer

The desktop computer serves as the interface between the user and the apparatus. A custom program was written in Python 3.7.2 that takes a G-code program and sends the G-code commands to the microcontroller, reads power measurements from the optical power meters, sends updated duty cycles to the microcontroller and displays the status of the program and apparatus.

The G-code commands are read from a file and sent one by one to the microcontroller in sequence through serial communication. After each successful execution of a G-code command the microcontroller responds with a report and the desktop computer sends the next G-code command.

The G-code commands set by the user include optical laser power. The desktop computer adjusts the optical power values to account for the reflections and converts them to the approximate duty cycle values, which it then sends to the microcontroller with the corresponding G-code command. The desktop computer continually measures the optical power of each laser and if needed recalculates the duty cycle and sends the correction to the microcontroller every 0.25 seconds. The threshold

for correction is a 1% deviation from the set optical power. The corrected duty cycle is calculated through a simple proportional control only:

$$D_{new} = \frac{P_{set}}{P_{measured}} D_{old}, \tag{3.4}$$

where $D_i \in [0.001, 1]$ are the new and old duty cycle and P_i are the set and measured optical powers. The minimum value is set to 0.001 to avoid multiplication by zero. Consequently the microcontroller is set to regard 0.001 as 0.

The desktop computer interprets the received updates and reports from the microcontroller and displays the status of the apparatus. This includes the current G-code command, the timestamp, the incubation chamber temperature, command status, lasers' optical powers and duty cycles.

3.5 Experiment Execution

All experiments were performed on hydrogel culture filled cuvettes. After hydrogel culture cuvettes and control samples were prepared (Chapter 3.1.1), they were kept in the refrigerator for up to three days before they were used in an experiment.

Before each experiment the lasers were powered up and left to warm up for about five to ten minutes. After the warmup the optical power of the lasers was measured and verified to be within the required range. If the optical power of the green laser was inadequate, the coupling of the laser into the fibre optic cable was adjusted until the required power was reached. The red lasers optical power output was regulated by introducing neutral density filters (NE05A or NE10A, Thorlabs) to maintain the optical power output between 22% and 100%. After the optical apparatus was prepared the rest of the periphery was powered on.

A hydrogel culture cuvette was then taken from the refrigerator in relative darkness and placed into the cuvette holder inside the incubation chamber. The control sample was placed on the bottom of the chamber. The front foam panel was refastened to block any ambient light. With the cuvette in place the experiment G-code program was run from the desktop computer. The experiments were ran for three hours plus the additional time it took for the incubation chamber to reach $37°C$, which was somewhere between five and ten minutes.

Half of steady-state experiments were run with one hour overlap as opposed to being run after the completion of the previous experiment. In such cases a hydrogel culture filled cuvette to be used in the next experiment was placed into the incubation chamber before the completion of the current experiment. The cuvette was placed in the chamber when the running experiment had a few minutes less than an hour left before completion. This was performed with haste in relative darkness

to minimize any disturbance. At the end of the running experiment the original cuvette was replaced with the incubating cuvette and at the one hour mark since incubation the next experiment was started.

At the end of each experiment the hydrogel culture cuvette was removed and placed into an ice bath for about five minutes to suppress growth. The sample was labelled, wrapped and placed back into the refrigerator. The cuvette samples were kept there for up to three days before they were sliced and imaged. Figure 3.14 depicts the entire execution.

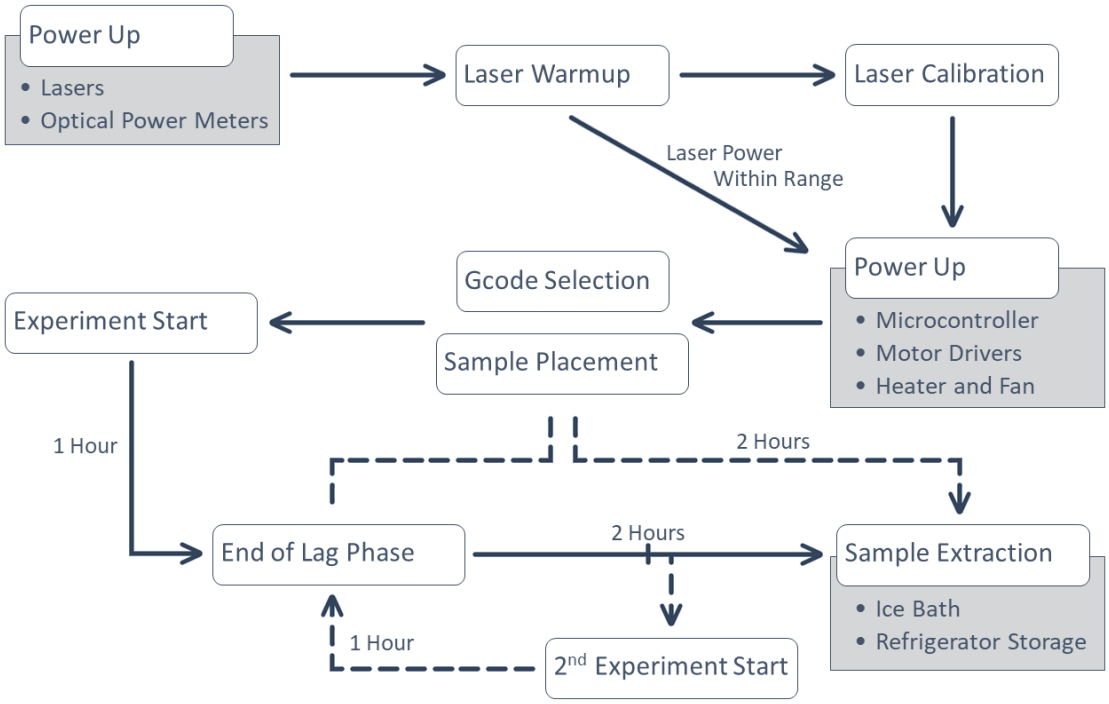


Figure 3.14: *Flow chart depicting the execution of experiments. The dashed lines indicate the execution of experiments ran with an overlap.*

3.6 Data Collection

3.6.1 Physical Slicing of Hydrogel

The hydrogel culture that underwent an experiment was physically sliced in order to be imaged, to determine the distribution of gene expression. Due to the lack of adequate commercial microtomes available, a custom slicing jig (Figure 3.15) was designed in Fusion 360. The slicing jig is made of three main components: the base, the guide and the slicer. With the exception of the microtome blade (MX35 Ultra, Epredia) and the translation stage (DT12/M, Thorlabs), all of the components were 3D-printed using the material jetting 3D printer.

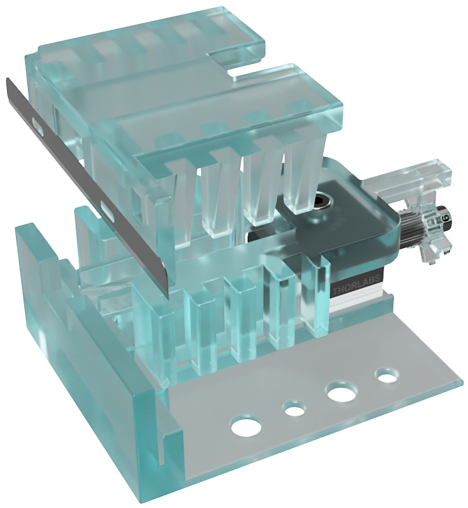


Figure 3.15: *Render of the slicing jig used to slice the hydrogel culture.*

The base of the jig holds the hydrogel culture and a microscope slide (SuperFrost Plus, Epredia). The guide is connected to the base via the translation stage, which allows for movements of 0.35 mm per revolution. The slicer was 3D-printed to smoothly fit into the guide's finger joint. With the two components joined the translation stage can be used to position the blade of the slicer to the desired distance from the microscope slide, in this case 1 mm. The blade was superglued to the front of the slicer facing the microscope slide. Above the blade on one side is a window that was used to measure the distance from the blade and the microscope slide using the back end of a caliper. A wheel with seven numbered spokes was 3D-printed and attached to the micrometer knob, which enabled movements of approximately 50 μm.

The hydrogel culture was extracted from the cuvette by inserting a steel spatula between the wall of the cuvette and the hydrogel all the way to the bottom. The spatula was then slightly pressed against the hydrogel and partly withdrawn. This was repeated one to three times to remove the hydrogel without causing any damage or permanent deformation.

After extraction, the hydrogel culture was placed onto the base of the slicing jig. The hydrogel culture was then sliced at a distance away from the area of interest in order to create a flat surface. A microscope slide was then inserted and the hydrogel culture was pressed against it, which was done by pushing it with the metal spatula so it gently slid towards the microscope slide. The water from the hydrogel provided sufficient lubrication for smooth movement. With the hydrogel culture gently touching the microscope slide, the slicer is pressed into the guide making a smooth cut resulting in a slice (Figure 3.16).

Before retracting the slicer, the guide was retracted by rotating the micrometer knob for a full rotation. This moves the blade and the remaining hydrogel culture far enough so that upon the retraction of the blade the cut slice does not stick to the blade or the remaining hydrogel culture. The microscope slide was then shifted by about one centimeter to make room for the next slice. The process was then repeated by pressing the remaining hydrogel culture against the microscope slide and rotating the micrometer knob back into position. Every four slices the microscope slide was replaced with a new one. Each microscope slide was marked noting the location of the slices within the stack. The alignment of slices was gently corrected with the spatula to align with the edges of the microscope slides.

The hydrogel culture's height was measured using a ruler before and after 16 slices were made to determine the average slice thickness. The average thickness across 30 samples was $0.97 \pm 0.02\ mm$, where the $0.02\ mm$ standard deviation is the deviation of the 30 average values and not individual slice thicknesses.

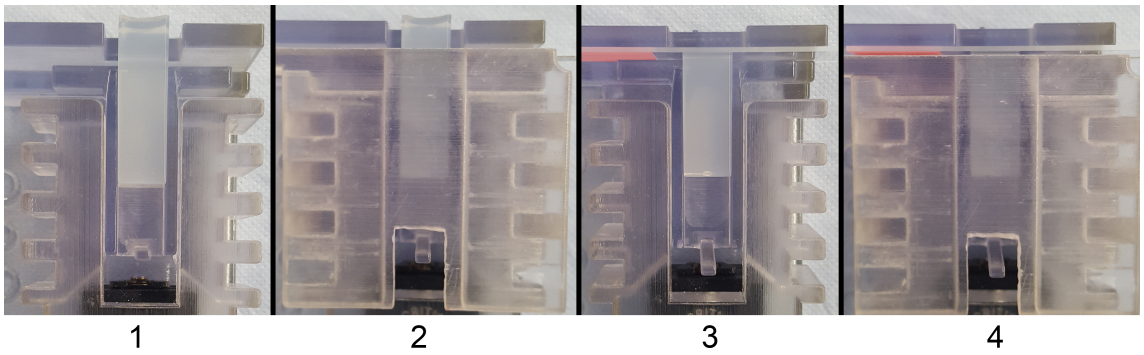


Figure 3.16: *The figure shows four steps in physical slicing of the hydrogel culture. The hydrogel culture is placed on the base (1) at a rough position and cut (2). A microscope slide is then inserted and the hydrogel culture is pressed against it (3) and then cut (4). The microscope slide is then repositioned and steps 3 and 4 are repeated.*

3.6.2 Gene Expression Imaging

Imaging was done using a laser scanner (Typhoon, Amersham Biosciences). A laser scans a 2D grid where each laser position represents a pixel in the final image. The wavelength of the laser and filter were set to $488nm$ allowing collection of the emitted light at $544\ nm$ from the excited fluorogenic ligand. Light is collected and directed to a photomultiplier. The gain of the photomultiplier was adjusted by setting the voltage on it to $500\ V$. This voltage was the same for every image. The pixel size was chosen to be $10\ \mu m$ and the images were recorded in 16-bit grayscale without compression.

Each fluorescence image of an individual experiment consisted of four control sample slices on one microscope slide and 16 hydrogel culture slices on four microscope slides. The microscope slides with the slices were placed on a thin transparent plastic film (Breathe-Easy, Diversified Biotech) to protect the imaging bed's surface from scratches. The plastic film also suppressed an interference pattern that otherwise forms due to the air gap between two glass surfaces (Figure 3.17).

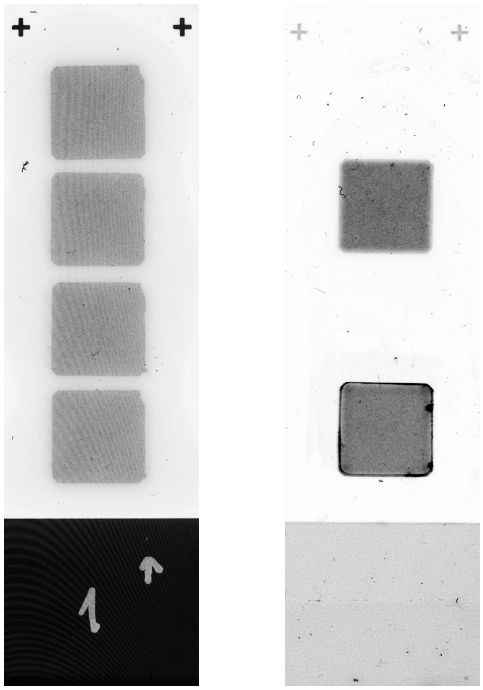


Figure 3.17: *Left, fluorescence image of four hydrogel culture slices on a microscope slide exhibiting an interference pattern due to an air gap between the microscope slide and the imaging platform of the laser scanner. Right, fluorescence image of two hydrogel culture slices on a microscope slide. The top slice is covered in agarose hydrogel, whereas the bottom one is not.*

The slices have sharp edges and flat surfaces, which caused numerous internal reflections when the laser scaned near the slices' edges. By encasing the slices in a 2% (w/v) agarose hydrogel the reflections were suppressed (Figure 3.17). The agarose hydrogel coating was done by heating the gel to $60°C$ and pipetting it onto the microscope slides, around and above the slices. Melting of slices was prevented by cooling the microscope slides and slices to $4°C$ beforehand. The prepared microscope slides and slices are shown in Figure 3.18.

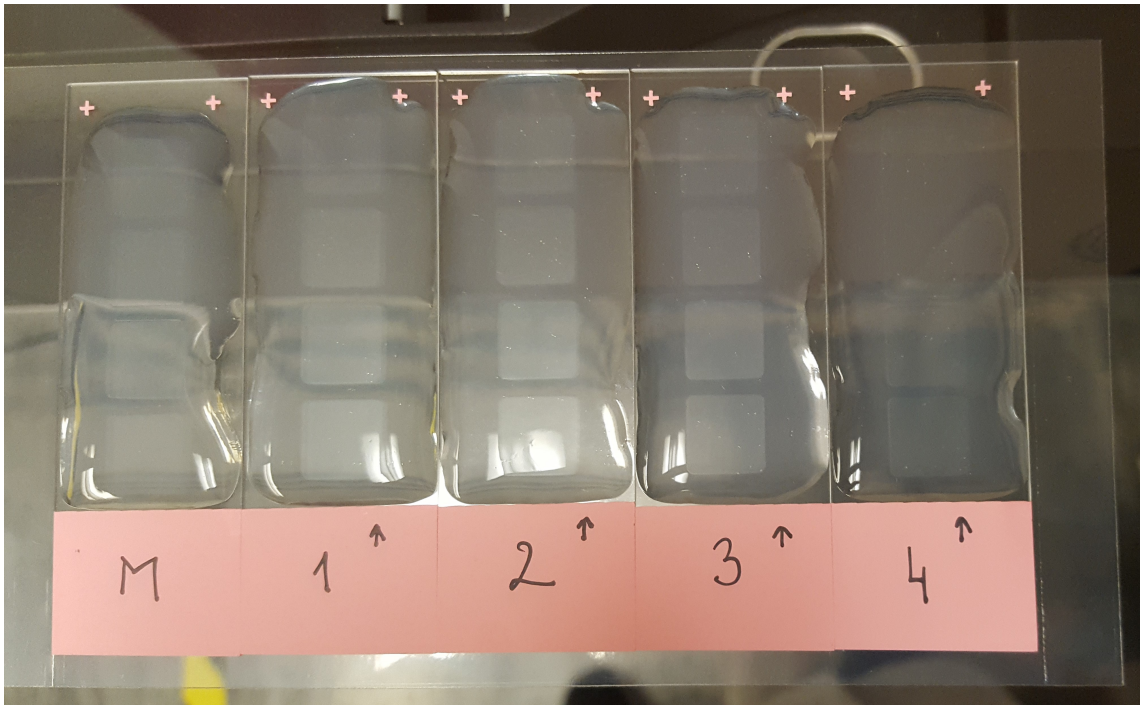


Figure 3.18: *Microscope slides with slices placed on the imaging bed of the laser scanner ready to be imaged. Four control slices were marked "M" as medium only and the rest were marked with the order in which they were sliced. The arrow denotes the direction of slicing – bottom first, top last.*

3.6.3 Image Processing

Fluorescence images were processed using a custom program written in Python 3.7.2. The input for the program is a raw data image (16-bit grayscale) generated by the laser scanner. The program first isolates the slices from the input image (Figure 3.19(a)), which it does by creating a binary image (Figure 3.19(b)) of the input image and determines the contours of each slice (Figure 3.19(c)). The threshold values that determine the binary image were determined semi-manually. The pixel values of the input image were gathered in a histogram and the location of the peaks in said histogram determined the rough values for the image thresholds. The binary image generated from these thresholds was then manually inspected and the individual thresholds were corrected until the binary image represented the slices. The histogram of each input image will generally have three peaks, excluding the peak corresponding to background. The three peaks correspond to their respective area within the image of hydrogel culture slices. These areas are: the area within hydrogel culture slices not affected by the halo effect, the whole hydrogel culture slices, and the control slices. Examples of these areas are contoured and shown in Figure 3.19(c).

With all the slices isolated, the hydrogel culture slices of interest were then manually selected (Figure 3.19(c)). Slices of interest exhibit an increased fluorescence value due to green light exposure during the experiment. Individual images of the selected slices are extracted by the program and aligned, it draws a minimum area rectangle around the individual selected slices (Figure 3.19(d)) and reorients the images so that the rectangle edges are now horizontal and vertical. The orientation is verified through visual inspection and in rare cases, where the reorientation was not successful, the edges of the rectangle were manually selected and rotated.

Once automatically aligned the individual images were further inspected, verifying that the entire slice and only the slice was in the image, if that was not the case, the image would be manually cropped. The images of slices of interest were overlapped and the pixel values were summed together thus generating a summed slices image (Figure 3.19(e)).

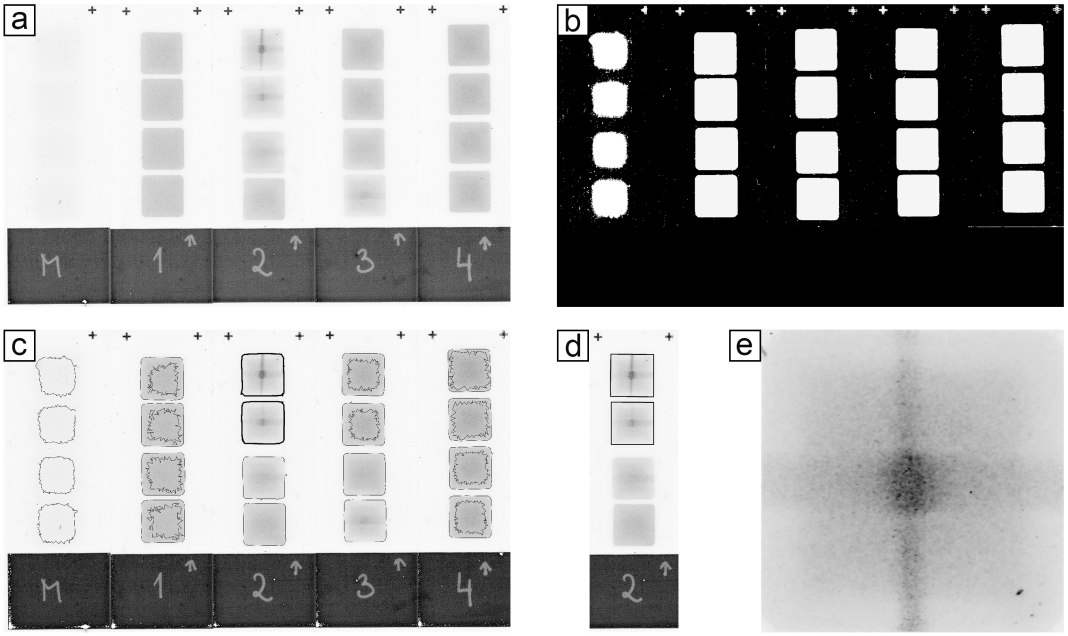


Figure 3.19: *Intermediate images generated during image processing.* (a) *Input image.* (b) *Composition of two binary images obtained by two thresholds – hydrogel culture and control slices.* (c) *Contours generated from binary images, drawn on the input image. The two bold contours mark the selected slices. The inner contours roughly mark the areas not affected by a halo effect.* (d) *Minimum area rectangles drawn around the selected slices.* (e) *Aligned, overlapped and summed slices resulting in a summed slices image. Shown images are arbitrarily rescaled for better visual presentation.*

The summed slices images consist of two or four main regions depending on whether red light illumination was present during the experiment:

- The voxel – region where gene expression was desired.
- The suppressed region – regions where induced gene expression was suppressed.
- The red only region – regions where only red light was present.
- The background region – regions that were not directly illuminated by red or green light.

The fifth region – the halo region – was excluded from analysis. Figure 3.19 depicts where these regions appear on an image of a summed slice. During program execution all regions were manually selected on summed slices images.

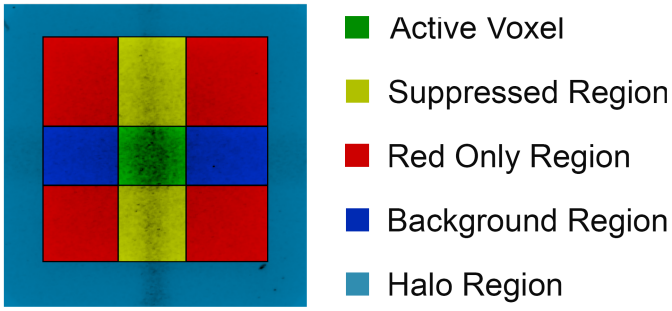


Figure 3.20: *Colored summed slices image indicating five regions of the image.*

After the slices have been properly extracted, the program calculates and outputs the following:

- Average fluorescence value of control sample slices – ambient background.

  The ambient background was calculated from all the pixels belonging to all control sample slices. This value was expected to include the average fluorescence contribution of the microscope slide, the plastic film, the M9 medium, the agarose and the unbound fluorogenic ligand.

- Average fluorescence value of hydrogel culture slices of little interest – background.

  The background was calculated from pixels belonging to all non-selected slices. Pixels that were deemed part of the halo region were ignored.

- Average fluorescence value of parts of hydrogel culture slices under red illumination only – suppressed background.

  The suppressed background was calculated from all pixels belonging to red only region in the slices of interest (slices with induced gene expression), provided that red light illumination was present during experiment.

  The above three averages were further refined to exclude contributions from dust particles present in the image. Standard deviation was calculated for each average. Pixel values that deviated from their respective average by two respective standard deviations or more were excluded from the second calculation of the average thus reducing the offset from dust.

- Average fluorescence values of columns parallel to green beam path (Figure 3.21).

- Maximum of the average fluorescence values of columns parallel to the green beam path bound by the voxel region – average voxel maximum.

- Maximum of the average fluorescence values of columns parallel to the green beam path bound by the suppressed region – average suppressed region maximum.

  The columns parallel to the green beam path were cut into two parts for two regions – the voxel and the suppressed region. The average value of each part of each column was calculated to obtain average fluorescence values parallel to the beam for each region (Figure 3.21). The largest average fluorescence values of all column parts belonging to each region are the respective average maximums.

- Average fluorescence values on the green beam path (Figure 3.21).

  Average fluorescence values on the green beam path were determined using the average of 11 pixels. The center pixel corresponded to the centre of the beam with the other 10 pixel equally split on both sides (Figure 3.21). The average of these pixels is used to reduce the significant variation in values at the beam centre. Given the width of the green beam – $\approx 1\ mm$ – these points fall within 2% of the maximum amplitude a of Gaussian beam with the same width.

- An image of fluorescence values of the hydrogel culture slices summed image.

The path of the green beam was not perfectly parallel to the slices' vertical edges. The beam direction and position were determined by the maximum pixel values in each row of the image. Note that the slice images were always oriented so that the beam direction was almost parallel to the pixel columns of the image. A linear fit was performed on the location of maximum-value pixels and the resulting linear function gave an accurate position and direction of the centre of the beam. The linear fit was further refined to ignore maximum-value pixel locations, which were due to dust or other noise, by ignoring points whose residuals were greater than two standard deviations with regards to the initial linear fit.

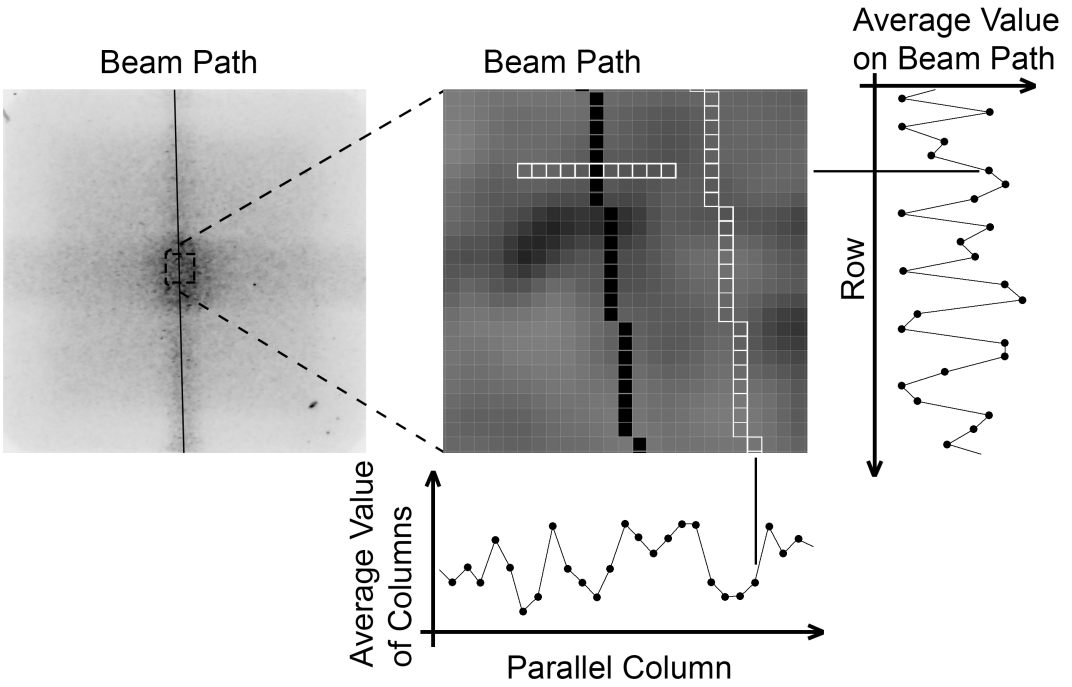


Figure 3.21: *Schematic representation of calculation of average fluorescence values of columns parallel to the beam path and of average value on the beam path. The angle of the beam path is exaggerated in the zoomed in image. The zoomed image shows the beam path, one example of a column of parallel pixels and one example of a row of* 11 *pixels. The* 11 *pixels centered around the beam path in each row were used to calculate the average value on the beam path.*

3.6.4 Experiment Simulation Methods

Experiment simulations of gene expression were calculated using Mathematica 13.0 (Wolfram Research, Inc.). Equations (2.3) and (2.9) were numerically solved to obtain total gene expression distribution over time. The spatial domain was discretized as shown in Figure 3.22. The points are unevenly spaced with the highest concentration around the centre of the incoming green beam to save computation time with a minimal loss of accuracy. The determination of the temporal domain was left to *NDSolve*, a built in function for numerically solving differential equations. The time interval was set from 0 to 120 minutes with a maximum allowed time step of 0.5 minutes.

The cell growth in (2.9) was approximated with exponential growth with its growth rate determined in Chapter 4.1. The intensity profile of the green beam used in the simulation was measured and is shown in Chapter 4.3.1. The measured data was linearly interpolated and then subsampled to fit the spatial domain of the simulation. The red beam intensity profile was approximated with two values each corresponding to intensity of a plane in the intensity profile. The intensity in the gap is determined in Chapter 5. The red intensity profile used in the simulation extends across the entire side of the spatial domain ($10\ mm \times 3\ mm$), with a gap in the centre measuring $2\ mm \times 3\ mm$. The red light intensity profile was extended to compensate for the lack of scattering in the simulation. The tails of the green beam intensity profile would otherwise have too much influence. The green beam was aligned with the X axis and the red beam was aligned with the Y axis.

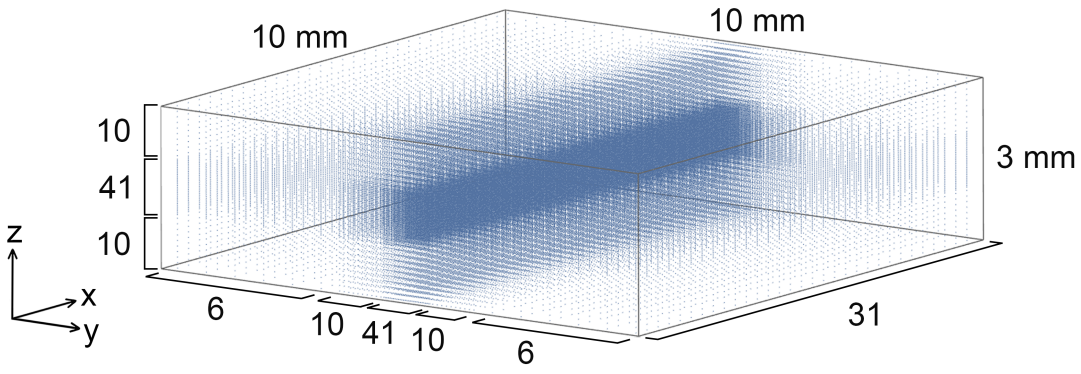


Figure 3.22: *Points in space used in simulation around the beam propagating in the X direction. X coordinates of points are equally spaced with a spacing of* 0.33 *mm. Y coordinates of points are densest in the middle with a spacing of* 0.025 *mm, thinning out to* 0.1 *mm and finally* 0.625 *mm. Z coordinates of points are densest in the middle with a spacing of* 0.025 *mm and are thinned out to* 0.1 *mm at the edges.*

Simulation of gene expression in multiple voxels was done on a modified spatial domain to accommodate the two locations of the incident green beam (Figure 3.23). To obtain the final 2D images, with one or two location of the green beam, total gene expression at 120 *min* is integrated along Z axis to obtain the integrated total gene expression.

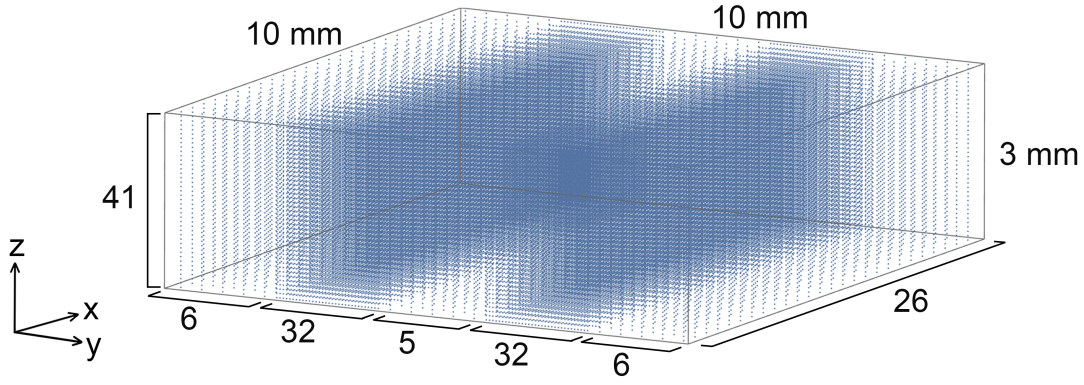


Figure 3.23: *Points in space used in simulation of two beams propagating in the X direction. X coordinates of points are equally spaced with a spacing of* 0.4 *mm. Y coordinates of points around the beam positions have a spacing of* 0.0625 *mm and otherwise* 0.4 *mm. Z coordinates have a spacing of* 0.075 *mm.*

Chapter 4

Equipment Characterisation

Equipment Characterisation describes the methods used to determine the cell population growth curve parameters; the attenuation of light due to reflections, absorption and scattering; the incident beams' intensity profiles and the scattered beams' intensity profiles. Parameters that were obtained in this chapter and were also used in the optogenetic model are: the duration of lag phase, exponential growth rate, attenuation of green and red light in the hydrogel culture and the intensity profiles of incident green and red beam.

4.1 Cell Population Growth

Bacterial cell population goes through several phases as cells divide. Population growth is characterized by the bacterial growth curve and it consists of four main phases: The lag phase, the exponential phase, the stationary phase and the death phase.

The lag phase occurs when cells are introduced into a new environment. In this phase the number of cells remains constant or grows very slowly [73]. After a certain period of time cells acclimate to their new situation. If the environment is suitable (i.e. there is enough space between individual cells, there is enough food, the temperature is within the desired range etc.) the bacteria enter the exponential phase. In the exponential phase the cells divide through binary fission and their population doubles after each generation. Thus their population grows exponentially. In this exponential phase their metabolism is expected to be at its highest point. Exponential growth continues until the environment can no longer supports such growth, either due to lack of food, space, accumulation of waste or some other factor. At that point cell population enters the stationary phase. In this phase the amount of new cells equals the amount of dying cells and the total population number stabilizes. Their metabolism slows down as they start to compete for resources. After a certain point this state can no longer be sustained, as the food grows too scarce or the environment becomes too toxic. In the final death phase, cells die rapidly and the population experiences an exponential decline.

To determine the duration of the lag phase and the rate of growth, the cell population was indirectly measured by measuring the optical density, OD_{700}, over a period of 12 hours with a sampling rate of once every 10 minutes at $37°C$. The measurements were carried out using a microplate reader (Spark, Tecan Trading AG) and a 96-well flat-bottomed microplate (Greiner µClear, Greiner Bio-One International). Three sets of measurements were performed on three hydrogel cultures prepared on separate days. Each set of measurements was used to calculate a separate average OD_{700} of wells with cells and/or medium for each time point. The average OD_{700} of cells alone was obtained by subtracting the average OD_{700} of hydrogel medium from the average OD_{700} of hydrogel culture. The measurements and the averaged OD_{700} of cells are shown in Figure 4.1. The standard deviations of the hydrogel culture and hydrogel medium OD_{700} were determined at each time point from their respective set of measurements.

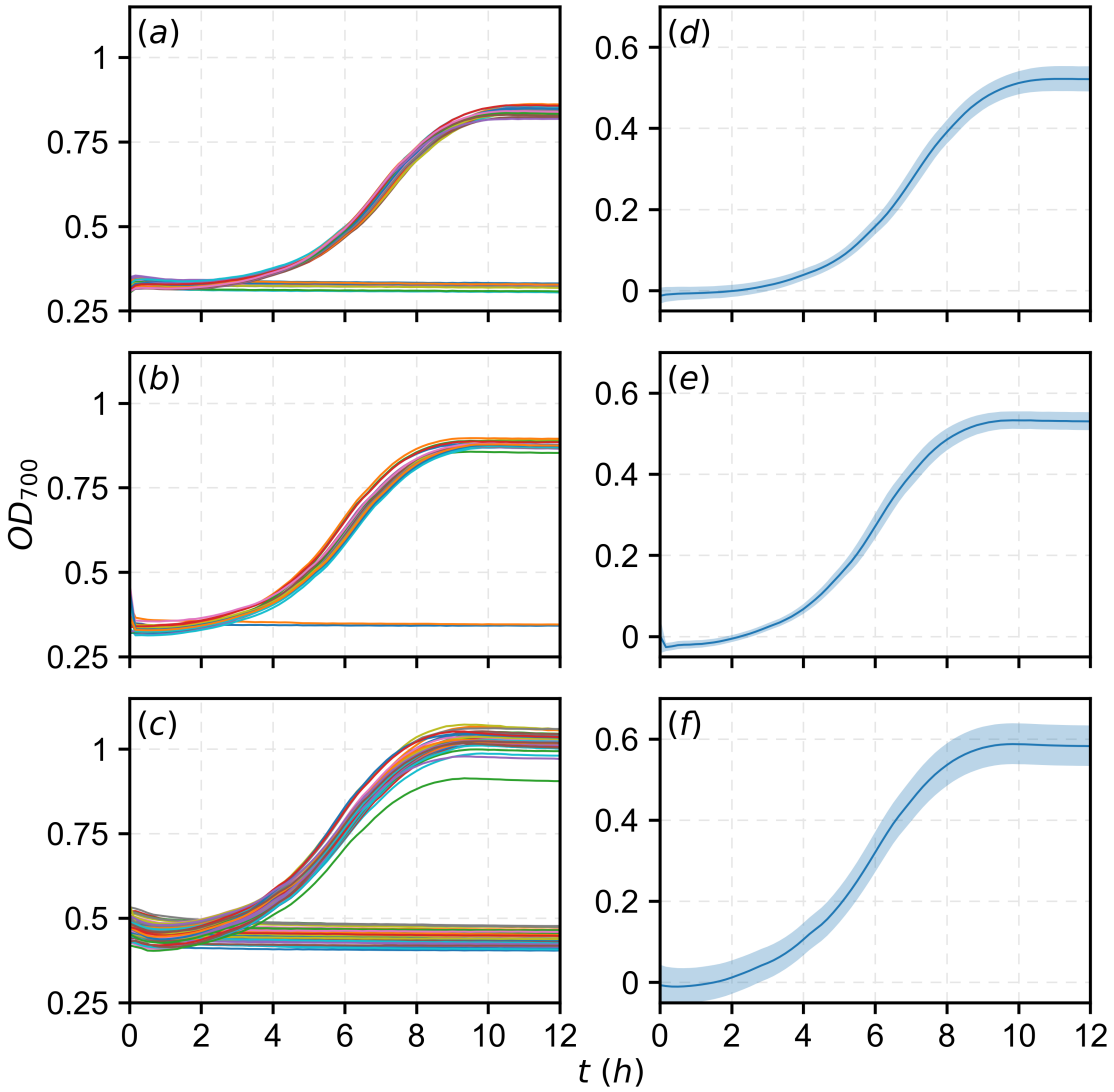


Figure 4.1: *Measurements of cell growth over a period of* 12 *hours in a hydrogel medium without the fluorogenic ligand.* $(a) - (c)$ *Plots of* OD_{700} *for each well of the respective measurement set. Plots in* (a), (b) *and* (c) *show* 24, 20 *and* 47 *measurements of wells with hydrogel culture and* 13, 2 *and* 39 *measurements of wells with hydrogel medium respectively.* $(d) - (f)$ OD_{700} *of cells only for the respective measurements shown in* $(a) - (c)$. *Solid line is the average and the shaded area represents one standard deviation.* (c) *Well plate was prepared with a different 8-channel pipette than the well plates for* (a) *and* (b).

To determine the growth rate of the cells in the hydrogel culture a simple growth model [73] was employed. The model assumes that the initial behaviour of the cell population consists of only the lag phase which then instantly transitions into the exponential phase. The population can then be described as follows:

$$N(t) = \begin{cases} N_0 & t \leq t_{Lag} \\ N_0\, e^{k_{exp}(t - t_{Lag})} & t_1 < t \end{cases}, \tag{4.1}$$

where N and N_0 are the number and the initial number of cells, t_{Lag} is the duration of the lag phase and k_{exp} is the growth rate in the exponential phase. However, the initial average cell OD_{700} (Figure 4.1$(d) - (f)$) is consistently negative after subtraction of the average medium OD_{700}. The cause of this behaviour is not clear; however, it was assumed that this is an offset that does not change over time.

The fitting function was as follows:

$$OD_{700}(t) = \begin{cases} OD_{700}^0 - OD_{offset} & t \leq t_{Lag} \\ OD_{700}^0\, e^{k_{exp}(t - t_{Lag})} - OD_{offset} & t_{Lag} < t \end{cases}, \tag{4.2}$$

where OD_{offset} is the unknown offset in optical density and OD_{700}^0 is the initial optical density. Optical density at small values is linearly proportional to the number of cells and could thus be substituted. The fit was performed in Wolfram Mathematica 13.0 using a built-in function *NonlinearModelFit*. The values of OD_{offset}, OD_{700}^0 and t_{Lag} were constrained to $[OD_{700}^0, 0.03]$, $[0, 0.03]$ and $[0, 10000\ s]$ respectively. The selected data range was between zero and 5.67 hours, which is before the inflection point of the curve. The resulting fitted functions are shown in Figure 4.2 and the estimated parameters are shown in Table 4.1.

OD_{700}^0 and OD_{offset} varied significantly across the three measurement sets. Furthermore, OD_{700}^0 was much greater than expected. Due to the form of (4.2), OD_{700}^0 and OD_{offset} are not very independent and almost behave as a single parameter and therefore a larger OD_{offset} yields a larger OD_{700}^0. There also exists coupling between k_{exp} and OD_{700}^0, as a larger OD_{700}^0 will result in a smaller k_{exp} in order for the function to fit to the same measurement. Similar reasoning holds for the estimate of t_{Lag}.

Given the impossibly large values of OD_{700}^0 and the unclear behaviour of OD_{offset} it is very likely that (4.2) does not adequately represent the measurements. For this reason a series of fits were performed where OD_{700}^0 was fixed to 0.005 or t_{Lag} was fixed to either 0 or 3600 s. In all these cases across all measurement sets the growth rate remained between $1.2 \times 10^{-4}\ s^{-1}$ and $2.0 \times 10^{-4}\ s^{-1}$ and most estimates were around $1.6 \times 10^{-4}\ s^{-1}$. The distribution of these fit estimates is unknown; however, due to most values being near $1.6 \times 10^{-4}\ s^{-1}$ and also due to OD_{700}^0 being closer to 0.005

in these cases, it was estimated that the growth rate of cells is $1.6 \pm 0.2 \times 10^{-4}\ s^{-1}$. The estimate of the lag phase is likewise ambiguous and was therefore rounded to an hour.

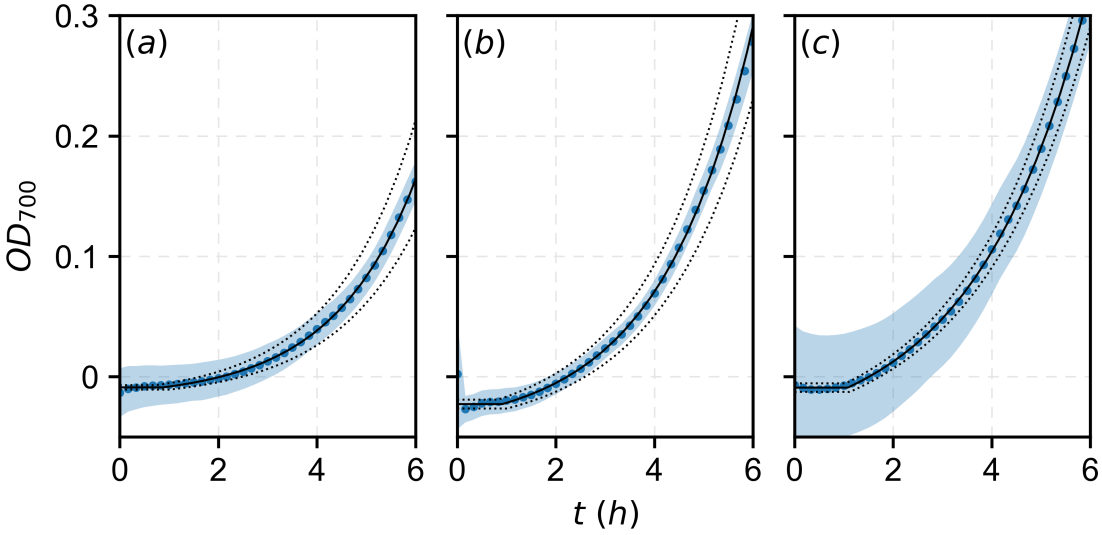


Figure 4.2: *Fit of* (4.2) *to the averaged measurements of* OD_{700} *shown in Figure 4.1*$(d) - (f)$*. The curve fits were performed on a data range from zero to* 5.67 *hours. The centres of blue circles are the data points, shaded area is one standard deviation, solid black curve is the best fit and the dotted black curves are the curve fits with parameters one standard deviation from the estimate.*

Table 4.1: *Estimated parameters and their standard deviations obtained from fitting* (4.2) *to the averaged measurements of* OD_{700}*.* (a)*,* (b) *and* (c) *correspond to the respective plots shown in Figure 4.2.*

Parameter	(a)	(b)	(c)	Average
OD_{offset}	0.018 ± 0.001	0.045 ± 0.002	0.052 ± 0.003	0.038 ± 0.018
$OD_{700}\ (t = 0)$	0.009 ± 0.001	0.022 ± 0.002	0.043 ± 0.002	0.025 ± 0.017
$t_{Lag}\ (s)$	3150 ± 480	3300 ± 340	3900 ± 150	3450 ± 400
$k_{exp}\ (10^{-4}s^{-1})$	1.63 ± 0.02	1.48 ± 0.03	1.22 ± 0.015	1.4 ± 0.2

4.2 Light Attenuation

The power measured at the optical power meters (Figure 3.12) is not the power that reaches the hydrogel in the cuvette. The cause of this discrepancy are the transparent acrylic box and the polystyrene cuvette. Both reflect a significant amount of light at each air-plastic interface.

Two measurements were made to determine the amount of reflected light at each interface. The attenuation due to the reflection on the acrylic box (Figure 3.6) was measured using two optical power meters, a beam splitter and the green laser. One optical power meter was used to measure the optical power inside the printing chamber of one arm of the beam splitter and the other power meter was used to measure the other. The difference between the measurements given by the two optical power meters was then used to determine the attenuation.

The attenuation of the cuvette was determined in the same way, by placing the cuvette in front of one optical power meter and then comparing the measured optical powers. The measured attenuation corresponds to four reflective surfaces. However, when the cuvette is filled with hydrogel the reflectance of two inner surfaces is lower. To measure the attenuation of the cuvette-hydrogel interface water was used as a substitute in the measurement, as the refractive index is nearly the same. The results of measurements are shown in Table 4.2.

Table 4.2: *Measured attenuation of green* 515 *nm light following an interface and reflections calculated from refractive indices [74, 75] of respective media using Fresnel equations. PS refers to polystyrene.*

Interface	Measured Attenuation	Calculated Reflection
Acrylic/Air	$4.1\% \pm 0.5\%$	$3.93\% \pm 0.05\%$
PS/Air	$5.0\% \pm 0.5\%$	$5.33\% \pm 0.05\%$
PS/Water	$1.0\% \pm 0.5\%$	$0.824\% \pm 0.005\%$

Accounting for the attenuation on the interfaces the optical power reaching the hydrogel is $86.5\% \pm 2\%$ of the measured optical power. Additional reflections occur as the light exits the cuvette, increasing the total optical power inside the cuvette. However, these contribute less than 1% due to attenuation caused by the sample. The reflections from the back of the acrylic cover are of the same order but are not aligned with the incoming light. The attenuation of red 650 *nm* light is the same within the error estimate.

An additional attenuation measurement was performed on a cuvette filled with the hydrogel culture. The sample was placed inside the printing chamber where the temperature was maintained on average at $37°C$. The optical power meter was placed outside the printing chamber behind the cuvette and the acrylic cover. The measurement was performed over a period of 12 hours, which captured transmission during the growth of cells. The initial transmission of the sample, ignoring interface reflections, was approximately $T(t = 1h) = 35\%$ which dropped down to approximately $T(t = 3h) = 25\%$ at three hours. The transmission measurements are plotted in Figure 4.3 and selected values are shown in Table 4.3. For the purposes of simulation the attenuation coefficients were also determined at 2.5 hours for both green and red light, $\mu_G = 120 \pm 10\ m^{-1}$ and $\mu_G = 45 \pm 10\ m^{-1}$.

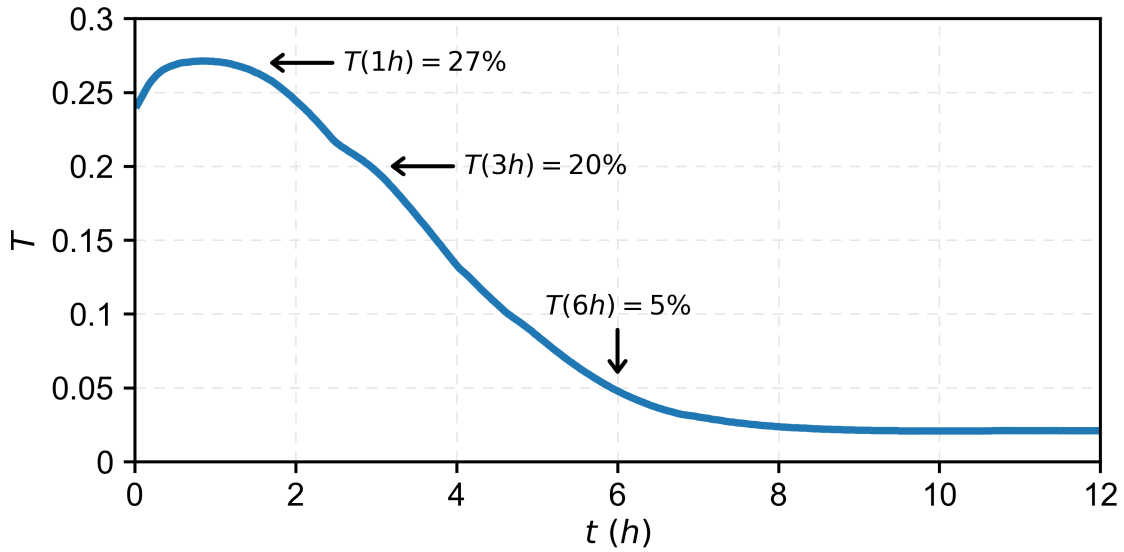


Figure 4.3: *Transmission, T, of green light through the acrylic cover, cuvette, and hydrogel culture over a period of 12 hours. The initial rise in transmission can be explained by warming of the hydrogel.*

Table 4.3: *Transmission and attenuation coefficients for green (515 nm) light at three different times. The attenuation coefficients are calculated for base e.*

Time	Measured Transmission	Transmission without Reflections	Attenuation Coefficient of Populated Hydrogel	Attenuation Coefficient of Bacteria
1 h	$27\% \pm 0.5\%$	$36\% \pm 1.5\%$	$100 \pm 10\ m^{-1}$	$30 \pm 5\ m^{-1}$
3 h	$20\% \pm 0.5\%$	$26\% \pm 1\%$	$135 \pm 10\ m^{-1}$	$60 \pm 5\ m^{-1}$
6 h	$4.8\% \pm 0.2\%$	$6.4\% \pm 0.4\%$	$275 \pm 10\ m^{-1}$	$200 \pm 5\ m^{-1}$

The rate of gene expression will depend on the metabolism of the cell. In the exponential phase the metabolic activity is highest and as such the exponential phase is expected to support the highest gene expression rate. However, as the cell population grows the turbidity of the environment also increases and with it light attenuation. Elevated light attenuation can be prohibitive for adequate light distribution during experiments, as light intensity within the bulk material can diminish to an order of magnitude less when compared to light intensity at the surface. It was thus decided to run the experiments for three hours.

4.3 Light Intensity Profile

4.3.1 Incident Beam Profiles

The intensity profiles of the green and red beam were measured using the intensity profile measurement equipment (Chapter 3.3.5). The translation system was positioned so that the camera sensor was at the crossing of both beams. The camera sensor was rotated by 90 degrees in place when needed in order to measure both beams. Before the measurement the lasers were warmed up for half an hour and were kept at 100% during the measurement. A neutral density filter (NE20A-A, Thorlabs) was introduced into the optical path to prevent sensor saturation. The measured intensity profiles are shown in Figures 4.4 and 4.5. The green beam intensity profile is a single image, whereas the red beam intensity profile is a composition of five images taken sequentially by translating the sensor. The interference pattern seen in the red beam's intensity profile (Figure 4.5) is due to diffraction of the light off of the edges of the screen used to shape the beam (Figure 3.10).

The green intensity profile was approximated by a Gaussian beam. The largest relative deviation from the approximation can be seen in the tails of the beam (Figure 4.4$(b), (c)$). The red intensity profile was approximated with two constant values, one for the bulk of the intensity and one for the intensity within the gap. These two values were calculated as the average of each respective region (Figure 4.5(a)) with respect to input power.

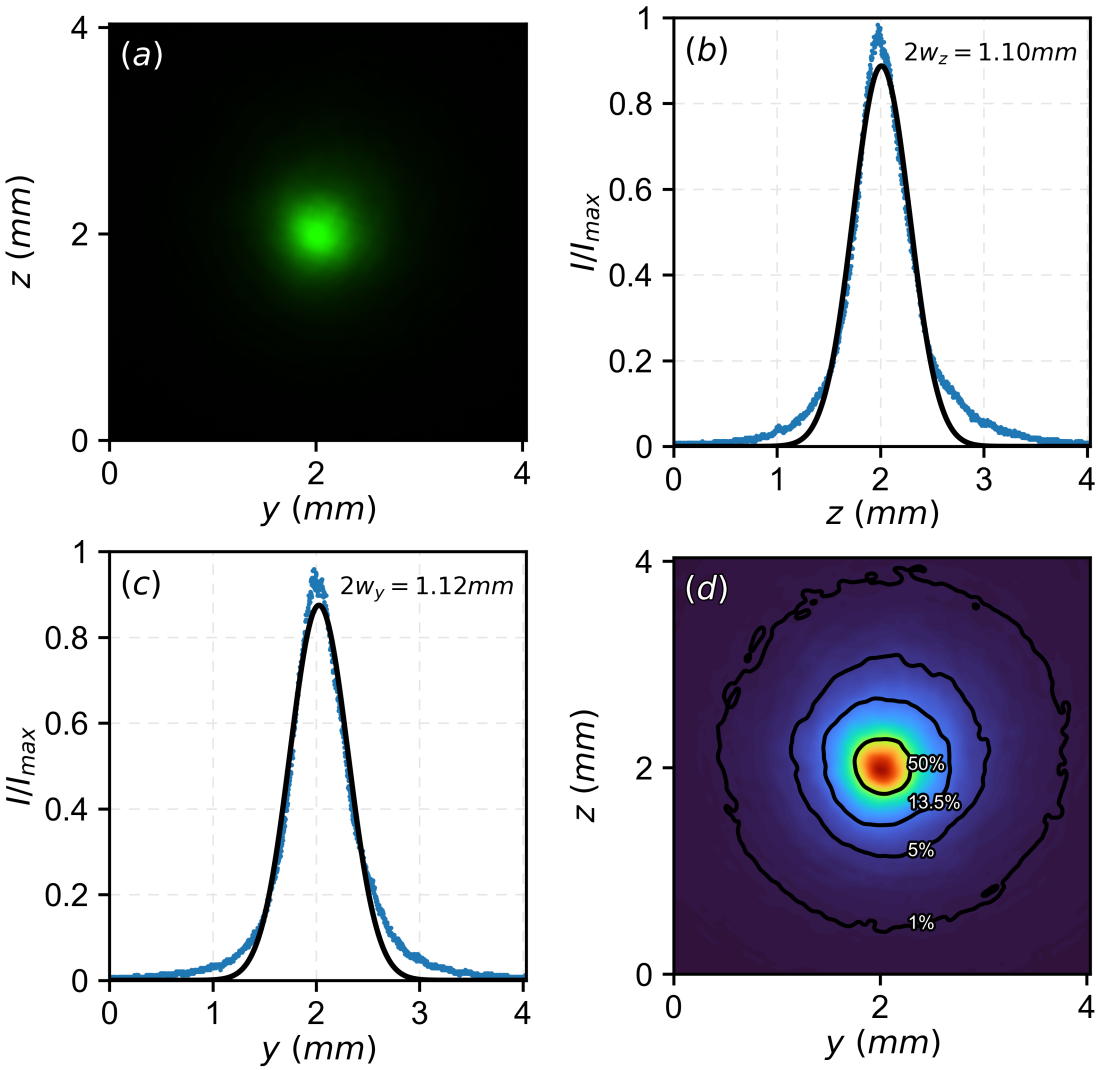


Figure 4.4: *(a) Colored measured intensity profile of the green laser beam at the centre of the build volume. (b), (c) Normalized intensity, I/I_{max}, plots in the Z and Y direction respectively, at maximum intensity of the intensity profile shown in (a). The black line graphs are the best fit of one-dimensional Gaussian beam intensity. The best fit estimates for $1/e^2$ beam diameters, $2w_z$ and $2w_y$, are 1.10 mm and 1.12 mm respectively. (d) Smoothed density plot of normalized intensity with contours at four levels of intensity.*

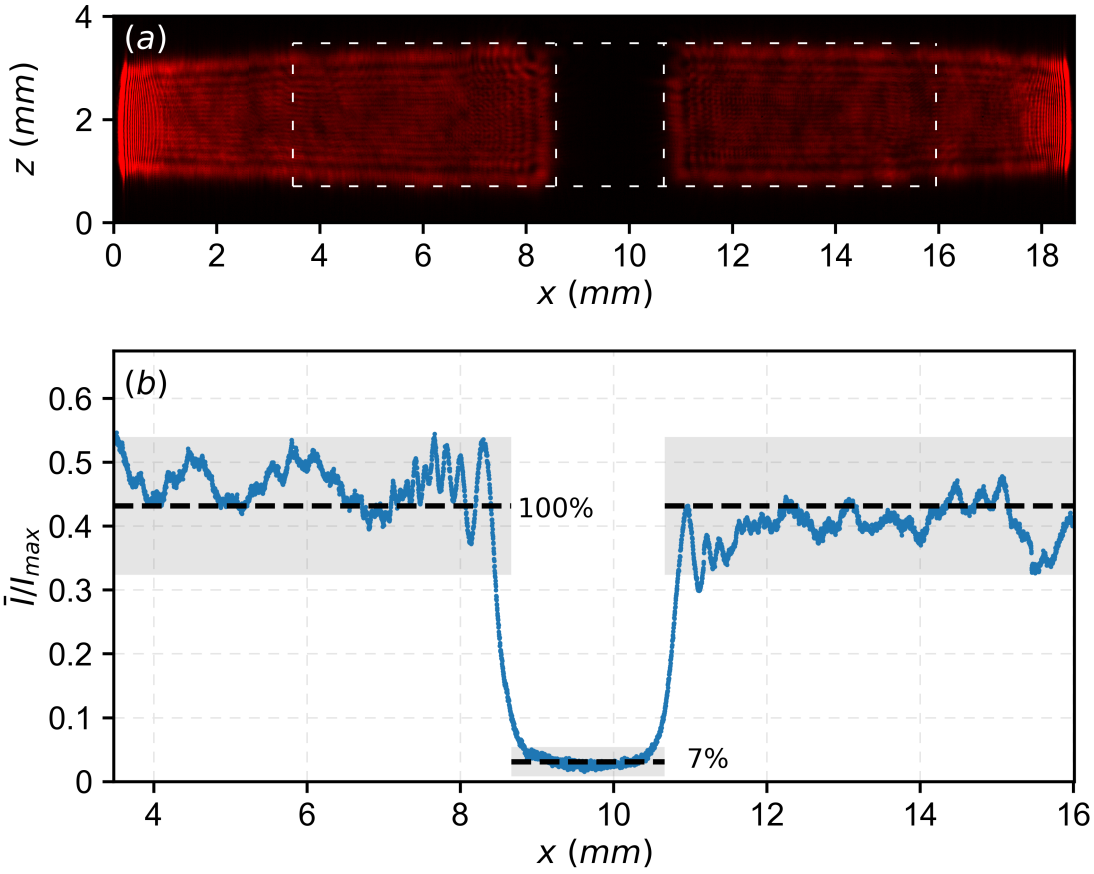


Figure 4.5: *(a) Colored measured intensity profile of the red light at the centre of the build volume. The rectangles mark the areas used in calculating the average intensity values. The gap in the profile marked by the middle rectangle measures 2.0 mm × 2.3 mm. (b) Plot of average intensity averaged in the Z direction and normalized to the maximum intensity value, $\bar{I}/I_{max}$. The black dashed lines represent the two average intensity values. One is the average of the two side rectangles and the other is the average of the middle rectangle. The grey area represents one standard deviation of all intensity values in the respective rectangles. The light intensity measured in the gap is 7% of the light intensity measured in the side rectangles.*

4.3.2 Scattered Beam Profiles

Light passing through a hydrogel culture filled cuvette was imaged to estimate any scattering effects. The cuvette sample was incubated for three hours before it was placed directly in front of the camera. The distance between the camera sensor and the back of the cuvette was $4 \pm 1\ mm$. The position of the camera was at crossing of both beams. The laser beam was shone through the hydrogel culture filled cuvette onto the camera and the resulting intensity profile was imaged. The scattered intensity profiles for green and red are show in Figure 4.6 (a) and Figure 4.7 (a) respectively. Both exhibit the speckle pattern due to scattering off of cells.

The best fits of a Gaussian beam to the measured green intensity profile (Figure 4.6$(b), (c)$) suggest that the beam noticeably widens when compared to the incident beam (Figure 4.4); however, this width is likely not a very meaningful parameter. The first issue is that the intensity was imaged a few millimeters behind the cuvette, which gives the beam some distance to expand. The second issue is that the Gaussian beam function is not sufficient to describe this intensity profile. It is likely that too much weight is given to the tails, widening the best fit estimate. It is better to compare the contours in the smoothed density plots in figures 4.4 and 4.6. The area above 13.5% is roughly the same in both cases, whereas the area above 5% and 1% is noticeably larger for the scattered beam.

Only the middle of the scattered red beam intensity profile was measured, as the interest was in determining the relative amount of red light present in the gap of the intensity profile. From the averaged values shown in Figure 4.7(b) it can be seen that there is a noticeable increase in relative light intensity in the gap when compared to the incident beam. The relative intensity within the gap increased from 7% (Figure 4.5) to 16%. Much like the increased leakiness of light into the gap, scattering also slightly rounded the edges of the gap making the threshold less sharp.

In both cases only forward scattering was measured, which in the case for *E. coli* in water [76] is the most prominent. This suggests that the majority of light that was scattered by the cells has been measured. Some light scattered by the agarose hydrogel is expected to have been measured as well. These measurements represent only an approximate picture of the intensity distribution of light within the build volume and do not account for any of the light scattered at larger angles. Therefore, the intensity profiles are somewhat different within the hydrogel culture. In the case of the green beam the tails are likely even more pronounced and in the case of the red beam red light leakiness is expected to be somewhat greater.

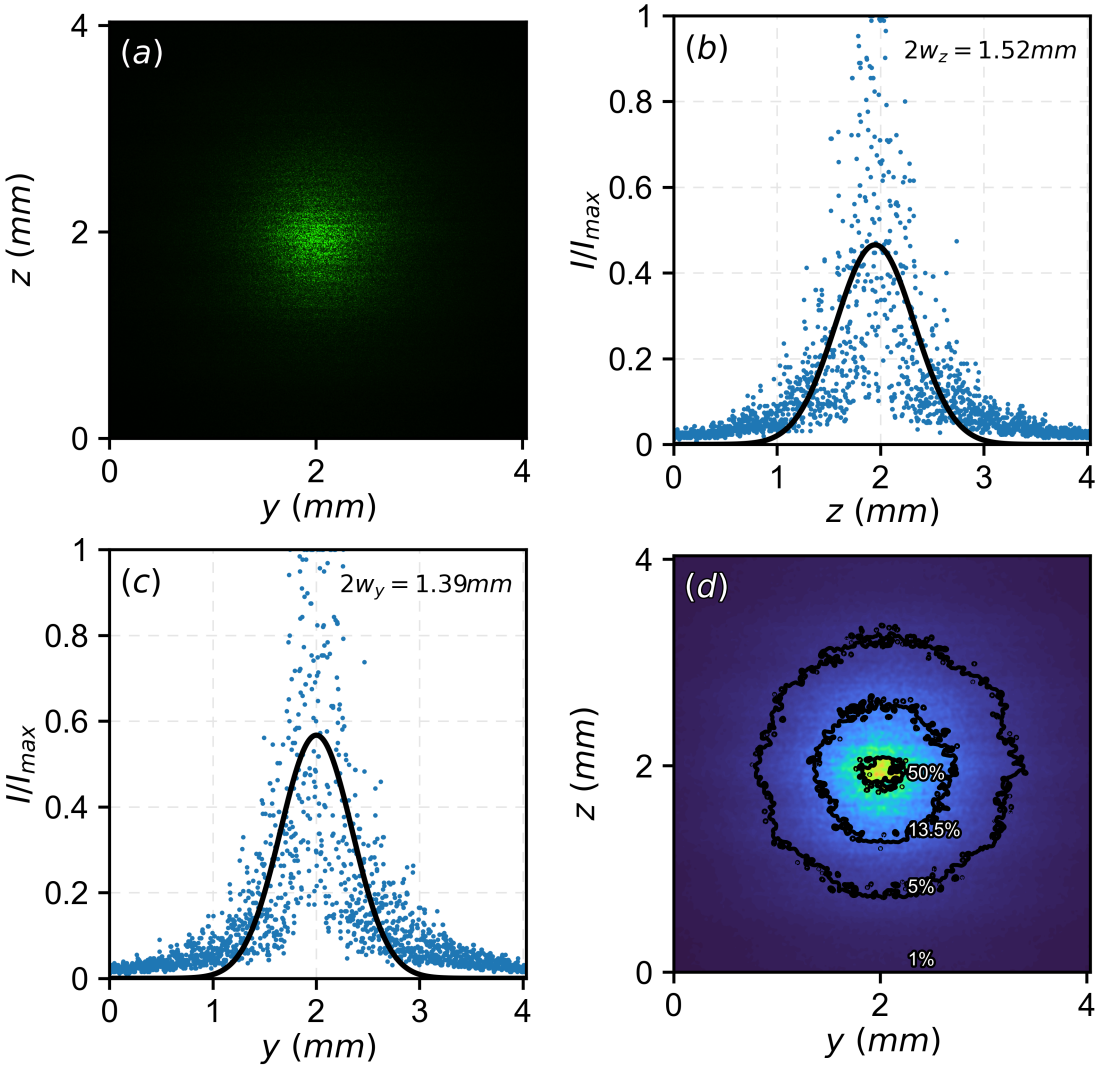


Figure 4.6: *(a) Colored measured intensity profile of the scattered green beam 4 ± 1 mm behind the wall of the hydrogel culture filled cuvette. (b), (c) Normalized intensity, I/I_{max}, plots in the Z and Y direction respectively, at maximum intensity of the intensity profile shown in (a). The black line graphs are the best fit of one-dimensional Gaussian beam intensity. The best fit estimates for $1/e^2$ beam diameters, $2w_z$ and $2w_y$, are 1.52 mm and 1.39 mm respectively. (d) Smoothed density plot of normalized intensity with contours at three levels of intensity. Intensity between the frame and the 5% contour is at least 1%*

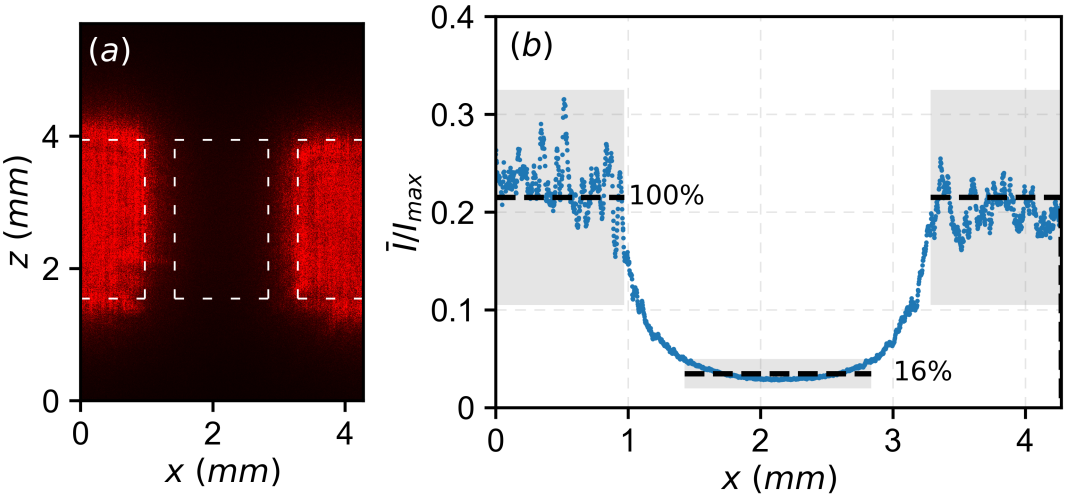


Figure 4.7: *(a) Colored measured intensity profile of the red light after passing through a hydrogel culture filled cuvette. Image was taken at* 4 ± 1 *mm away from the back wall of the cuvette. The rectangles mark the areas from where the average intensity values were calculated. The middle rectangle measures* $1.3\ mm \times 2.3\ mm$*. (b) Plot of average intensity averaged in the Z direction and normalized to the maximum intensity value,* $\bar{I}/I_{max}$*. The black dashed lines represent two normalized average intensity values. One is the average of the two side rectangles and the other is the average of the middle rectangle. The grey area is one standard deviation of all normalized intensity values in the respective rectangles. The light intensity in the gap is* 16% *of the light intensity in the sides.*

Chapter 5

Localized Steady-State Gene Expression

Localized Steady-State Gene Expression introduces the steady-state solution of the optogenetic model, which is applicable to constant illumination of cells. Steady-state experiments were performed in order to estimate the ratio between a' and b' and analyze the behaviour of gene expression in response to different combinations of red and green light intensities and their intensity profiles. Further experiments were carried out to verify whether active-state photoreceptors were present at the beginning of the steady-state experiments. Finally, given the results of steady-state experiments, another estimation was carried out to determine the amount of red light leaking into the voxel.

5.1 Steady-State Solution

According to (2.9) and (2.8), the time dependant part of the solution of the optogenetic model – the total gene expression density – is the evolving cell population density and the ratio between active and ground-state photoreceptors, $R(t)$. In a steady state $R(t)$ reduces to a ratio between the forward and effective reverse conversion rate of photoreceptors. Following from the definition of $R(t)$ and (2.3), the steady-state ratio is:

$$R_{ss} = \lim_{t\to\infty} \frac{\eta(t)}{1-\eta(t)} = \frac{I_{515nm}\ \hat{k}_1(515nm)}{I_{650nm}\ \hat{k}_2(650nm) + k_{growth}}\,, \tag{5.1}$$

where I_{515nm} and I_{650nm} are the respective green and red light intensities. Under constant illumination the fraction of active-state photoreceptors, $\eta(t)$, behaves exponentially (Equation (2.6)), which means (5.1) becomes a good approximation after only a couple of characteristic times, $\tau_k = 1/k_{sum}$ (Equation (2.4)). Substituting R_{ss} in (2.8) and solving (2.9) gives the steady-state total gene expression density:

$$g^{ss} = b' + a' \frac{R_{ss}^n}{K^n + R_{ss}^n} = b' + a'\ h^{ss}\left(I_{515nm}, I_{650nm}\right)\,, \tag{5.2}$$

where h^{ss} is the normalized steady-state gene expression rate and b' and a' are the total background expression and total maximum expression respectively:

$$\begin{aligned} a' &= \int_0^{t_{End}} a(t)\rho_{bacteria}(t)\ dt\,, \\ b' &= \int_0^{t_{End}} b(t)\rho_{bacteria}(t)\ dt\,. \end{aligned} \tag{5.3}$$

While $h(t)$ can be considered constant for sufficiently large k_{sum}, this is not necessarily the case for a and b. They are rewritten as $a(t)$ and $b(t)$ to account for the case where they change due to changes in cell metabolism. This change is likely to be highest in the transition from the lag phase to the exponential phase of cell growth. However, as the majority of gene expression occurs during later stages of growth, where population is larger, the contribution from non-constant a and b is less influential.

5.2 Results

The *summed* images shown in Figure 5.1 are summations of fluorescence images of slices from the steady-state experiments. Experiments were performed at seven different green light intensities and at three different red light intensities, with the incoming light configured as shown in Figure 3.11. A single voxel was illuminated in the center of the build volume, which is 5 mm from the walls and 15 mm from the bottom of the cuvette. Half of experiments were performed with constant illumination from the beginning to end at three hours. Whereas the other half was illuminated from the one hour mark to the end. This was done to determine whether or not there is negligible gene expression during the lag phase. Due to the concurrent presence of red and green light during these steady-state experiments, gene expression can be thought of as suppressed as opposed to deactivated.

Each row in Figure 5.1 is a different group of experiments. Each group of experiments was done over a course of two to four days and for each day a new batch of hydrogel culture filled cuvettes was prepared. A group of experiments was done at most once a week. Overall, experiment groups were staggered over a course of a few months. The first half of rows for each red light intensity section in Figure 5.1 are images where there was no illumination in the first hour of the experiment. The second half of rows are images where illumination was present throughout. No discernible difference, that can be attributed to illumination during the lag phase, can be seen between the two types and no conclusive difference was detected in later analysis.

The majority of summed images are a superposition of two images of individual slices. Due to the Z dimension of the voxel and slices' thickness both being 1 mm, most voxels are cut in two during physical slicing, as there is a lack of exact absolute positioning. However, some summed images are a superposition of three or four images of individual slices. This is the case where gene expression was noticeable in a volume that spans more that two slices. On the other hand, there are summed images of only one slice, where noticeable gene expression was fully contained within that slice. Summed images that are not composed of two images were thus adjusted for visual comparison by either subtracting or adding the appropriate multiple of their average background. This way the scale of all summed images shown in Figure 5.1 is comparable to the scale of summation of two images.

A *halo* effect can be seen in the majority of images in Figure 5.1. The halos are 1 ± 0.2 mm thick and usually well defined. The hypothesis is that this is due to some interaction with the cuvette walls and most likely the plastic they are made from. It is unclear whether the halo effect is due to reduced growth rate of cells, gene expression or both. The halo region was excluded in analysis.

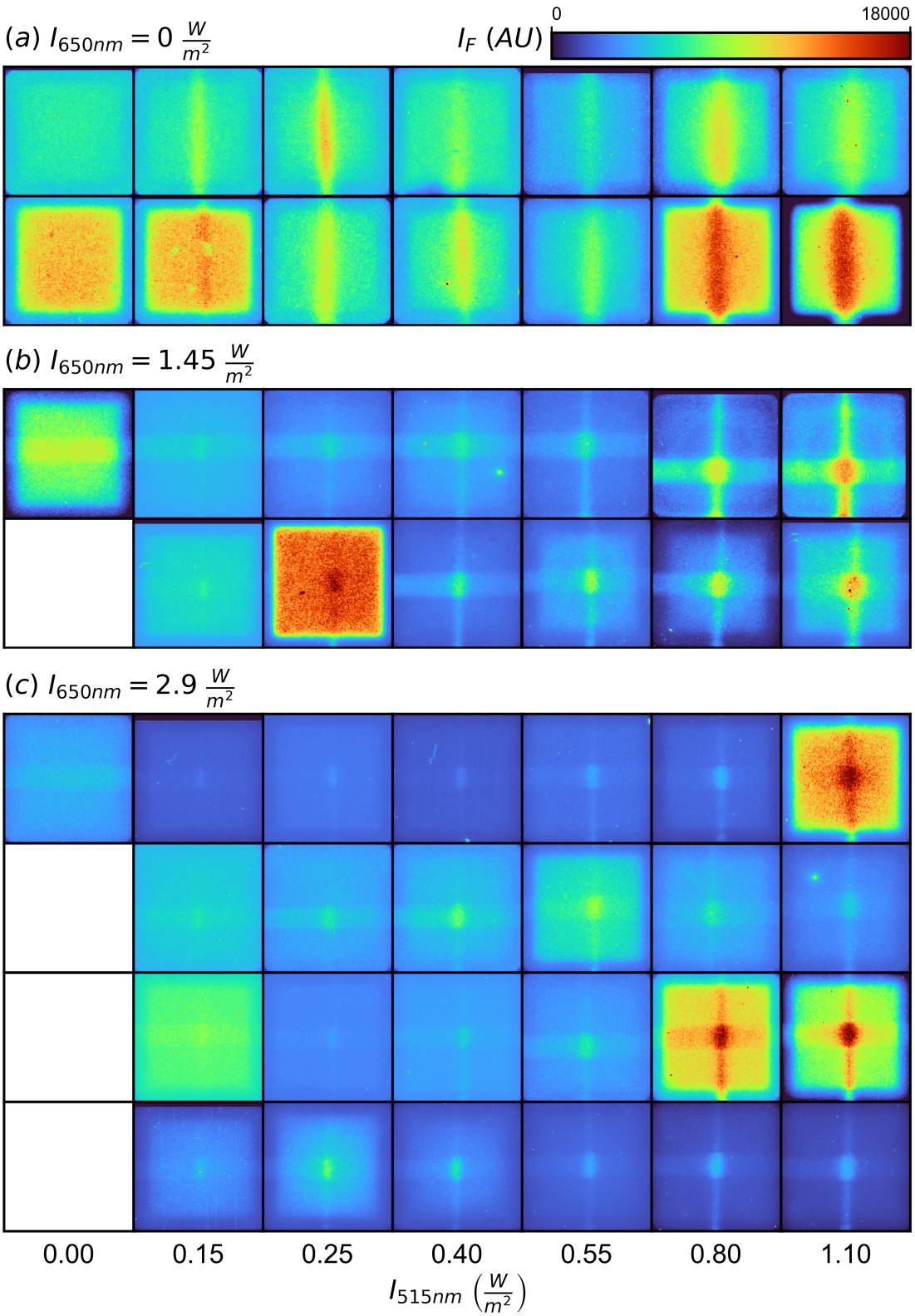


Figure 5.1: *Measurements of gene expression in a single voxel steady-state experiments with various green, I_{515nm}, and red, I_{650nm}, light intensities. Shown is the total intensity of fluorescent light, I_F, emitted from sliced hydrogel slices and background in arbitrary units. Each image is a superposition of mainly two but up to four images of individual 1 mm thick slices. The individual slices span the total volume around the voxel where any gene expression could visually be perceived. Each image in the grid is a square with 10.2 mm sides. Due to the grid nature of the figure the green light intensities are within 0.04 W/m^2 of the actual values.*

The cause of the grainy pattern in the images is unclear. Each pixel in an image of an individual slice represents a volume of 10 $\mu m \times 10\ \mu m \times 1\ mm$ or 0.1 nl. In this volume there should be, assuming $OD^0_{700} = 0.005$, 3 ± 1 cells at the beginning and 10 ± 3 cells at the end of experiment. The numbers are sufficiently small that it is likely that from pixel to pixel the cell distribution is inhomogeneous enough to cause the grainy pattern. Alternatively the effect could be caused by diffraction of light on the cells. A speckle pattern, which forms when a laser is shone through a cell populated volume, has similar visual characteristics to the grainy pattern observed. It is unclear how well the speckle pattern can manifest with the imaging technique used. However, the grainy pattern is not due to the speckle pattern generated by the incident green or red light during the experiment, as the pattern is also present in control experiments where there was no light.

In Figure 5.1 the voxel can be clearly seen in all images where green and red light were present. However, gene expression due to green light entering and exiting the voxel was almost fully suppressed only in experiments with the lowest green intensities (Figure 5.1, $I_{515nm} \leq 0.25\ W/m^2$). Moreover, two other effects can be seen from Figure 5.1. One, the width of gene expression in the voxel is greater that what would be expected from an $\approx 1\ mm$ wide Gaussian beam, which is most noticeable at larger green light intensities (Figure 5.1, $I_{515nm} \geq 0.80\ W/m^2$). Two, there is an apparent increase in gene expression in the gap of the red light illumination, creating a band across all images (Figure 5.1$(b), (c)$). This includes experiments with no green light illumination (Figure 5.1$(b), (c)$, $I_{515nm} = 0\ W/m^2$).

5.2.1 Scope of Green Light Influence

Figure 5.2 shows a grid of plots of normalized average fluorescence values parallel to green beam path. These plots show the average shape of gene expression in the voxel as seen from the direction of the green beam. A single group of experiments for each red light intensity illumination is shown as an example. The plots are of average values of columns parallel to the green beam (Figure 3.21). Each of these columns is cut short to only span the two regions which have no red light illumination – the voxel and background region. The plotted average values are subtracted by their respective background and normalized to their new respective maximum values. The measured value of background of each experiment has an uncertainty between 10% and 15%. The background for each plot was thus manually adjusted within this range to better visually represent the data.

It can be seen from Figure 5.2 that by increasing the intensity of green light the width of the peak of gene expression in the voxel increases. This is consistent with a Gaussian beam due to the nonlinearity of the Hill function, which describes

the normalized gene expression rate, h. The larger the ratio, R, with respect to the half-maximum parameter, K, the smaller is the change in h due to a change in R. R_{ss} directly depends on the magnitude of green light intensity and as a result so does gene expression. Due to higher green light intensities being less effective, normalized gene expression widens with increasing green light intensity. However, this behaviour does not sufficiently explain the observed distribution of normalized average fluorescence in Figure 5.2.

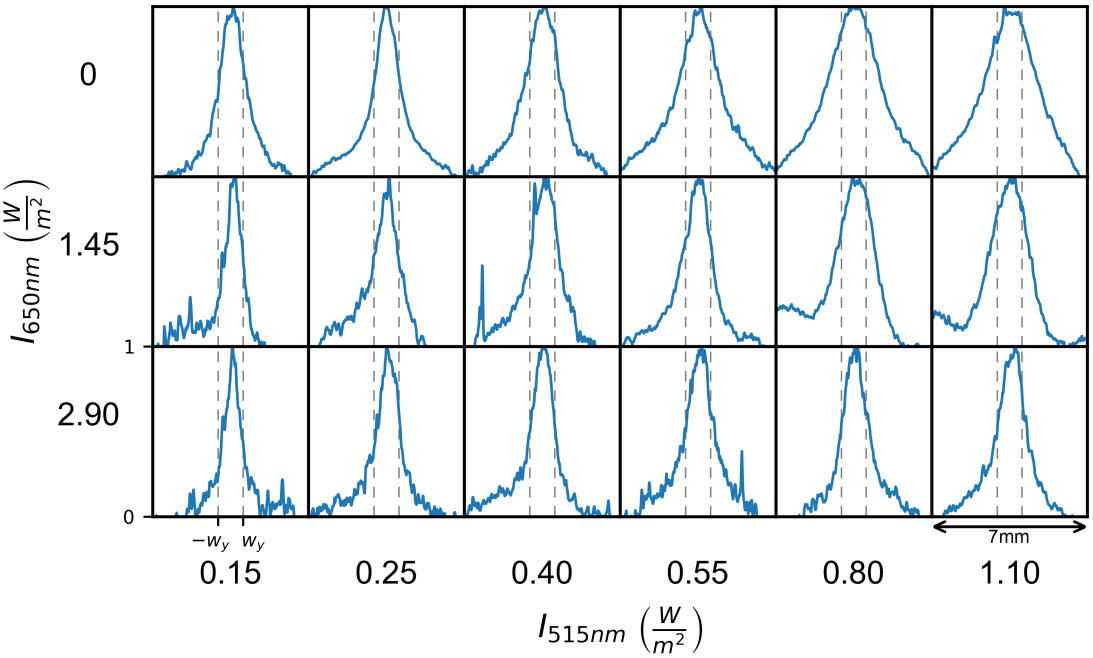


Figure 5.2: *Normalized average fluorescence values of columns parallel to the green beam path in the voxel with subtracted background. Each row are values obtained from summed images of one group of experiments at a given red light intensity, I_{650nm}, and different green light intensities, I_{515nm}. The plots were centered around the peak and the range was truncated from 10 mm to 7 mm for better visualisation. The grey dashed lines are a visual aid for the width of a Gaussian beam, $2w_y$, estimated from the best fit to the measured green light intensity profile shown in Figure 4.4(c).*

The graphs in Figure 5.3(a) show a one-dimensional steady-state Hill function normalized by its maximum, h^{ss}/h^{ss}_{max}, as a result of illumination by green light with a one-dimensional Gaussian beam intensity profile. The beam width w_y is an estimate from the best fit of the Gaussian beam to the measured green beam intensity profile at maximum in the Y orientation (Figure 4.4(c), black line). The graphs in Figure 5.3(b) again show h^{ss}/h^{ss}_{max} but as a result of the measured one-dimensional green intensity profile instead (Figure 4.4(c), blue points). The difference is significant and the width of the response roughly doubles from minimum to maximum green light intensity, whereas the width of the response to the Gaussian beam intensity profile comparatively only slightly increases and it mostly broadens only at the

peak. This is the saturation effect where additional light intensity becomes less and less effective. The point at which intensity becomes less effective is determined by the half-maximum parameter, K. Due to this behaviour, approximating the measured light intensity profile with a Gaussian beam profile is not ideal. The amount of light intensity present in the *tails* of the measured light intensity profile significantly deviates from the Gaussian beam intensity profile and the difference in response is amplified by the nonlinearity the Hill function.

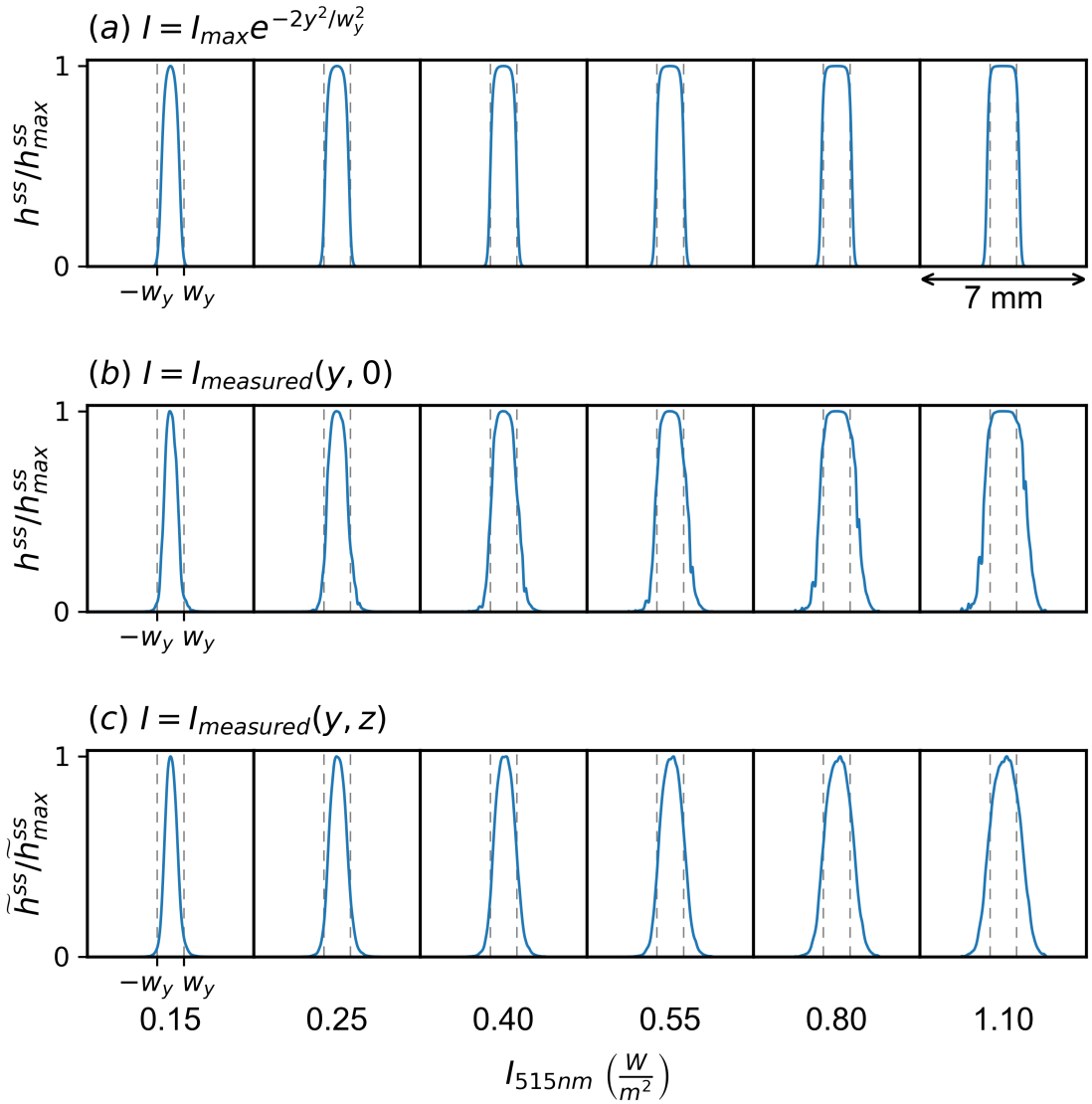


Figure 5.3: *(a) Graphs of the normalized steady-state Hill function, h^{ss}/h^{ss}_{max}, for different green light intensities, I_{515nm}, with a one-dimensional Gaussian beam intensity profile, $I = I_{max}\exp\left(-2y^2/w_y^2\right)$, with a beam radius w_y estimated from the best fit to the measured green light intensity profile. (b) Graphs of the normalized steady-state Hill function for different intensities of the one-dimensional measured green beam intensity profile. (c) Graphs of normalized summed steady-state Hill function, $\tilde{h}^{ss}/\tilde{h}^{ss}_{max}$ for different intensities of the measured two-dimensional beam intensity profile shown in Figure 4.4(a). The grey dashed lines are a visual aid for the width of a Gaussian beam, $2w_y$, estimated from the best fit to the measured green light intensity profile shown in Figure 4.4(c)*

The normalized average fluorescence plots shown in Figure 5.2 do not indicate gene expression resulting from a one-dimensional intensity profile, but instead indicate a normalized average gene expression summed in the Z direction in response to a two-dimensional green light intensity profile. The normalized summed steady-state gene expression is equivalent to the integration of the steady-state Hill function:

$$\tilde{h}^{ss}(y) = \int_{z_1}^{z_2} h^{ss}(I_{515nm}(y,z), I_{650nm}(x,z)=0)\ dz\,, \tag{5.4}$$

where $I_{515nm}(y,z)$ is the measured green intensity profile centered at $z = 0$ (Figure 4.4(a)). z_1 and z_2 were chosen to be $-1.5\ mm$ and $1.5\ mm$ respectively. This range covers the majority of light in the measured green intensity profile and reflects the thickness of the two to three slices that comprise the summed images. The graphs of the normalized integrated steady-state Hill function, $\tilde{h}^{ss}/\tilde{h}^{ss}_{max}$, are shown in Figure 5.3(c). These graphs most resemble the normalized average fluorescence plots with a red intensity of 2.9 W/m^2 in Figure 5.2. While the shape of the calculated gene expressions appears to be in rough agreement with measurements, the comparison also depends on the determination of the background. If background is too low, the tails become more pronounced and the peak appears wider and if it is too high, the tails disappear and the peak appears thinner. Furthermore, it is likely that the background is not a constant value independent of position.

There are three ways that were identified that can affect the shape of gene expression as a result of green light illumination. First is the halo effect around the edges. While there is a relatively sharp change in fluorescence at 1 mm from the edges of the slice, it is possible that the effect extends beyond this boundary; however, in a diminished fashion.

The second way is that there is significant scattering within the build volume. Figure 4.6(d) suggests that the area where intensity is above 13.5% is mostly unaffected, whereas the area where intensity is below 5% is noticeably larger due to scattering. The increase in the area with intensity below 1% is less of a factor in the Z direction due to the range covered by the slices included in the analysis. With sufficiently high green light intensity, the measured scattered light could noticeably contribute to the widening of the voxel due to the nonlinearity of the Hill function. However, voxels whose dimensions are defined by a properly scaled intensity are not expected to be significantly affected by the measured scattering. This is again due to the nonlinearity of the Hill function, but instead at low green light intensities where R is small compared to K. Importantly, the measured scattered green light intensity profile does not account for all scattered light. Light scattered at larger angles than measured could noticeably contribute to the apparent widening of the green beam.

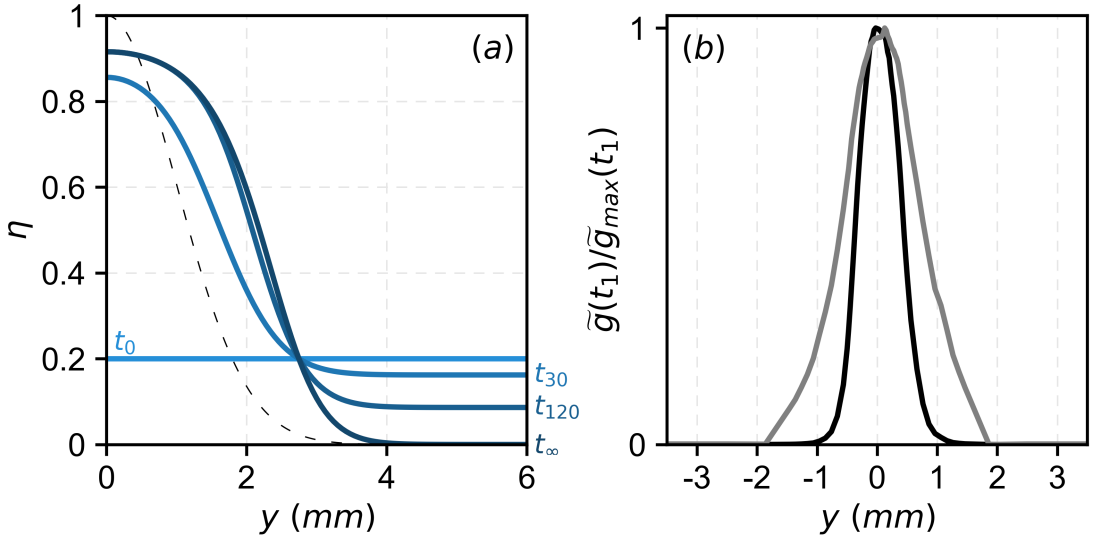


Figure 5.4: *(a) Fraction of active-state photoreceptors, η, in response to a green Gaussian beam intensity profile at four different times. At time $t_0 = 0$ the initial fraction was set to 20% with the following graphs showing the distribution at $t_{30} = 30$ min, $t_{120} = 120$ min and $t_\infty \to \infty$. The black dashed line is a Gaussian beam intensity profile centered at $y = 0$ with a beam radius of $w = 2$ mm with a maximum intensity of $I_{max} = 2.5\ W/m^2$. (b) Normalized integrated total gene expression density, $\tilde{g}(t_1)$, further normalized by its maximum, $\tilde{g}(t_1)/\tilde{g}_{max}(t_1)$, calculated for the measured green beam intensity profile. The graphs show the values at time $t_1 = 2$ hours at a depth of 5 mm with the maximum intensity of the green beam $I_{max} = 1.1\ W/m^2$ at the surface. The black line is the graph where the initial fraction of active photoreceptors was 0% and the grey line is the graph where the initial fraction was 50%.*

The third way that gene expression can be influenced is by the activation of photoreceptors during hydrogel culture preparation or in general before the experiment. As reported by Olson [67], dark reversion rate is negligible or nonexistent. This means that any active-state photoreceptors remained active until being deactivated by red light. In an ideal steady-state experiment this does not matter, as a specific end state is achieved in this system regardless of the starting point. However, the real experiments were too short for the areas illuminated by the tails of the green light to reach a steady state. Furthermore, given the parameters (Table 2.1), the time constants for the change in the fraction of active-state photoreceptors, η, at a given maximum green light intensity, range from 90 minutes at the lowest to 30 minutes at the highest intensity.

The nonlinearity of the Hill function helps in this regard, as the experiments with sufficient green intensity reach the effective maximum of gene expression in a single time constant. With the presence of an initial population of active-state photoreceptors the time needed to reach a steady state can be further shortened. However, in the tails of the green light intensity profile the steady-state η is poten-

tially much smaller than the initial fraction of active-state photoreceptors, η_0. In this case η would have to drop significantly to reach a steady state. In the absence of red light the only mechanism that achieves this is the introduction of new ground-state photoreceptors through population growth. The cell growth is relatively slow and during the active two hours of growth during the experiment η_0 can only be cut in two or three. This can be further slowed down by low intensity green light whose resulting photoconversion rate is comparable to the growth rate.

Figure 5.4(a) shows an example of how η behaves over time given a substantial initial fraction and a Gaussian beam intensity profile. It can be seen that after 30 minutes η already reached values above 45% almost all the way to the waist of the Gaussian beam at 2 mm. At this percentage the Hill function is mostly saturated, $> 85\%$. Further away from the centre, it can be seen that the initial fraction barely dropped in the absence of green and red light.

Figure 5.4(b) shows a comparison between two graphs of normalized integrated total gene expression density:

$$\tilde{g}(t_1, y) = \int_0^{t_1} \int_{z_1}^{z_2} h\left(t, I_{515nm}(y, z), 0\right)\, \rho_{cells}(t)\, dz\, dt\,, \tag{5.5}$$

where h is the time dependant Hill function. Both graphs are calculated for the measured green light intensity profile, over the course of two hours of exponential bacterial growth, where one has initial fraction of active-state photoreceptors of 0% and the other 50%. Significant widening can be seen similar to the one seen in the first row of Figure 5.2.

Figure 5.5 shows a direct comparison between two calculated functions indicating gene expression and two normalized average fluorescence values. The steady-state calculation, that assumes negligible contributions from the background and transient effects, is compared to the measurement in Figure 5.5(a), and a time dependant calculation, that assumes significant initial fraction of active-state photoreceptors is compared to the measurement in Figure 5.5(b). The latter best resembles measurements of gene expression from experiments without any red light. This suggests that in experiments without the red light steady state was not reached in areas with lower green light intensity. As these areas exhibit more gene expression than expected, a likely explanation is that there was indeed a significant initial fraction of active-state photoreceptors that was not reduced sufficiently fast enough for it to resemble the steady state. A better match to the steady-state calculation are experiments with red light, which suggests that there is a non-negligible amount red light within the voxel. Red light intensity within the voxel would explain the discrepancy between the measurements with and without red light. With the aid of red light, the tails

of the green light intensity profile contribute relatively much less to the overall gene expression when compared to higher green light intensity overlapped by the same red light intensity. Furthermore, with the addition of red light, the dynamics of the system hasten and a steady state is achieved sooner. As a consequence, red light also helps limit the influence of the initial fraction of active-state photoreceptors by increasing the rate at which it decays.

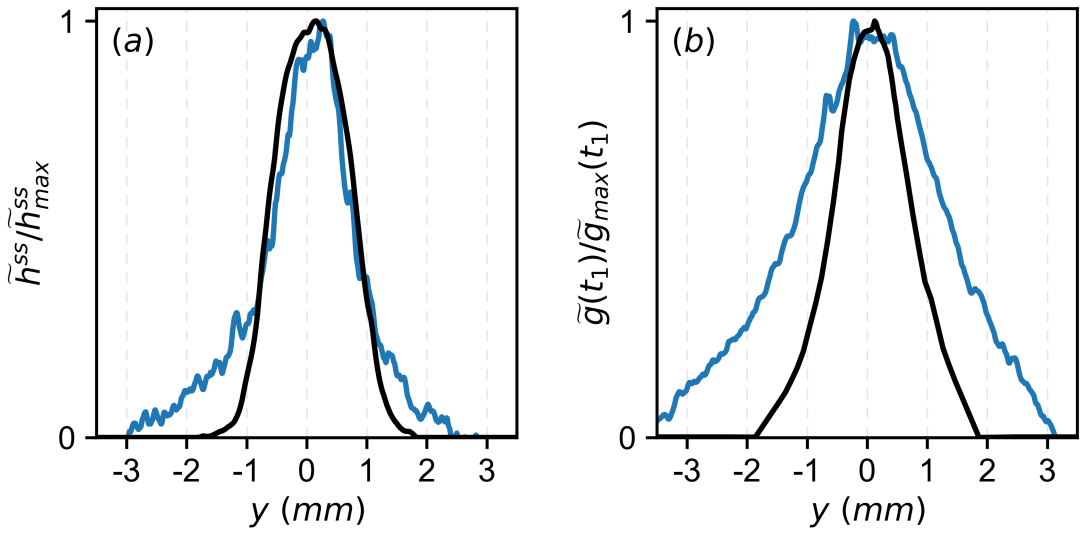


Figure 5.5: *Comparison between simulated normalized gene expression rate, normalized total gene expression, and normalized average fluorescent values of columns parallel to beam path. Black lines are simulation graphs and blue lines are plotted measurements. (a) Plotted values were obtained from a steady-state experiment with red light intensity of* $2.9\ W/m^2$ *and peak green light intensity of* $1.1\ W/m^2$*. The graph of the normalized integrated steady-state Hill function,* $\tilde{h}^{ss}/\tilde{h}^{ss}_{max}$ *was calculated for the measured green beam intensity profile at depth of* $5\ mm$ *at a surface peak intensity of* $1.1\ W/m^2$*. (b) Plotted values were obtained from a steady-state experiment with no red light and peak green light intensity of* $1.1\ W/m^2$*. The graph of normalized integrated total gene expression density,* $\tilde{g}(t_1)/\tilde{g}_{max}(t_1)$*, was also calculated for the measured green beam intensity profile at a depth of* $5\ mm$ *at a surface peak intensity of* $1.1\ W/m^2$ *at time* $t_1 = 2\ hours$*.*

5.2.2 Scope of Red Light Influence

Figure 5.6 shows a grid of plots of normalized fluorescence values on the green beam path with one group of experiments as an example for each red light intensity. Measurements shown in Figure 5.6 are of the same experiments that are shown in Figure 5.2. Likewise, the plotted values are subtracted by their respective background and normalized to their new respective maximum.

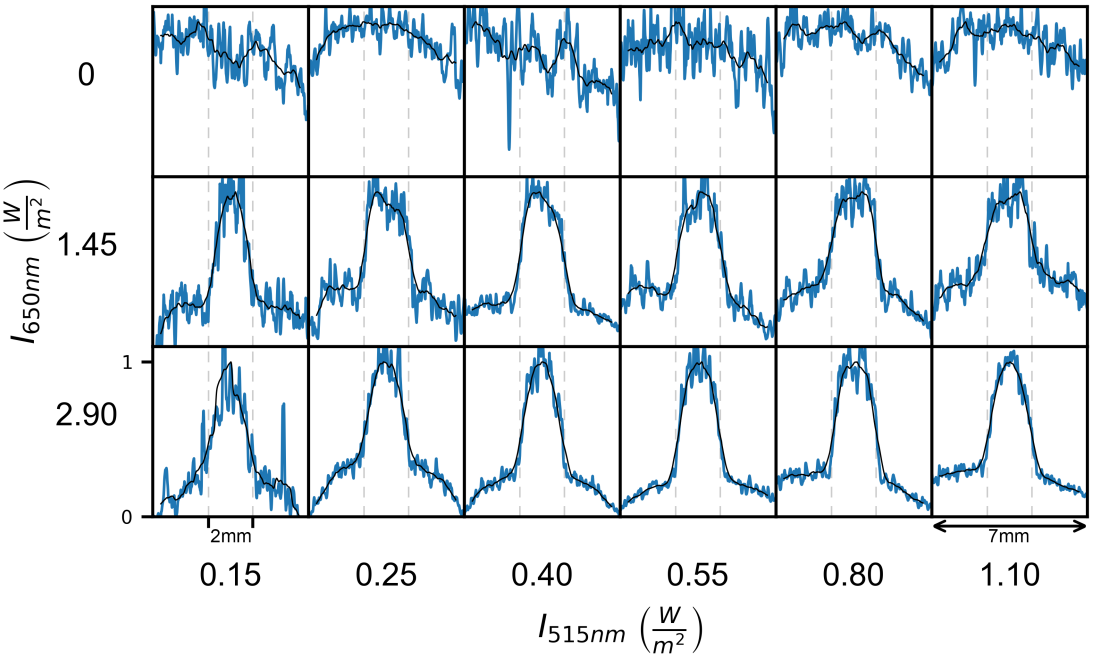


Figure 5.6: *Normalized average fluorescence values on the green beam path. Each row are values obtained from summed images of one group of experiments done at a red light intensity, I_{650nm}, and different green light intensities, I_{515nm}. Blue lines are plots of values obtained from measurements. Black lines are the moving average for each plot. The plots are normalized by the maximum of the moving average of each plot. The plots are centered around the peak and the plot range is truncated from 10 mm to 7 mm for better visualisation. The grey dashed lines are a visual aid for the width of the gap in the red light intensity profile (Figure 4.5).*

As expected in the absence of red light there is continuous gene expression that is decreasing from left to right, which is the direction of the green beam and its attenuation (Figure 5.6, $I_{650nm} = 0\ W/m^2$). With the presence of red light illumination gene expression drops significantly. The shape of the red light intensity profile with its 2 *mm* gap is reflected in gene expression with a 2 *mm* wide peak. By increasing the intensity of red light it is expected that gene expression would be further suppressed in relation to the non-suppressed gene expression. However, the relative amount of gene expression does not appear to noticeably decrease, which could indicate that suppression is already as high as it could be and that the measured gene expression is only due to background. The nonzero values around the peaks in Figure 5.6, $I_{650nm} \geq 1.45\ W/m^2$ should then be attributed to erroneously calculated background. However, by observing the entire area of summed images in Figure 5.1(b) and (c), we see that this is not the case, as the influence of the green beam can clearly be seen. Instead, it is possible that the intensity of red light within the voxel is sufficiently high, that by increasing the overall intensity, the suppression of gene expression within the voxel is also noticeably increased, therefore upon normalization the suppression in the suppressed region does not appear as strong.

Measurements shown in Figures 4.5 and 4.7 suggest that the relative amount of red light present in the gap of the red light intensity profile is on average at least 7% up to 16% or more depending on whether there is significant scattering at larger angles. These values are significant and could account for the previously described behaviour, where it would appear that increased red light intensity does not further suppress gene expression.

The band of increased gene expression seen in the summed images of fluorescence from experiments with red and no green light (Figure 5.1) is evidence of an initial fraction of active-state photoreceptors, η_0. Determination of η_0 was attempted by subtracting the average fluorescence value of the red only regions – suppressed background – from the average fluorescence value of slices of little interest – background. The slices of little interest were limited to slices which were at least 6 mm away from the voxel to try and limit the influence of red and green light. The average difference between these two backgrounds was calculated for all experiments with average red light intensity of 1.45 W/m^2 and for all experiments with average red light intensity of 2.9 W/m^2. The two averages are shown in Table 5.1. It can be seen that the average difference in experiments with higher red light intensity is statistically smaller when compared to experiments with lower red light intensity. This suggests two things. One, η_0 under direct red light illumination was largely deactivated in both cases and it happened before any significant gene expression could occur; and two, the scattered red light had sufficient influence several millimeters from the voxel to significantly deactivate η_0 in these regions as well. This occurrence prevents a reliable determination of η_0 in these experiments and also suggests that there is significant scattering of red light at larger angles.

Table 5.1: *Average fluorescence values in arbitrary units, AU, of the suppressed background and the difference between the suppressed background and the background from slices at least 8 mm away from the voxel. Average values were obtained from all experiments for the respective average red light intensities, I_{650nm}, regardless of green light intensities. Errors are one standard deviation. Large errors of the average suppressed background are due to some outlying experiments where gene expression was high overall, omitting those yields a relative error of* $\approx 30\%$ *as opposed to* $\approx 60\%$.

I_{650nm} (W/m^2)	Average Suppressed Background (AU)	Average Difference Between Backgrounds (AU)
1.45	2500 ± 1400	820 ± 250
2.90	2000 ± 1300	380 ± 170

Figure 5.7 shows fluorescence values for two experiments contrasted to background. Contrasted here refers to subtraction of background from the signal and then dividing the difference by the background. While normalization in this work refers to rescaling of values to be between 0 and 1, contrast will specifically refer to the induced gene expression as a multiple of background gene expression.

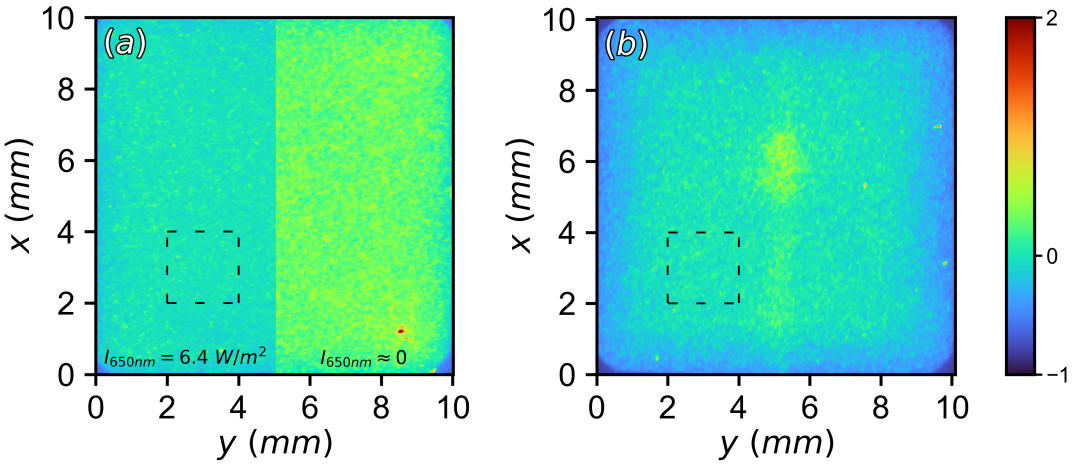


Figure 5.7: *Background contrasted fluorescence images of two separate experiments where the volume of interest was illuminated with a red light intensity of* 6.4 W/m^2 *for the first half an hour of the three hour experiment. The average background was calculated from the area indicated by the dashed square for the respective image. This average was subtracted from the fluorescence values of the respective image and the difference was divided by the average background to obtain the contrasted fluorescence images.* (*a*) *Composite fluorescence image of two different slices from the same experiment. The half on the left is a slice that was under direct red light illumination while the right half is a slice that was* 8 *mm above red light illumination.* (*b*) *Fluorescence image of a slice containing the voxel in it's entirety. The average red and peak green intensities were* I_{650nm} = 3.2 W/m^2 *and* I_{515nm} = 0.6 W/m^2.

Both experiments shown in Figure 5.7 were illuminated with the red light intensity profile without the gap for the first half an hour of the experiment. In the second experiment, shown in Figure 5.7(*b*), at the one hour mark the voxel was continuously illuminated until the end of experiment at three hours. The voxel was in the same volume that was previously illuminated by red light. In the first experiment there is a clear difference between the background, where η_0 was deactivated, and the background where that is not the case. In the second experiment it can be seen that there is no band with increased gene expression. Visible is only the influence of green light in the voxel and the suppressed region. This is in direct contrast to summed images in Figure 5.1 where the band can be seen in all experiments. Given that in this case both experiments were illuminated with red light before any significant gene expression could take place, it is reasonable to conclude that there indeed is an initial fraction of active-state photoreceptors that is responsible for the increased gene expression in the steady-state experiments.

The lack of a band in the second experiment also indicates that red light does not noticeably influence background gene expression, which is not due to η_0. This means that what was previously referred to as the *suppressed* background gene expression can be thought of only as *the* background gene expression. What was previously referred to as the background gene expression is instead gene expression due to the presence of unwanted active-state population of photoreceptors and it will be referred to as an *active* background gene expression. The main distinction between the two is that the active background can be influenced by light, whereas the background cannot. This is in contrast with the previous definitions, which suggested that the background could be influenced by red light.

5.3 Parameter Estimations

Data from three regions in the summed images were extracted for parameter estimations: the background, which is the average fluorescence value from the red only region; the average voxel maximum, which is the maximum of the average fluorescence values of columns parallel to the green beam path bound by the voxel region; and the average suppressed region maximum, which is the maximum of the average fluorescence values of columns parallel to the green beam path bound by the suppressed region. Given the values shown in Table 2.1, (5.2) only has two unknowns, a' and b'. The total background expression b' can be obtained from the background of the summed images by dividing the value by the combined thickness of the slices comprising the image; however, due to arbitrary units this has no meaning outside the scope of these experiments and the imaging equipment. The same arbitrarity applies to the total maximum expression a'. Furthermore, because the cell population density varies significantly between experiments, at least 15% at the end of experiment from the uncertainty of $k_{growt1h}$ alone, any determination of a' and b' from these experiments would also be quite inaccurate. Indeed, this variation can be seen in the standard deviation of the average *suppressed* background in Table 5.1. By ignoring a few outliers the background standard deviation is ≈30%, which should reflect the variation in cell population.

The data from the summed images was thus used to try and estimate only the following two quantities: the relative amount of red light present in the voxel and the ratio between a' and b'. The ratio between a' and b' will be referred to as maximum contrast, as the measured background fluorescence intensity has to be subtracted from the fluorescence intensity due to active gene expression to obtain a quantity related to a'.

5.3.1 Error Estimates

The three values obtained from the summed images of fluorescence are: the average measured background, s_B, the measured average voxel maximum, s_V, and the measured average suppressed region maximum, s_S.

The error estimate for the measured background, Δs_B, was set equal to the standard deviation of the background in the summed image:

$$\Delta s_B = \sigma_B \,, \tag{5.6}$$

where σ_B was chosen over the standard error due to the background not being very constant in most cases, instead it tends to decrease towards the edges of the slice. Furthermore, the selection of the background region during image processing could be too large and include values not representative of the background.

The error estimate for the measured average voxel maximum, Δs_V, was determined in the following way:

$$\Delta s_V = MAX\left(\sigma_V, \Delta s_V'\right) , \tag{5.7}$$

where σ_V is the standard deviation of the values at the center of the green beam that determine the average voxel maximum and $\Delta s_V'$ is the estimated error due to misalignment. Misalignment can occur in two ways: the addition of slices was offset or the selection of regions during image processing was not exact. Error due to angle misalignment was deemed negligible for values in the voxel. $\Delta s_V'$ was estimated in the following way:

$$\Delta s_V' = \bar{g}_V - s_V = \frac{\bar{g}_V' - m\ \bar{g}_S}{1-m} - s_V \approx \frac{m}{1-m}\left(s_V - s_S\right) , \tag{5.8}$$

where $\bar{g}_V$ is the exact average maximum voxel gene expression, $\bar{g}_V'$ is the perceived average maximum voxel gene expression due to misalignment, $\bar{g}_S$ is the exact average maximum suppressed region gene expression and m is the proportion of misalignment relative to voxel size. m was estimated to be 10%, which corresponds to 0.2 mm, 20 pixels or 2% of the entire image. Since the exact values g_V' and g_S are not known, they were approximated by the ones measured – s_V and s_S. σ_V and $\Delta s_V'$ are very correlated. With increased misalignment the values in the voxel on the beam path vary more, which increases σ_V. σ_V can be an underestimation in cases where the misaligned parts of the voxel are cut off during manual region selection. For this reason the maximum of both is chosen as the error estimate. In most cases the errors estimates are similar in magnitude. It should be noted that with the exception of random noise, there are no effects that can cause the measured value

to be greater than the exact value. Therefore, measured values are strongly biased towards smaller values and in this case errors mostly estimate how much greater the measured value should be.

The error estimate for the measured average suppressed region maximum, Δs_S, was set equal to the standard deviation of the average maximum values on the beam path in the suppressed region:

$$\Delta s_S = \sigma_S \,. \tag{5.9}$$

Similar to the background error estimate, the average value of the maximum is possibly subjected to the halo effect, misalignment and region selection. Unlike the average voxel maximum, misalignment contributes less to the overall error of the average suppressed region maximum due to a larger area being averaged.

The last error estimate is for the background contribution not associated with gene expression – the ambient background, $s_{AmbientB}$. Which was obtained from four control slices. The standard deviation of the average ambient background for each sample was 5% to 10%, which includes random noise and the slight decrease of the background towards the edges of the slice. However, the values for the average ambient background of different experiments would differ by a slightly greater value than the average standard deviation of the background of each experiment. Therefore, the error estimate for the average ambient background, $\Delta s_{AmbientB}$, was set to a standard deviation of all values of $s_{AmbientB}$ from all experiments:

$$\Delta s_{AmbientB} = \sigma_{\{s_{AmbientB,i}\}} \,. \tag{5.10}$$

This was done to try cover any deviations due to slice thickness differences. This error estimate was 10% and on average it increased the individual ambient background error estimates.

Cells themselves exhibit fluorescence; however, they are not present in the control samples, which were used to determine the ambient background. Cell fluorescence was measured separately in relation to control samples and it was determined to add approximately 10% of additional fluorescence. Ambient background was thus multiplied by this value to account for fluorescence of cells. Any error incurred was estimated small enough to be subsumed into $\Delta s_{AmbientB}$.

5.3.2 Red Light Leakage Estimation

Without known values of a' and b', the relative amount of red light intensity within the voxel can be estimated by fitting the ratio between the average maximum voxel gene expression, $\bar{g}_V$, and the average maximum suppressed region gene expression, $\bar{g}_S$, to the ratio of the respective average maximum fluorescence values, all with subtracted background gene expression, $\bar{g}_B$. The ratio is as follows:

$$\begin{aligned}
\frac{\bar{g}_V - \bar{g}_B}{\bar{g}_S - \bar{g}_B} &= \frac{\frac{1}{x_2 - x_1} \int_{z_1}^{z_2} \int_{x_1}^{x_2} \left(b' + a' h_V^{ss}\right) - b' \; dx \, dz}{\frac{1}{x_1 - x_0} \int_{z_1}^{z_2} \int_{x_0}^{x_1} \left(b' + a' h_S^{ss}\right) - b' \; dx \, dz + \frac{1}{x_3 - x_2} \int_{z_1}^{z_2} \int_{x_2}^{x_3} \left(b' + a' h_S^{ss}\right) - b' \; dx \, dz} = \\
&= \frac{\Delta x_S}{\Delta x_V} \frac{\int_{z_1}^{z_2} \int_{x_1}^{x_2} h^{ss}\left(I_{515}^m\left(y_c,\ z\right) \cdot e^{-\mu_G x},\ \eta_R I_{650} \cdot e^{-\mu_R y_c}\right) dx \, dz}{\int_{z_1}^{z_2} \left(\int_{x_0}^{x_1} h^{ss}\left(I_{515}^m\left(y_c,\ z\right) \cdot e^{-\mu_G x},\ I_{650} \cdot e^{-\mu_R y_c}\right) dx + \int_{x_2}^{x_3} h_S^{ss} \; dx \right) dz} = \\
&= f\left(\eta_R, I_{515}, I_{650}\right), \\
& y_c = 5 \; mm, \quad \mu_G \approx 120 \; m^{-1}, \quad \mu_R \approx 45 \; m^{-1},
\end{aligned} \tag{5.11}$$

where x_0, x_1, x_2 and x_3 are 1, 4, 6, and 9 mm respectively, denoting the boundaries between the halo region, the suppressed region and the voxel, z_1 and z_2 are -1.5 mm and 1.5 mm respectively, h_V^{ss} is the steady-state Hill function in the voxel, h_S^{ss} is the steady-state Hill function in the suppressed region, Δx_V and Δx_S are the X coordinate spans of the voxel and suppressed regions, I_{515}^m is the measured incident green light intensity profile, I_{650} is the average value of incident red light intensity, y_c is the center of the voxel with respect to the Y coordinate, μ_G and μ_R are estimated green and red attenuation coefficients at 2.5 hours of the experiment and η_R is the fraction of the average red light intensity present within the voxel – red light leakage. After integration the ratio is a function of only one unknown parameter – η_R – making it independent from sample to sample cell population differences and a and b parameter variations.

To fit the ratio between the voxel and suppressed region gene expression, the measured data was calculated in the same manner:

$$\frac{(s_V \pm \Delta s_V) - (s_B \pm \Delta s_B)}{(s_S \pm \Delta s_S) - (s_B \pm \Delta s_B)} = r_{V/S} \pm \Delta r_{V/S}\,, \tag{5.12}$$

where $\Delta r_{V/S}$ is the error of the ratio. The relative error estimate of the difference between the fluorescence value in the suppressed region and the background fluorescence in the denominator of the ratio is on the order of 50% to 200%. The distribution of $r_{V/S}$ is exceedingly non-Gaussian for normally distributed random errors of the denominator of such magnitude. Normal error propagation is thus not possible. In lieu of that the error was determined by calculating the ratio's extreme values from the extreme values of the measurements. An extreme value of the measurement is given by its estimated error. In cases where the extreme value for $r_{V/S}$ was negative, that data point's positive relative error was set to 1000%. These errors estimates exhibit an obvious bias towards large values of $r_{V/S}$.

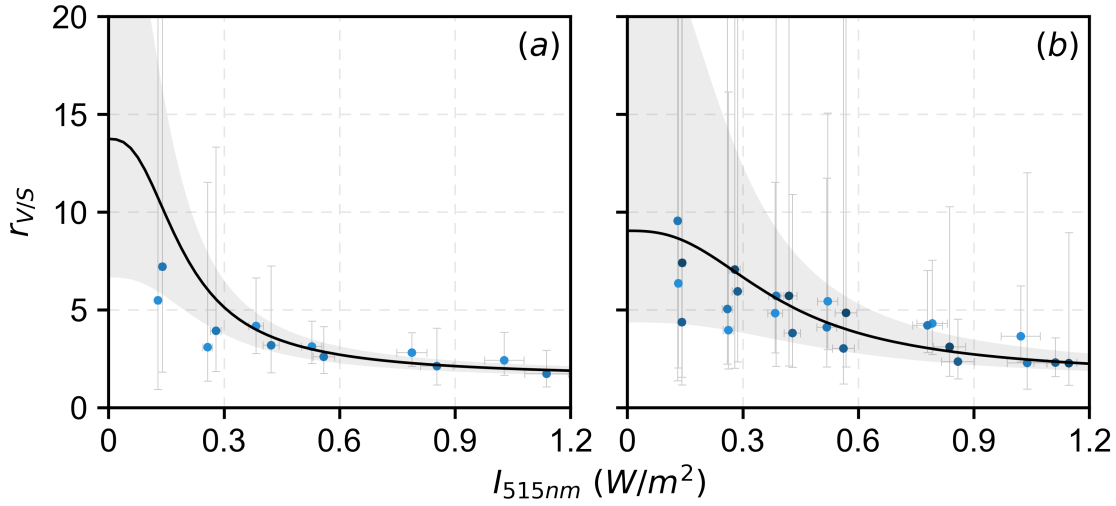


Figure 5.8: *Best fit of the ratio between the average maximum voxel gene expression and the average maximum suppressed region gene expression to the measured values, $r_{V/S}$. Each blue shade of the plotted data corresponds to one group of steady-state experiments. The solid black line graphs are the best fit estimates and the grey shaded areas are determined by parameter error estimates. The green intensity, I_{515nm}, relative error estimate is 5%. (a) Fit to measurements with red light intensity of $I_{650nm} = 1.45\ W/m^2$. (b) Fit to measurements with red light intensity of $I_{650nm} = 2.9\ W/m^2$. I_{515nm} values of data points were randomly perturbed for up to 2% during plotting for better visualisation.*

The best fits of $r_{V/S}$ to steady-state measurements for both values of red light intensity are shown in Figure 5.8 and the best fit parameter estimates are shown in Table 5.2. The fits were performed in Mathematica 13.0 with the *NonlinearModelFit* function. The data points were weighted using the inverse square of their positive error estimate. Due to the non-Gaussian nature of data points' errors, the errors of parameter estimates in Table 5.2 do not represent one standard deviation but rather generally reflect the uncertainty. Despite this, $r_{V/S}$ appears to be a reasonably good fit and the average estimate obtained for η_R is $20\% \pm 10\%$, which agrees well with the transmitted light profile measurements. In light of these results the value of η_R for future calculations was set to 20%.

Table 5.2: *Estimates of red light leakage, η_R, obtained by performing a best fit of (5.11) to the measured data (Figure 5.8) and their average. The errors are rough estimates of uncertainty and do not represent the confidence interval associated with one standard deviation.*

I_{650nm} (W/m^2)	η_R	$\bar{\eta}_R$
1.45	0.10 ± 0.14	0.20 ± 0.10
2.90	0.29 ± 0.14	

5.3.3 Estimation of the Ratio between the Maximum and Background Gene Expression

The ratio between the maximum gene expression rate, a, and background gene expression rate, b, could potentially be estimated from the ratio between a' and b':

$$r_{a'/b'} = \frac{a'}{b'} = \frac{a}{b} \cdot \frac{\int_0^{t_{End}} f_a(t)\rho_{cells}(t)\ dt}{\int_0^{t_{End}} f_b(t)\rho_{cells}(t)\ dt} = \frac{a}{b} \cdot f_{a/b}(t_{End})\,, \tag{5.13}$$

where f_a and f_b are unknown functions of time for the corresponding rate. Ideally these two functions do not differ too much and the function $f_{a/b}$ is or is almost equal to 1. To obtain the maximum contrast – the ratio between a' and b' – the average background gene expression, $\bar{g}_B$, has to be subtracted from the average maximum

gene expression, $\bar{g}$, and the difference divided by said background:

$$\frac{\bar{g}-\bar{g}_B}{\bar{g}_B} = \frac{\dfrac{1}{x_2-x_1}\displaystyle\int_{z_1}^{z_2}\int_{x_1}^{x_2}\left(b' + a' h^{ss}\right) - b'\; dx\, dz}{\displaystyle\int_{z_3}^{z_4} b'\; dz} = \tag{5.14}$$

$$= \frac{a'}{b'} \cdot \frac{1}{\Delta x \Delta z}\int_{z_1}^{z_2}\int_{x_1}^{x_2} h^{ss}\left(I^m_{515}\left(y_c,\ z\right)\cdot e^{-\mu_G x},\ I_{650}\cdot e^{-\mu_R y_c}\right)\; dx\, dz\,,$$

where $\Delta x = x_2 - x_1$, x_1 and x_2 are boundaries of a region in X coordinates, $\Delta z = z_4 - z_3$, z_3 and z_4 are 0 mm and 1 mm respectively, I_{650} is the average value of incident red light intensity, other parameters are the same as in (5.11). The background is assumed to be constant throughout the build volume, therefore the choice for z_3 and z_4 is arbitrary. Equation (5.14) can be thought of as a fill factor. Its value equals $r_{a'/b'}$ when the volume given by the background, Δz, exhibits maximum possible gene expression. This value was set to 1 mm due to the target volume of the voxel. However, because the reach of green light goes beyond the voxel, $z_2 - z_1$ is set to 3 mm, which means that given an infinite green light intensity the value of (5.14) can reach $3 \cdot r_{a'/b'}$.

Data from steady-state experiments, to be fit by (5.14), was calculated in the following way to obtain the contrast:

$$\frac{\left(s_{\{V,S\}} \pm \Delta s_{\{V,S\}}\right) - \left(s_B \pm \Delta s_B\right)}{\left(s_B \pm \Delta s_B\right) - \left(s_{AmbientB} \pm \Delta s_{AmbientB}\right)} = r_{\{V,S\}/B} \pm \Delta r_{\{V,S\}/B}\,, \tag{5.15}$$

where $r_{\{V,S\}/B}$ is the contrast in either the voxel or suppressed region, $\Delta r_{\{V,S\}/B}$ is the error of $r_{\{V,S\}/B}$ and $s_{\{V,S\}}$ is the measured average maximum of one of two areas. The error estimates of the denominator of $r_{\{V,S\}/B}$ are on the order of 15% and thus the distribution of $r_{\{V,S\}/B}$ remains largely Gaussian and normal error propagation can be used.

The best fits of (5.14) to $r_{\{V,S\}/B}$ are shown in Figure 5.9 and the best fit parameter estimates are shown in Table 5.3. The fits were again performed in Mathematica 13.0 with the *NonlineraModelFit* and the data points were weighted with the inverse square of their error estimates. In the case of best fits to $r_{V/B}$, where gene expression is subjected to red light leakage, three estimates were calculated. Two additional best fits were performed for the two estimated extreme values of η_R – $\eta_R \in \{0.1, 0.2, 0.3\}$. The resulting values of $r_{a'/b'}$ were considered equally likely, which is an overestimation, and were used to estimate the standard deviation of the

average $r_{a'/b'}$. The resulting standard deviation estimate was twice as large as the one obtained from the best fit with $\eta_R = 0.2$.

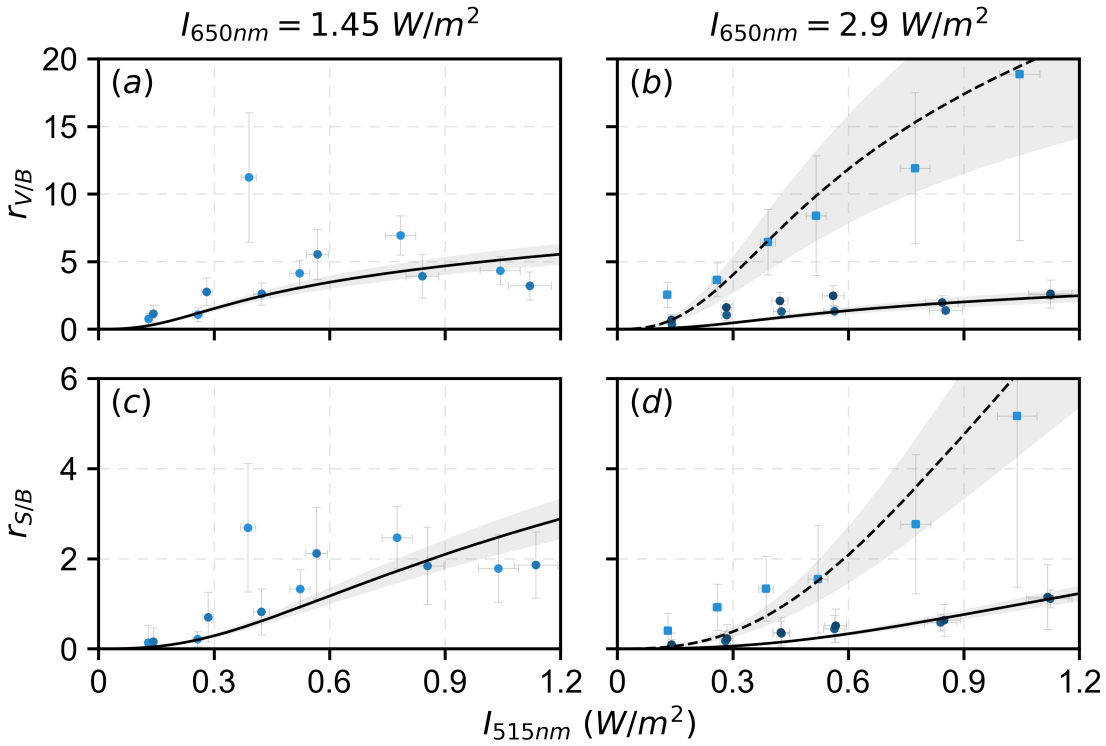


Figure 5.9: *Best fit estimates of* (5.14) *to the measured contrast,* $r_{\{V,S\}/B}$*, in the respective regions. Each blue shade of the plotted data corresponds to one group of steady-state experiments. The solid black line graphs are the best fit estimates and the grey shaded areas are determined by parameter error estimates. The green intensity's,* I_{515nm}*, relative error estimate is* 5%*.* (*a*)*,* (*b*) *Best fit estimates of* (5.14) *to* $r_{V/B}$*.* (*c*)*,* (*d*) *Best fit estimates of* (5.14) *to* $r_{S/B}$*.* (*a*) *and* (*c*) *are best fits to measurements from experiments with red light intensity of* $I_{650nm} = 1.45\ W/m^2$*.* (*b*) *and* (*d*) *are best fit estimates to measurements with red light intensity of* $I_{650nm} = 2.9\ W/m^2$*. The dashed lines are the best fit estimates for the group of measurements denoted by squares.* I_{515nm} *values of data points were randomly perturbed for up to* 2% *during plotting for better visualisation.*

The best fit estimations in Figure 5.9 appear to follow the trend set by the data points; however, it can be seen that the data points are much more scattered when compared to data in Figure 5.8, which is to be expected, as there are more parameters that may vary. It follows that a' and b' are the likely source of this dispersion. Despite this, the estimates of $r_{a'/b'}$ generally agree and the average of the estimates is 4.8 ± 1.1. While this number is much smaller than what was reported by Ong and Tabor [68] it is of the same order as what was reported by Nakajima et al. [70]. Optimally, experiments would have been run at a high green light intensity with a constant sharp step-like profile, which clearly separates the voxel from the rest of the volume. However, light scattering might still skew the results in such a case.

Table 5.3: *Parameter estimates of maximum contrast, $r_{a'/b'}$, obtained by a best fit of* (5.14) *to the measured data (Figure 5.9). The $\bar{r}_{\{V,S\}/B}$ column shows the average value of $r_{a'/b'}$ of all four estimates. The $r_{\square\{V,S\}/B}$ columns are the best fit parameter estimates for data points denoted by squares in Figure 5.9*(b) *and* (d).

	$r_{a'/b'}$				
I_{650nm} (W/m^2)	$r_{V/B}$	$r_{S/B}$	$\bar{r}_{\{V,S\}/B}$	$r_{\square V/B}$	$r_{\square S/B}$
1.45	5.7 ± 0.8	5.7 ± 0.9	4.8 ± 1.1	-	-
2.90	3.1 ± 0.6	4.8 ± 0.7		27 ± 9	30 ± 9

More interestingly, data points denoted by squares in Figure 5.9 show a significant deviation from others and suggest a five- to six-fold better ratio than other experiments. To a certain degree this could be explained by an incorrect value of individually red or green light intensity; however, the error would need to be of the same order – five- to six-fold. This was deemed unlikely. By examining Figure 5.1 it can be seen that no whole group noticeably stands out in terms of absolute fluorescence, which suggest that this increased $r_{a'/b'}$ is more likely to be due to lower background gene expression rather than increased induced gene expression. The plasmid DNA was verified by Sanger sequencing before and after these experiments and showed no change. With these considerations it is likely that the background gene expression was somehow affected by either hydrogel culture formulation, preparation or handling in this particular group of samples.

Figure 5.10 shows the same grid of summed images as Figure 5.1 except that the images were contrasted – shown pixel values were calculated according to (5.15), where individual measured pixel values were used instead of $s_{\{V,S\}}$.

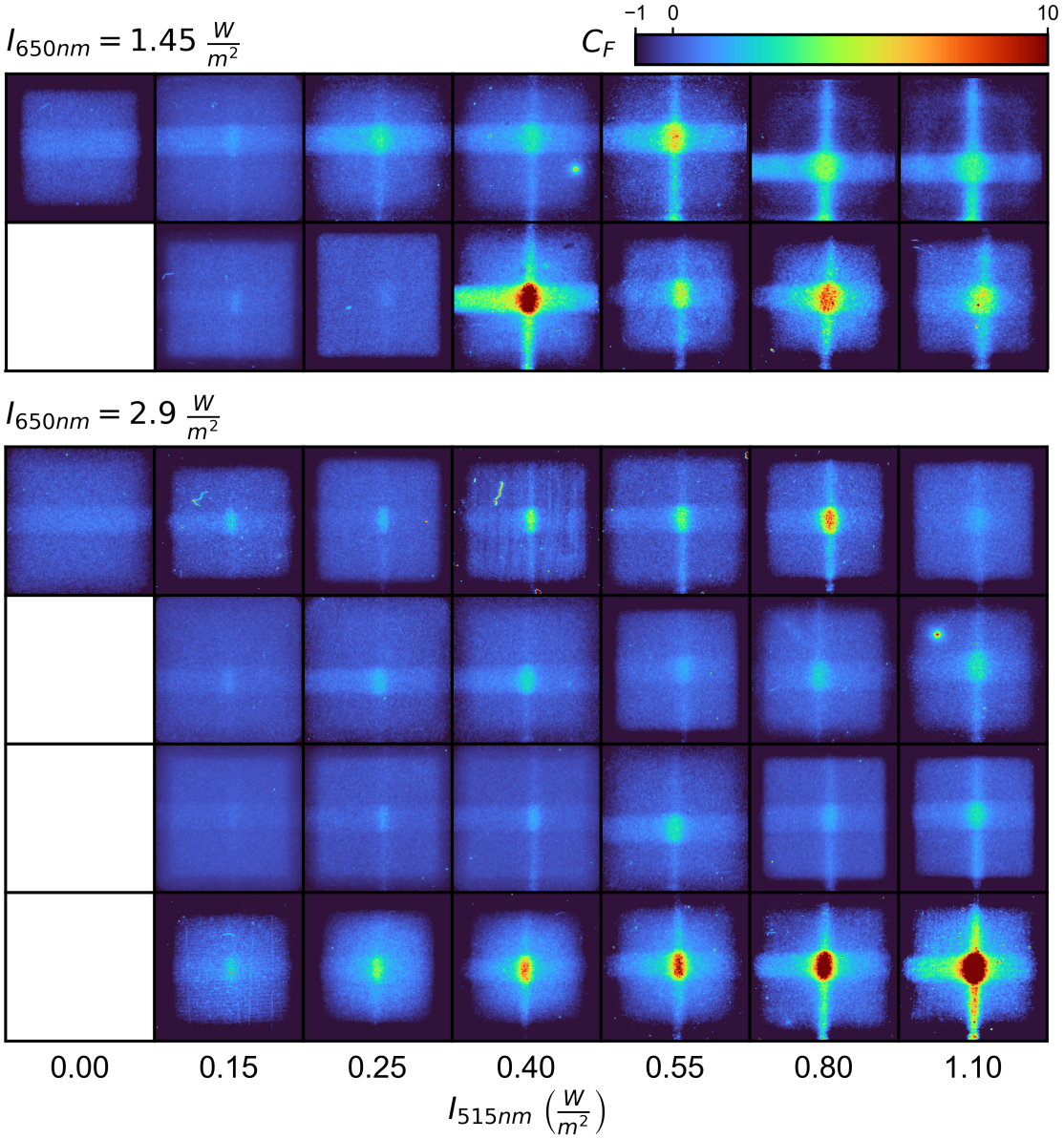


Figure 5.10: *Contrasted fluorescence images of voxels from steady-state experiments, which are also shown in Figure 5.1. Contrasted fluorescence values, C_F, of each image are relative to their respective backgrounds. Images of experiments without red light are not shown, as background gene expression is not known due to the initial active-state photoreceptor population. Each image in the grid is a square with 10.2 mm sides. Due to the grid nature of the figure the green light intensities are within 0.04 W/m^2 of the actual values.*

5.4 Conclusion

Steady-state experiments have shown that is it possible to induce gene expression in a localized volume given a proper overlap of the activating and deactivating light distributions. The two different sets of experiments have also demonstrated that there is negligible gene expression during the lag phase of cell growth. To achieve a well defined voxel in a steady-state configuration, care has to be taken in order to minimize any stray green light due to persistent activation of photoreceptors resulting in noticeable gene expression. Furthermore, any activation of photoreceptors occurring before an experiment will persist and contribute to the unwanted background gene expression, which can also manifest as an apparent widening of the voxel. The deactivating red light can greatly mitigate these effects. Illumination during the lag phase of the hydrogel culture can deactivate any initial population of active-state photoreceptors; however, red light will not reduce any regular background gene expression during the rest of the experiment. The experiments also showed that the red light leakage due to scattering and the shape of the beam is significant and noticeably alters gene expression in the voxel. Best fit estimates to the measured data place the red leakage value at $20\% \pm 10\%$, which is consistent with the measurements of the red light intensity profile. Lastly, best fit estimates determined that the maximum contrast of gene expression in hydrogel culture filled cuvette is 4.8 ± 1.1. Notably, there were experiments that exhibited a maximum contrast of up to 30; however, the cause is unclear and it is probably due to some variation in hydrogel culture formulation, preparation or handling.

Chapter 6

Gene Expression under Discontinuous Illumination

Gene Expression under Discontinuous Illumination introduces an illumination procedure, which is an improvement over the steady-state approach. This illumination procedure leverages deactivation of active-state photoreceptors as opposed to suppression. Deactivation is fundamentally different to suppression and results in gene expression rate that depends on the individual radiant exposures instead of the ratio of intensities. While in the steady-state approach transient effects were ignored, here they are exploited to achieve better contrasted gene expression. The procedure was tested on single illumination, which verified its viability and the persistence of the active-state photoreceptors; and periodic illumination, which showed that the system can be refreshed at various intervals to maintain high activity. Given that this procedure is highly time dependant, experiments also reveled an inconsistency in the reported photoconversion rates of the CcaSR system.

6.1 Single Illumination

In the previous chapter it was shown that the initial population of active-state photoreceptors significantly affects the gene expression during the experiment and an effective way of deactivating said population is through red light illumination in the lag phase of cell growth. It stands to reason that it is then possible to activate the photoreceptors in the early stage and still achieve significant localized gene expression over the duration of the experiment.

6.1.1 Hill Function Approximation

The amount of total gene expression is determined by the amount of active cells, duration of cell growth and the fraction of active-state photoreceptors, η. η depends on light intensities, time of illumination and cell growth rate. The Hill function, h, which translates η into normalized gene expression rate, is nonlinear and the efficacy of changes in η towards gene expression depends on the value of η. According to (2.8), maximum gene expression rate is achieved when η is at 100%; however, maintaining such η is inefficient and a high gene expression rate can be reached at much lower fractions.

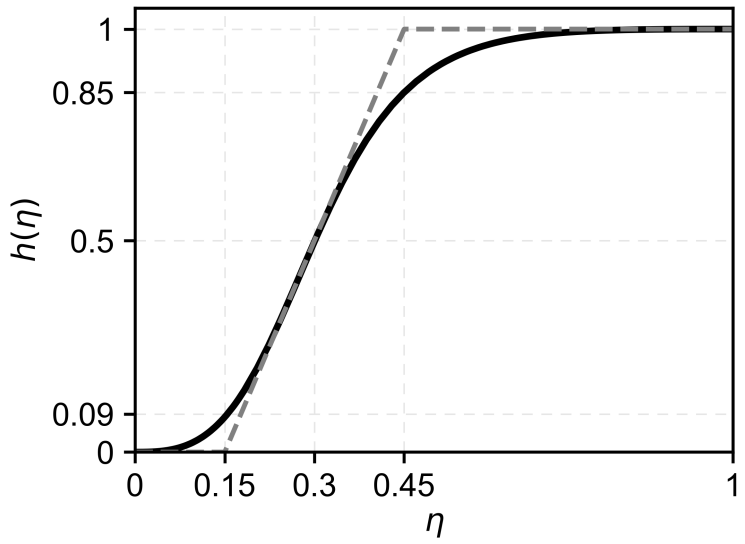


Figure 6.1: *Hill function, $h(\eta)$, and its approximation versus the proportion of active photoreceptors, η. Black line is the Hill function with parameters $K = 0.43$ and $n = 2.7$ and the grey dashed line is its approximation, $h_{approx}(\eta)$. 0.09 and 0.85 are the actual values of the Hill function at η_{min} and η_{max} respectively in contrast to the approximate values of 0 and 1.*

In order to choose the cutoff for the effective maximum and effective minimum gene expression rate, $h(\eta)$ was approximated with the following function:

$$h_{approx}(\eta) = \begin{cases} 0 & \eta \leq \eta_{min} \\ \dfrac{\eta - \eta_{min}}{\eta_{max} - \eta_{min}} & \eta_{min} < \eta \leq \eta_{max} \\ 1 & \eta_{max} < \eta \end{cases}, \tag{6.1}$$

where η_{min} and η_{max} were determined by the intersection of the slope of the Hill function at $h(\eta) = 0.5$ with the function's maximum and minimum value. The approximate values for η_{min} and η_{max} for the given K and n are 0.15 and 0.45 respectively. The approximate and accurate Hill function are shown in Figure 6.1.

By employing (6.1) the effective maximum gene expression rate can be reached at η of only 45% and effective background gene expression is achieved by maintaining η at or below 15%. It should be noted that while in this approximation the values do not change much in absolute terms, the effective maximum contrast, $r^E_{a/b}$, can change significantly. For this particular approximation and given $r_{a'/b'}$ of 4.8, $r^E_{a/b}$ equals 2.8. Were $r_{a'/b'}$ much larger, the difference would be even greater. While technically $r_{a/b}$ has no upper limit, $r^E_{a/b}$ is capped at the ratio between the actual values of the Hill function at the effective minimum and maximum:

$$r^E_{a/b} = \frac{a_E}{b_E} = \frac{\frac{a}{b}h(\eta_{max})}{1 + \frac{a}{b}h(\eta_{min})} \xrightarrow{\frac{a}{b} \gg 1} r^E_{a/b} = \frac{h(\eta_{max})}{h(\eta_{min})} \approx 9.4 \ . \tag{6.2}$$

This shows that while $r_{a/b}$ is an important ratio it is not the only factor when the extreme values of the Hill function are not reasonably achievable. In such cases the larger the Hill coefficient, n, the more the Hill function resembles a step function and the more defined is the difference between the maximum and minimum.

6.1.2 Deactivation Procedure Model

With a known fraction of active-state photoreceptors to be reached, the light intensity can be determined for a given duration of constant illumination. Provided the duration of illumination is short compared to the time constant of cell growth, $\tau_{growth} = 1/k_{growth}$, green light intensity can be determined analytically by rewriting (2.4):

$$I_{515nm} \approx -\frac{1}{\hat{k}_1 t} \ln\left(\frac{1 - \eta_{high}}{1 - \eta_0}\right), \tag{6.3}$$

where t is the duration of illumination, η_{high} is the target fraction greater than the initial fraction of active-state photoreceptors, η_0, and $k_2 = 0$. In the case where duration of illumination is not short enough, (2.4) has to be solved numerically for I_{515nm}, as k_{growth} cannot be neglected.

If there is a nonzero η_0 that is to be deactivated, then the required red light intensity for a given duration of illumination is obtained by rewriting (2.7):

$$I_{650nm} = -\frac{1}{\hat{k}_2 t} \ln\left(\frac{\eta_{low}}{\eta_0}\right) - \frac{k_{growth}}{\hat{k}_2}, \tag{6.4}$$

where η_{low} is the target fraction smaller than η_0, and $k_1 = 0$.

In both (6.3) and (6.4) the steady-state fraction of active photoreceptors is an extreme – either 100% for green light only illumination or 0% for red light only illumination. When both colors of light are present the steady-state fraction of active photoreceptors is given by the following fraction:

$$\eta^{ss} = \frac{k_1}{k_1 + k_2 + k_{growth}} \approx \frac{1}{1 + \frac{k_2}{k_1}}. \tag{6.5}$$

The effective maximum gene expression can be reached when the ratio $k_2/k_1 < 1.2$ resulting in $\eta^{ss} > \eta_{max}$. On the other hand, the effective minimum gene expression is reached when the ratio $k_2/k_1 > 5.7$, which results in $\eta^{ss} < \eta_{min}$. Given the estimated value of red light leakage, $\eta_R = 0.2$, the two ratios of k_2/k_1 are just enough apart that by employing steady-state illumination effective maximum gene expression can be reached within the voxel ($5.7 \cdot 0.2 = 1.14 < 1.2$) and effective minimum gene expression is maintained outside.

A measurement from steady-state experiments, which would fulfil these ratios, would be placed in between the 3th and 4th column of Figure 5.10(a) and in between the 5th and 6th column of Figure 5.10(b). From existing steady-state measurements it can be seen that the suppressed gene expression is still quite pronounced. To entirely suppress induced gene expression the red light intensity would need to be infinite according to the model. However, this would still not yield desired results unless η_R was also zero, as otherwise gene expression within the voxel would be entirely suppressed as well.

Instead of suppression a better approach can be to deactivate the active-state photoreceptors. With such an approach the end fraction of active-state photoreceptors does not depend on the ratio between the light intensities, instead it depends on their radiant exposure. This can be seen by setting up an illumination procedure, where the voxel is first illuminated by only green light until η reaches values close to 100%, followed by red light illumination until η_0 in the suppressed region

reaches 15% or less. The procedure consist of two steps and it starts with green light illumination which raises the fraction of active-state photoreceptors:

$$\eta_S(t_1) \approx \eta_V(t_1) \approx \eta(t_0) + (1 - \eta(t_0))\left(1 - e^{-k_1 \Delta t_1}\right) = \eta_{high}\,, \tag{6.6}$$

where $\eta_S(t_1)$ and $\eta_V(t_1)$ are fractions of active-state photoreceptors at time t_1 in the suppressed region and the voxel respectively, $\eta(t_0) = 0$, $\Delta t_1 = t_1 - t_0$ and η_{high} is the targeted fraction near 100%. The intensity of green light is determined by Δt_1 and η_{high} through (6.3). $\eta_S(t_1)$ and $\eta_V(t_1)$ are set to be equal, as at large values of η_{high} the variation of green light intensity due to attenuation affects gene expression less. Following green is the red light illumination:

$$\begin{aligned} \eta_S(t_2) &= \eta_{high} e^{-\left(k_2 + k_{growth}\right)\Delta t_2} = \eta_{low}\,, \\ \eta_V(t_2) &= \eta_{high} e^{-\left(\eta_R k_2 + k_{growth}\right)\Delta t_2}\,, \end{aligned} \tag{6.7}$$

where $\Delta t_2 = t_2 - t_1$ and η_{low} is the targeted minimum fraction of active-state photoreceptors. The intensity of red light is determined by Δt_2 and η_{low} through (6.4). With both *green* and *red* steps it can be seen that the end fraction of active photoreceptors depends on the product between the intensity and duration of individual illuminations.

As $\eta_V(t_2)$ and $\eta_S(t_2)$ share the duration of illumination, Δt_2, $\eta_V(t_2)$ can be expressed in terms of $\eta_S(t_2)$:

$$\eta_V(t_2) = \eta_{high}\left(\frac{\eta_{low}}{\eta_{high}}\right)^{\frac{\eta_R k_2 + k_{growth}}{k_2 + k_{growth}}} \approx {\eta_{low}}^{\eta_R} = \eta_S(t_2)^{\eta_R}\,. \tag{6.8}$$

For sufficiently high η_{high} and k_2, the fraction of active-state photoreceptors within the voxel depends only on the targeted η_{low} in the suppressed region and η_R. If η_R is zero, η_V and η_S can be set to an arbitrary value independent of each other, with some restrictions due to growth. If η_R was indeed zero, a steady-state approach could achieve the same results; however, it would be less practical due to (6.5), as red light intensity would need to be significantly higher to counteract the green light.

In the case of the *deactivation procedure* $\eta_V(t_2)$ can be set to 45% and given the estimated value of η_R, the required η_{low} would only be 2%. If instead a higher maximum gene expression is desired, η_{low} can be set higher, for example to 10% and the resulting $\eta_V(t_2)$ would be 63%, in which case both values would be well beyond η_{max} and η_{min} achieving an effective maximum and minimum gene expression.

Equation (6.8) describes the state of η at the end of the deactivation procedure. If this illumination is done during the lag phase of cell growth, the duration of illumination is not important as long as sufficient radiant exposure is reached to result in the targeted η. In the case where the deactivation procedure is begun during the exponential growth phase, the duration is important. This is not only due to the effect it might have on the validity of the approximation in (6.8) but also on the total gene expression. If the first step, which is the green illumination, lasts long enough to be comparable to the duration of the experiment, there would be additional gene expression in the *not yet* suppressed region, which would be comparable to gene expression in the voxel after the procedure.

Figure 6.2 shows η and h over time. Two sets of graphs show the behaviour for the two different illumination strategies: steady-state and deactivation procedure. It can be seen from the first row of Figure 6.2 that while the ratio k_2/k_1 is kept constant, the magnitude of intensities matters for the time evolution of the system. Furthermore, as the ratio $k_2/k_1 = 5.7$ is calculated under the assumption of high green light intensity (Equation (6.5)). It can be seen in the second graph of the first row, that while the system just about reaches the steady state in the voxel, η is below the targeted value of 45% due to continuous dilution from cell growth.

Much like in the steady-state approach, the magnitude of light intensity is important for the time evolution of η in the deactivation procedure, which is shown in the third row of Figure 6.2. The higher the green light intensity, the less time gene expression will occur in the suppressed region. In a similar manner, a higher red light intensity will result in the end state being reached quicker where $\eta = \eta_{low}$. Due to the higher initial target – η_{high} – the light intensities have to generally be much higher when compared to the steady-state approach. Further affecting η here is the cell growth, which has a positive and a negative component in how it affects the deactivation procedure. As the population grows, gene expression is greater, which means that any initial unwanted gene expression will have had a smaller effect on the ratio between the voxel and suppressed region. On the other side the dilution of active-state photoreceptors reduces η over time and with it gene expression rate.

Figure 6.3 shows the Hill equation over time for three different illumination procedures, which result in comparable gene expression rate profiles. As seen in Figure 6.2, with the deactivation procedure intensities can be made arbitrarily high in order to minimize the time to reach the desired state. In Figure 6.3$(b), (c)$ the width of the red striped area depends on the radiant exposure of both colours. Thus by having faster dynamics, the total gene expression in the suppressed area can be reduced (same can be inferred from the third row in Figure 6.2). Gene expression in the voxel is not as affected by dynamics when illumination time represents a small fraction of the overall experiment time.

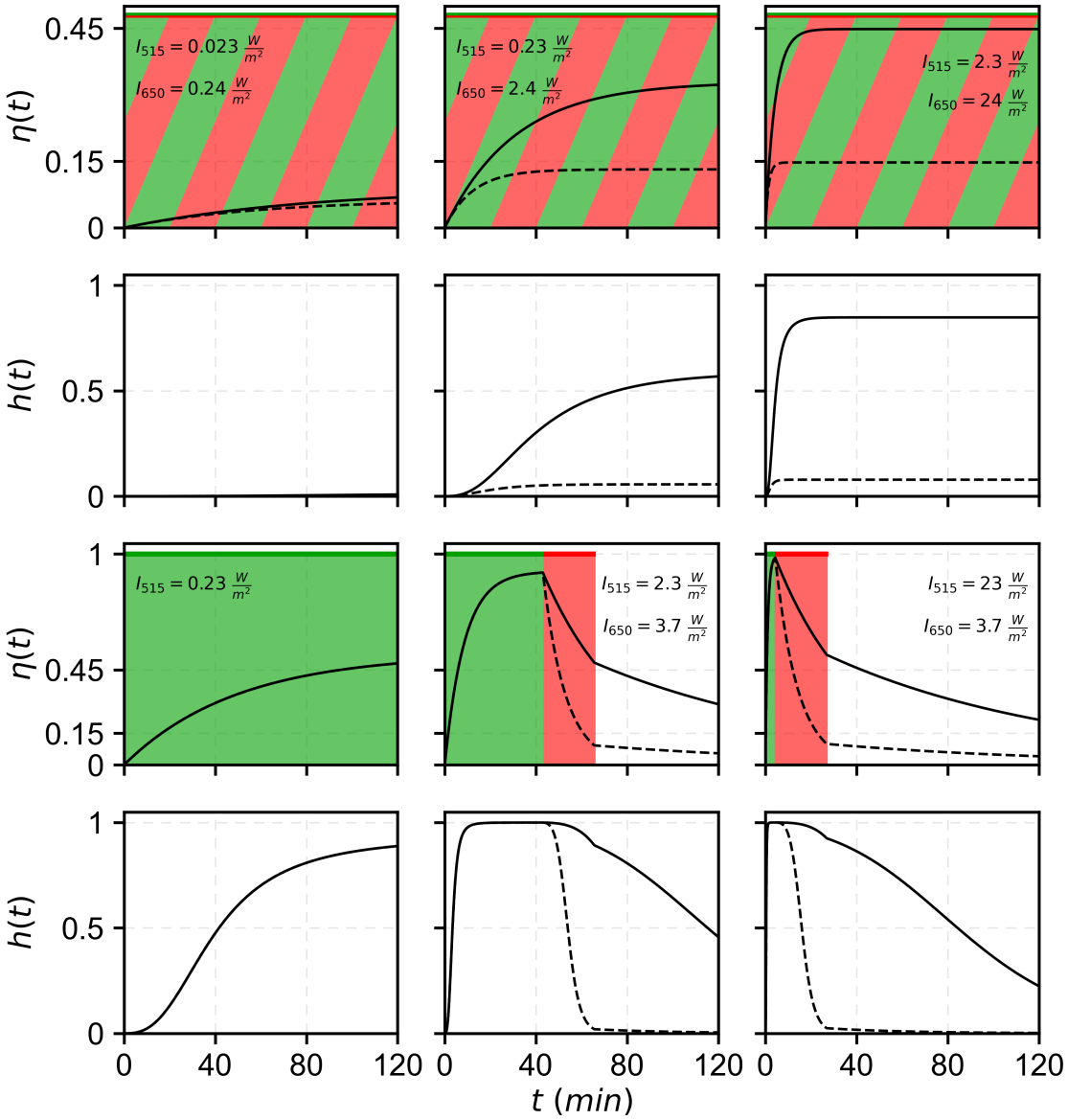


Figure 6.2: *Response of the fraction of active-state photoreceptors, $\eta(t)$, and normalized gene expression rate, $h(t)$, to two different single voxel illumination strategies: steady-state and deactivation procedure. Solid black line graphs show the state within the voxel and the dashed black line graphs show the state within the suppressed region. η_R is 20% for all solid line graphs. The first row are graphs of η versus time under continuous illumination of red and green light and the second row are graphs of h in response to the η above. The ratio between k_2 and k_1 is kept constant at 5.7 with increasing intensities from left to right by a factor of ten. The third row are graphs of η versus time following the deactivation procedure, at three different green light intensities. Duration of green light illumination depends on η reaching $\eta_{high} = 0.99$ and the duration of red light illumination depends on η_S reaching $\eta_{low} = 0.10$. The fourth row are graphs of h in response to η in the third row.*

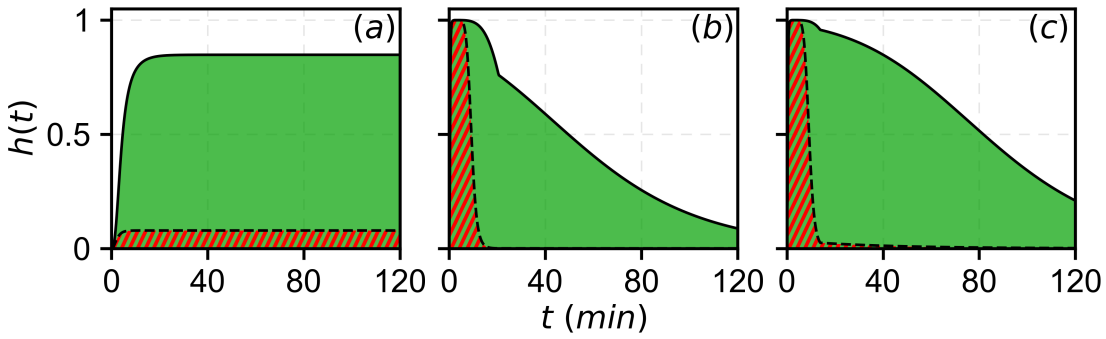


Figure 6.3: *Normalized gene expression rate, $h(t)$, in response to three different illuminations. The solid lines are $h(t)$ in the voxel and the dashed lines are $h(t)$ in the suppressed region. Green coloured areas under the curve are related to the total gene expression, $g(t_{End})$, in the voxel and the red coloured areas under the dashed curve are related to $g(t_{End})$ in the suppressed region. The colours reflect the presence of the respective light in the respective region, they do not indicate the duration or intensity of illumination. (a) Response to continuous illumination. Intensities of green and red are 2.3 W/m^2 and 24 W/m^2 respectively, which results in the ratio of $k_2/k_1 \approx 5.7$. (b) Response to single illumination following deactivation procedure. Green light illumination lasts until η reaches $\eta_{high} = 0.99$, which is followed by red light illumination lasting until η_V reaches 45% and η_S reaches $\eta_{low} = 0.02$. Intensities of green and red are 23 W/m^2 and 9.2 W/m^2 respectively. (c) Response to single illumination following deactivation procedure. Green light illumination lasts until η reaches $\eta_{high} = 0.99$, which is followed by red light illumination lasting until η_V reaches 63% and η_S reaches $\eta_{low} = 0.10$. Intensities of green and red are 23 W/m^2 and 9.2 W/m^2 respectively.*

The difference between the two deactivating procedures in Figure 6.3$(b),(c)$ shows the importance of choosing the right value of η_{low}. In Figure 6.3(b) η_{low} is set to 0.02, whereas in Figure 6.3(c) η_{low} is set to 0.10. In the first case red light illumination last slightly longer in order to reduce η_S from 0.10 to 0.02. This additional illumination barely affects h in the suppressed region; however, h in the voxel plummets significantly. This is of course due to nonzero η_R which causes red light to significantly affect η_V. Choosing an arbitrarily small η_{low} is thus not an optimal approach, as there is little benefit in reducing η_S beyond a certain point while at the same time affecting η_V.

While steady-state total gene expressions in Figure 6.3(a) is comparable to the ones in Figure 6.3$(b),(c)$, the same ratios between total gene expression in the voxel and suppressed region cannot be achieved in both approaches without sacrificing the absolute value of total gene expression in the voxel. This is where the two approaches really differ when η_R is not zero; ratios between total gene expressions heavily depend on intensities in the steady-state approach, whereas in the deactivation approach they heavily depend to the radian exposure.

6.1.3 Experiments' Illumination Procedure

Two experiments of a single voxel single illumination that follows the deactivation procedure were carried out. The first was done with only single green light illumination and the second also included red light illumination. The nature of the deactivation procedure allowed four voxels to be illuminated in the same build volume during the same experiment, instead of a single voxel per experiment and cuvette. The voxels were positioned on top of each other with equal vertical spacing of 5 mm to avoid the vast majority of light overlap. The experiments' illumination procedure is shown in Figure 6.4. Due to higher intensities required for shorter illumination times, the green laser required a warm up period in order to guarantee the necessary intensity during the entire illumination period.

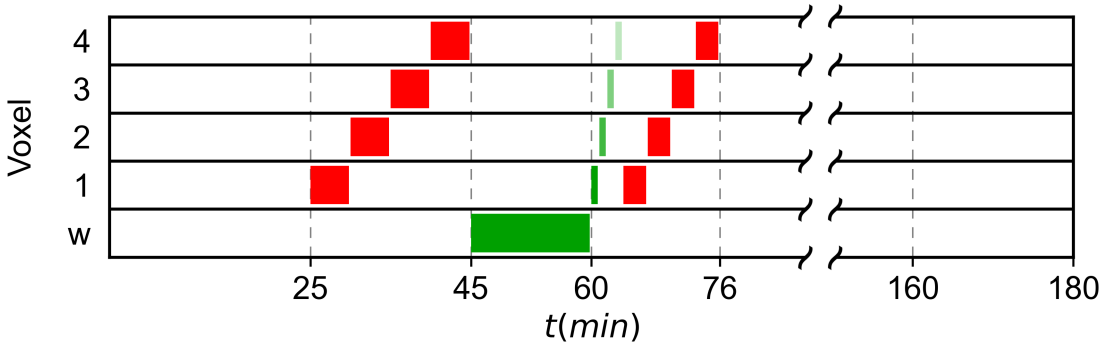


Figure 6.4: *Schematic of the illumination procedure for a four voxel single illumination experiment. The initial* 5 *minute red illumination segments with average intensity of* 32 W/m^2 *deactivate any active-state photoreceptors. The* 15 *minute green segment in row w, represents the green laser warm up period. Following that, each of the four voxels is illuminated for* 1 *minute with decreasing peak green intensity in even steps from* 120 W/m^2 *to* 30 W/m^2 *indicated by the shade of green. During the second experiment after all voxels have been activated by green light, the suppressed regions are deactivated by red light for* 3 *minutes with an average intensity of* 38.4 W/m^2 *in the sequence they were activated.*

In both experiments each voxel had a different intensity of green illumination followed by the same intensity of red light illumination. The duration of green light illumination was set to 1 minute and the highest peak intensity was set to 120 W/m^2. With this peak incident intensity, and accounting for attenuation, η_V should reach near 99%. The duration of the red light illumination was set to 3 minutes and the average incident intensity was set to 38.4 W/m^2. When accounting for attenuation this should be sufficient to deactivate the photoreceptors so that η_S drops to 10% and η_V drops to 63%. During the remaining duration of the experiment η_V is expected to drop to 20% at the end.

6.1.4 Results

Figure 6.5(a) shows the results of the first experiment where four voxels were illuminated with only green light at four different levels. With the exception of the voxel illuminated with the lowest intensity the fluorescence distribution appears to be mostly the same for all voxels. More importantly, the width of induced gene expression is much wider than what would be expected for the lower intensity illuminations.

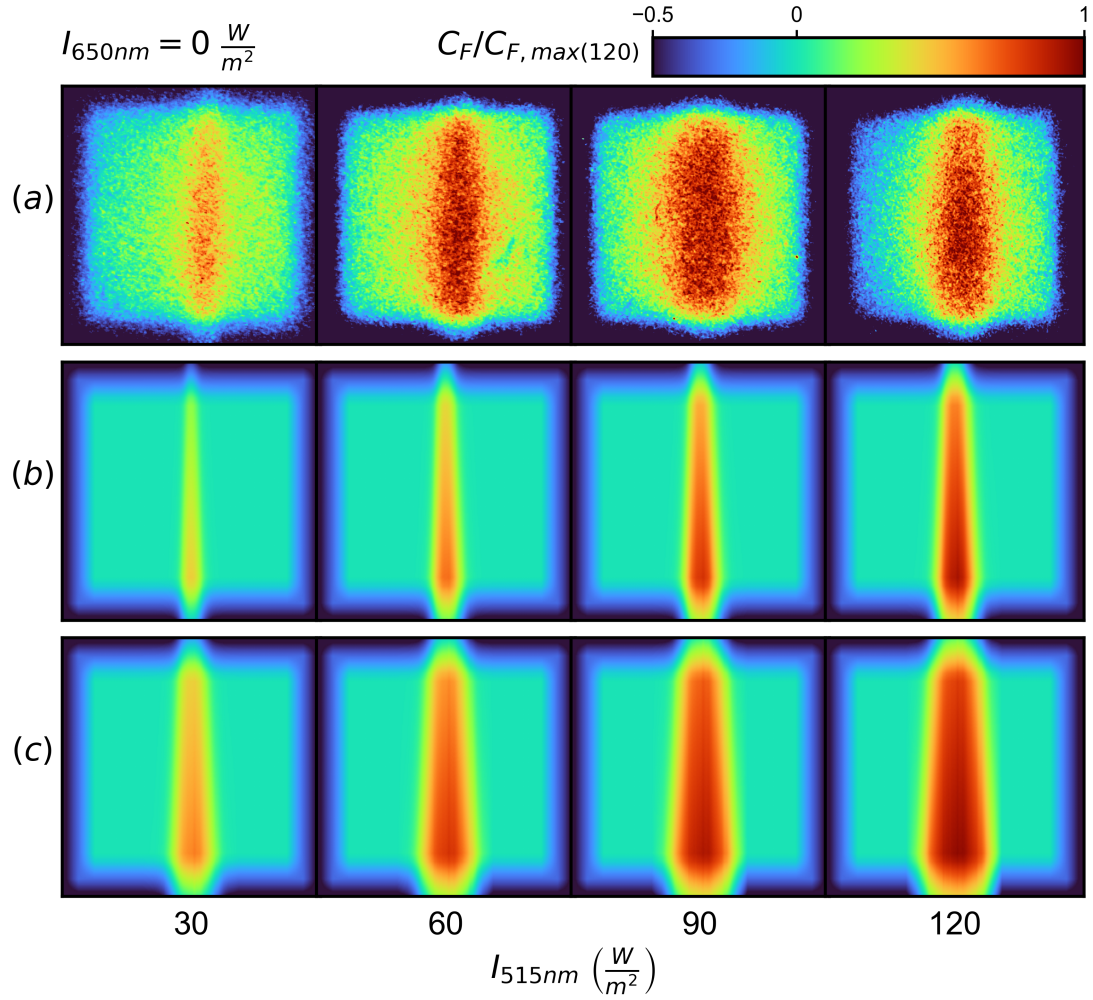


Figure 6.5: *Measurements and simulations of a four voxel single illumination experiment without red light illumination following the procedure shown in Figure 6.4.* (a) *Summed images of normalized contrasted fluorescence,* $C_F/C_{F,max(120)}$ *of each voxel. The contrasting background was determined from slices between the voxels, which were deactivated prior to experiment. Images were normalized with the maximum fluorescence value of the summed image where green light intensity,* I_{515nm}*, was* 120 W/m^2*.* (b) *Simulation of normalized integrated total gene expression using parameters shown in Table 2.1.* (c) *Exact same simulation as shown in row* (b) *with the exception of increased forward conversion rate* $\hat{k}_1' = 5\hat{k}_1$*. Normalization of simulations was done with the maximum value obtained from the simulation with* I_{515nm} = 120 W/m^2 *in the respective row. The halo effect in simulations was added qualitatively as a visual aid and to illustrate the rounding shape near the edges.*

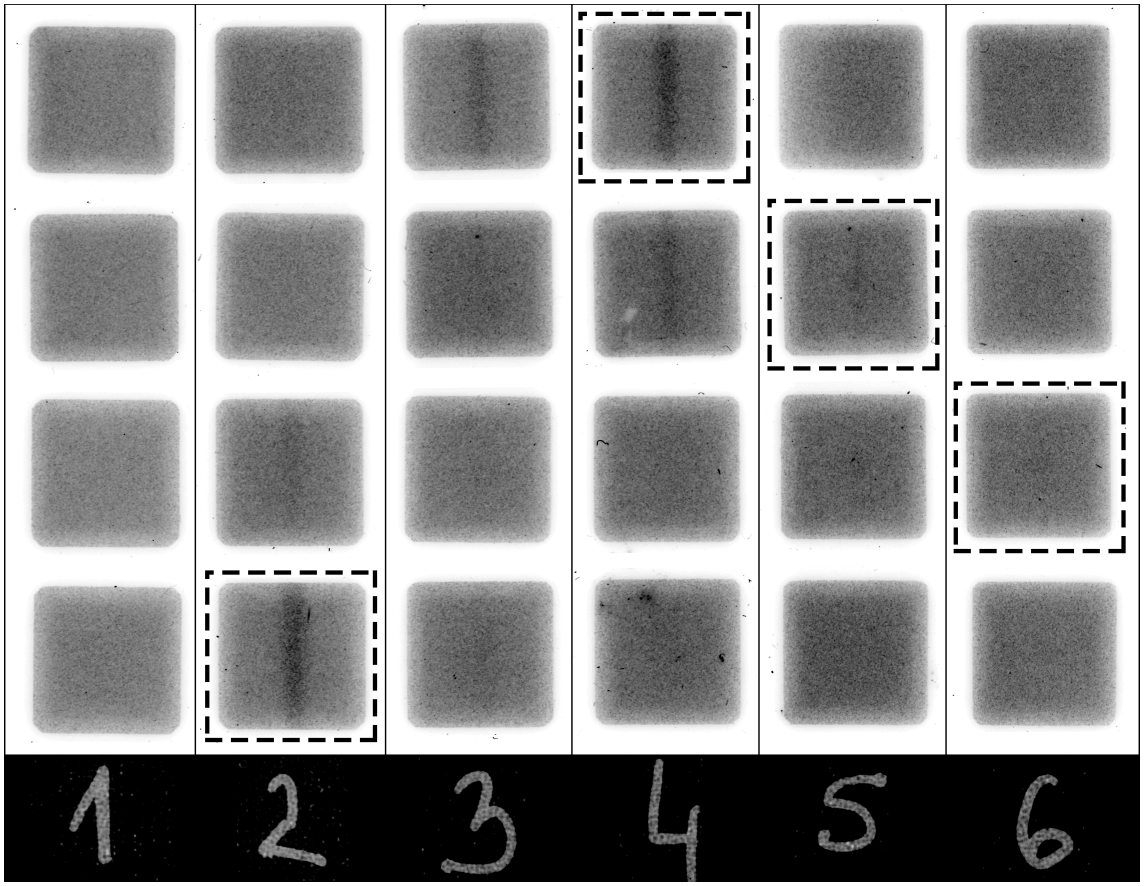


Figure 6.6: *Composite image of raw images of fluorescence of individual slices, which underwent the hybrid initial illumination experiment. Each column are slices from the microscope slide denoted by its number. The slices were realigned to fit into a grid. The slices' position in the grid was vertically mirrored to help with the perception of slices' position. The left top slice's position in the hydrogel culture filled cuvette is the highest, followed by the slices in its column, the right bottom slice's position is the lowest. The dashed line squares indicate each voxel illumination position.*

The results of the second experiment are not shown, as there was simply no perceivable induced gene expression. The experiment was repeated and again yielded no results. The hypothesized reason was that red light illumination was so strong that the majority of active-state photoreceptors was also deactivated within the voxel. To verify this, a hybrid experiment was ran. Its illumination procedure was as shown in Figure 6.4 with the exception that only two voxels were illuminated by red light after the initial green illumination, which was the same for all four. Figure 6.6 is the resulting raw image of fluorescence of all individual slices that span the active part of the build volume during this experiment. The four dashed line squares indicate the slices where each voxel was illuminated. It can be seen that only two voxels exhibited additional gene expression, whereas the other two exhibited none that can be discerned beyond the background noise. This strongly indicated that indeed red light illumination was the cause of the phenomenon.

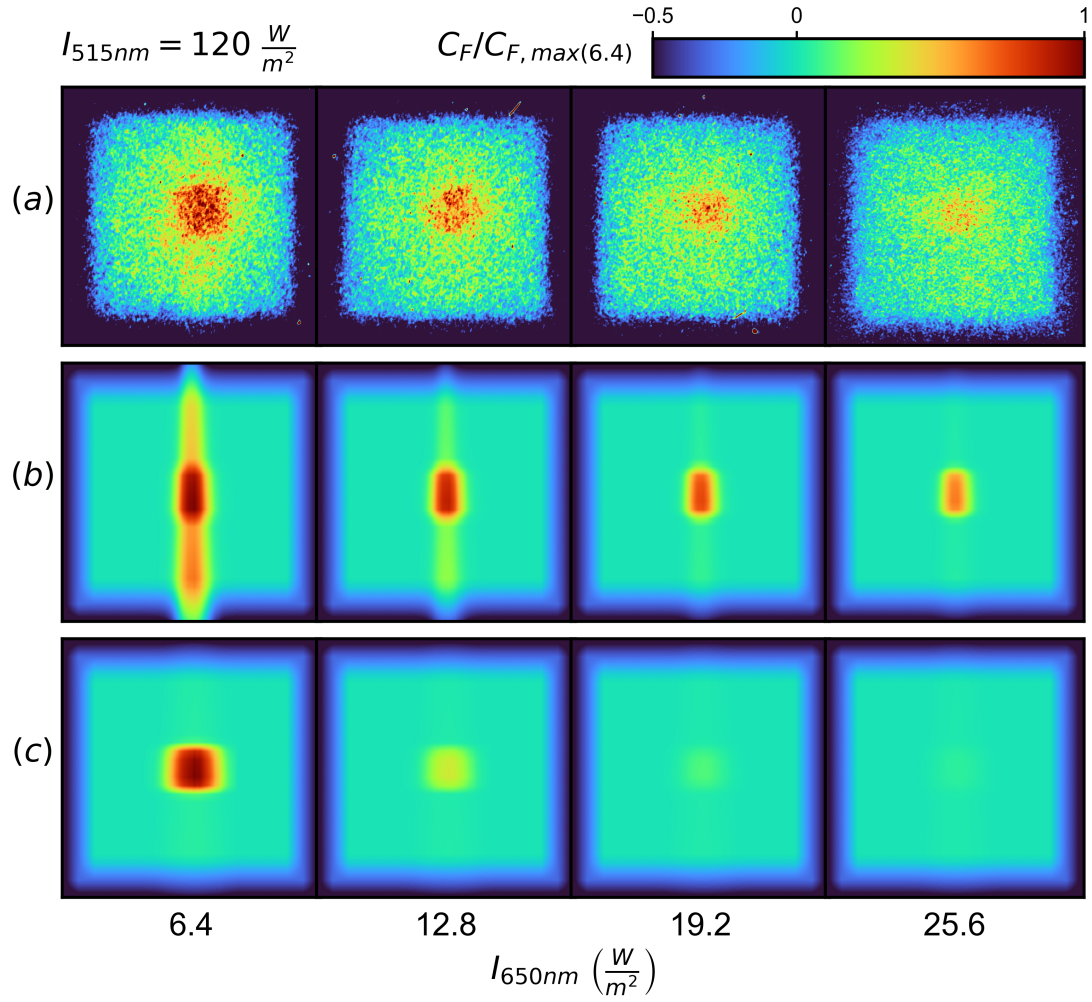


Figure 6.7: *Measurements and simulations of a four voxel single illumination experiment following the procedure shown in Figure 6.4. However, green light intensity was kept the same at* $I_{515nm} = 120\ W/m^2$ *and red light intensity,* I_{650nm}*, was varied in equal steps from* $6.4\ W/m^2$ *to* $25.6\ W/m^2$*. (a) Summed images of normalized contrasted fluorescence of each voxel. The contrasting background was determined from the respective red only regions of each summed image. Images were normalized with the maximum fluorescence value of the summed image where* $I_{650nm} = 6.4\ W/m^2$*. (b) Simulation of normalized integrated total gene expression using parameters shown in Table 2.1 with* $\eta_R = 0.2$*. (c) Exact same simulation as shown in row (b) with the exception of increased forward and reverse conversion rates,* $\hat{k}_1' = 5\hat{k}_1$ *and* $\hat{k}_2' = 5\hat{k}_2$*. Normalization of simulations was done with the maximum value obtained from the simulation with* $I_{650nm} = 6.4\ W/m^2$ *in the respective row. The halo effect in simulations was added qualitatively as a visual aid and to illustrate the rounding shape near the edges.*

In light of the results of the hybrid experiment, the *second* experiment of the deactivation procedure was changed and adjusted. Instead of four different green light intensities, green light intensity was kept the same and voxels were illuminated with four different red light intensities. The summed images of this experiment are shown in Figure 6.7(a). In this case there is visible induced gene expression within the voxel. With increasing red light intensity, gene expression within the voxel is significantly affected confirming the presence of a notable amount of red light.

Given the results of the aforementioned experiments, the experiments were simulated using the optogenetic model to qualitatively determine the effectiveness of red and green light. Figures 6.5(b) and 6.7(b) show the normalized integrated total gene expression during each experiment as obtained through the model. Simulations and measurements were normalized for easier comparison between the shape and relative change of integrated total gene expression. It can be seen that the shape of the predicted gene expression noticeably deviates from the measurements. In both cases the most obvious difference is the width of gene expression. This indicates that the green light intensity used in the simulation is not large enough in order for the tails of the green light intensity profile to activate a sufficient fraction of photoreceptors. Furthermore, in Figure 6.7(b) the simulated effect of red light does not reflect the measurement in two related ways. First, the voxel gene expression shows only a small variation in magnitude between the simulations, whereas in measurements it almost vanishes with the largest red light intensity. Second, the ratio between gene expression in the voxel and the suppressed region in the simulations is not similar to the one in the measurements. With the lowest red light intensity the simulation effectively produces a line, which is clearly not the case in the measurement.

Red light intensity used in the *unsuccessful* second experiment and the hybrid experiment was such that it should have deactivated the activated photoreceptors in the suppressed region down to a fraction of 10%, which should have resulted in near zero total gene expression. Given that in these experiments red light caused η_V to be small enough that there is no noticeable gene expression, it is likely that the effectiveness of red light is much greater than suggested by the reported reverse photoconversion rate. As only a fraction of red light, given by η_R, was able to thoroughly deactivate the photoreceptors in the voxel, it is reasonable to conclude that the reverse photoconversion rate is greater by a factor of at least $1/\eta_R$. However, this seemingly had no great effect in the expected gene expression in steady-state experiments. Consequently it is likely that the effectiveness of green light or forward photoconversion rate is also greater by the same factor. This is due to gene expression under steady-state illumination largely depending only on the ratio between the two intensities. If the ratio is maintained the individual magnitudes of intensities are not as relevant.

The estimated increased green and red light effectiveness thus heavily relies on the estimated value of η_R and the measurements of the *second* experiment shown in Figure 6.7(a). The first voxel, illuminated under the lowest red light intensity, is just barely exhibiting gene expression in the suppressed region. The second voxel illuminated by the second lowest red light intensity already shows none. The red light intensity in the first voxel is 1/6 of the intensity that is expected to effectively deactivate almost all active photoreceptors and prevent gene expression in the suppressed region. Due to the second voxel red light intensity being 1/3 of original intensity, this places the factor of increased effectiveness somewhere in between 3 and 6. Furthermore, gene expression is barely visible in the fourth voxel, which was subjected to red light intensity four times greater than the first voxel.

To further validate this magnitude choice of green and red light effectiveness, the experiments were simulated using new values of forward and reverse photoconversion rates – $\hat{k}_1' = 5\hat{k}_1$ and $\hat{k}_2' = 5\hat{k}_2$. The results of these simulations are shown in 6.5(c) and 6.7(c). With the new values the simulation produces results that are qualitatively very close to the measurements. Any remaining discrepancies can also be attributed to the uncertainty of other parameters.

6.2 Periodic Illumination

Single illumination has been shown to be sufficient in achieving localized gene expression. However, the gene expression rate decays over time (Figures 6.2 and 6.3) due to the dilution of active-state photoreceptors as a result of cell growth. Ideally, the gene expression rate would remain constant throughout the duration of the experiment and at the same time the background gene expression would be kept as low as possible. This issue can be addressed by repeatedly illuminating the voxel and thus repeatedly activate the population of newly grown ground-state photoreceptors.

6.2.1 Periodic Illumination Model

The periodic illumination is in essence the same as the single illumination but repeated. Each instance of illumination follows the same deactivation procedure in an attempt to reach the best ratio between the voxel and suppressed region gene expression. The first instance of illumination is exactly the same as with single illumination, the equations used to determine the respective light intensities are (6.3) and (6.4) and the procedure is governed by (6.6) and (6.7), which results in the relationship between η_V and η_S as described by (6.8).

Steps following the initial illumination are slightly different. Equation (6.3) for subsequent illuminations has a nonzero starting fraction of active-state photoreceptors:

$$\eta_1 = \eta_{high} e^{-\eta_R k_2 \Delta t_2 - k_{growth} \Delta t_I} , \tag{6.9}$$

where η_1 is the fraction of active-state photoreceptors right before the first illumination step after the initial illumination, Δt_2 is the duration of red light illumination and Δt_I is the time interval between the illumination steps. In the case where there is only green light illumination, all subsequent starting fractions of active photoreceptors, η_n, have the same value:

$$\eta_1 = \eta_2 = ... = \eta_n = \eta_{high} e^{-k_{growth} \Delta t_I} , \tag{6.10}$$

provided that the green light intensity during each step equals:

$$I_{515nm,i}(k_2 = 0) \approx -\frac{1}{\hat{k}_1 \Delta t_1} \ln\left(\frac{1 - \eta_{high}}{1 - \eta_{high} e^{-k_{growth} \Delta t_I}} \right) , \tag{6.11}$$

where Δt_1 is the duration of green light illumination and growth was neglected during said illumination. The following approximation of the above equation for small values of $\Delta t_I k_{growth}$:

$$k_1 \Delta t_1 \approx k_{growth} \Delta t_I \cdot \frac{\eta_{high}}{1 - \eta_{high}} , \tag{6.12}$$

shows that green light illumination indeed just compensates for what was lost to dilution due to growth. Factor $\eta_{high}/(1 - \eta_{high})$ simply reflects that green light acts on ground-state population of photoreceptors and dilution due to growth acts on the active-state population of photoreceptors. Dotted line in Figure 6.8 shows the response of η and h to repeated green-only illumination.

By including red light to achieve localized gene expression, the required intensities become dependant on each other. For specific η_{high} or η_{low}, the intensities depend on each other even if η_R is zero. The intensities for the initial illumination do not change; however, the green illumination for the following steps is:

$$I_{515nm,i} \approx -\frac{1}{\hat{k}_1 \Delta t_1} \ln\left(\frac{1 - \eta_{high}}{1 - \eta_{high} e^{-\eta_R k_2 \Delta t_2 - k_{growth} \Delta t_I}} \right) , \tag{6.13}$$

where the approximation is still due to the k_1 being expected to be much greater than k_{growth}. After the initial illumination and after the first green light illumination step, red light is again required to achieve localized gene expression. η_V at this point is equal to η_{high}; however, η_S was risen by green light illumination from approximately

η_{low} to an intermediate value. To obtain the optimal red light intensity during each step, which maintains optimal η_V and results in η_S reaching η_{low} from the intermediate value, the following equation has to be numerically solved for $k_{2,i} = I_{650nm,i}\hat{k}_2$:

$$e^{-k_{2,i}\Delta t_2 - k_{growth}\Delta t_I} = \frac{1}{1 + \frac{1-\eta_{low}}{\eta_{low}} \cdot \frac{\eta_{high}\left(1 - f\left(k_{2,i}, \eta_R\right)\right)}{\eta_\infty^G - \eta_{high} f\left(k_{2,i}, \eta_R\right)}}\,, \tag{6.14}$$

where

$$f\left(k_{2,i}, \eta_R\right) = e^{-\eta_R k_{2,i}\Delta t_2 - k_{growth}\Delta t_I}\,, \qquad \eta_\infty^G = \frac{k_{1,i}}{k_{1,i} + k_{growth}} \approx 1\,.$$

In the case where optimal conditions are unnecessary, the solution to (6.14) is approximately equal to (6.4) when $\eta_{high} = 1$. Having a large η_{high} is desirable regardless, as due to η_R, η_V is brought to a lower value than η_{high} anyway. In the limit of many very short pulses, values of η_V and η_S are still approximately related by (6.8). In conclusion, for large values of η_{high} the required green and red light intensities are as follows:

$$I_{515nm,0} \approx -\frac{1}{\hat{k}_1\Delta t_1}\ln\left(1 - \eta_{high}\right)\,, \quad \eta_0 = 0\,, \tag{6.15}$$

$$I_{515nm,i} \approx -\frac{1}{\hat{k}_1\Delta t_1}\ln\left(\frac{1-\eta_{high}}{1 - \eta_{high}\left(\frac{\eta_{low}}{\eta_{high}}\right)^{\eta_R} e^{-k_{growth}\Delta t_I(1-\eta_R)}}\right), \tag{6.16}$$

$$I_{650nm,0} = I_{650nm,i} \approx -\frac{1}{\hat{k}_2\Delta t_2}\ln\left(\frac{\eta_{low}}{\eta_{high}}\right) - \frac{k_{growth}\Delta t_I}{\hat{k}_2\Delta t_2}\,. \tag{6.17}$$

Figure 6.8 shows the response of η and the h to periodic illumination, which follows the deactivation procedure where light intensities are determined by (6.15), (6.16) and (6.17). It can be seen that as long as η_V is maintained above η_{max}, it is preferable to have less repeated illumination in order to keep the gene expression in the suppressed region as low as possible. The dotted lines again show that in the absence of red light leakage the ratio between η_V and η_S can be improved almost arbitrarily.

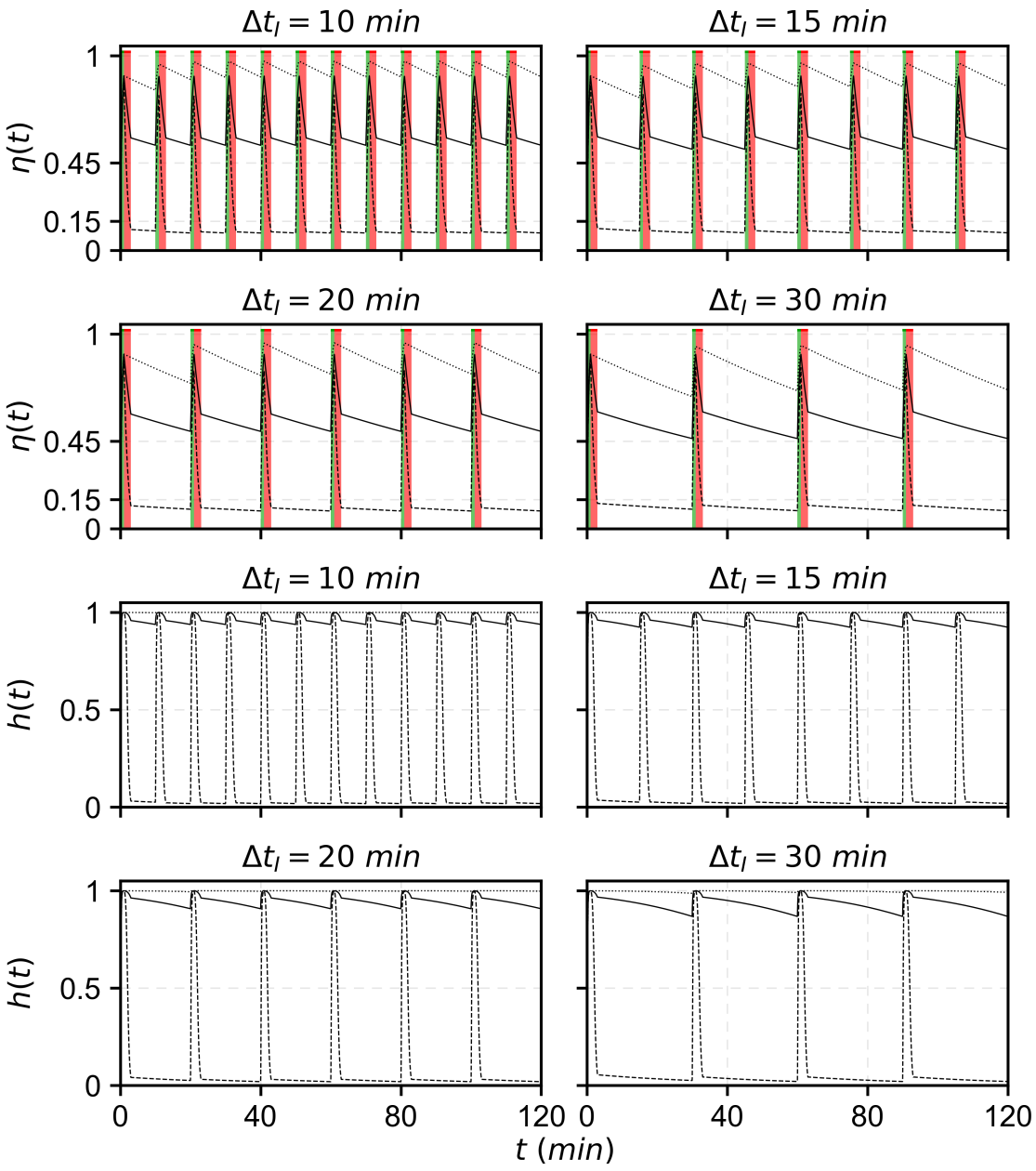


Figure 6.8: *Response of the fraction of active-state photoreceptors, $\eta(t)$, and normalized gene expression rate, $h(t)$, to periodic voxel illumination at four different intervals. The dotted black line graphs show the state in the voxel and suppressed region in the absence of red light illumination. The solid black line graphs show the state in the voxel in the presence of red light illumination. The dashed black line graphs show the state in the suppressed region in the presence of red light illumination. With the exception of interval duration all parameters are the same for all graphs: $\eta_R = 0.2$, $\eta_{high} = 0.95$, $\eta_{low} = 0.10$, green light illumination duration is $\Delta t_1 = 1min$, and red light illumination duration is $\Delta t_2 = 2min$. The green and red bands indicate the duration of the respective illumination; however, the intensities are different and are determined from the corresponding parameters.*

6.2.2 Experiments' Illumination Procedure

As with the single illumination experiments, two experiments were performed for the periodic illumination. One with only green illumination and one with both red and green illuminations. In each experiment four voxels were separately illuminated and were vertically separated by 5 mm. The illumination procedure for both experiments after the first hour is shown in Figure 6.9, where the green light only experiment does not include red light illumination. During the first hour the procedure is the same as shown in Figure 6.4.

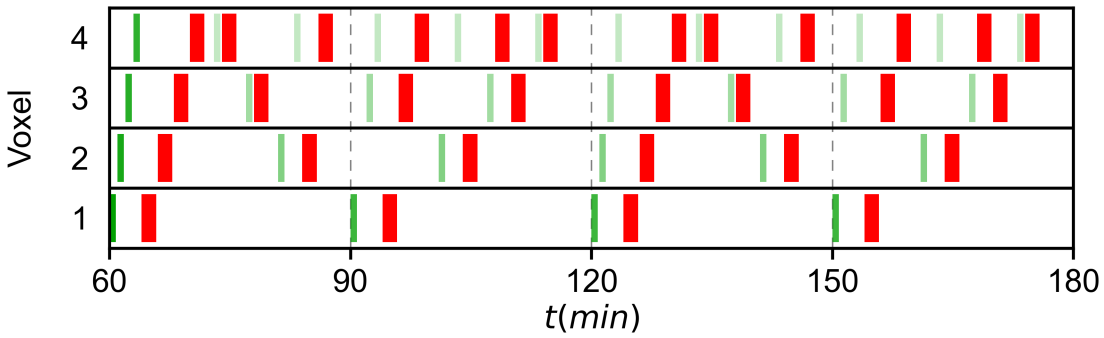


Figure 6.9: *Schematic of the periodic illumination procedure of a four voxel illumination experiment. Initially each of the four voxels is illuminated for* 1 *minute with peak green light intensity of* 25 W/m^2, 22.5 W/m^2, 21 W/m^2 *and* 20 W/m^2. *These correspond to four different intervals of illumination* 30 *min,* 20 *min,* 15 *min and* 10 *min respectively. Green intensities during each following illumination step are* 6.5 W/m^2, 4 W/m^2, 3 W/m^2 *and* 2 W/m^2 *respectively and are denoted with different shades of green. In the second experiment red light illumination was added with an average intensity of* 64 W/m^2 *for all voxels and its duration was* 2 *minutes.*

During the green light only experiment the duration of each illumination was set to 1 minute, which is short enough to allow for all four voxels to be illuminated without overlap and still maintain four different intervals of illumination. The target proportion of active-state photoreceptors, η_{high}, for each voxel should be set to $\eta_{max} \exp k_{growth} \Delta t_I$ according to (6.10). This results in green light intensity that keeps the illuminated area above η_{max} throughout the experiment. However, the green intensity was regardless set higher due to the nature of imaging of gene expression, if maximum gene expression is only reached at the peak, the measured signal might be relatively weak. The green light intensity was thus raised by 40%, which would, according to reported values of parameters, result in a voxel with a diameter of 0.4 mm where η is above η_{max} throughout the experiment. Should the forward conversion rate be five times greater than reported, the resulting voxel would have a diameter of 1 mm. The calculation of these values is valid at the surface of the build volume, as it does not include attenuation of green light.

The setup for the second experiment that includes red light illumination was the same as the first experiment including the magnitude of green light intensities. The same green light intensity is kept, as the effect of η_R was not included in its calculation. The red light illumination duration was set to 2 minutes and its intensity was calculated according to (6.17). Additionally, the red light intensity was increased to compensate for attenuation. During the experiment the sequence of red light illumination was such that it was carried out as soon as possible after its corresponding green light illumination without affecting the order of green light illuminations (Figure 6.9).

6.2.3 Results

Figure 6.10(a) shows the results of the experiment with repeated green light only illumination. Each summed fluorescent image is of a voxel at a different height illuminated with a different interval of illumination. All four voxels largely exhibit the same level of gene expression, which given the set parameters was expected. However, the width of gene expression is again too wide for the given green light intensities. As with the single illumination experiments, these indicate that green light's effect is stronger than expected.

The results of the the experiment that included red light illumination are again not shown, as there was no perceivable gene expression. While the effect of η_R was ignored when determining the light intensities, there should still be some noticeable gene expression, which again points to red light's effect being stronger than expected.

Much like with single illumination experiments, another experiment was ran. Its procedure is shown in Figure 6.11. Unlike the first set of experiments here the interval between illuminations is the same for all four voxels and is set to 30 minutes. As in the previous experiments, η_R was neglected when calculating green light intensity. However, green light intensity was significantly increased to try to ensure visible gene expression and was the same for all four voxels. The variable between the voxels is the intensity of red light illumination, with the lowest being reduced by tenfold when compared to red light intensity dictated by the illumination procedure shown in Figure 6.9.

Figure 6.12(a) shows the results of the experiment with repeated illumination of four voxels at four different red light intensities. This time gene expression in the voxel region can clearly be seen. While not as obvious as with the results of the single illumination experiment (Figure 6.7), the gene expression within the voxel also diminishes with increasing red light intensity, which is another strong indication that red light leakage is significant.

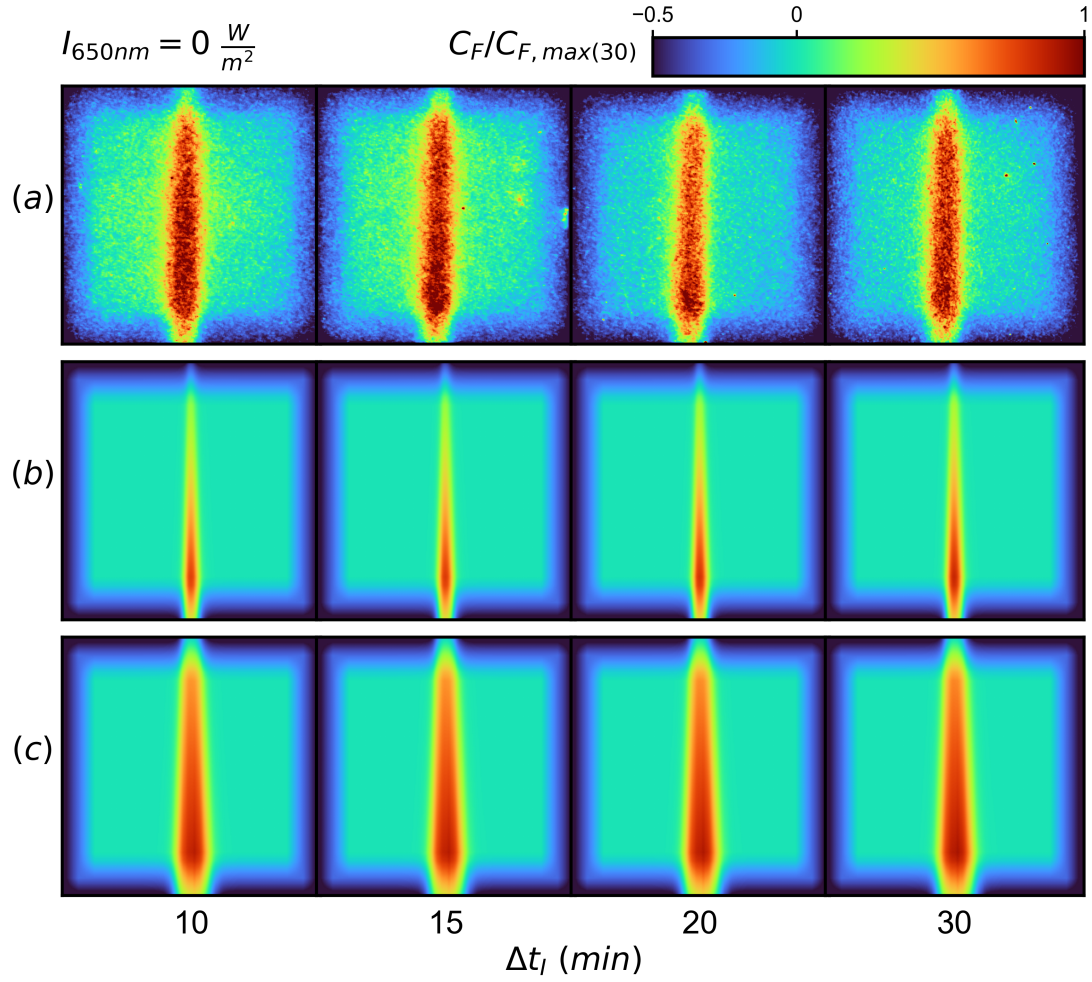


Figure 6.10: *Measurements and simulations of a four voxel periodic illumination experiment without red light illumination following the procedure shown in Figure 6.9.* (*a*) *Summed images of normalized contrasted fluorescence of each voxel illuminated at four different intervals,* Δt_I. *The contrasting background was determined from slices between the voxels, which were deactivated prior to experiment. Images were normalized with the maximum fluorescence value of the summed image where* $\Delta t_I = 30min$. (*b*) *Simulation of normalized integrated total gene expression using parameters shown in Table 2.1.* (*c*) *Exact same simulation as shown in row* (*b*) *with the exception of increased forward conversion rate* $\hat{k}_1' = 5\hat{k}_1$. *Normalization of simulations was done with the maximum value obtained from the simulation with* $\Delta t_I = 30min$ *in the respective row. The halo effect in simulations was added qualitatively as a visual aid and to illustrate the rounding shape near the edges.*

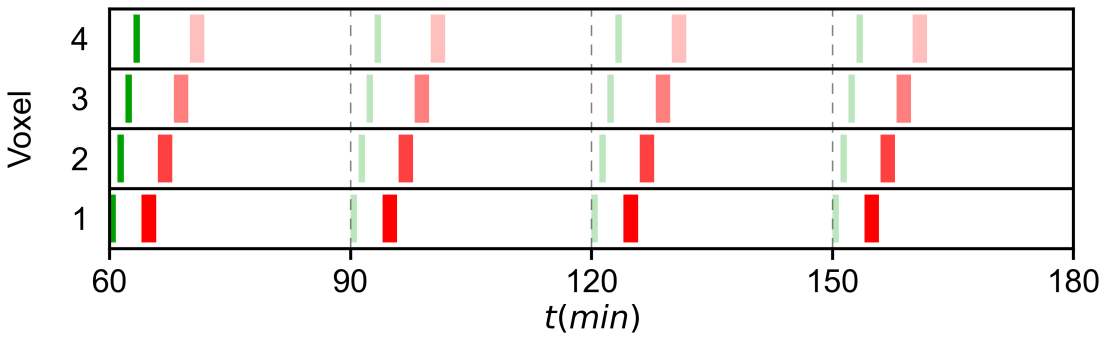


Figure 6.11: *Schematic of the periodic illumination procedure of a four voxel illumination experiment with a single period for each voxel. Initially all of the four voxels are illuminated for* 1 *minute with a peak green light intensity of* 45 W/m^2. *All voxels are illuminated at* 30 *minute intervals. Green intensity during each following illumination step is* 11.5 W/m^2. *The duration of red light illumination was* 2 *minutes. Voxels were illuminated separately with red light intensities of* 6.4 W/m^2, 12.8 W/m^2, 19.2 W/m^2 *and* 25.6 W/m^2, *denoted by the shades of red.*

The experiments were again simulated using the optogenetic model to simulate their outcome. Simulated normalized integrated total gene expression is shown in Figures 6.10(b) and 6.12(b). Simulations and measurements were again normalized for easier comparison between the shape and relative change of integrated total gene expression. In Figure 6.10(b) with green-only illumination, the simulation predicts gene expression in a thin line, whereas the measurements shows a much wider line of gene expression. Similarly in Figure 6.12(b) the gene expression in the voxel is much lower and narrower than expected.

Increasing the effectiveness of green and red light, by increasing the forward and reverse conversion rate by a factor of five, yields simulations shown in Figures 6.10(c) and 6.12(c) that predict the shape of gene expression quite well in these experiments. As with the single illumination experiments, near zero gene expression is reached in the suppressed region between experiments with 1/5 and 3/10 of the required red light intensity (Figure 6.12(c), I_{650nm} = 12.8 W/m^2 and I_{650nm} = 19.2 W/m^2). Slightly more than expected reduction in voxel total gene expression can be seen in simulations shown in Figure 6.10(c). To some extent the effect is similar in simulations of the single illumination experiments (Figure 6.7). This could be indicative that the effectiveness of red light was overestimated; however, it can also be due to an underestimation of red light attenuation or an overestimation of η_R.

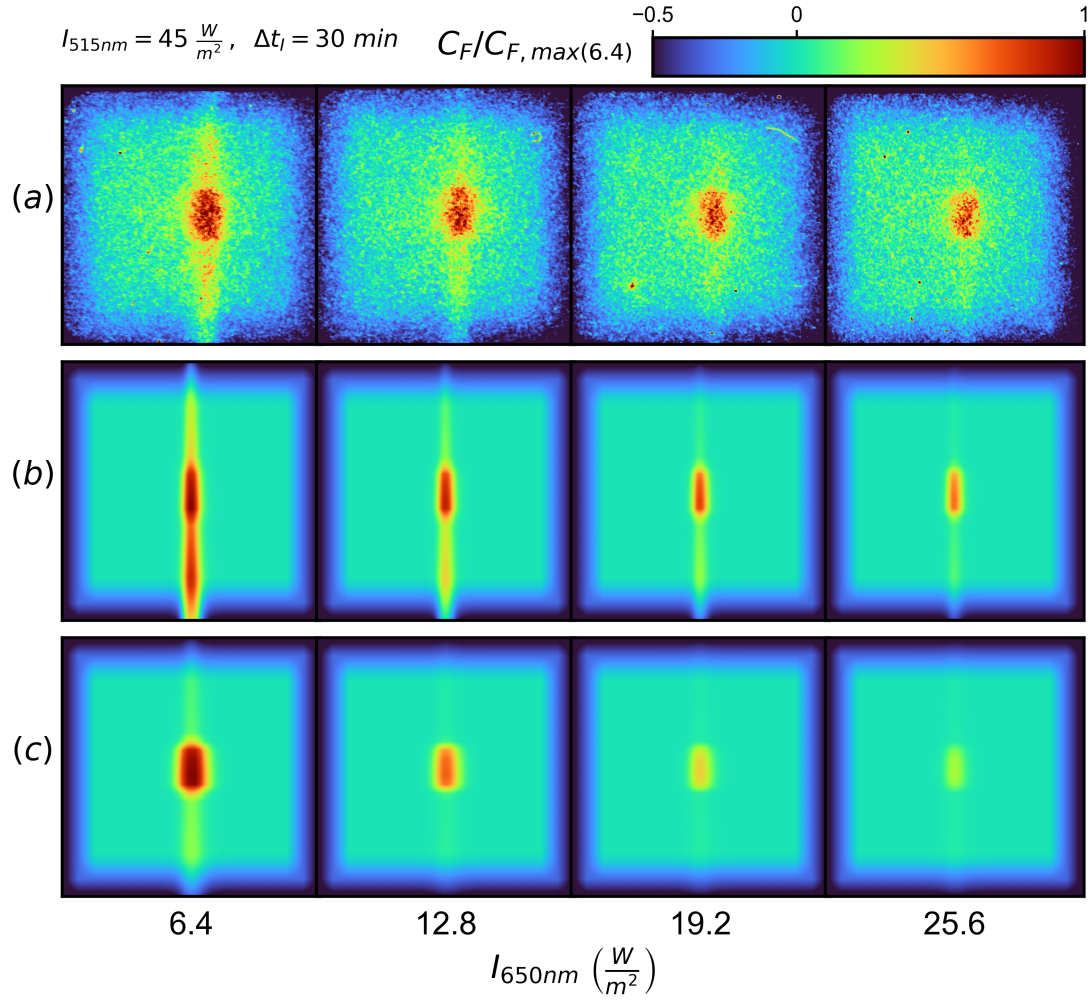


Figure 6.12: *Measurements and simulations of a four voxel periodic illumination following the procedure shown in Figure 6.11.* (*a*) *Summed images of normalized contrasted fluorescence of each voxel illuminated at four different red light intensities,* I_{650nm}. *The contrasting background was determined from the red only regions of each summed image. Images were normalized with the maximum fluorescence value of the summed image where* $I_{650nm} = 6.4\ W/m^2$. (*b*) *Simulation of normalized integrated total gene expression using parameters shown in Table 2.1 with* $\eta_R = 0.2$. (*c*) *Exact same simulation as shown in row* (*b*) *with the exception of increased forward and reverse conversion rates,* $\hat{k}_1' = 5\hat{k}_1$ *and* $\hat{k}_2' = 5\hat{k}_2$. *Normalization of simulations was done with the maximum value obtained from the simulation with* $I_{650nm} = 6.4\ W/m^2$ *in the respective row. The halo effect in simulations was added qualitatively as a visual aid and to illustrate the rounding shape near the edges.*

6.3 Conclusion

With time dependant illumination, it has been shown that steady-state illumination is not necessary for gene expression, localized or otherwise. Furthermore, non-concurrent green and red light illumination is favourable to localized gene expression due to the presence of significant red light leakage, η_R. The initial illumination experiments showed that active-state photoreceptors are indeed persistent and their apparent reduction is likely only due to dilution from cell growth. While initial illumination only results in a localized gene expression, repeated periodic illumination can increase the contrast between the desired gene expression within the voxel and undesired background gene expression. Both sets of experiments – initial and periodic illumination – have shown a significant discrepancy when it comes to the effectiveness of green and red light. In the steady-state experiments the resulting gene expression largely relied on the ratio between the forward and reverse conversion rate and by extension the ratio between green and red light intensity. While the dynamic nature of the initial and repeated illumination experiments revealed the higher effectiveness of green and red light, the steady-state experiments indicate that the ratio between the two should remain the same.

With this new estimation of the forward and reverse photoconversion rates, the best fit estimates carried out in chapter 5.3 were redone and the results are shown in Figures 6.13 and 6.14. The new estimated parameter values are shown in Tables 6.1 and 6.2. In future calculations η_R remains at 20% and forward and reverse conversion rates are $\hat{k}_1' = 53.5 \times 10^{-3}\ \frac{1}{min}\frac{m^2 s}{\mu mol}$ and $\hat{k}_2' = 23 \times 10^{-3}\ \frac{1}{min}\frac{m^2 s}{\mu mol}$ respectively.

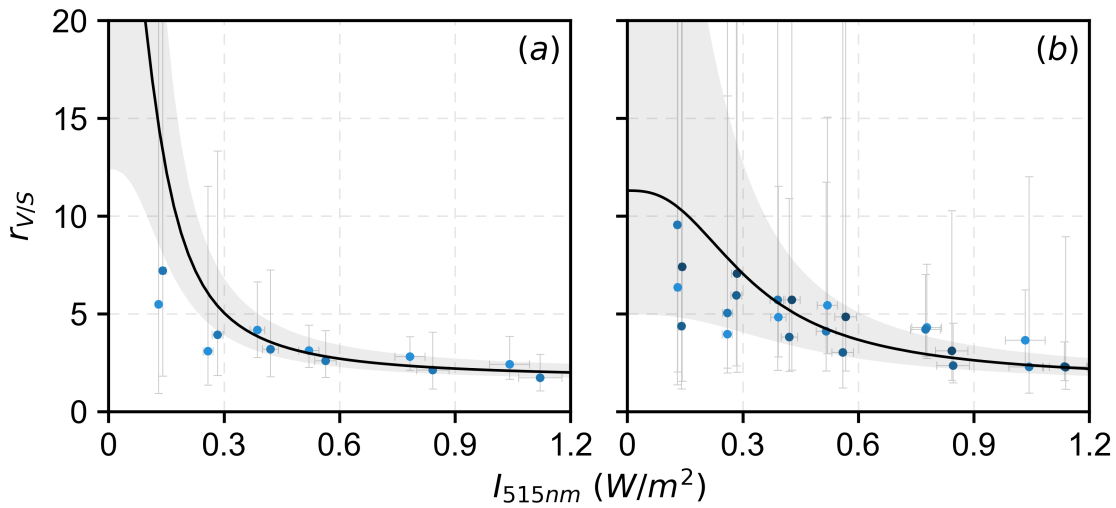


Figure 6.13: *Best fit of the ratio between the average maximum voxel gene expression and the average maximum suppressed region gene expression to the measured values, $r_{V/S}$. Parameters used in the best fit estimation were updated to include the five-fold more effective green and red light intensities. Each blue shade of the plotted data corresponds to one group of steady-state experiments. The solid black line graphs are the best fit estimates and the grey shaded areas are determined by parameter error estimates. The green intensity, I_{515nm}, relative error estimate is 5%. (a) Fit to measurements with red light intensity of I_{650nm} = 1.45 W/m^2. (b) Fit to measurements with red light intensity of I_{650nm} = 2.9 W/m^2. I_{515nm} values of data points were randomly perturbed for up to 2% during plotting for better visualisation.*

Table 6.1: *Estimates of red light leakage, η_R, obtained by performing a best fit of (5.11) to the measured data (Figure 6.13) and their average with updated values for the forward and reverse conversion rates. The errors are rough estimates of uncertainty and do not represent the confidence interval associated with one standard deviation.*

I_{650nm} (W/m^2)	η_R	$\bar{\eta}_R$
1.45	0.20 ± 0.11	0.27 ± 0.09
2.90	0.34 ± 0.13	

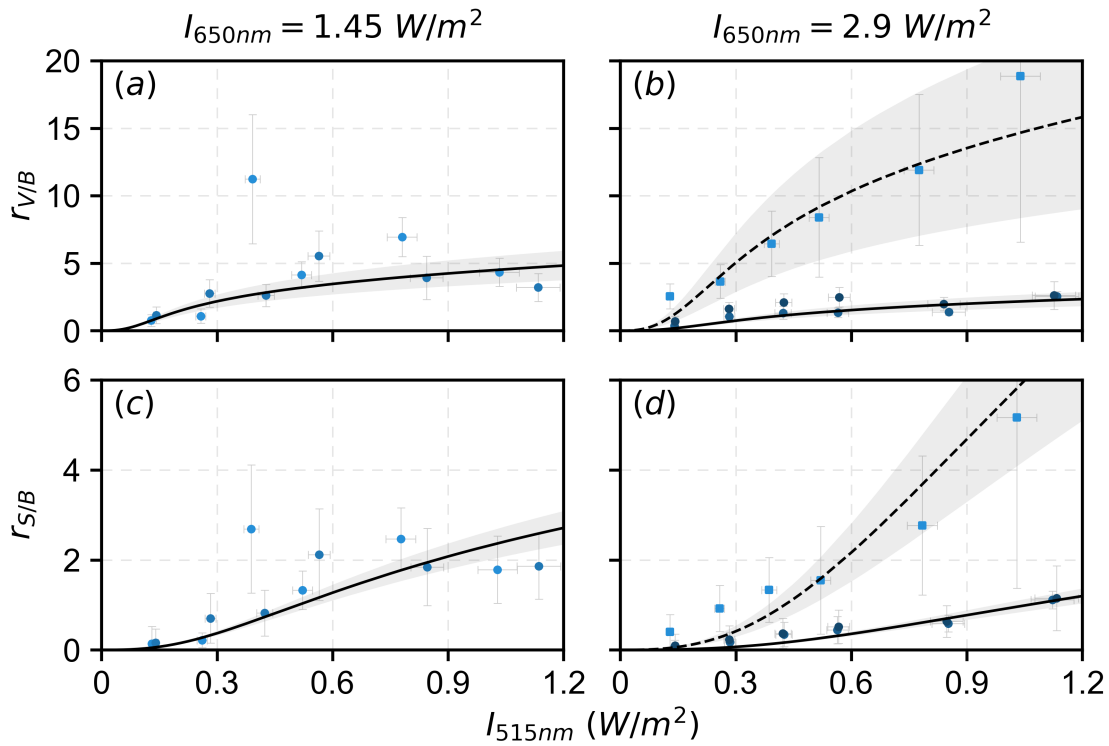


Figure 6.14: *Best fit estimates of* (5.14) *to the measured contrast,* $r_{\{V,S\}/B}$*, in the respective regions. Parameters used in the best fit estimation were updated to include the five-fold more effective green and red light intensities. Each blue shade of the plotted data corresponds to one group of steady-state experiments. The solid black line graphs are the best fit estimates and the grey shaded areas are determined by parameter error estimates. The green intensity's,* I_{515nm}*, relative error estimate is* 5%*.* (*a*)*,* (*b*) *Best fits of* (5.14) *to* $r_{V/B}$*.* (*c*)*,* (*d*) *Best fits of* (5.14) *to* $r_{S/B}$*.* (*a*) *and* (*c*) *are best fits to measurements from experiments with red light intensity of* $I_{650nm} = 1.45\ W/m^2$ *and* (*b*) *and* (*d*) *are best fits to measurements with red light intensity of* $I_{650nm} = 2.9\ W/m^2$*. The dashed lines are the best fit estimates for the group of measurements denoted by squares.* I_{515nm} *values of data points were randomly perturbed for up to* 2% *during plotting for better visualisation.*

Table 6.2: *Parameter estimates of maximum contrast,* $r_{a'/b'}$*, obtained by a best fit of* (5.14) *to the measured data (Figure 6.14) with updated values for the forward and reverse conversion rates. The* $\bar{r}_{\{V,S\}/B}$ *column shows the average value of* $r_{a'/b'}$ *of all four estimates. The* $r_{\square\{V,S\}/B}$ *columns are the best fit parameter estimates for data points denoted by squares in Figure 6.14*(*b*) *and* (*d*)*.*

	$r_{a'/b'}$				
$I_{650nm}\ (W/m^2)$	$r_{V/B}$	$r_{S/B}$	$\bar{r}_{\{V,S\}/B}$	$r_{\square V/B}$	$r_{\square S/B}$
1.45	3.5 ± 0.8	4.4 ± 0.6	3.5 ± 0.8	-	-
2.90	2.2 ± 0.5	3.9 ± 0.5		15 ± 7	24 ± 7

Chapter 7

Gene Expression in Multiple Voxels

Producing a 3D object requires gene expression in more than a single voxel per plane. Distribution of the red and green light prevents steady-state gene expression in multiple voxels; therefore, time dependant illumination procedures for the case of two voxels were investigated. First is the straightforward alternating illumination that alternates between the voxels in equal time intervals and with equal settings. Second is illumination that results in gene expression within multiple voxels at the same time – concurrent gene expression. Last is illumination that induces gene expression in one voxel at a time – separate gene expression.

7.1 Voxel Arrangements

There are three different general arrangements for the simplest case of two voxels in a plane in reference to the geometry of the two light sources used in experiments (Figure 3.11). These arrangements will be referred to as horizontal, vertical and diagonal. In horizontal arrangement the two voxels lay on a line that is perpendicular to the optical axis of green light and parallel to the optical axis of red light. Inversely, in vertical arrangement the voxels are aligned parallel to the optical axis of green light and perpendicular to the optical axis of red light. Finally, in diagonal arrangement the voxels lay on a line that is at an angle compared to the optical axes of green and red light. The angle chosen here was 45°. All three arrangements are shown in Figure 7.1. In horizontal arrangement, during sequential illumination of both voxels, red light illumination remains stationary and only green light illumination changes its relative position. Similarly, in vertical arrangement green light illumination remains stationary and red light changes its relative position. And clearly, in diagonal arrangement both illuminations change their relative positions to the build volume.

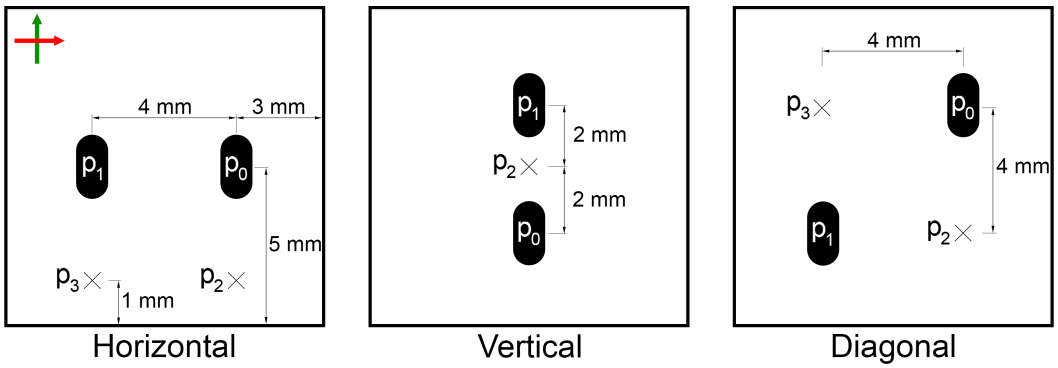


Figure 7.1: *Schematic of three arrangements of two voxels, which are denoted as p_0 and p_1. Crosses mark the locations where significant unwanted gene expression is expected. These points are denoted as p_2 and p_3. The green and red arrow indicate the direction of the optical axes of green and red light respectively.*

7.2 Alternating Illumination

Given the geometry of green and red light illumination, the simplest continuation of the steady-state illumination is the alternating illumination, where the experiment is divided into several intervals during which one voxel is continuously illuminated. Illumination alternates between the voxels after each interval until the end of experiment. The green and red light intensities remain the same for the duration of illumination.

7.2.1 Horizontal Arrangement

Voxels in horizontal arrangement are as independent as they can be, the only coupling exists due to red light leakage, η_R. When red light is used to define the active voxel it also affects the other. During the interval when the active voxel is illuminated the gene expression can be considered steady-state for sufficiently large green and red light intensities. In order to maximize total gene expression during the experiment, green and red light intensities should be high, which allows the maximum gene expression rate to be achieved as quickly as possible.

However, it should be noted that for sufficiently small values of η_R greater than zero, there exists an optimal light intensity of red and green light that maximizes gene expression in both voxels. This would be due to the weaker effect of red light leakage, which would not cause sufficient deactivation within the other voxel while the active voxel was being illuminated. If said deactivation is low enough, the subsequent activating illumination can be weaker and still result in the same fraction of active-state photoreceptors, η, as in the first voxel. In turn this causes an even lower deactivation in the previously illuminated voxel. This way a certain level of concurrent gene expression can be achieved using alternating illumination. However, this effect is no longer present for the parameters and η_R used here.

Model

The steady-state η reached within each voxel is described by (6.5). However, the light intensity reaching the individual voxel depends on its position within the build volume due to light attenuation. By considering light attenuation the steady-state fractions of active-state photoreceptors, η^{ss}, at each point of interest in horizontal arrangement during direct illumination and by neglecting growth rate are approximately:

$$\eta^{ss}(p_1) \approx \frac{1}{1+\eta_R\dfrac{A_{2,1}k_2}{A_{1,1}k_1}}\,, \qquad \eta^{ss}(p_0) \approx \frac{1}{1+\eta_R\dfrac{A_{2,0}k_2}{A_{1,0}k_1}}\,,$$

$$\eta^{ss}(p_3) \approx \frac{1}{1+\dfrac{A_{2,3}k_2}{A_{1,3}k_1}}\,, \qquad \eta^{ss}(p_2) \approx \frac{1}{1+\dfrac{A_{2,2}k_2}{A_{1,2}k_1}}\,, \tag{7.1}$$

$$p_i = (x_i,\, y_i)_H \text{ for } i \in \{0,1,2,3\}\,,$$

where $A_{1,i}$ and $A_{2,i}$ are the factors of attenuation experienced by green and red light respectively at each point p_i. By adjusting intensities and consequently the values

of k_1 and k_2 at point p_3 to account for attenuation, the factors of attenuation only reflect the distance between the relevant points:

$$\begin{aligned} A_{1,3}k_1 \to k_1 \;\Rightarrow\quad & A_{1,1} = e^{-\mu_G(x_1 - x_3)} = A_1\,, \quad A_{1,0} = e^{-\mu_G(x_0 - x_2)} = A_1\,, \\ & A_{1,3} = 1\,, \qquad\qquad\qquad\quad A_{1,2} = 1\,, \\ A_{2,3}k_2 \to k_2 \;\Rightarrow\quad & A_{2,1} = 1\,, \qquad\qquad\qquad\quad A_{2,0} = e^{-\mu_R(y_0 - y_1)} = A_2\,, \\ & A_{2,3} = 1\,, \qquad\qquad\qquad\quad A_{2,2} = e^{-\mu_R(y_2 - y_3)} = A_2\,, \end{aligned} \tag{7.2}$$

where A_1 and A_2 are attenuation factors of green and red light respectively corresponding to the change of depth at p_0.

η^{ss} of all four points in uniquely defined given the constant ratio between the incident red and green light intensity. Therefore, η^{ss} can be selected at only one point. Point p_2 is exposed to the highest green light intensity and the lowest red light intensity. By setting $\eta^{ss}(p_2)$ to equal η_{low}, it follows that any unwanted gene expression everywhere else in the plane will be lower when compared to gene expression at p_2. The light intensity ratio is then:

$$\eta^{ss}(p_2) = \frac{1}{1 + \dfrac{A_2 k_2}{k_1}} = \eta_{low} \;\Rightarrow\; \frac{I_{650}}{I_{515}} = \frac{\hat{k}_1}{\hat{k}_2} \cdot \frac{1}{A_2} \frac{1 - \eta_{low}}{\eta_{low}}\,. \tag{7.3}$$

With the given dot arrangement the highest η^{ss} is then at point p_0:

$$\eta^{ss}(p_0) = \frac{1}{1 + \dfrac{\eta_R}{A_1} \cdot \dfrac{1 - \eta_{low}}{\eta_{low}}}\,, \tag{7.4}$$

this is the same result that is obtained for steady-state illumination for the given light intensity ratio with the exception being the green light intensity attenuation factor, A_1. This factor worsens the system's performance by effectively increasing the influence of η_R.

The ratio between the steady-state fractions of active-state photoreceptors of each voxel is:

$$\frac{\eta^{ss}(p_0)}{\eta^{ss}(p_1)} = 1 + \frac{1 - A_2}{A_2} \cdot \frac{1}{1 + \dfrac{A_1}{\eta_R} \cdot \dfrac{\eta_{low}}{1 - \eta_{low}}}\,, \tag{7.5}$$

which shows that greater the distance between the voxels and/or greater the red light attenuation results in a greater ratio and a lower homogeneity between the voxels. Gene expression distribution that results from setting $\eta^{ss}(p_2) = \eta_{low}$ to η_{min} will be referred to as $\eta_{min} - p_2$.

Figure 7.2 shows the normalized gene expression rate, h, and the normalized total gene expression, g/g_{max}, over time for each point of interest. The ratio between the red and green light intensity was determined by (7.3) for $\eta_{low} = \eta_{min} = 0.15$. It can be seen that even though the second voxel at p_1 exhibits lower gene expression rate, the total gene expression is slightly higher when compared to the first voxel at p_0. The reason lies in the cell population which is higher when voxel at p_1 is active. However, in both voxels the end normalized total gene expression is much lower than 50%, which is what would ideally be expected when half of the growing duration is allocated to each voxel.

When determining η in voxels that would lead to the desired distribution of total gene expression, the delay between illumination and gene expression, τ, is not considered. While τ is used in the simulation with the reported value of 12 minutes, the value of τ was not measured here and it is unclear what delay the system actually has. To maintain the same profile of gene expression rate despite τ, the duration of the experiment should be extended by the same amount to let the system respond.

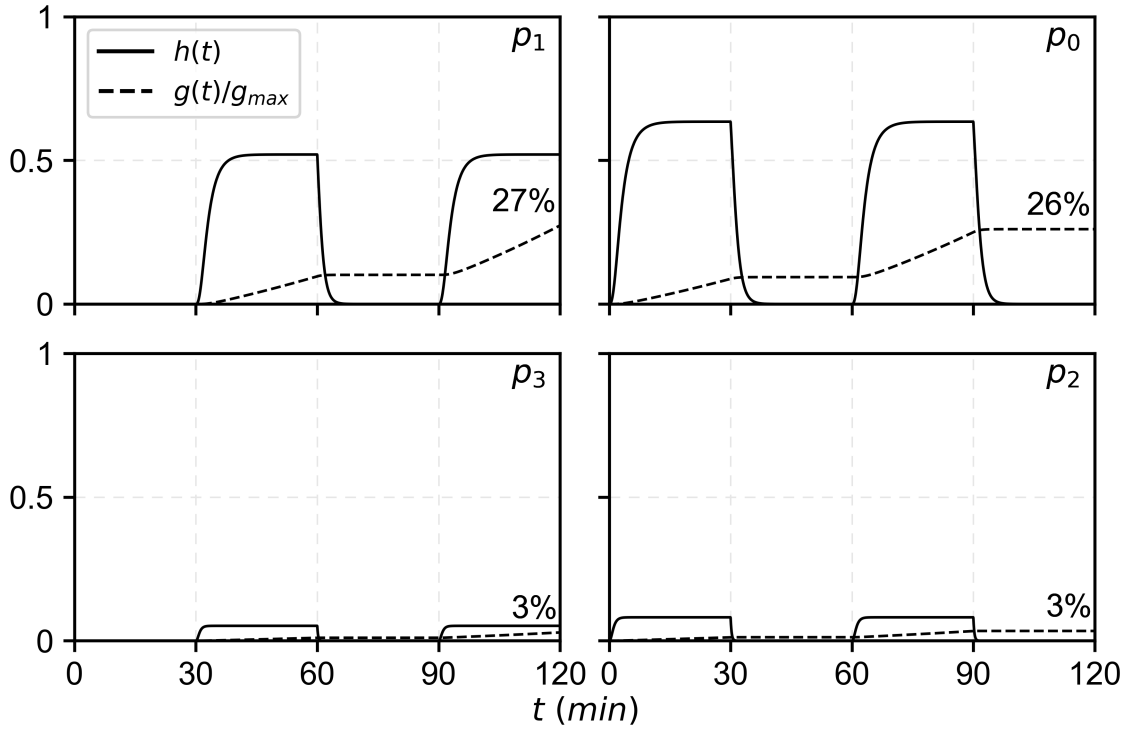


Figure 7.2: *Response of the normalized gene expression rate, $h(t)$, and normalized total gene expression, $g(t)/g_{max}$, in horizontally arranged voxels to alternating illumination. Each graph corresponds to the respective point of interest p_0, p_1, p_2 and p_3, for the horizontal arrangement with positions and distances as shown in Figure 7.1. Peak incident green light intensity was set to 1.2 W/m^2 and the average incident red light intensity was set to 14.7 W/m^2, which results in $\eta^{ss}(p_2) = \eta_{min}$. The percentage of maximum possible total gene expression density after two hours is shown for each point of interest.*

Experiment's Illumination Procedure

During the first hour of the experiment the voxel plane was deactivated with red light and the green laser was warmed up, this part of the procedure is equivalent to the one shown in Figure 6.4 but for a single voxel. The experiment was split into four 30 minute intervals, which mostly evens out the effects of the exponentially growing cell population. The illumination procedure is shown in Figure 7.3 for the four points of interest.

The red light intensity used in the experiment was lower than required for an illumination procedure where η does not exceed η_{min} in the suppressed regions. The intensity to achieve $\eta_{min} - p_2$ was not employed in the experiment, as significant background gene expression was expected. As shown in Figure 7.4 the predicted normalized integrated total gene expression under higher red light intensity is relatively weak and the contrast between the induced and background gene expression in fluorescence images was expected to be very low. The illumination procedure also does not account for any possible delay in response, τ, there may be in the system.

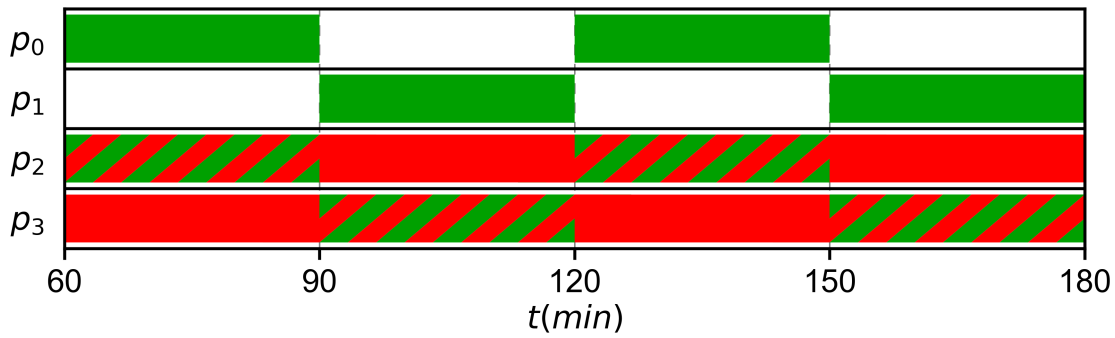


Figure 7.3: *Schematic of the alternating illumination procedure for an experiment with two voxels in horizontal arrangement. Each row shows the presence of the respective green or red light over time for all four points of interest. The peak green light intensity was* 1.2 W/m^2 *and the average red light intensity was* 9.6 W/m^2.

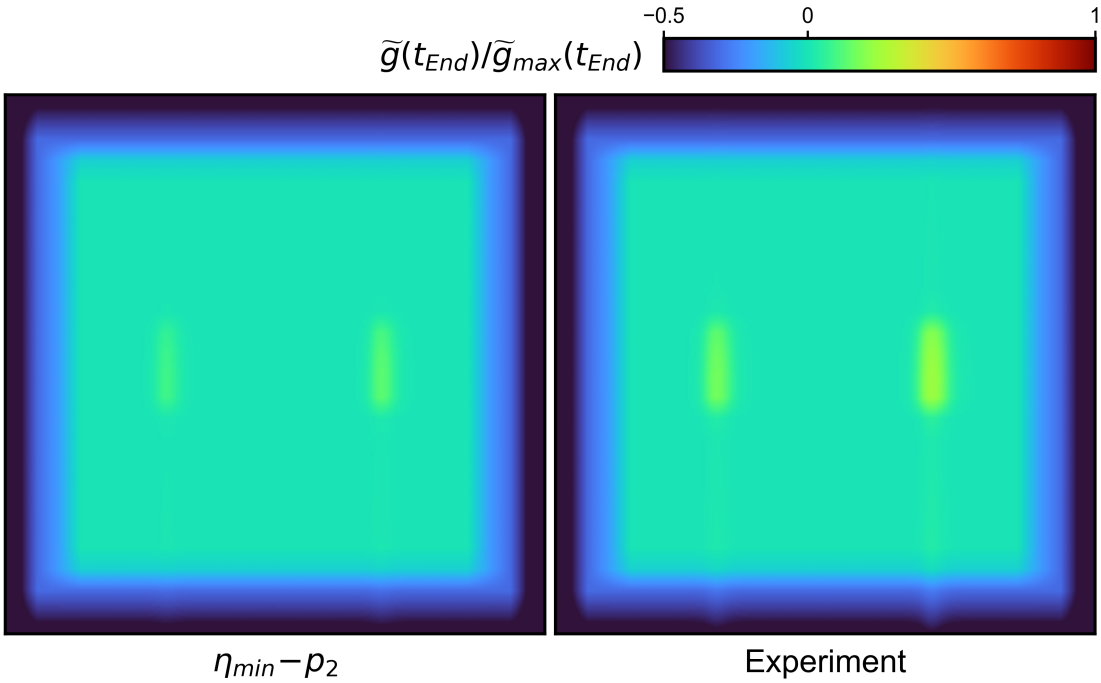


Figure 7.4: *Simulations of normalized integrated total gene expression, $\tilde{g}(t_{End})/\tilde{g}_{max}(t_{End})$, in two voxels in horizontal arrangement subjected to alternating illumination procedure as shown in Figure 7.3. Left, simulation of normalized $\tilde{g}(t_{End})$ for incident red light intensity $I_{650} = 14.7\ W/m^2$ where η_{min} at p_2 is achieved. Right, simulation of normalized $\tilde{g}(t_{End})$ for incident red light intensity used in the experiment $I_{650} = 9.6\ W/m^2$. In both simulations the peak incident green intensity was $1.2\ W/m^2$. Both simulations are normalized to maximum possible $\tilde{g}(t_{End})$ within a thickness of 1 mm. The halo effect in the simulations was added qualitatively as a visual aid.*

Experiment Results

Figure 7.5 shows the normalized contrasted fluorescence of the experiment, $C_F/r_{a'/b'}$. The fluorescence was contrasted to background, measured in the red only regions. It was then further normalized by $r_{a'/b'}$ in order to represent the fluorescence in terms of maximum possible fluorescence in a 1 mm thick active voxel. The 1 mm thickness is determined by the thickness of the slice from which the local background was determined. With this normalization the scale of the measurement shown in Figure 7.5 is equivalent to the scale of the simulation shown in Figure 7.4. In Figure 7.5(a) it can be seen that the two voxels exhibit roughly the same gene expression as predicted by the simulation shown in Figure 7.4. However, averaging of the normalized fluorescence in the band around the points of interest (Figure 7.5(b)), showed that gene expression is greater in the voxel at p_1, which is opposite to what was predicted by the simulation shown in Figures 7.2 and 7.4. This discrepancy could be due to η_R varying along the depth of red light propagation with η_R being

larger farther in. The unwanted gene expression in points p_2 and p_3 is as predicted but does appear to be slightly higher in p_2; however, the variation in background gene expression is too great to determine these values with reliable precision.

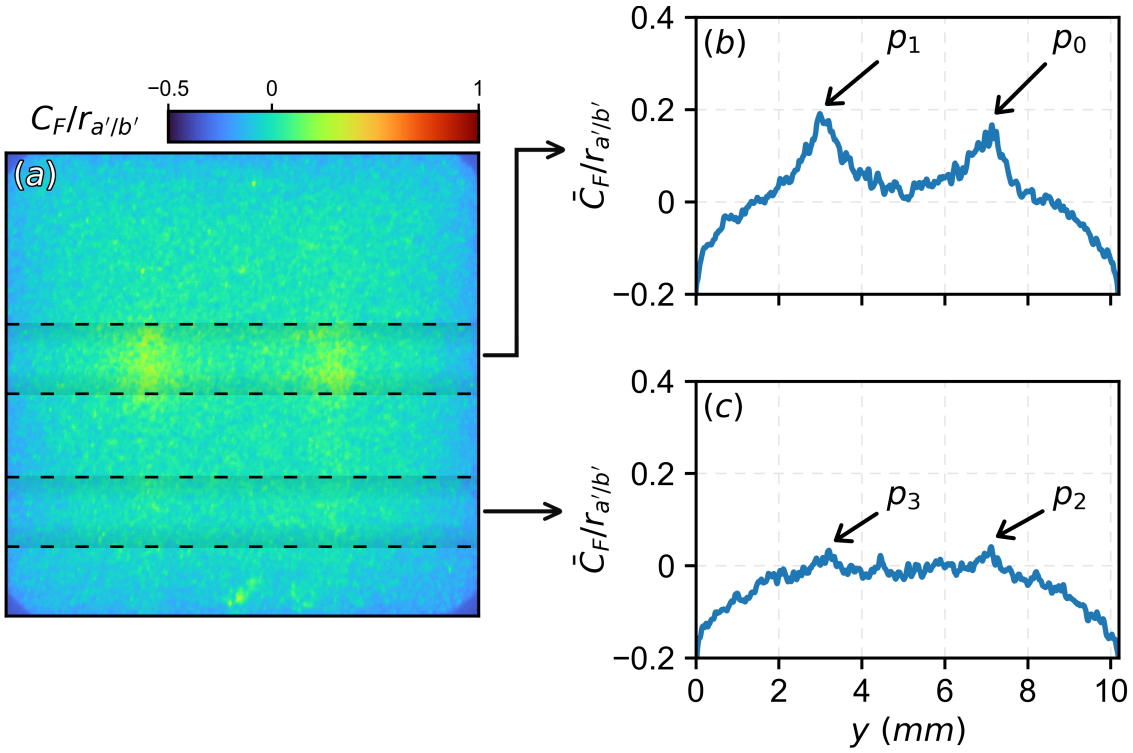


Figure 7.5: *Measurement of fluorescence of two voxels in horizontal arrangement subjected to alternating illumination procedure shown in Figure 7.3. (a) Summed image of normalized fluorescence with two bands of interest indicated by the dashed lines. Additional light shading was added to the dashed lines to better highlight the bands. (b) Normalized fluorescence averaged in the band of interest around points p_0 and p_1. (c) Normalized fluorescence averaged in the band of interest around points p_2 and p_3. The value of $r_{a'/b'}$ used was 3.5 .*

Table 7.1 shows a comparison between the normalized gene expression values predicted by the simulations and values from the measurement for each point of interest. Comparison of values between the two simulations also shows that while $\eta_{min} - p_2$ maximizes the effective contrast, indicated by p_1/p_2 in Table 7.1, it does so at a cost of absolute gene expression of the two voxels, while homogeneity, indicated by p_0/p_1 in Table 7.1, is roughly maintained. Notably, the normalized integrated gene expression at p_1 predicted for $\eta_{min} - p_2$ is also noticeably different to that at p_0, while Figure 7.2 suggests they should be almost the same. This discrepancy arises from τ being present in the simulation, which results in less gene expression in the last 30 minutes of the experiment at which time the voxel at p_1 is being illuminated.

Table 7.1: *Normalized integrated total gene expression at four points determined from two simulations, $\eta_{min} - p_2$ and Experiment, and from the summed fluorescence image of the experiment following the alternating illumination procedure shown in Figure 7.3 for two voxels in horizontal arrangement. p_0/p_1 and p_1/p_2 refer to ratios between the normalized integrated total gene expressions at the respective points. The majority contributor to the error estimates of the measured values is the background gene expression.*

	$\tilde{g}(t_{End})/\tilde{g}_{max}(t_{End})$		
	$\eta_{min} - p_2$	Experiment	$\bar{C}_F/r_{a'/b'}$
p_0	0.13	0.23	0.17 ± 0.09
p_1	0.08	0.16	0.19 ± 0.09
p_2	0.01	0.04	0.04 ± 0.07
p_3	0.01	0.04	0.03 ± 0.07
p_0/p_1	1.49	1.41	0.9 ± 0.5
p_1/p_2	6.95	4.32	5 ± 10

7.2.2 Vertical Arrangement

Unlike with the horizontal arrangement, voxels in vertical arrangement cannot be illuminated independently given the geometry of incoming light. When the active voxel is illuminated the other is directly exposed to green and red light. Because the other voxel is exposed to both green and red light it will always reach the steady state before the active voxel (Equation (2.4)). Any level of activation in one voxel will result in a greater level of deactivation in the other. Given this and the symmetry of the duration of illumination and the illumination intensities, it follows that no transient effects can be exploited to achieve a more optimal gene expression.

Furthermore, suppressed region is continuously illuminated by red and green light and provided that intensities are high enough it is in a steady state throughout the experiment. This means that gene expression rate in each voxel is at worst the same as in the suppressed region. The best contrast is achieved when dynamics are as fast as possible, this way the active voxel reaches the highest possible gene expression rate as fast as possible during its illumination. At a given ratio of green and red light intensity, it is thus best to have high intensities of both colours.

In contrast to horizontal arrangement, the point of interest that marks the unwanted gene expression in vertical arrangement is between the two voxels, as opposed to the entry point of green light. In this arrangement the distinguishment of the two voxels was deemed more important than the minimum possible background.

Model

In vertical arrangement the steady-state fractions of active-state photoreceptors, η^{ss}, for each point of interest during direct illumination and considering light attenuation are approximately:

$$\begin{aligned}
\eta^{ss}(p_1) &\approx \frac{1}{1+\eta_R\dfrac{A_{2,1}k_2}{A_{1,1}k_1}}\,,\\[2ex]
\eta^{ss}(p_2) &\approx \frac{1}{1+\dfrac{A_{2,2}k_2}{A_{1,2}k_1}}\,,\\[2ex]
\eta^{ss}(p_0) &\approx \frac{1}{1+\eta_R\dfrac{A_{2,0}k_2}{A_{1,0}k_1}}\,,
\end{aligned} \tag{7.6}$$

$$p_i = (x_i,\, y_i)_V \text{ for } i \in \{0,1,2\}\,,$$

where $A_{1,i}$ and $A_{2,i}$ are attenuation factors for green and red light respectively at each point p_i. The incident light intensities are adjusted so that the attenuation factors can be rewritten to again only reflect the relative positions between the points of interest:

$$\begin{aligned} A_{1,0}k_1 \to k_1 \;\Rightarrow\; A_{1,1} &= e^{-\mu_G(x_0 - x_1)} = A_1^2\,, \\ A_{1,2} &= e^{-\mu_G(x_0 - x_2)} = A_1\,, \\ A_{1,0} &= 1\,, \\ A_1^2 < A_1 &< 1\,, \end{aligned} \tag{7.7}$$

$$\begin{aligned} A_{2,0}k_2 \to k_2 \;\Rightarrow\; A_{2,1} &= 1\,, \\ A_{2,2} &= 1\,, \\ A_{2,0} &= 1\,, \end{aligned}$$

where A_1 is the attenuation factor of green light corresponding to the change of depth at p_2 and due to symmetry A_1^2 is the attenuation factor at p_1.

As with horizontal arrangement, the η^{ss} of all three points is uniquely defined by the ratio between the red and green light intensity. An optimal intensities ratio would maximize the ratio $\eta^{ss}(p_1)/\eta^{ss}(p_2)$ and keep ratio $\eta^{ss}(p_0)/\eta^{ss}(p_1)$ equal to one. These two ratios – distinguishability and homogeneity – oppose each other and their preferred states are met individually at opposite extremes of the intensities ratio, at infinity and at zero. The intensities ratio can be expressed as a function of $\eta^{ss}(p_2)$, which can be set to an arbitrary value η. The intensity ratio is then determined in the following way:

$$\eta^{ss}(p_2) = \frac{1}{1 + \dfrac{1}{A_1}\dfrac{k_2}{k_1}} = \eta \quad \Rightarrow \quad \frac{I_{650}}{I_{515}} = \frac{\hat{k}_1}{\hat{k}_2} \cdot A_1 \frac{1-\eta}{\eta}\,. \tag{7.8}$$

Expressing $\eta^{ss}(p_0)/\eta^{ss}(p_1)$ and $\eta^{ss}(p_1)/\eta^{ss}(p_2)$ in terms of $\eta^{ss}(p_2) = \eta$ yields:

$$\frac{\eta^{ss}(p_0)}{\eta^{ss}(p_1)} = 1 + \frac{1 - A_1^2}{A_1^2} \cdot \frac{1}{1 + \dfrac{1}{\eta_R A_1}\dfrac{\eta}{1-\eta}}\,, \qquad \frac{\eta^{ss}(p_1)}{\eta^{ss}(p_2)} = \frac{1}{\eta + \eta_R \dfrac{1}{A_1}(1-\eta)}\,. \tag{7.9}$$

The graphs of the two functions are shown in Figure 7.6. Similarly as before, the two quantities oppose each other; however, $\eta^{ss}(p_1)/\eta^{ss}(p_2)$ increases quicker when η approaches zero indicating that having lower η is less of a detriment to homogeneity between the two voxels than to the distinguishability. Regardless, setting $\eta^{ss}(p_2) = \eta$ to zero is not a solution, as doing so sets η at all other positions to zero as well. By

setting $\eta^{ss}(p_2) = \eta_{min}$ it is set as low as it is efficient to do so, while achieving the best distinguishability. If the absolute gene expression at p_0 and p_1 is preferred over their distinguishability, which can be the case when there is significant background gene expression, the intensities ratio can be expressed in terms of $\eta^{ss}(p_1) = \eta_{max}$. Conveniently, the parameters of this system are such that $\eta^{ss}(p_0)$ and $\eta^{ss}(p_1)$ are near η_{max} when $\eta^{ss}(p_2) = \eta_{min}$.

As with horizontal arrangement attenuation is a detriment to the target distribution of η. This can be clearly seen in the limiting case where $\eta^{ss}(p_2) = 0$:

$$\frac{\eta^{ss}(p_0)}{\eta^{ss}(p_1)}(\eta=0) = \frac{\eta_R}{\eta_R}\frac{1}{A_1^2}, \qquad \frac{\eta^{ss}(p_1)}{\eta^{ss}(p_2)}(\eta=0) = \frac{A_1}{\eta_R}. \tag{7.10}$$

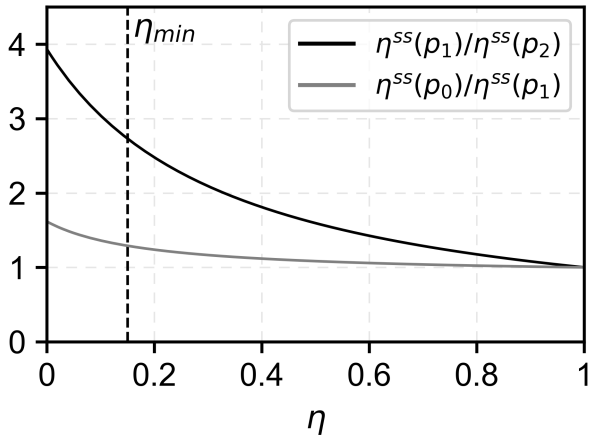


Figure 7.6: *Two ratios, $\eta^{ss}(p_1)/\eta^{ss}(p_2)$ and $\eta^{ss}(p_0)/\eta^{ss}(p_1)$, relating to distinguishability and homogeneity of voxels in vertical arrangement subjected to alternating illumination as a function of $\eta^{ss}(p_2) = \eta$.*

Figure 7.7 shows the normalized gene expression rate, h, and the normalized total gene expression, g/g_{max}, over time for each point of interest. The ratio between the red and green light intensity was determined by (7.8) for $\eta = \eta_{min}$. It can be seen that gene expression is kept at a constant low rate at p_2 and gene expression at p_0 and p_1 is almost at a maximum during the illumination interval.

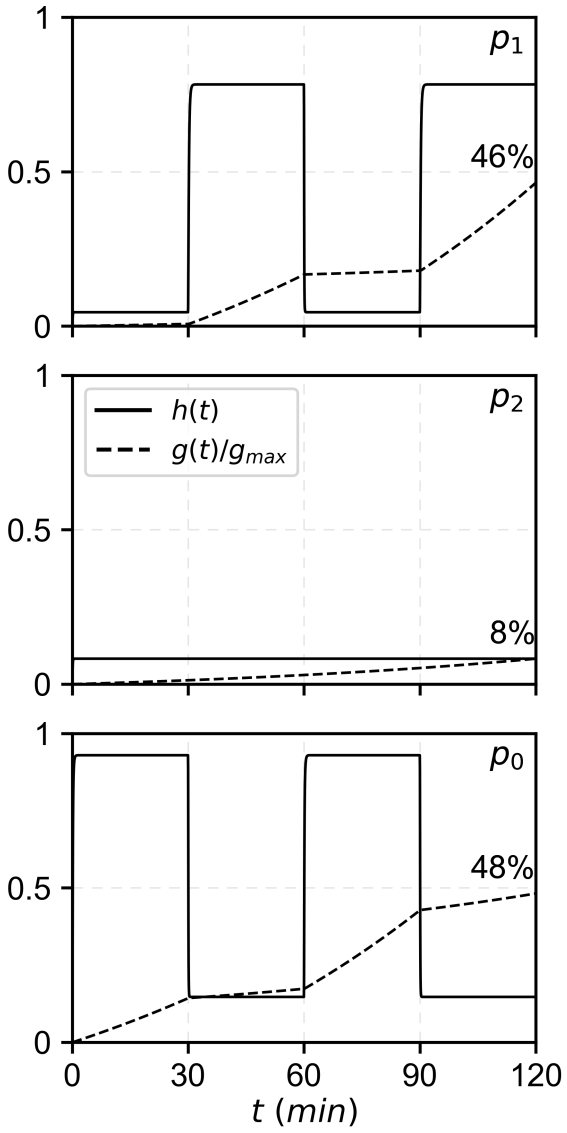


Figure 7.7: *Response of the normalized gene expression rate, $h(t)$, and normalized total gene expression, $g(t)/g_{max}$, in vertically arranged voxels to alternating illumination. Each graph corresponds to the respective point of interest p_0, p_1 and p_2, for the vertical arrangement with positions and distances as shown in Figure 7.1. Peak incident green light intensity was set to 18.6 W/m^2 and the average incident red light intensity was set to 133.4 W/m^2, which results in $\eta^{ss}(p_2) = \eta_{min}$. The percentage of maximum possible total gene expression density after two hours is shown for each point of interest.*

Experiment's Illumination Procedure

During the first hour the voxel plane was deactivated with red light and the green laser was warmed up. As with horizontal arrangement, the experiment was split into four 30 minute intervals during each a single voxel was illuminated. The illumination procedure is shown in Figure 7.8 for the three points of interest.

The red light intensity used in the experiment for a given green light intensity was lower than what is predicted by the model to achieve $\eta_{min} - p_2$. This was done in an attempt to have a better contrast between the induced gene expression and the background. Figure 7.9 shows the theoretical prediction of normalized integrated gene expression with parameters required to achieve $\eta_{min} - p_2$ and the theoretical prediction as a result of parameters used during the experiment.

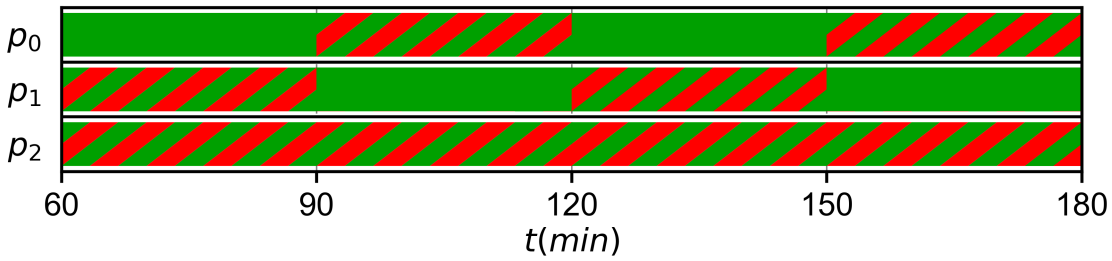


Figure 7.8: *Schematic of the alternating illumination procedure for an experiment with two voxels in vertical arrangement. Each row shows the presence of the respective green or red light over time for all three points of interest. The peak incident green light intensity was* 18.6 W/m^2 *and the average incident red light intensity was* 42.4 W/m^2.

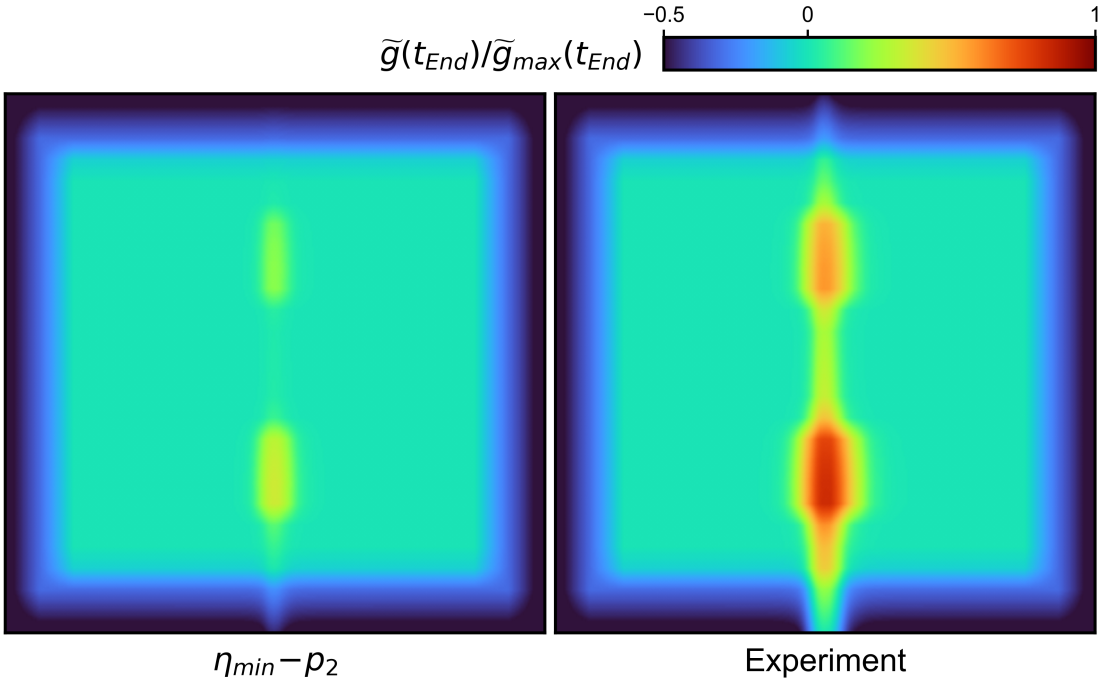


Figure 7.9: *Simulations of normalized integrated total gene expression,* $\tilde{g}(t_{End})/\tilde{g}_{max}(t_{End})$*, in two voxels in vertical arrangement subjected to alternating illumination procedure as shown in Figure 7.8. Left, simulation of normalized* $\tilde{g}(t_{End})$ *for incident red light intensity* $I_{650} = 133.4\ W/m^2$ *where* η_{min} *at* p_2 *is achieved. Right, simulation of normalized* $\tilde{g}(t_{End})$ *for incident red light intensity used in the experiment* $I_{650} = 42.4\ W/m^2$*. In both simulations the peak incident green intensity was set to* $18.6\ W/m^2$*. Both simulations are normalized to maximum possible* $\tilde{g}(t_{End})$ *within a thickness of* $1\ mm$*. The halo effect in the simulations was added qualitatively as a visual aid.*

Experiment Results

Figure 7.10 shows the normalized contrasted fluorescence of the experiment, $C_F/r_{a'/b'}$. The plotted data was calculated in the same manner, as the data from the experiment of two voxels in horizontal arrangement – the fluorescence was contrasted to the background measured in the red only regions and then further normalized by $r_{a'/b'}$. The measurement agrees with the theoretical prediction in Figure 7.9 and stronger gene expression can be seen at p_0 when compared to p_1. The overall gene expression is stronger than predicted; however, well within the margin of error. Gene expression is noticeably higher at p_0 when compared to p_1. This is most likely due to τ as p_1 will have less time to express genes. A small contribution also comes from the smaller attenuation experienced by green light at p_0.

Table 7.2 shows a comparison between the predicted normalized gene expression values and measured values. The comparison between gene expression values of the two simulations demonstrates the trade-off between the distinguishability, indicated by p_1/p_2 in Table 7.2; the magnitude of gene expression at p_0 and p_1; and the homogeneity, indicated by p_0/p_1 in Table 7.2. The measured values are in relative agreement to the predicted ones while slightly higher. However, due to the estimated error it is unclear whether there is any behavioural discrepancy.

Table 7.2: *Normalized integrated total gene expression determined from two simulations – $\eta_{min} - p_2$ and Experiment – and from fluorescence image of the experiment following the alternating illumination procedure shown in Figure 7.8 for two voxels in vertical arrangement. p_0/p_1 and p_1/p_2 refer to ratios between normalized integrated total gene expressions at the respective points. The majority contributor to the error estimates of the measured values is the background gene expression.*

	$\tilde{g}(t_{End})/\tilde{g}_{max}(t_{End})$		
	$\eta_{min} - p_2$	Experiment	$\bar{C}_F/r_{a'/b'}$
p_0	0.34	0.80	0.9 ± 0.6
p_1	0.20	0.56	0.7 ± 0.5
p_2	0.03	0.29	0.3 ± 0.3
p_0/p_1	1.72	1.44	1.4 ± 0.7
p_1/p_2	7.73	1.91	2.3 ± 2.4

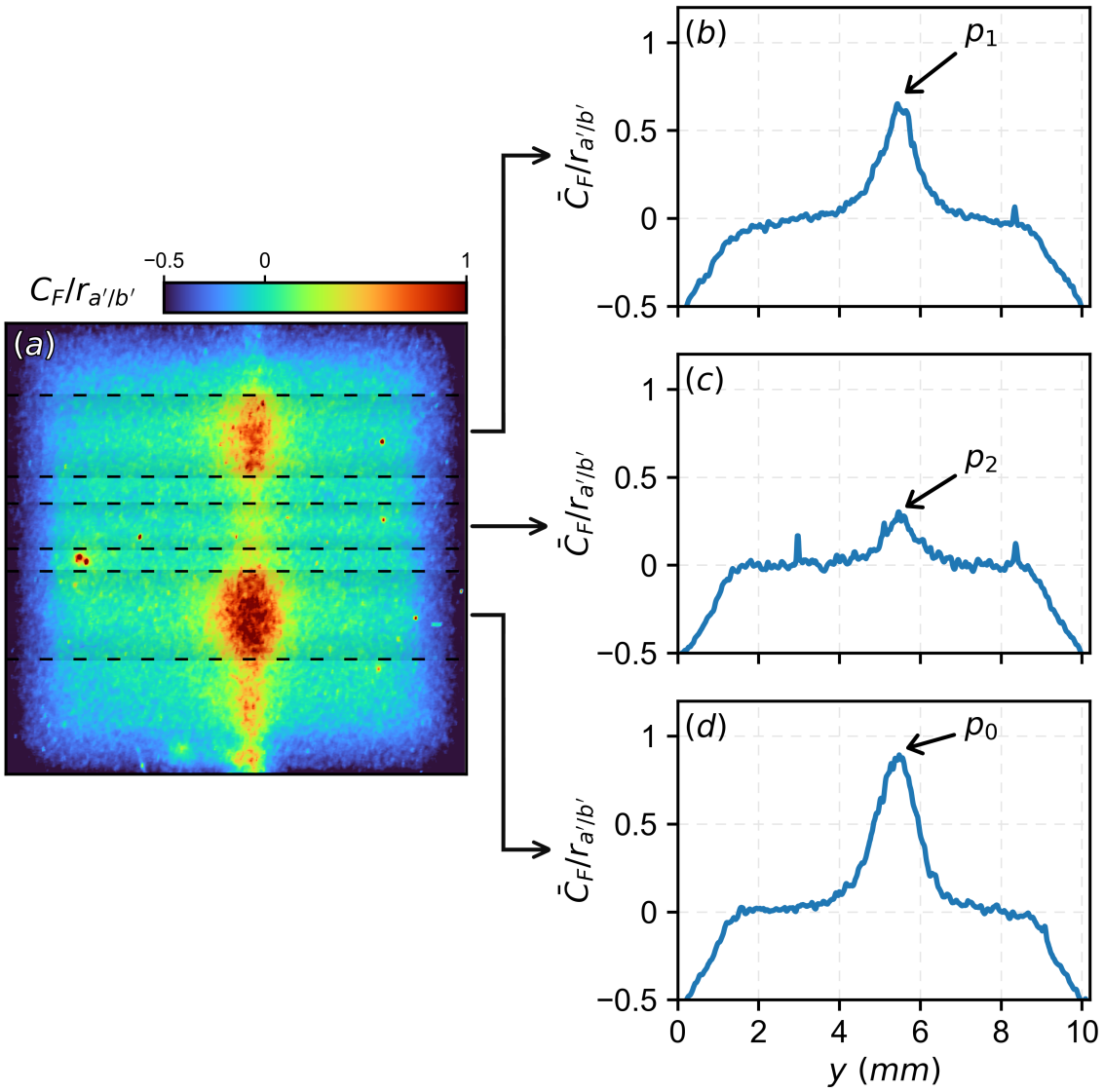


Figure 7.10: *Measurement of an experiment of two voxels in vertical arrangement subjected to alternating illumination procedure shown in Figure 7.8. (a) Summed image of normalized fluorescence with three bands of interest indicated by the dashed lines referring to three points of interest. Additional light shading was added to the dashed lines to better highlight the bands. (b), (c) and (d) Normalized fluorescence averaged in the bands of interest around points p_1, p_2 and p_0 respectively. The value of $r_{a'/b'}$ used was 3.5 .*

7.2.3 Diagonal Arrangement

Voxels in diagonal arrangement are coupled through red light illumination. When the active voxel is illuminated the other is directly exposed to red light illumination. When considering only the voxels, at p_0 and p_1, there exists an optimal green light intensity that maximizes total gene expression provided that the rate of deactivation is comparable to or smaller than the rate of activation. However, in diagonal arrangement p_2 and p_3 are either in darkness or experience green and red light illumination at the same time. Therefore, in the case where deactivation and activation are comparable, η at these points is around 50% throughout the illumination procedure. As this value of η is larger than η_{max}, gene expression rate at these points is effectively at a maximum for the entire duration of illumination. However, this is not the case for the voxels at p_0 and p_1 where photoreceptors are constantly activated and deactivated. Interestingly such a configuration could result in an inverted distribution of total gene expression density with small contrast, where voxels would be better defined at p_2 and p_3 instead. This is not readily achievable in practice due to significant η_R and attenuation along with background variations. When deactivation rate is greater than the activation rate it is better to illuminate with intensities of large magnitudes in order to reach the maximum gene expression rate as quickly as possible.

Model

In diagonal arrangement the steady-state fractions of active-state photoreceptors, η^{ss}, during direct illumination are approximately:

$$\eta^{ss}(p_3) \approx \frac{1}{1+\dfrac{A_{2,3}k_2}{A_{1,3}k_1}}, \qquad \eta^{ss}(p_0) \approx \frac{1}{1+\eta_R\dfrac{A_{2,0}k_2}{A_{1,0}k_1}},$$

$$\eta^{ss}(p_1) \approx \frac{1}{1+\eta_R\dfrac{A_{2,1}k_2}{A_{1,1}k_1}}, \qquad \eta^{ss}(p_2) \approx \frac{1}{1+\dfrac{A_{2,2}k_2}{A_{1,2}k_1}}, \tag{7.11}$$

$$p_i = (x_i,\, y_i)_D \text{ for } i \in \{0,1,2,3\},$$

where $A_{1,i}$ and $A_{1,i}$ are attenuation factors for green and red light respectively at each point p_i. The incident light intensities, as with previous voxel arrangements, are adjusted so that attenuation factors reflect the distances between the points of interest. In this case incident light is adjusted so that is appears as if there is no

attenuation at p_1:

$$\begin{aligned} A_{1,1}k_1 \rightarrow k_1 \Rightarrow A_{1,3} &= e^{-\mu_G(x_3 - x_1)} = A_1\,, & A_{1,0} &= e^{-\mu_G(x_0 - x_2)} = A_1\,, \\ A_{1,1} &= 1\,, & A_{1,2} &= 1\,, \\ A_{2,1}k_2 \rightarrow k_2 \Rightarrow A_{2,3} &= 1\,, & A_{2,0} &= e^{-\mu_R(y_0 - y_3)} = A_2\,, \\ A_{2,1} &= 1\,, & A_{2,2} &= e^{-\mu_R(y_2 - y_1)} = A_2\,, \end{aligned} \tag{7.12}$$

where A_1 and A_2 are attenuation factors of green and red light respectively corresponding to the change of depth at p_0.

In line with previous two arrangements, η^{ss} of all four points is uniquely defined by the ratio between the red and green light intensity. Due to the symmetric depth in X and Y direction, $\eta^{ss}(p_0)/\eta^{ss}(p_1)$ depends on the green and red light attenuation. Should the attenuations be comparable the ratio would be almost equal to one and only very weakly depend on the ratio of intensities. On the other hand, p_2 in relative terms experiences high green and low red light intensity due to geometry. Coupled with the fact that it never experiences direct red light only illumination it is expected to generate the highest unwanted gene expression. Setting $\eta^{ss}(p_2) = \eta_{min}$ to determine the intensities ratio will result in a $\eta_{min} - p_2$ gene expression distribution. As with other voxel arrangements, this achieves the efficient maximum contrast at the expense of magnitude of gene expression. The required intensities ratio is then:

$$\eta^{ss}(p_2) = \frac{1}{1 + A_2\dfrac{k_2}{k_1}} = \eta_{min} \quad \Rightarrow \quad \frac{I_{650}}{I_{515}} = \frac{\hat{k}_1}{\hat{k}_2} \cdot \frac{1}{A_2}\frac{1 - \eta_{min}}{\eta_{min}}\,. \tag{7.13}$$

Expressing $\eta^{ss}(p_0)/\eta^{ss}(p_1)$ in terms of η_{min} yields:

$$\frac{\eta^{ss}(p_0)}{\eta^{ss}(p_1)} = 1 + \frac{A_1 - A_2}{A_2} \cdot \frac{1}{1 + \dfrac{A_1}{\eta_R} \cdot \dfrac{\eta_{min}}{1 - \eta_{min}}}\,, \tag{7.14}$$

which shows that when A_1 and A_2 are the same the distribution of gene expression between the voxels is homogeneous regardless of other factors.

Figure 7.11 shows the normalized gene expression rate, h, and the normalized total gene expression, g/g_{max}, over time for each point of interest. The intensities ratio was determined by (7.13). It can be seen that even though gene expression rate is not that much greater at p_1 during illumination, it still results in greater total gene expression due to higher cell population. Similarly to voxels in horizontal arrangement, the end normalized total gene expression does not reach 50% for the given $\eta = \eta_{min}$.

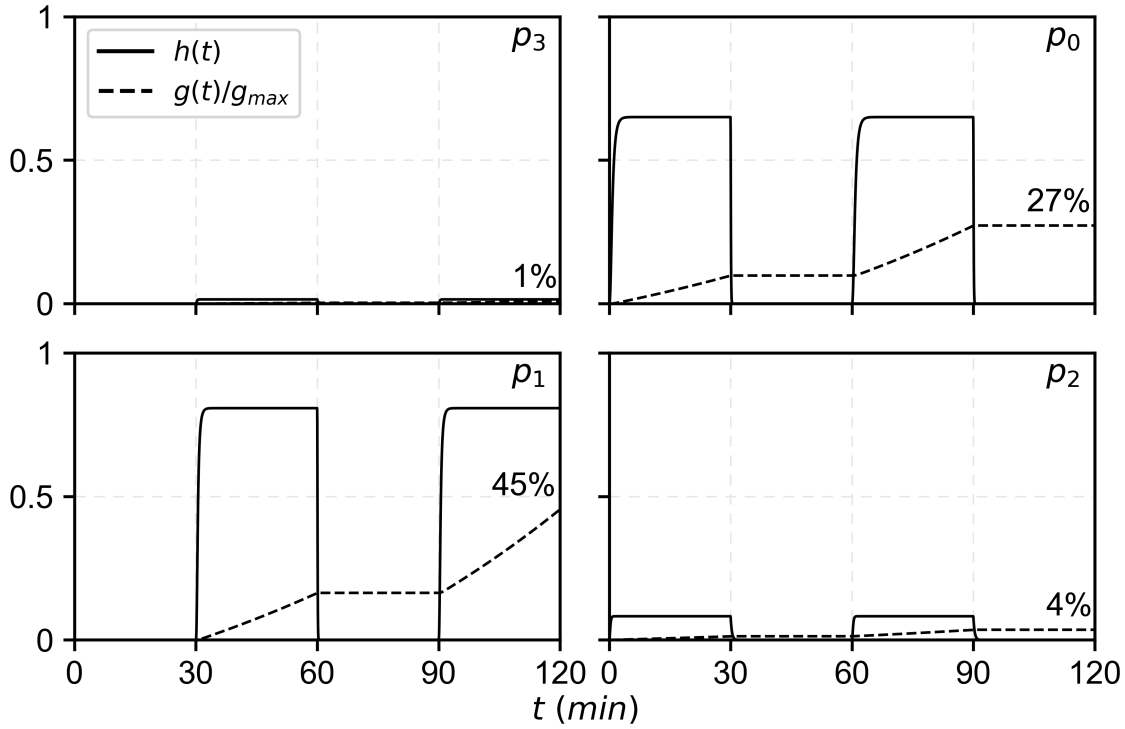


Figure 7.11: *Response of the normalized gene expression rate, $h(t)$, and normalized total gene expression, $g(t)/g_{max}$, in diagonally arranged voxels to alternating illumination. Each graph corresponds to the respective point of interest p_0, p_1, p_2 and p_3, for the diagonal arrangement with positions and distances as shown in Figure 7.1. Peak incident green light intensity was set to 5.8 W/m^2 and the average incident red light intensity was set to 58.0W/m^2, which results in $\eta^{ss}(p_2) = \eta_{min}$. The percentage of maximum possible gene expression density after two hours is shown for each point of interest.*

Experiment's Illumination Procedure

As with the two previous illumination procedures, during the first hour the voxel plane was deactivated by red light, the green laser was warmed up and the following two hours were split into four intervals of 30 minutes. This illumination procedure is shown in Figure 7.12.

Figure 7.13 shows the theoretical prediction of normalized integrated total gene expression for an intensity ratio required to achieve $\eta_{min} - p_2$ and an intensity ratio used during the experiment. For the intensities ratio, which achieves $\eta_{min} - p_2$, the predicted integrated gene expression in voxels is relatively low as is the case with previous voxel arrangements. Due to background gene expression present during the experiment, to achieve better contrast, red light intensity used in the experiment was a factor of 7 lower than the one required to achieve $\eta_{min} - p_2$ for the given green light intensity.

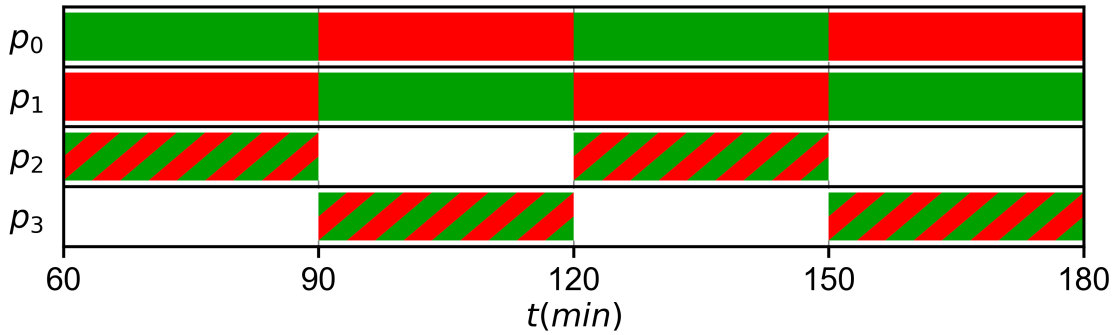


Figure 7.12: *Schematic of the alternating illumination procedure for an experiment with two voxels in diagonal arrangement. Each row shows the presence of the respective green or red light over time for all four points of interest. The incident peak green light intensity was* $5.8\ W/m^2$ *and the average incident red light intensity was* $8.3\ W/m^2$.

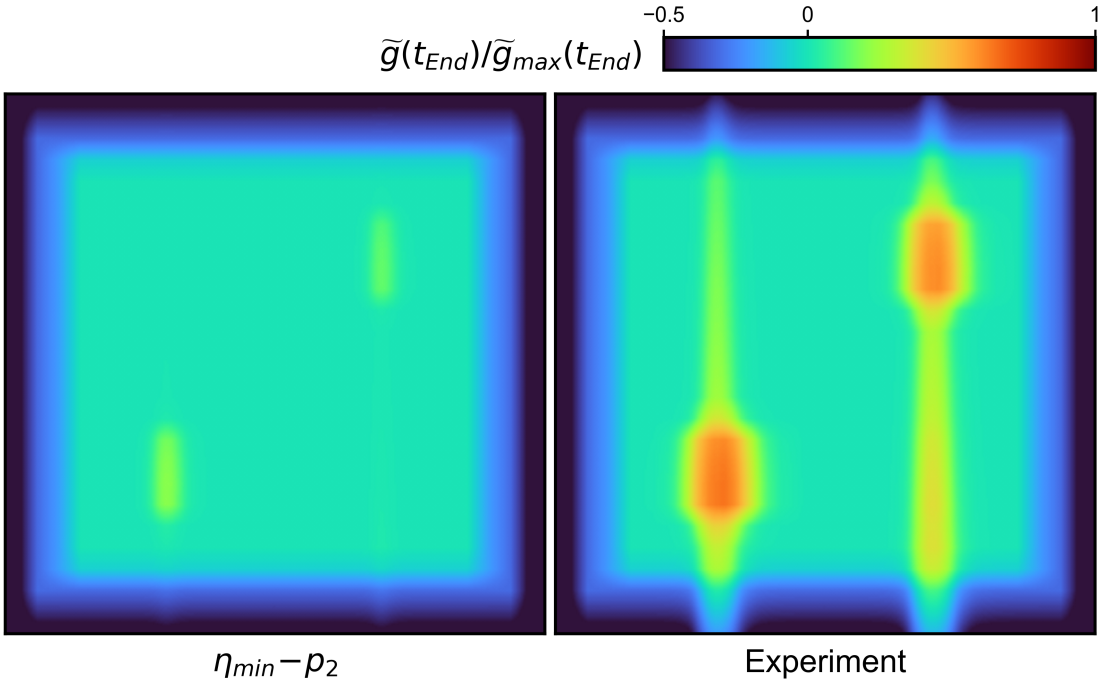


Figure 7.13: *Simulations of normalized integrated total gene expression, $\tilde{g}(t_{End})/\tilde{g}_{max}(t_{End})$, in two voxels in diagonal arrangement subjected to alternating illumination procedure as shown in Figure 7.12. Left, simulation of normalized $\tilde{g}(t_{End})$ for incident red light intensity $I_{650} = 58.0\ W/m^2$ where η_{min} at p_2 is achieved. Right, simulation of normalized $\tilde{g}(t_{End})$ for incident red light intensity used in the experiment $I_{650} = 8.3\ W/m^2$. In both simulations the peak incident green intensity was set to $5.8\ W/m^2$. Both simulations are normalized to maximum possible $\tilde{g}(t_{End})$ within a thickness of $1\ mm$. The halo effect in the simulations was added qualitatively as a visual aid.*

Experiment's Results

Figure 7.14 shows the normalized contrasted fluorescence of the experiment, $C_F/r_{a'/b'}$. As with previous two arrangements, the plotted fluorescence is contrasted to the background measured in the red only regions, which is then further normalized by $r_{a'/b'}$. The measurement agrees with the theoretical prediction shown in Figure 7.13 in that the ratio of total gene expression between the voxels is nearly the same and that the highest active background is at p_2. The effect from the delay in gene expression works in favour of homogenizing the distribution between the voxels, as the behaviour predicted by Figure 7.11 implies a much greater gene expression at p_1. However, absolute total gene expression in the experiment was noticeably greater at all points of interest. This is most likely due to either the background being measured too small or it actually being smaller along with potentially greater value of a resulting in a larger maximum contrast, $r_{a'/b'}$. Table 7.3 shows a comparison between the predicted normalized gene expression values and measured values.

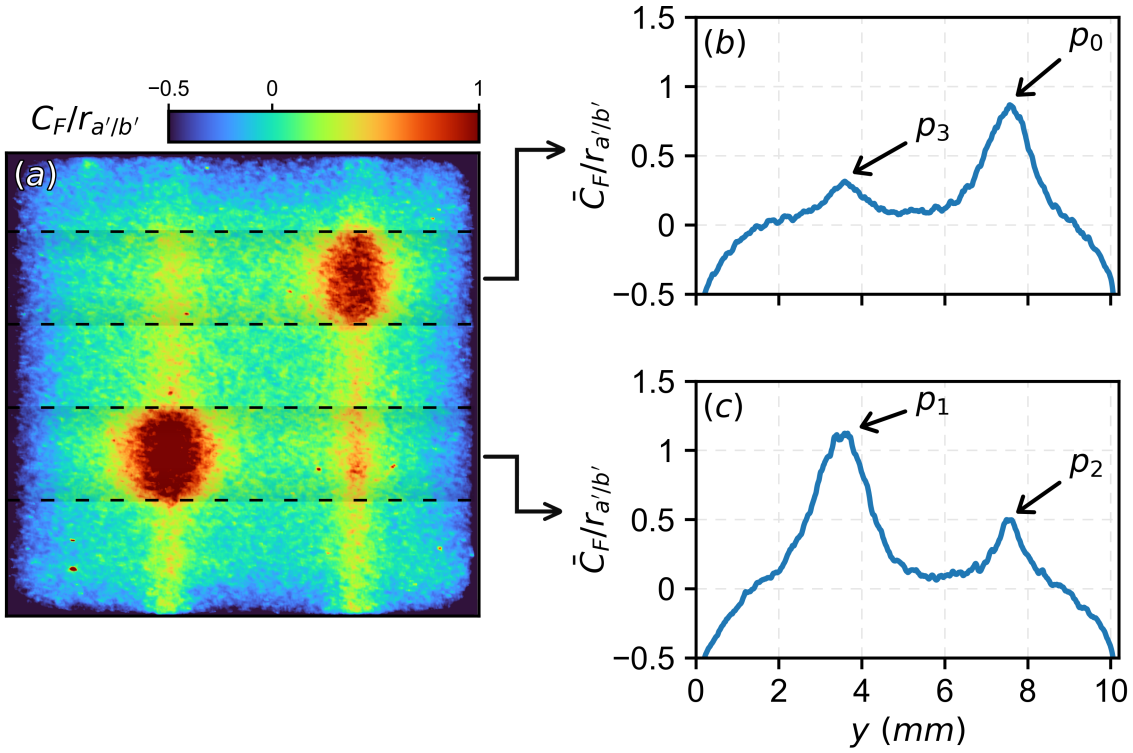


Figure 7.14: *Measurement of an experiment of two voxels in diagonal arrangement subjected to alternating illumination procedure shown in Figure 7.12.* (*a*) *Summed image of normalized fluorescence with two bands of interest indicated by the dashed lines. Additional light shading was added to the dashed lines to better highlight the bands.* (*b*) *Normalized fluorescence averaged in the band of interest around points* p_3 *and* p_0. (*c*) *Normalized fluorescence averaged in the band of interest around points* p_1 *and* p_2. *The value of* $r_{a'/b'}$ *used was* 3.5 .

Table 7.3: *Normalized integrated total gene expression at four points determined from two simulations, $\eta_{min} - p_2$ and Experiment, and from the summed fluorescence image of the experiment following the alternating illumination procedure shown in Figure 7.12 for two voxels in diagonal arrangement. p_0/p_1 and p_0/p_2 refer to ratios between the normalized integrated total gene expressions at the respective points. The majority contributor to the error estimates of the measured values is the background gene expression.*

	$\tilde{g}(t_{End})/\tilde{g}_{max}(t_{End})$		
	$\eta_{min} - p_2$	Experiment	$\bar{C}_F/r_{a'/b'}$
p_0	0.14	0.58	0.9 ± 0.3
p_1	0.20	0.62	1.1 ± 0.4
p_2	0.01	0.37	0.5 ± 0.2
p_3	0.002	0.17	0.3 ± 0.1
p_0/p_1	0.70	0.94	0.8 ± 0.1
p_0/p_2	10.9	1.56	1.7 ± 0.4

7.2.4 Discussion

The theoretical prediction and measurements of two voxels subjected to alternating illumination for three different arrangements were generally in agreement further indicating the validity of the model and the choice of increased forward and reverse conversion rates, $\hat{k}_1'$ and $\hat{k}_2'$. However, it seems that τ is not sufficiently small to be completely neglected in determining the illumination procedures and as such affects the system's behaviour to a noticeable degree. Regardless these discrepancies do not appear sufficient to impact the general goal of localized gene expression in two voxels.

All in all, alternating illumination appears to be a viable approach for localized gene expression in two voxels. However, employing this procedure for a more complex geometry than two voxels is not optimal. The requirement for constant red and green light intensities is unnecessary. Green and red light illumination do not need to occur at the same time and illumination does not need to be present for the entire duration of gene expression at a particular voxel.

7.3 Illumination for Concurrent Gene Expression

Under alternating illumination the voxel not actively illuminated is generally deactivated by red light and does not exhibit gene expression during that time. The aim of illumination for concurrent gene expression is to achieve the maximum possible but equal fraction of active-state photoreceptors, η, in both voxels during the same interval of illumination while elsewhere η is kept at or below η_{min}. This distribution of η results in gene expression that is the same for both voxels during the entire duration of illumination and gene expression elsewhere is at an effective minimum.

7.3.1 Horizontal Arrangement

For voxels in horizontal arrangement the simplest illumination that achieves concurrent gene expression consists of three steps. During the first two steps each voxel is individually illuminated by green light followed by the last step where both voxels are defined using red light, which deactivates active-state photoreceptors in the suppressed regions. Red light is not necessary during the first two steps and only complicates the relationship between the two voxels. As such this illumination procedure is equivalent to the deactivation procedure investigated in Chapter 6.1.2 with an added step of second voxel green light illumination. Alternatively, the two voxels could be individually activated by green light and deactivated by red light illumination thus requiring four illumination steps. This approach is expected to perform worse due to red light leakage, which would in this case affect both voxels twice.

Model

Illumination for concurrent gene expression no longer relies on the steady state; however, the green and red light intensities are kept constant during each illumination step regardless. In this case the solution for η after each step is given by (2.4). The time evolution of the system can thus also be expressed as a series of solutions for which the initial state is the end state of the solution of the previous step. Given the conditions for the concurrent gene expression, only three points need to be considered p_0, p_1 and p_2. In horizontal arrangement p_3 can be excluded, as p_2 experiences the same green light intensity but lower red light intensity and is therefore expected to have the highest unwanted gene expression. The solution for

$\eta(t)$ at the three points, where p_0 is illuminated first, is as follows:

$$\eta(t_{end}, p_0) = \frac{1}{1 + \frac{k_{growth}}{A_1 k_1}} \left(1 - e^{-(A_1 k_1 + k_{growth})\Delta t_1}\right) e^{-k_{growth}\Delta t_2} e^{-(\eta_R A_2 k_2 + k_{growth})\Delta t_3},$$

$$\eta(t_{end}, p_1) = \frac{1}{1 + \frac{k_{growth}}{A_1 k_1}} \left(1 - e^{-(A_1 k_1 + k_{growth})\Delta t_2}\right) e^{-(\eta_R k_2 + k_{growth})\Delta t_3},$$

$$\eta(t_{end}, p_2) = \frac{1}{1 + \frac{k_{growth}}{k_1}} \left(1 - e^{-(k_1 + k_{growth})\Delta t_1}\right) e^{-k_{growth}\Delta t_2} e^{-(A_2 k_2 + k_{growth})\Delta t_3},$$

$$p_i = (x_i, y_i)_H \text{ for } i \in \{0, 1, 2\}, \tag{7.15}$$

where $t_{end} = \Delta t_1 + \Delta t_2 + \Delta t_3$ and Δt_i are the durations of each individual illumination step. A_1 and A_2 are the attenuation factors as defined by (7.2). For set light intensities the Δt_i are the three unknowns and given the two conditions:

$$\eta(t_{end}, p_0) = \eta(t_{end}, p_1), \qquad \eta(t_{end}, p_2) = \eta_{min}, \tag{7.16}$$

one of the Δt_i can be freely chosen. $\eta(t_{end}, p_0)$ is expected to be larger than $\eta(t_{end}, p_1)$ due to weaker red light illumination. Therefore, Δt_2 was chosen such so that $\eta(\Delta t_1 + \Delta t_2, p_1) = \eta_{high}$. Δt_2 can then be expressed as:

$$\Delta t_2 = -\frac{1}{A_1 k_1 + k_{growth}} \ln\left(1 - \eta_{high}\right). \tag{7.17}$$

Ideally $\eta_{high} = 1$; however, this would require an infinite amount of time. Instead, η_{high} can be chosen as close to one as possible limited only by the time constraints given by the duration of the experiment.

System of equations (7.16), when $A_1 \neq 1$, can be solved only numerically. However, the system can be solved analytically by approximating $\eta(\Delta t_1, p_2) = 1$. This can be justified by observing that $\eta(\Delta t_1, p_2) > \eta(\Delta t_1, p_0)$ due to $A_1 < 1$. From the condition that η_{high} is large, $\eta(\Delta t_1, p_0)$ has to be large as well in order to satisfy the condition for equal gene expression at p_0 and p_1. The error incurred from this approximation results in longer red light illumination, which manifests as $\eta(t_{end}, p_2)$ being less than the assigned value of η_{min} and lower values of $\eta(t_{end}, p_0)$ and $\eta(t_{end}, p_1)$. For large enough intensities a further approximation can be made

by neglecting k_{growth}, which simplifies the solutions for illumination durations:

$$\begin{aligned}
\Delta t_1 &\approx -\frac{1}{A_1 k_1} \ln\left(1 - \eta_{min}^{\frac{1-A_2}{A_2}\eta_R}\right), \\
\Delta t_2 &\approx -\frac{1}{A_1 k_1} \ln\left(1 - \eta_{high}\right), \\
\Delta t_3 &\approx -\frac{1}{A_2 k_2} \ln\left(\eta_{min}\right).
\end{aligned} \tag{7.18}$$

Substituting the illumination durations into (7.15) yields:

$$\begin{aligned}
\eta(t_{end}, p_0) &\approx \eta(t_{end}, p_0) \approx \eta_{min}^{\frac{\eta_R}{A_2}}, \\
\eta(t_{end}, p_2) &\approx \eta_{min}.
\end{aligned} \tag{7.19}$$

The end fraction of active-state photoreceptors in both voxels is the same as with the deactivation procedure for a single voxel (Equation (6.8)), with the main difference being the red light attenuation factor, which depends on the distance between the voxels. The higher the attenuation or the farther apart the voxels the lower the end fraction of active state photoreceptors; however, the fraction is still equal between the voxels.

Due to of cell growth, single illumination is not sufficient to maintain a high rate of gene expression for the entire duration of the experiment. Therefore the illumination procedure for concurrent gene expression has to be repeated. Equations (7.15) only hold when the the initial fraction of active-state photoreceptors is zero, which is no longer the case after repeated illuminations. For this illumination procedure this results in higher $\eta(t_{end}, p_0)$. Due to $\eta(t_{end}, p_0) > \eta_{max}$ for $\eta(t_{end}, p_2) = \eta_{min}$ to begin with, the increase does not affect the rate of gene expression too much.

Figure 7.15 shows the normalized gene expression rate, h, and the normalized total gene expression, g/g_{max}, over time for each point of interest. For given intensities the illumination durations were determined by (7.18). It can be seen that gene expression occurs at about the same rate at both voxels with relatively large contrast. As expected, total gene expression is slightly greater at p_0 due to repeated illumination.

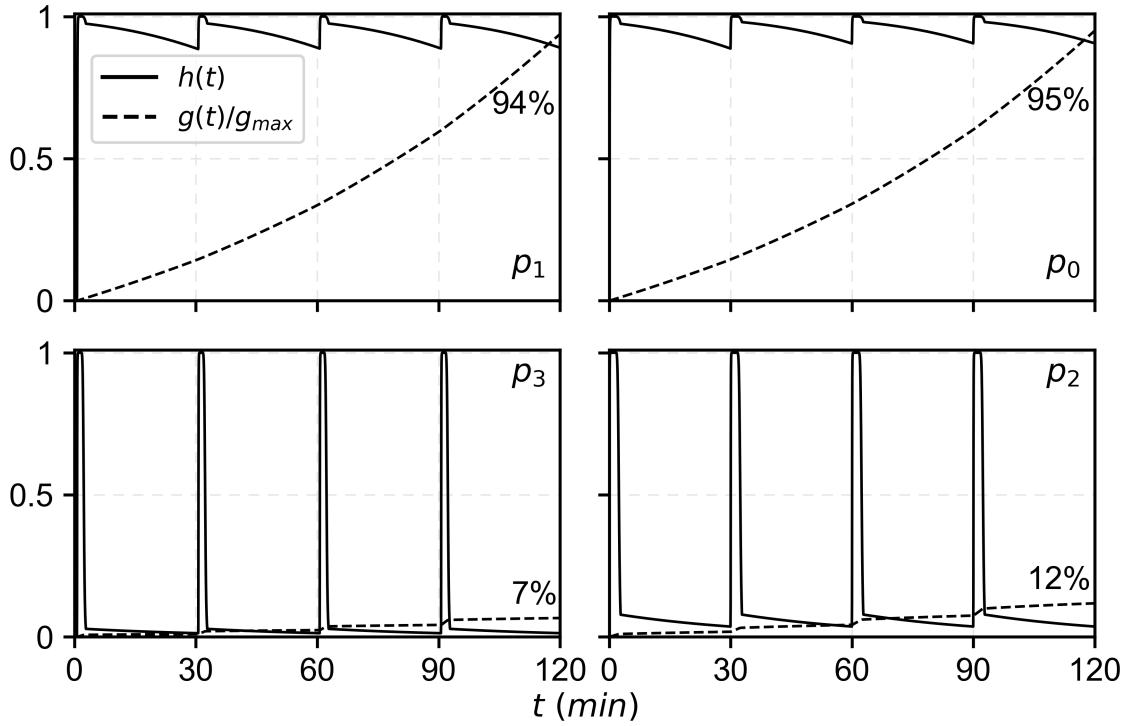


Figure 7.15: *Response of normalized gene expression rate, $h(t)$, and normalized total gene expression, $g(t)/g_{max}$, in horizontally arranged voxels to illumination for concurrent gene expression repeated four times at 30 minute intervals. Each graph corresponds to the respective point of interest p_0, p_1, p_2 and p_3, for the horizontal arrangement with positions and distances as shown in Figure 7.1. Peak incident green light intensity was set to 34.8 W/m^2 and the average incident red light intensity was set to 18.4W/m^2. The illumination durations for these intensities and $\eta_{high} = 0.992$ are $\Delta t_1 = 36$ s, $\Delta t_2 = 65$ s and $\Delta t_3 = 67$ s. The percentage of maximum possible gene expression density after two hours is shown for each point of interest.*

Experiment's Illumination Procedure

The illumination procedure for concurrent gene expression in two voxels in horizontal arrangement is shown in Figure 7.16 for the four points of interest. As with previous experiments, the first hour is used for deactivation of the voxel plane with red light and warm up of the green laser. The concurrent gene expression illumination procedure is split into four 30 minute intervals to replenish η, which during each interval decays by $\approx 25\%$ due to cell growth.

Figure 7.17 shows the theoretical prediction of normalized integrated total gene expression for intensities and illumination durations that satisfy (7.16) and for intensities and illumination durations used during the experiment (Figure 7.16). The peak green light intensity was doubled for the experiment when compared to the values that satisfy (7.16) and the duration was increased. This was done in an attempt to ensure a measurable response. However, according to Figure 7.17, the increase in red light duration during the experiment is too much and should result in weaker gene expression in the voxels.

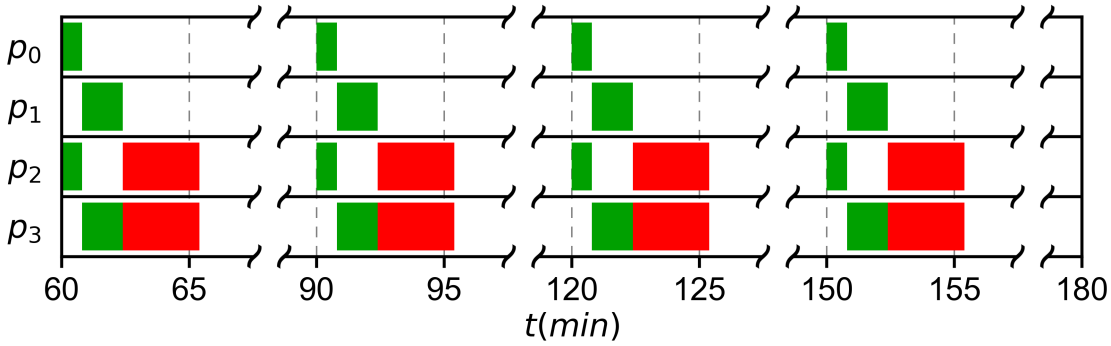


Figure 7.16: *Schematic of the concurrent gene expression illumination procedure for an experiment with two voxels in horizontal arrangement. Each row shows the presence of the respective green or red light over time for all four points of interest. The peak incident green light intensity was* 69.7 W/m^2 *and the average incident red light intensity was* 18.4 W/m^2*. The durations of each illumination step* Δt_1*,* Δt_2 *and* Δt_3 *were* 48 *s,* 96 *s and* 180 *s respectively.*

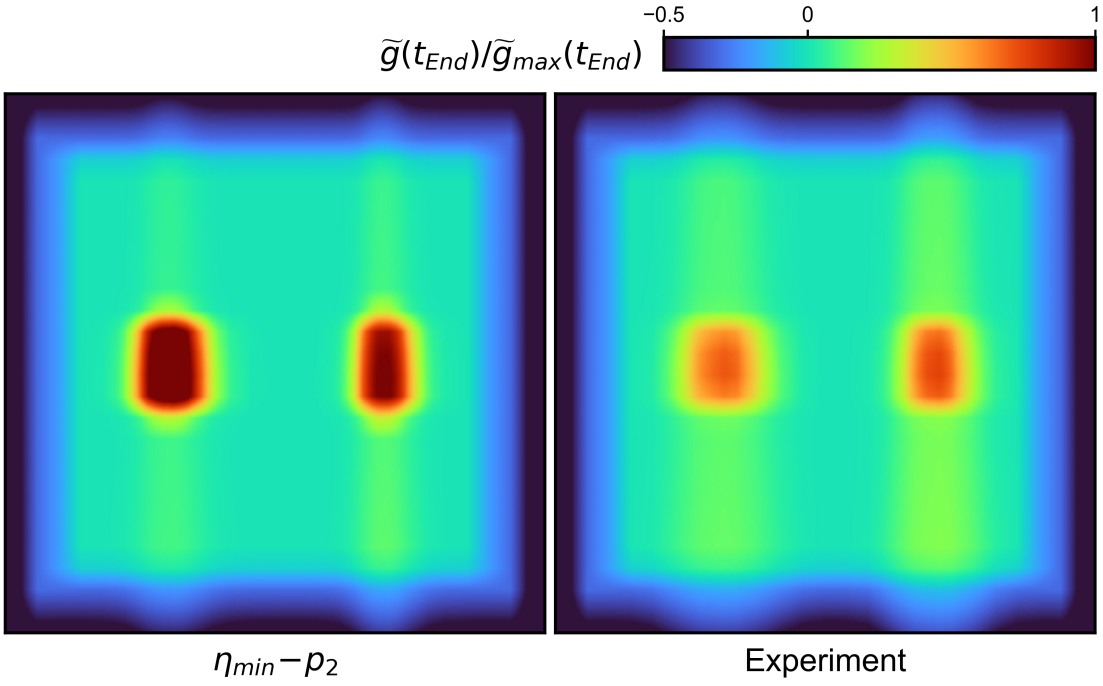


Figure 7.17: *Simulations of normalized integrated total gene expression,* $\tilde{g}(t_{End})/\tilde{g}_{max}(t_{End})$*, in two voxels in horizontal arrangement subjected to concurrent gene expression illumination procedure as shown in Figure 7.16. Left, simulation of normalized* $\tilde{g}(t_{End})$ *for incident peak green light intensity* I_{515} = 34.8 W/m^2 *and average red light intensity* I_{650} = 18.4 W/m^2*. The durations of each illumination step* Δt_1*,* Δt_2 *and* Δt_3 *are* 36 *s,* 65 *s and* 67 *s respectively. These values satisfy* (7.16)*. Right, simulation of normalized* $\tilde{g}(t_{End})$ *of the experiment. The intensities and illumination durations are the same as shown in Figure 7.16. Both simulations are normalized to maximum possible* $\tilde{g}(t_{End})$ *within a thickness of* 1 *mm. The halo effect in the simulations was added qualitatively as a visual aid.*

Experiment's Results

Figure 7.18 shows the normalized contrasted fluorescence of the experiment, $C_F/r_{a'/b'}$. The measurement of the experiment exhibits noticeably greater integrated total gene expression at p_1 instead of at p_0. According to Figure 7.15, this should not be the case. However, simulation of $\eta_{min} - p_2$ does exhibit this behaviour. The distribution of η given by (7.19) for the points of interest is only valid for red and green intensities at those exact points. On the other hand, integrated total gene expression depends on the distribution of η in the entire vertical stack at a given point. Therefore, the reason for the discrepancy in the simulation of $\eta_{min} - p_2$ lies with the larger $\eta(\Delta t_1 + \Delta t_2, p_1)$, the green beam intensity profile and the nonlinearity of (2.4). The distribution of η around each point does not linearly depend on the amount of radiant exposure, which is why when η is near 100% any change in radiant exposure will have a substantially lower effect when compared to η that is near zero. The change of η around each point is dictated by the green beam intensity profile and because $\eta(\Delta t_1 + \Delta t_2, p_1)$ is appreciably larger than $\eta(\Delta t_1, p_0)$ and very close to 100%, the distribution of η around p_1 drops slower with distance when compared p_0. This saturating effect thus results in a larger integrated total gene expression in p_1.

Figure 7.18 also shows that gene expression in the experiment was noticeably wider around p_1 when compared to the simulation in Figure 7.17. This can most likely be attributed to scattering of the green light which is not included in the simulation. At these relatively high radiant exposures the contribution from scattering becomes more apparent as gene expression near the center of the beam is more saturated. Effectively, this significantly widens the beam and would explain why the simulation of the experiment does not indicate higher gene expression at p_1.

The uneven background gene expression is another effect that possibly contributes to a wider appearance of gene expression at p_1 and can also account for the unusually low gene expression at p_2 and p_3. It appears as that during this experiment the halo effect is quite uneven and possibly extends well beyond 1 mm away from the cuvette wall. This, coupled with a very wide influence of green light illumination does not leave a lot of area from which a good measurement of the local background can be obtained.

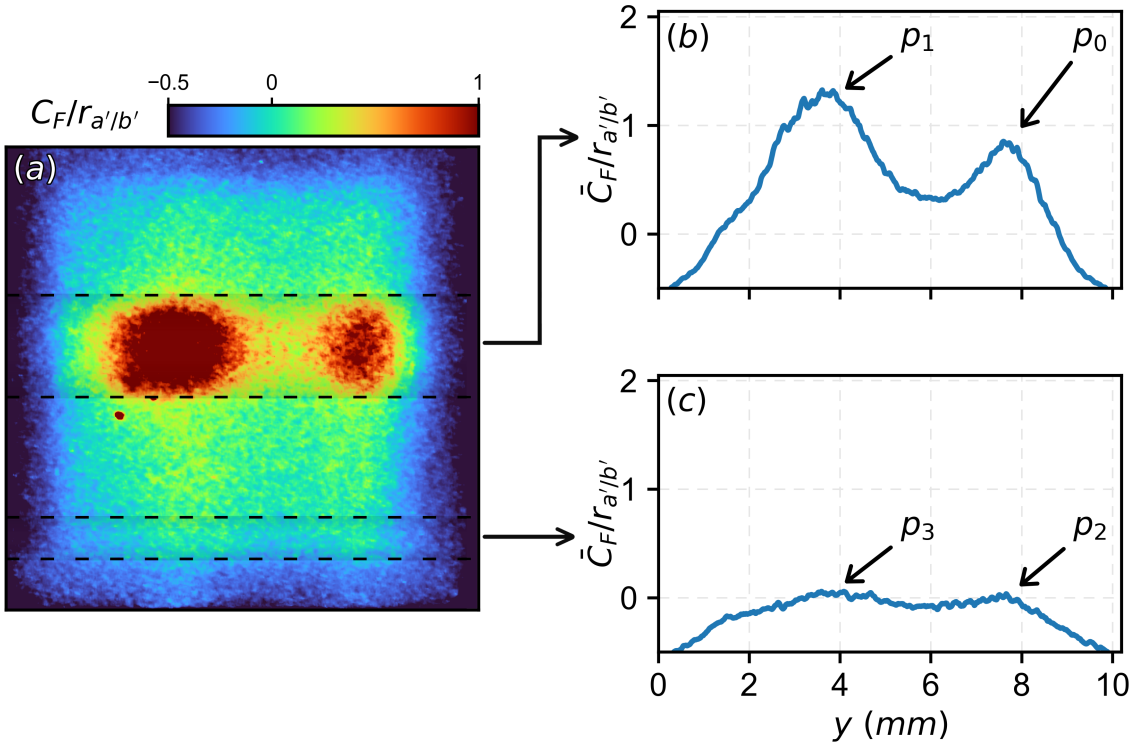


Figure 7.18: *Measurement of an experiment of two voxels in horizontal arrangement subjected to concurrent gene expression illumination procedure shown in Figure 7.16.* (*a*) *Summed image of normalized fluorescence with two bands of interest indicated by the dashed lines. Additional light shading was added to the dashed lines to better highlight the bands.* (*b*) *Normalized fluorescence averaged in the band of interest around points* p_1 *and* p_0. (*c*) *Normalized fluorescence averaged in the band of interest around points* p_3 *and* p_2. *The value of* $r_{a'/b'}$ *used was* 3.5 .

The discrepancy between the simulation and the measurement is quite clear in values shown in Table 7.4. The unclear value of the background gene expression significantly affects the determination of all values, especially those at p_2 and p_3. The value of the contrast, indicated by p_0/p_3 in Table 7.4, is completely undetermined for this experiment due to low gene expression at p_3 and high background uncertainty.

Values of normalized integrated total gene expression larger than one indicate that voxel widening also occurs in the Z direction. Because integrated total gene expression is normalized within the height of 1 mm, it is possible to obtain values higher than one when there is sufficient gene expression beyond this range. In the case of $\eta_{min} - p_2$ simulation this extra gene expression comes from the tails of the green intensity profile. In the case of the measurement it likely comes from green light scattering. However, the integrated normalized gene expression in the measurements is in reality likely less than one at p_1 and was measured this high only due to inconsistencies with background measurements.

Table 7.4: *Normalized integrated total gene expression at four points determined from two simulations, $\eta_{min} - p_2$ and Experiment, and from the summed fluorescence image of the experiment following the concurrent gene expression illumination procedure shown in Figure 7.16 for two voxels in horizontal arrangement. p_0/p_1, p_0/p_2 and p_1/p_2 refer to ratios between the normalized integrated total gene expressions at the respective points. The majority contributor to the error estimates of the measured values is the background gene expression.*

	$\tilde{g}(t_{End})/\tilde{g}_{max}(t_{End})$		
	$\eta_{min} - p_2$	Experiment	$\bar{C}_F/r_{a'/b'}$
p_0	1.00	0.73	0.9 ± 0.7
p_1	1.21	0.67	1.3 ± 0.9
p_2	0.14	0.19	0.0 ± 0.4
p_3	0.10	0.15	0.0 ± 0.5
p_0/p_1	0.82	1.09	0.6 ± 0.4
p_0/p_2	7.17	–	> 10
p_1/p_2	–	3.47	–

7.3.2 Vertical Arrangement

For two voxels in vertical arrangement there are two simple illumination procedures that achieve concurrent gene expression. The one investigated here consists of two steps. The first step illuminates the first voxel with red and green light. This generates a large η in the illuminated voxel and a suppressed η in the other voxel. The second step only uses red light illumination on the second voxel, which mostly deactivates the large η in the first voxel bringing it to the same level as the second voxel. The other illumination procedure consists of three steps. The first step illuminates both voxels with only green light, followed by two steps of red light illumination defining each voxel individually. (The second illumination procedure is detailed in the appendix)

Model

As with the horizontal arrangement, the concurrent gene expression illumination for voxels in vertical arrangement consists of steps where light intensities are kept constant, which provides an analytical solution to η in each step given by (2.4). Following the two illumination steps – red and green illumination followed by red only illumination – the solution for $\eta(t)$ at all three points, where p_0 is illuminated first, is as follows:

$$\eta(t_{end}, p_1) = \frac{1}{1 + \frac{k_2}{A_1^2 k_1} + \frac{k_{growth}}{A_1^2 k_1}} \left(1 - e^{-(A_1^2 k_1 + k_2 + k_{growth})\Delta t_1}\right) e^{-(\eta_R k_2 + k_{growth})\Delta t_2},$$

$$\eta(t_{end}, p_2) = \frac{1}{1 + \frac{k_2}{A_1 k_1} + \frac{k_{growth}}{A_1 k_1}} \left(1 - e^{-(A_1 k_1 + k_2 + k_{growth})\Delta t_1}\right) e^{-(k_2 + k_{growth})\Delta t_2},$$

$$\eta(t_{end}, p_0) = \frac{1}{1 + \frac{\eta_R k_2}{k_1} + \frac{k_{growth}}{k_1}} \left(1 - e^{-(k_1 + \eta_R k_2 + k_{growth})\Delta t_1}\right) e^{-(k_2 + k_{growth})\Delta t_2},$$

$$p_i = (x_i, y_i)_V \text{ for } i \in \{0, 1, 2\}, \tag{7.20}$$

where $t_{end} = \Delta t_1 + \Delta t_2$, Δt_1 and Δt_2 are the durations of the first and second illumination step. A_1 is the attenuation factor as defined by (7.7). The same conditions given by (7.16) apply here, which means that for given light intensities, Δt_1 and Δt_2

are uniquely defined. Inserting (7.20) into (7.16) yields the following equations:

$$\Delta t_2 = -\frac{1}{k_2 + k_{growth}} \ln\left(\frac{\eta_{min}}{\eta(\Delta t_1, p_2)}\right), \tag{7.21}$$

$$\frac{\eta(\Delta t_1, p_0)}{\eta(\Delta t_1, p_1)} = \exp\left(k_2(1-\eta_R)\Delta t_2\right) = \left(\frac{\eta_{min}}{\eta(\Delta t_1, p_2)}\right)^{-\frac{(1-\eta_R)k_2}{k_2 + k_{growth}}}. \tag{7.22}$$

Equation (7.22) can only be solved numerically for Δt_1. However, solving (7.22) for Δt_1 does not provide any information whether the choice of intensities will yield a large value of $\eta(t_{end}, p_0)$ or $\eta(t_{end}, p_1)$. Δt_1 can instead be chosen such that:

$$\eta(\Delta t_1, p_0) = \frac{1}{1 + \frac{k_2}{A_1^2 k_1} + \frac{k_{growth}}{A_1^2 k_1}} \cdot f_{\eta_0}, \tag{7.23}$$

which defines Δt_1 to be:

$$\Delta t_1 = -\frac{1}{k_1 + \eta_R k_2 + k_{growth}} \ln\left(1 - f_{\eta_0}\right), \tag{7.24}$$

where f_{η_0} is a faction as close to 1 as possible, which quantifies how close $\eta(\Delta t_1, p_0)$ is to a steady state. By inserting said Δt_1 into (7.22) it can now be numerically solved for one of the intensities instead. For a given green or red intensity, solution to (7.22) will yield the other, which will result in the maximum possible $\eta(t_{end}, p_0)$ and $\eta(t_{end}, p_1)$ for the chosen f_{η_0}. The maximum is achieved because any time shorter than Δt_1 will result in η in all three points to be smaller after the first illumination step. The second illumination step can then only decrease η in all points and if the initial η is smaller so will be the final η. Therefore, the solution to (7.22) will provide the optimal ratio between the intensities for this illumination procedure.

Figure 7.19 shows the normalized gene expression rate, h, and the normalized total gene expression g/g_{max} over time for each point of interest. As expected, gene expression is about the same in both voxels. Any slight discrepancy is due to f_{η_0} not being close enough to one. It appears that this procedure results in total gene expression rate that is worse than that of alternating illumination (Figure 7.7).

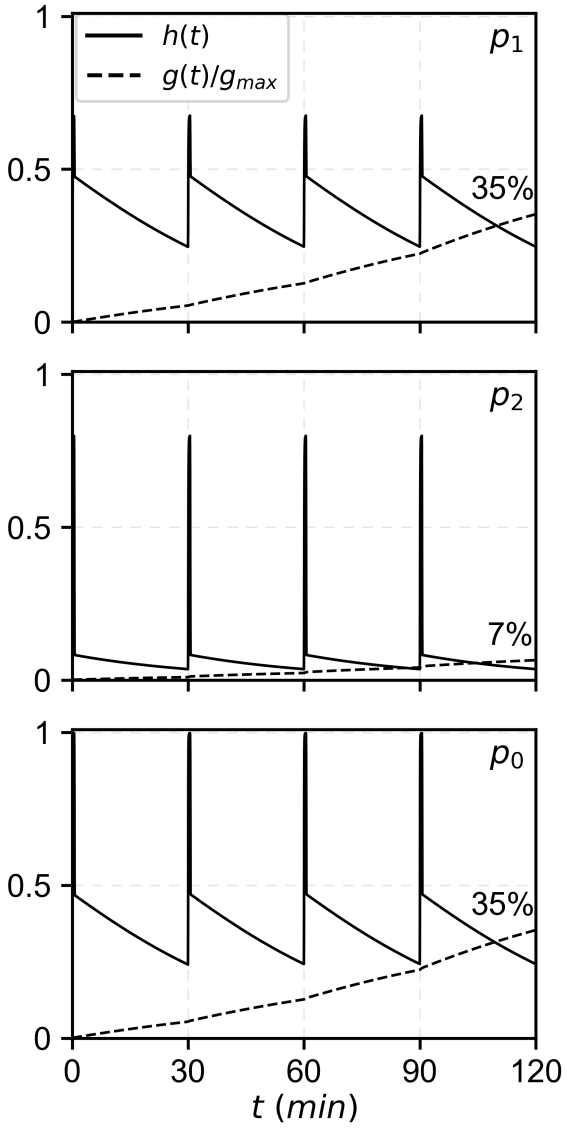


Figure 7.19: *Response of normalized gene expression rate, $h(t)$, and normalized total gene expression, $g(t)/g_{max}$, in vertically arranged voxels to illumination for concurrent gene expression repeated four times at 30 minute intervals. Each graph corresponds to the respective point of interest p_0, p_1 and p_2, for the vertical arrangement with positions and distances as shown in Figure 7.1. Peak incident green light intensity was set to 34.8 W/m^2 and $f_{\eta_0} = 0.99$. Equation (7.22) yields average incident red light intensity of 81.9W/m^2. The illumination durations are $\Delta t_1 = 31$ s and $\Delta t_2 = 7.8$ s. The percentage of maximum possible gene expression density after two hours is shown for each point of interest.*

Experiment's Illumination Procedure

Figure 7.20 shows the illumination procedure for concurrent gene expression in two voxels in vertical arrangement for the three points of interest. As with previous experiments, the hydrogel culture was incubated during first hour and deactivated with red light. The illumination procedure was also split into four 30 minute intervals to refresh η.

Figure 7.21 shows the theoretical prediction of normalized integrated total gene expression for parameters used in Figure 7.19, which satisfy (7.22) and for intensities and illumination durations used during the experiment (Figure 7.20). The duration of both illuminations steps during the experiment was increased by about four times to better even out any lasers' power fluctuations. In an attempt to achieve better contrast, only red light intensity was decreased to about a half. However, due to the complex relationship between parameters such simple adjustments do not necessarily lead to desired outcomes. Even though green radiant exposure is greater relative to red radiant exposure in this case, the simulation of the experiment shown in Figure 7.21 shows only slightly higher overall gene expression and much greater unevenness between the two voxels.

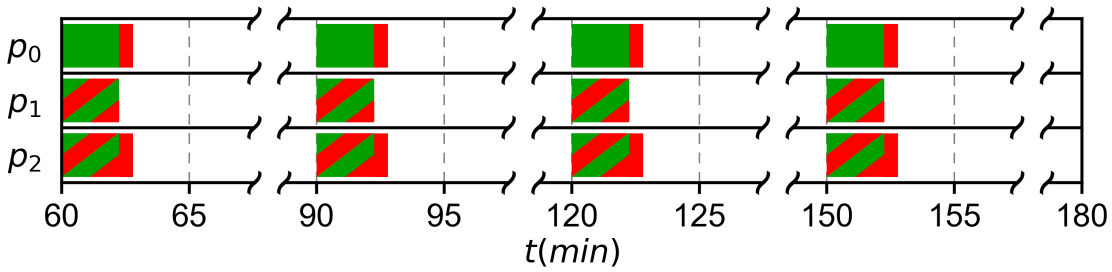


Figure 7.20: *Schematic of the concurrent gene expression illumination procedure for an experiment with two voxels in vertical arrangement. Each row shows the presence of the respective green or red light over time for all three points of interest. The peak incident green light intensity was* $34.8\ W/m^2$ *and the average incident red light intensity was* $45.0\ W/m^2$*. The durations of each illumination step* Δt_1 *and* Δt_2 *were* $135\ s$ *and* $33\ s$ *respectively.*

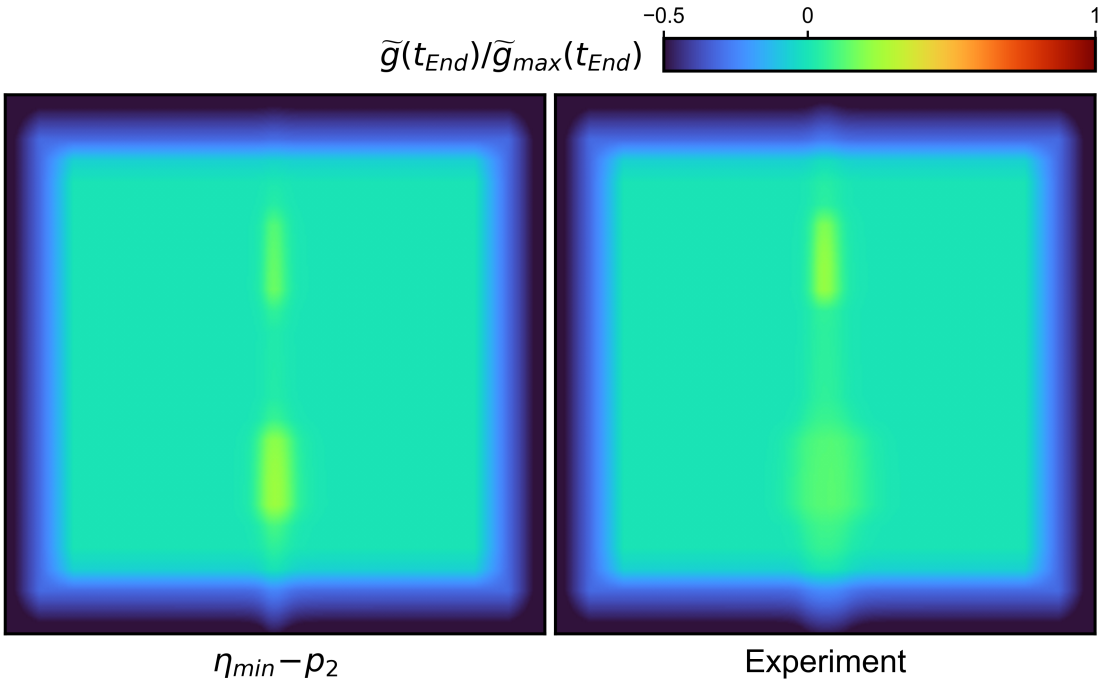


Figure 7.21: *Simulations of normalized integrated total gene expression, $\tilde{g}(t_{End})/\tilde{g}_{max}(t_{End})$, in two voxels in vertical arrangement subjected to concurrent gene expression illumination procedure. Left, simulation of normalized $\tilde{g}(t_{End})$ for incident peak green light intensity I_{515} = 34.8 W/m^2 and average incident red light intensity I_{650} = 81.9 W/m^2. The durations of each illumination step Δt_1 and Δt_2 are 31 s and 7.8 s respectively. Right, simulation of normalized $\tilde{g}(t_{End})$ of the experiment. The intensities and illumination durations are the same as shown in Figure 7.20. Both simulations are normalized to maximum possible $\tilde{g}(t_{End})$ within a thickness of 1 mm. The halo effect in the simulations was added qualitatively as a visual aid.*

Experiment's Results

Figure 7.22 shows the normalized contrasted fluorescence of the experiment, $C_F/r_{a'/b'}$. The integrated total gene expression is higher in the voxel at p_1 the same as predicted by the simulation of the experiment in Figure 7.21. The values of integrated total gene expression at each of the points of interest, shown in Table 7.5, also agree quite well with the simulation despite the large error estimates, which is to be expected when signal is low. Comparing the contrast, indicated by p_0/p_2 and p_1/p_2 in Table 7.5, between the two simulations is not too informative, as the mode of gene expression is different due to higher gene expression in the opposing voxels. Nevertheless, it does predict poorer performance for parameters used during the experiment. Interestingly the simulation of $\eta_{min} - p_2$ shows a noticeably smaller gen expression at p_1. While with alternating illumination this could be attributed to τ, here gene expression in concurrent. It is instead due to the distribution of η around p_1, which falls off less over distance from the centre. The effect is equivalent to that with voxels in horizontal arrangement subjected to illumination for concurrent gene expression.

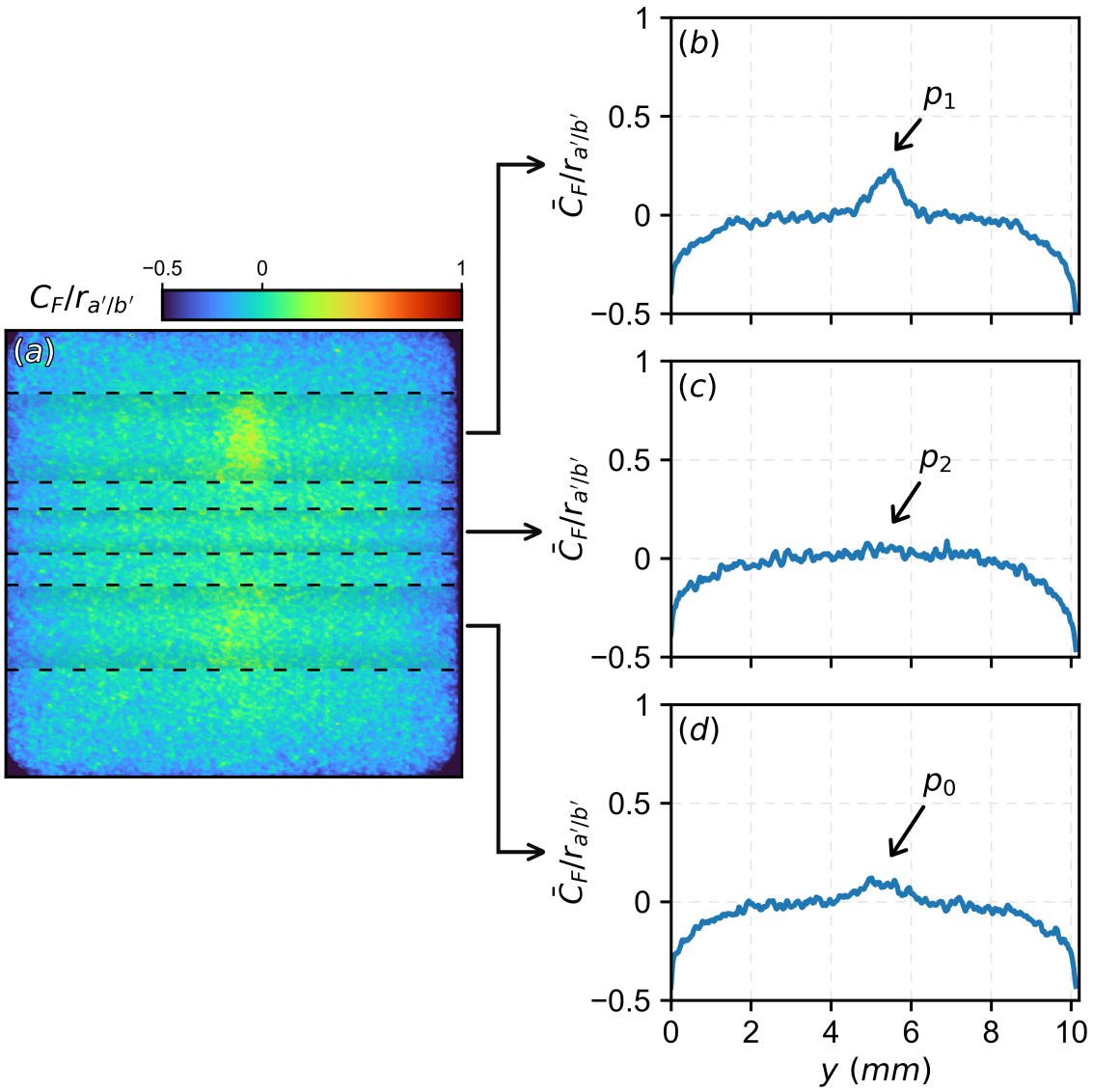


Figure 7.22: *Measurement of an experiment of two voxels in vertical arrangement subjected to concurrent gene expression illumination procedure shown in Figure 7.20.* (a) *Summed image of normalized fluorescence with three bands of interest indicated by the dashed lines. Additional light shading was added to the dashed lines to better highlight the bands.* (b), (c) *and* (d) *Normalized fluorescence averaged in the bands of interest around points* p_1, p_2 *and* p_0 *respectively. The value of* $r_{a'/b'}$ *used was* 3.5 .

Table 7.5: *Normalized integrated total gene expression at three points determined from two simulations, $\eta_{min} - p_2$ and Experiment, and from the summed fluorescence image of the experiment following the concurrent gene expression illumination procedure shown in Figure 7.20 for two voxels in vertical arrangement. p_0/p_1, p_0/p_2 and p_1/p_2 refer to ratios between the normalized integrated total gene expressions at respective points. The majority contributor to the error estimates of the measured values is the background gene expression.*

	$\tilde{g}(t_{End})/\tilde{g}_{max}(t_{End})$		
	$\eta_{min} - p_2$	Experiment	$\bar{C}_F/r_{a'/b'}$
p_0	0.23	0.12	0.12 ± 0.12
p_1	0.14	0.22	0.22 ± 0.12
p_2	0.03	0.05	0.04 ± 0.10
p_0/p_1	1.62	0.58	0.5 ± 0.6
p_0/p_2	–	2.27	3 ± 9
p_1/p_2	5.11	–	–

7.3.3 Diagonal Arrangement

An illumination procedure to achieve gene expression in two voxels in diagonal arrangement can be thought of as two individual illuminations of each voxel, where the first voxel is illuminated by to bring its η up to some value followed by illumination of the second voxel. When the second voxel is shaped by red light illumination, this red light also affects the first voxel due to geometry (Figure 7.1). Therefore, the approach is to illuminate second voxel with green light until its η is slightly below the η of the first voxel. After red illumination, both η will even out, the first through direct red light illumination and the second through red light leakage, η_R.

Model

The illumination procedure for two voxels in diagonal arrangement is in essence two separate but coupled deactivation procedures done at each voxel. The procedure as such thus consists of four illumination steps, starting with green illumination followed by red at the first voxel and ending with green illumination followed by red but at the second voxel. As the initial illumination that defines the first voxel at p_0 is seemingly independent of the second illumination, η at the end of the illumination

procedure at all points of interest is as follows:

$$\begin{aligned}
\eta(t_{end}, p_0) &= H_0\, e^{-(A_2 k_2 + k_{growth})\Delta t_4}\,, \\
\eta(t_{end}, p_1) &= \left(1 - e^{-(k_1 + k_{growth})\Delta t_3}\right) e^{-(\eta_R k_2 + k_{growth})\Delta t_4}\,, \\
\eta(t_{end}, p_2) &= H_2\, e^{-(\eta_R A_2 k_2 + k_{growth})\Delta t_4}\,, \\
\eta(t_{end}, p_3) &= \left(1 - e^{-(A_1 k_1 + k_{growth})\Delta t_3}\right) e^{-(k_2 + k_{growth})\Delta t_4}\,, \\
p_i &= (x_i,\, y_i)_D \text{ for } i \in \{0, 1, 2, 3\}\,,
\end{aligned} \tag{7.25}$$

where $t_{end} = \Delta t_1 + \Delta t_2 + \Delta t_3 + \Delta t_4$ and Δt_i are the durations of each individual illumination step. The attenuation factors A_1 and A_2 are as defined by (7.12). H_0 and H_2 are the fractions of active-state photoreceptors after the first deactivation procedure at p_0 and p_2, $H_0 = \eta(\Delta t_1 + \Delta t_2, p_0)$ and $H_2 = \eta(\Delta t_1 + \Delta t_2, p_2)$. Solving for Δt_3 and Δt_4 by applying the conditions given by (7.16) yields:

$$\Delta t_4 = -\frac{1}{\eta_R A_2 k_2 + k_{growth}} \ln\left(\frac{\eta_{min}}{H_2}\right), \tag{7.26}$$

$$\Delta t_3 = -\frac{1}{k_1 + k_{growth}} \ln\left(1 - H_0 \left(\frac{\eta_{min}}{H_2}\right)^{\frac{(A_2 - \eta_R)k_2}{\eta_R A_2 k_2 + k_{growth}}}\right). \tag{7.27}$$

Both illumination durations depend on the result of the deactivation procedure done at p_0. The relationship between H_0 and H_2 is obtained by considering the attenuation factors when deriving (6.8) and setting $\eta_{low} = H_2$:

$$H_0 \approx \eta_{high} \left(\frac{H_2}{1 - (1 - \eta_{high})^{\frac{1}{A_1}}}\right)^{\frac{\eta_R A_2 k_2 + k_{growth}}{A_2 k_2 + k_{growth}}} \approx H_2^{\eta_R}\,. \tag{7.28}$$

For a large enough η_{high} and large enough red light intensity, (7.28) is approximately the same as (6.8). Substituting (7.26) and (7.28) into $\eta(t_{end}, p_0)$ results in:

$$\eta(t_{end}, p_0) \approx H_2^{-\frac{1-\eta_R^2}{\eta_R}}, \tag{7.29}$$

which is a monotonically decreasing function and $\eta(t_{end}, p_0)$ is at a maximum when $H_2 = 0$. However, this results in $\Delta t_4 < 0$ and a non-zero Δt_4 is required in order to shape the second voxel. Therefore $H_2 > \eta_{min}$. As H_2 determines both Δt_4 and Δt_3 it also determines $\eta(t_{end}, p_3)$. In order to determine the exact value of H_2 another requirement is introduced:

$$\eta(t_{end}, p_3) = \eta_{min}\,. \tag{7.30}$$

Much like with $\eta(t_{end}, p_2)$ the choice of the target η at p_3 is arbitrary. Choosing it to be less than η_{min} will result in a lower final η at p_0 and p_1. Given that $\eta(t_{end}, p_2)$ was already set to η_{min}, setting $\eta(t_{end}, p_3)$ to less than η_{min} will not improve the contrast. Substituting the approximate values of Δt_3, Δt_4 and H_0 into (7.30) yields the following equation:

$$\left(1 - \left(1 - H_2^{\eta_R}\left(\frac{\eta_{min}}{H_2}\right)^{\frac{A_2-\eta_R}{\eta_R A_2}}\right)^{A_1}\right)\left(\frac{\eta_{min}}{H_2}\right)^{\frac{1}{\eta_R A_2}} = \eta_{min}\,, \tag{7.31}$$

which can be solved for H_2 only numerically. For sufficiently high η_{high}, k_2 and k_1, H_2 obtained from (7.31) then determines three of the four illumination durations. For completeness, Δt_1 and Δt_2 are:

$$\Delta t_1 = -\frac{1}{A_1 k_1 + k_{growth}} \ln\left(1 - \eta_{high}\right), \tag{7.32}$$

$$\Delta t_2 = -\frac{1}{A_2 k_2 + k_{growth}} \ln\left(\frac{H_2}{1 - \left(1 - \eta_{high}\right)^{\frac{1}{A_1}}}\right) \approx -\frac{1}{A_2 k_2 + k_{growth}} \ln\left(\frac{H_2}{\eta_{high}}\right). \tag{7.33}$$

Figure 7.23 shows the normalized gene expression rate, h, and the normalized total gene expression, g/g_{max}, over time for each point of interest. The slight discrepancy between total gene expression at p_0 and p_1 is due to (7.31) not including the non-zero η after applying the illumination procedure consecutively. The increased gene expression rate at p_3 after the second illumination is due to the same effect.

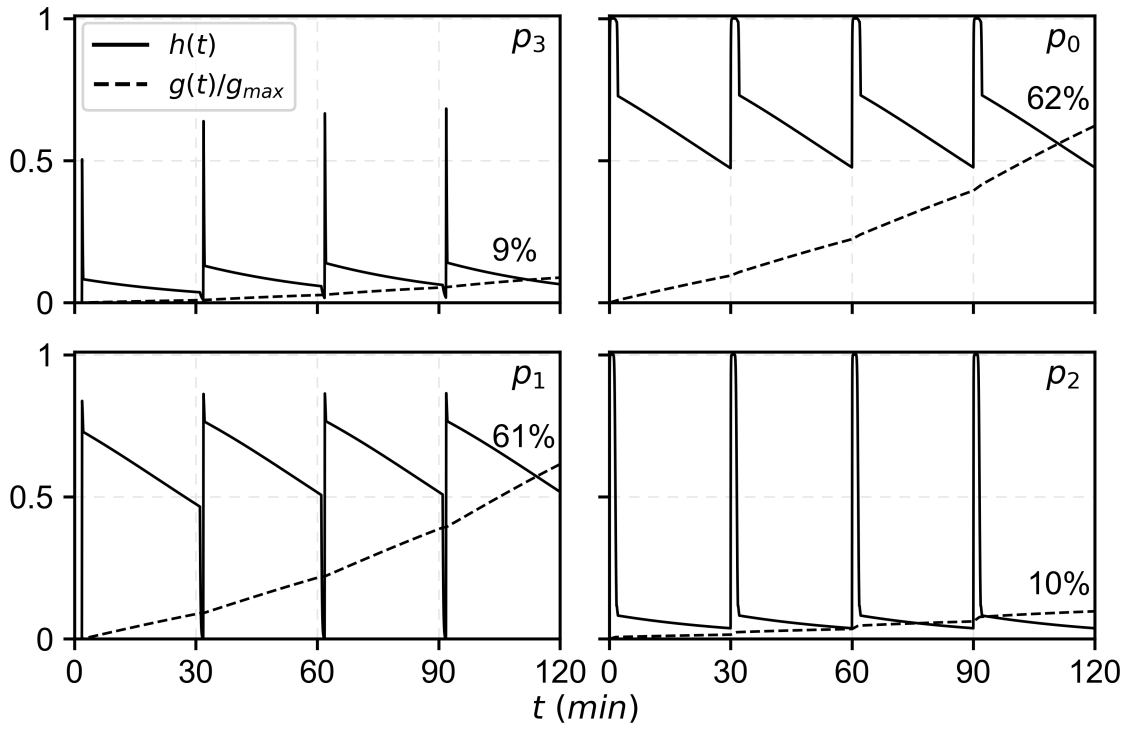


Figure 7.23: *Response of normalized gene expression rate, $h(t)$, and normalized total gene expression, $g(t)/g_{max}$, in diagonally arranged voxels to illumination for concurrent gene expression repeated four times at 30 minute intervals. Each graph corresponds to the respective point of interest p_0, p_1, p_2 and p_3, for the diagonal arrangement with positions and distances as shown in Figure 7.1. Incident green light intensity was set to 46.4 W/m^2 and the incident red light intensity was set to 23.9 W/m^2. With η_{high} set to 0.99. The resulting illumination durations are Δt_1 = 60 s, Δt_2 = 49 s, Δt_3 = 4.7 s and Δt_4 = 16 s. The percentage of maximum possible gene expression density after two hours is shown for each point of interest.*

Experiment's Illumination Procedure

Figure 7.24 shows the illumination procedure for concurrent gene expression in two voxels in diagonal arrangement for the four points of interest. As with previous experiments, the hydrogel culture was incubated during first hour and deactivated with red light. This illumination procedure was also split into four 30 minute intervals to refresh η, which decays due to cell growth.

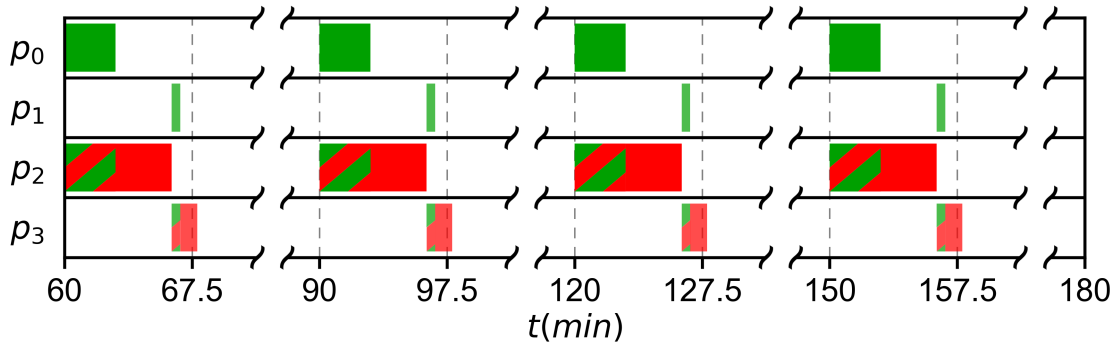


Figure 7.24: *Schematic of the concurrent gene expression illumination procedure for an experiment with two voxels in diagonal arrangement. Each row shows the presence of the respective green or red light over time for all four points of interest. The peak incident green light intensity was* 69.6 W/m^2 *and the average incident red light intensity was* 14.7 W/m^2 *during the illumination of the voxel at* p_0*. The durations of the first two illumination steps* Δt_1 *and* Δt_2 *were* 180 *s and* 200 *s respectively. During the illumination of the second voxel at* p_1 *the peak incident green light intensity was* 23.2 W/m^2 *and the average incident red light intensity was* 9.2 W/m^2*. The durations of the second two illumination steps* Δt_3 *and* Δt_4 *were* 30 *s and* 60 *s respectively*

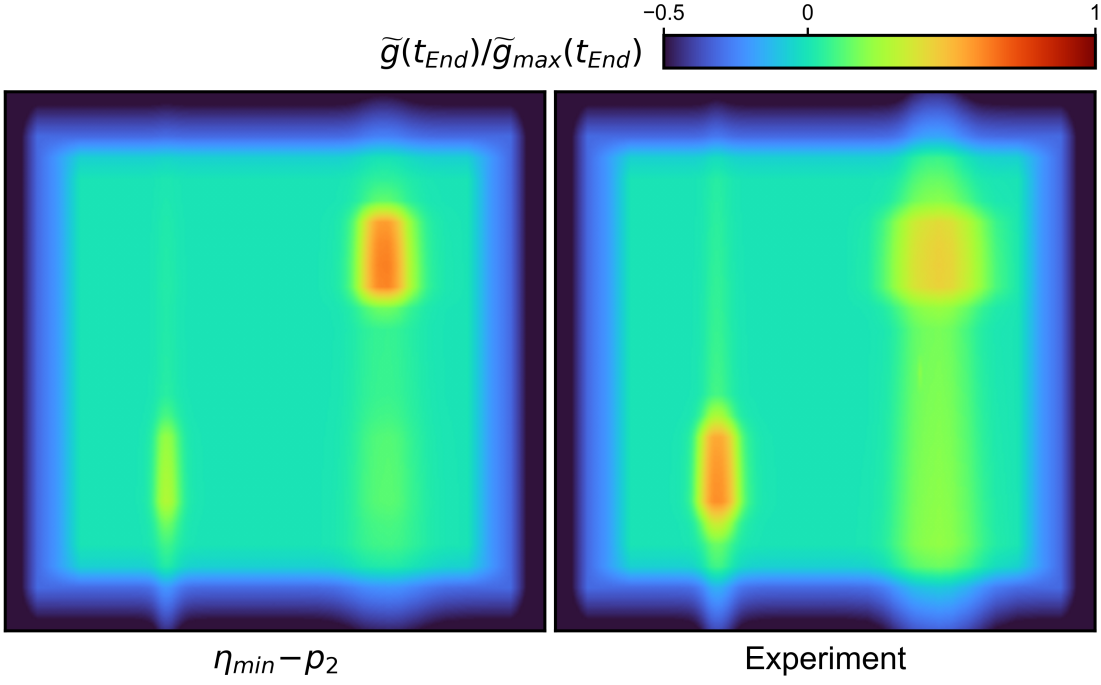


Figure 7.25: *Simulations of normalized integrated total gene expression,* $\tilde{g}(t_{End})/\tilde{g}_{max}(t_{End})$*, in two voxels in diagonal arrangement subjected to concurrent gene expression illumination procedure. Left, simulation of normalized* $\tilde{g}(t_{End})$ *for the same intensities and durations used in Figure 7.23. Right, simulation of normalized* $\tilde{g}(t_{End})$ *of the experiment. The intensities and illumination durations are the same as shown in Figure 7.24. Both simulations are normalized to maximum possible* $\tilde{g}(t_{End})$ *within a thickness of* 1 *mm. The halo effect in the simulations was added qualitatively as a visual aid.*

Figure 7.25 shows the theoretical prediction of normalized integrated total gene expression for parameters used in Figure 7.23 and for parameters using during the experiment shown in Figure 7.24. The illumination procedure of the experiment differs from the illumination procedure determined through the model in two ways. The first illumination step for each voxel included red light in addition to green and the intensities during the second illumination step for each voxel were lowered in order to increase the duration of illumination. With longer illumination optical power fluctuations even out. The introduction of red light in the first steps introduces steady-state fraction factors (Equation (6.5)) for η in (7.25) in all four points, which in turn modify (7.31). The theoretical prediction by following the illumination procedure determined through the model (Figure 7.25) suggests more than a two fold higher integrated total gene expression (Table 7.6) at p_0 compared to p_1. The condition of $\eta(t_{end}, p_0) = \eta(t_{end}, p_1)$ was thus adapted to $4\eta(t_{end}, p_0) = \eta(t_{end}, p_1)$. The factor 4 was somewhat arbitrarily chosen to be greater than 2 in an attempt to also account for additional gene expression in voxel at p_0, which is due to the first voxel requiring longer illumination and thus remaining in a transient state with higher η for longer.

Experiment's Results

Figure 7.27 shows the normalized contrasted fluorescence of the experiment, $C_F/r_{a'/b'}$. The integrated total gene expression at p_0 is wider than gene expression at p_1 as predicted by the simulation in Figure 7.25. The difference in width of the voxels is due to the model only considering the intensities at single points, whereas the simulation and experiment measure integrated total gene expression beyond these points. Because the green beam intensity profile is not box shaped, the intensities away from the peak and consequently radiant exposure, clearly result in a different response. Figure 7.26 shows the simulation of total gene expression in the experiment at p_0 and p_1 as a function of the Z coordinate. The green beam intensity profile can be approximated to be circularly symmetric, which means that graphs of total gene expression as a function of the Y coordinate, centered at $z = 0$, are the same as the ones shown in Figure 7.26. These graphs thus also demonstrate the widening effect, which is due to the nonlinear conversion of radiant exposure to gene expression. The effect is most prominent when radiant exposure is high and η is saturated. This results in the nearby intensity to be sufficient to also reach a very high η thus resulting in a wider voxel.

Furthermore, Figure 7.26 demonstrates the shortcomings of the imaging approach. The individual pixel values in Figure 7.27(a) correspond to the area below the curve of total gene expression at each pixel, the integrated total gene expression. However, the surface of an object is generally thought of as a boundary within which some value is above a certain threshold, in this case total gene expression. Judging from the simulation in Figure 7.26, voxel at p_0 would not be defined if the object threshold were set above 30% of $g_{max}(t_{End})$, whereas voxel at p_1 would have a clear boundary.

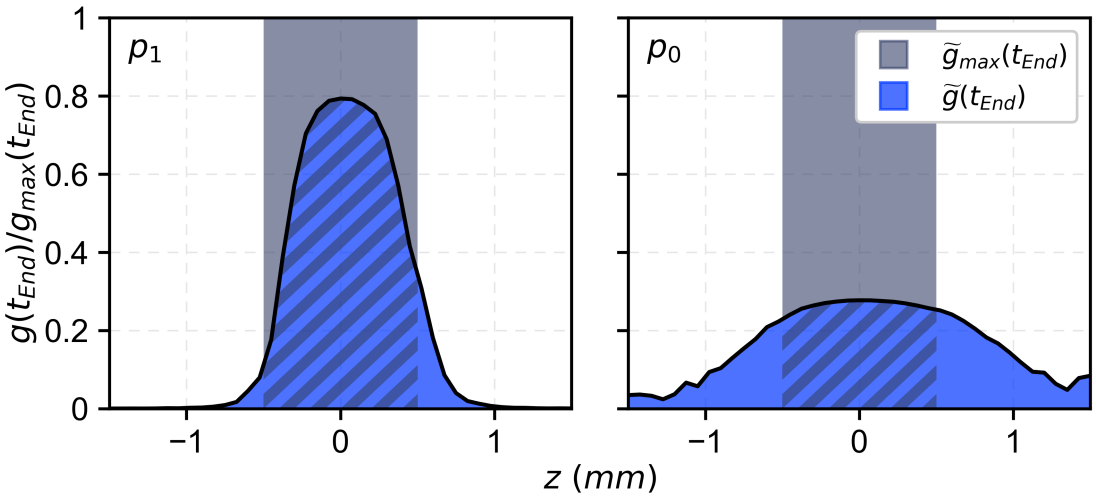


Figure 7.26: *Simulation of normalized total gene expression, $g(t_{End})/g_{max}(t_{End})$, in two voxels in diagonal arrangement at p_0 and p_1 subjected to illumination as shown in Figure 7.24. The coloured areas indicate the respective normalized integrated total gene expression. The Z coordinate is relative to the centre of the green beam.*

Table 7.6 shows the values of normalized integrated total gene expression at the points of interest for the two simulations and the experiment. The predicted higher gene expression at p_1 when compared to p_0 is not reflected in the experiment. A likely cause is the contribution of green light scattering, which the model does not account for, and possibly the contribution from the tails of the green beam profile, which are deactivated in the model but not necessarily during the experiment. At high radiant exposures, such as experienced near p_0, volumes beyond the reach of direct red light illumination can noticeably contribute to the integrated total gene expression. This reasoning is equivalent to the reasoning behind the widening effect demonstrated in Figure 7.26. Overall the simulated values mostly agree with the measurement with some indication that the background was slightly overestimated or that the value of $r_{a'/b'}$ was slightly overestimated. Similarly to voxels in vertical arrangement, contrast, indicated by p_0/p_2 and p_1/p_2 in Table 7.6, was calculated from different points in simulations and measurement due to a different mode of gene expression.

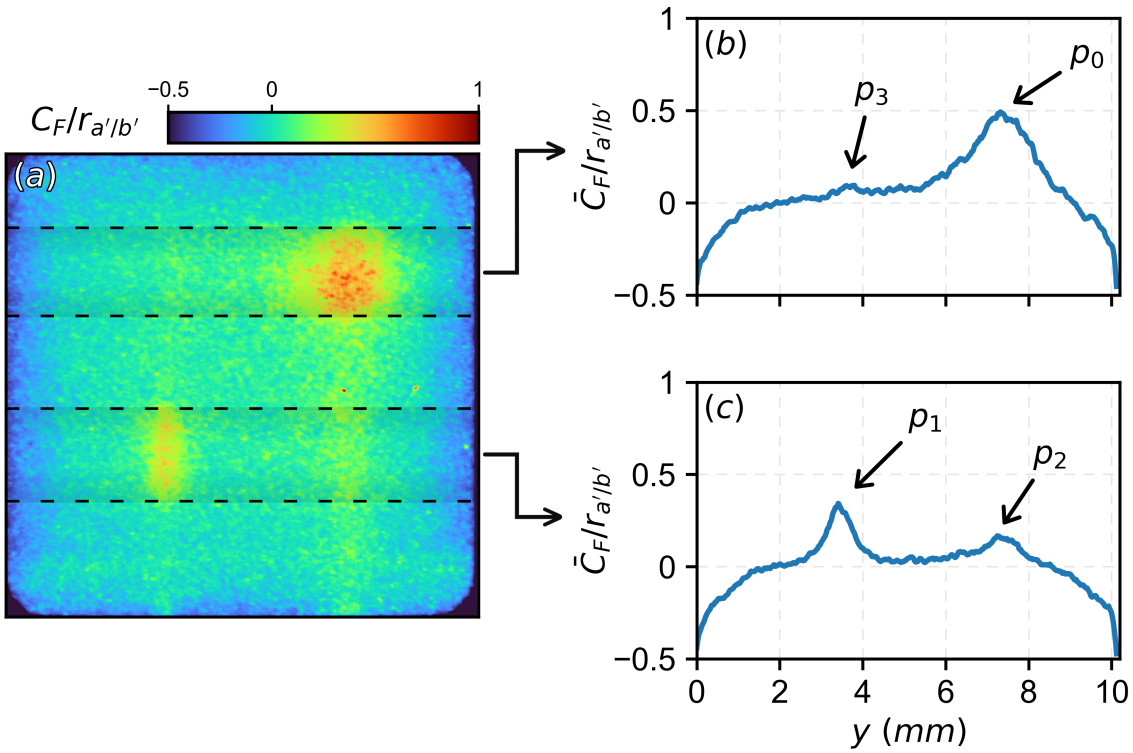


Figure 7.27: *Measurement of an experiment of two voxels in diagonal arrangement subjected to concurrent gene expression illumination procedure shown in Figure 7.24.* (*a*) *Summed image of normalized fluorescence with two bands of interest indicated by the dashed lines. Additional light shading was added to the dashed lines to better highlight the bands.* (*b*) *and* (*c*) *Normalized fluorescence averaged in the bands of interest around points* p_3 *and* p_0*, and* p_1 *and* p_2 *respectively. The value of* $r_{a'/b'}$ *used was* 3.5 .

When comparing homogeneity between the voxels, the simulated experiment and the experiment measurement itself offer seemingly better results than that of the η_{min} − *Background* simulation. However, as previously discussed, an object is defined through the threshold in total gene expression and not integrated total gene expression. In this regard an experiment following the concurrent gene expression illumination provided for $\eta_{min} - p_2$, is expected to provide better results in terms of object definition. This is due to peaks of total gene expression at p_0 and p_1 having the same height, although not the same width. This is guaranteed through the condition set by (7.16).

7.3.4 Discussion

Illumination for concurrent gene expression on its premise offers better performance than alternating illumination simply due to voxels being active through the entire experiment; however, by introducing the requirements for voxel homogeneity and contrast (distinguishability for voxels in vertical arrangement), the resulting total gene expression distribution generally offers slight improvement over the distribution

Table 7.6: *Normalized integrated total gene expression at four points determined from two simulations, $\eta_{min} - p_2$ and Experiment, and from the summed fluorescence image of the experiment following the concurrent gene expression illumination procedure shown in Figure 7.24 for two voxels in diagonal arrangement. p_0/p_1, p_0/p_2 and p_1/p_2 refer to ratios between the normalized integrated total gene expressions at respective points. The majority contributor to the error estimates of the measured values is the background gene expression.*

	$\tilde{g}(t_{End})/\tilde{g}_{max}(t_{End})$		
	$\eta_{min} - p_2$	Experiment	$\bar{C}_F/r_{a'/b'}$
p_0	0.61	0.42	0.46 ± 0.15
p_1	0.25	0.57	0.32 ± 0.11
p_2	0.13	0.20	0.15 ± 0.08
p_3	0.03	0.06	0.07 ± 0.07
p_0/p_1	2.41	0.77	1.5 ± 0.4
p_0/p_2	–	2.15	–
p_1/p_2	2.02	–	2.2 ± 1.1

resulting from the alternating illumination. This is the case for voxels in vertical and diagonal arrangement where the performance of illumination is more or less the same. On the other hand, gene expression in voxels in horizontal arrangement does shows significant improvement, as this arrangement is the only one that can fully exploit the concurrent gene expression.

The main benefit of concurrent gene expression illumination is the deactivating step after each activation, which as suggested in Chapter 6.1.2, can achieve better contrast. The largest downside is the complexity, especially when the intensity profile is not constant within the voxel. It is likely impossible to set the conditions for concurrent gene expression and also require for the different voxels to maintain the same shape when the intensity profile is not constant. The effect of uneven voxel size is slight in horizontal arrangement, noticeable in vertical arrangement and significant in diagonal arrangement.

Another difficulty of the concurrent gene expression illumination is the way the procedure is determined. In the case of vertical and diagonal arrangement it requires numerical solutions for adequate results. This additional layer of complexity is worse when including more than two voxels. With two voxels, equations can be rewritten so that solution is obtained by numerically solving one equation for one variable, for each additional voxel an additional equation is added to the system, which now has to be numerically solved for additional variables corresponding to the added voxels.

7.4 Illumination for Separate Gene Expression

In contrast to the previous chapter, the illumination for separate gene expression aims for a simple approach. The only requirement is that a voxel is adequately defined through illumination, ignoring any other potential voxels or the history of illumination. In this regard it is very similar to alternating illumination; however, it is not required that the intensities are constant nor does it require concurrent red and green illumination. In essence this illumination procedure is the deactivation procedure executed at each individual voxel at different points in time.

Model

The illumination for separate gene expression is just applying the deactivation procedure at different voxel locations, which for better results requires rewriting (6.6), (6.7) and (6.8) to include attenuation factors. The approximate versions of this procedure have already been employed in the previous chapter for horizontal arrangement (Equations (7.18) and (7.19)) and diagonal arrangement (Equation (7.28)) of voxels. Maintaining the same notation, with p_0 denoting the centre of the voxel and p_2 denoting the point to be deactivated, the illumination durations that result in $\eta(t_{end}, p_2) = \eta_{min}$ are:

$$\Delta t_1 = -\frac{1}{A_{1,0}k_1 + k_{growth}} \ln\left(1 - \eta_{high}\left(1 + \frac{k_{growth}}{A_{1,0}k_1}\right)\right), \tag{7.34}$$

$$\Delta t_2 = -\frac{1}{A_{2,2}k_2 + k_{growth}} \ln\left(\frac{\eta_{min}\left(1 + \frac{k_{growth}}{A_{1,2}k_1}\right)}{1 - \left(1 - \eta_{high}\left(1 + \frac{k_{growth}}{A_{1,0}k_1}\right)\right)^{\frac{A_{1,2}k_1 + k_{growth}}{A_{1,0}k_1 + k_{growth}}}}\right), \tag{7.35}$$

where $A_{1,i}$ and $A_{2,i}$ are the attenuation factors for green and red light respectively at each point i. η at p_0 after illumination is then:

$$\eta(t_{end}, p_0) = \eta_{high}\left(\frac{\eta_{min}\left(1 + \frac{k_{growth}}{A_{1,2}k_1}\right)}{1 - \left(1 - \eta_{high}\left(1 + \frac{k_{growth}}{A_{1,0}k_1}\right)\right)^{\frac{A_{1,2}k_1 + k_{growth}}{A_{1,0}k_1 + k_{growth}}}}\right)^{\frac{\eta_R A_{2,0}k_2 + k_{growth}}{A_{2,2}k_2 + k_{growth}}}, \tag{7.36}$$

where $t_{end} = \Delta t_1 + \Delta t_2$. The deactivation procedure can be made more general by including red light during the first illumination step; however, such addition does not seem to provide any noticeable benefits. This is likely due to the requirement for a large η_{high}, whose maximum possible value is determined by the steady-state η:

$$\eta_{high} \leq \frac{1}{1 + \frac{\eta_R A_{2,0} k_2}{A_{1,0} k_1} + \frac{k_{growth}}{A_{1,0} k_1}} \,. \tag{7.37}$$

In order for η_{high} to be nearly equal to one it is thus required for red light intensity to be low, as otherwise such η_{high} is unachievable.

Equations (7.34), (7.35) and (7.36) can of course be simplified by an approximation when η_{high} is large and light intensities are much greater than growth rate. Furthermore, given the geometry of light illumination, the attenuation factors $A_{2,0}$ and $A_{2,2}$ are identical during this procedure, as the point to be deactivated will be on the same line as the voxel, which is perpendicular to incident red light. The approximate quantities are then much more simple:

$$\Delta t_1 \approx -\frac{1}{A_{1,0} k_1} \ln\left(1 - \eta_{high}\right), \tag{7.38}$$

$$\Delta t_2 \approx -\frac{1}{A_{2,2} k_2} \ln\left(\eta_{min}\right), \tag{7.39}$$

$$\eta(t_{end}, p_0) \approx {\eta_{min}}^{\eta_R} \,. \tag{7.40}$$

Given the requirement, it is not unexpected that (7.38) and (7.39) are the same approximate durations, with included green and red light attenuation, as the ones obtained from (6.6) and (6.7), which relate to the single voxels deactivation procedure. Due to $A_{2,0} = A_{2,2}$, (7.40) is independent of light attenuation in the approximation, which results in the same expression as (6.8).

Part of the requirement is that illumination history is ignored, which means that illumination should be such that the end state is the same regardless of the initial state. Conveniently this is achieved by setting a large η_{high}, which ensures that radiant exposure is large enough that η changes from any initial state to a steady state. While radiant exposure could be adapted to account for the initial state, similarly as described in Chapter 6.2.1, it would require tracking the history of illumination at a given point, which significantly complicates the calculation. Such a correction might be desired, if the aim is to avoid saturation of η in the voxel.

Figure 7.28 shows the normalized gene expression rate, h, and the normalized total gene expression, g/g_{max}, over time for each point of interest in all arrangements. The points of interest were kept the same as with the previous illumination procedures for consistency. Given the geometry of illumination and consequently light attenuation, the points of interest should just be the point in the voxel and the point that coincides with the entry of the green laser beam into the build volume. The latter is the point where the highest activation occurs and requires the highest deactivation. However, with a large enough η_{high}, the attenuation of green light is not as relevant as indicated by (7.39). Therefore, the location of the latter point of interest can be approximately anywhere on the green beam's path.

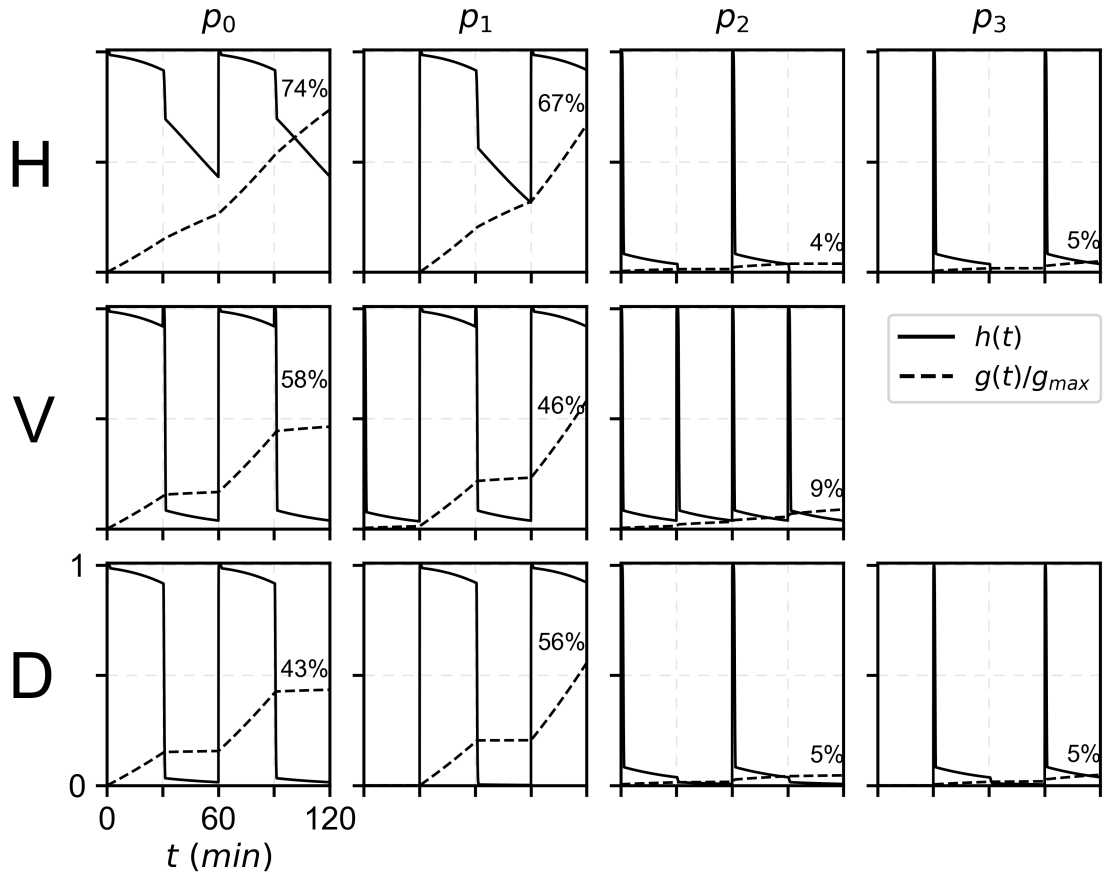


Figure 7.28: *Response of normalized gene expression rate, $h(t)$, and normalized total gene expression, $g(t)/g_{max}$, in horizontally, **H**, vertically, **V**, and diagonally, **D**, arranged voxels to illumination for separate gene expression repeated twice at each voxel. Each column corresponds to the respective point of interest p_0, p_1, p_2 and p_3, in their respective arrangements as shown in Figure 7.1. Incident green light intensity was set to 69.6 W/m^2, the incident red light intensity was set to 18.4 W/m^2 and η_{high} was set to 0.99 for all arrangements. The resulting illumination durations for each voxel are shown in Table 7.7.*

It can be seen in Figure 7.28 that indeed both voxels exhibit the same rate of gene expression during illumination regardless of their position or arrangement. The most notable difference can be observed when the voxel is not directly illuminated, which is due to the geometry of red light illumination. This is especially the case in the horizontal arrangement, where none of the voxels are never directly illuminated by red light and thus red light leakage is not sufficient to completely deactivate the previously activated voxel. Because the voxel at p_0 is activated first and it is never fully deactivated, it has more time to express genes resulting in a larger total gene expression. In the other two arrangements the situation is reversed with total gene expression being greater in the voxel illuminated second, p_1. This is due to the cell population growth, which results in greater overall gene expression near the end of the simulation.

Table 7.7: *Durations of illumination steps for separate gene expression illumination procedure for each voxel at p_0 and p_1 for all three voxel arrangements. The durations are determined based off of* (7.34) *and* (7.35) *using the attenuation factors for the respective arrangement with attenuation coefficients $\mu_G = 120\ m^{-1}$ and $\mu_R = 45\ m^{-1}$.*

	p_0		p_1	
Arrangement	$\Delta t_1\ (s)$	$\Delta t_2\ (s)$	$\Delta t_1\ (s)$	$\Delta t_2\ (s)$
Horizontal	32	67	32	56
Vertical	25	61	41	62
Diagonal	41	67	25	55

Experiments' Illumination Procedures

Figure 7.29 shows the illumination procedures for separate gene expression in two voxels in all three arrangements. Just as with concurrent gene expression illumination, after the first hour the experiment is split into four 30 minute intervals to counteract both effects of cell growth: η decay and increasing population.

The durations of illumination steps during experiments (Table 7.8) were not the same as the ones shown in Table 7.7, in an attempt to ensure a stronger response. By having the same intensities as detailed in Figure 7.28, the increased illumination durations increase the respective radiant exposure. The durations of the longer green illumination step were arbitrarily set to three minutes, with the duration for voxels in horizontal arrangement being slightly lower, as these voxels have a lower interaction with red light and photoreceptors stay active for longer (Figure 7.28). The duration of the shorter green illumination step was then scaled relatively to the first. Due to green light radiant exposure being high to begin with, this increase is mostly expected to result in a wider voxel, which will result in higher normalized integrated total gene expression. The durations of red light illumination were increased when compared to Table 7.7 to slightly mitigate the widening effect. As the increased green radiant exposure results in a negligible increase of η, the increased red light radiant exposure after illumination then results in a lower η overall. This effect is expected to help mitigate the widening of the voxel and the increase in the integrated total gene expression.

Figure 7.30 shows the theoretical prediction of normalized integrated total gene expression for parameters used in Figure 7.28 and for parameters shown in Figure 7.29, which were used for the experiments. The predicted response of experiments shows the expected widening of the voxels and an increased integrated total gene expression, both in the voxels and suppressed regions.

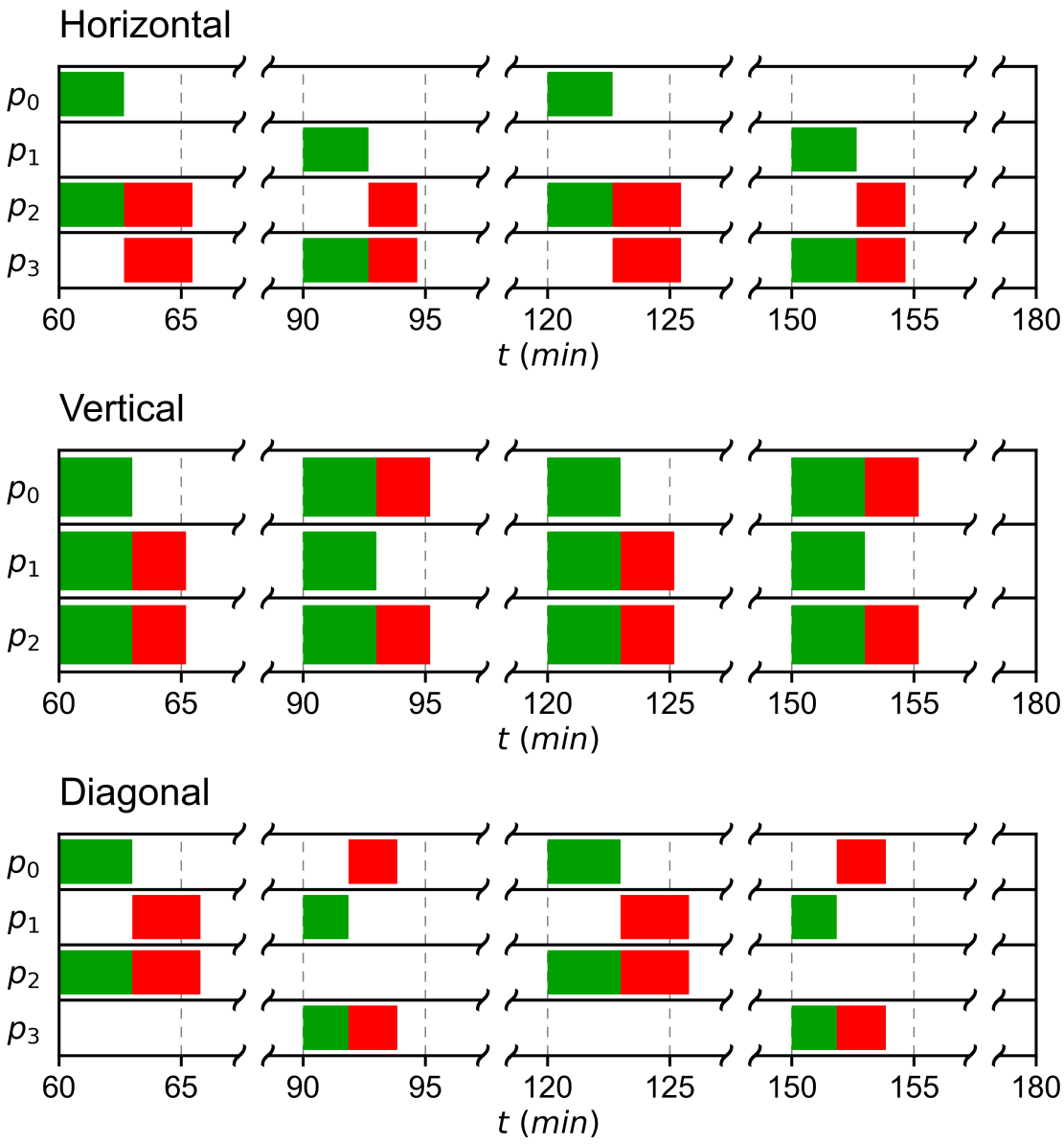


Figure 7.29: *Schematic of the separate gene expression illumination procedure for experiments with two voxels in all arrangements. Each row shows the presence of the respective green or red light over time for all points of interest for the respective arrangement. The peak incident green light intensity was* 69.6 W/m^2 *and the average incident red light intensity was* 18.4 W/m^2 *for all arrangements and voxels. The durations of illumination steps are shown in Table 7.8.*

Table 7.8: *Durations of illumination steps for separate gene expression illumination experiments for each voxel at p_0 and p_1 for all voxel arrangements.*

	p_0		p_1	
Arrangement	Δt_1 (s)	Δt_2 (s)	Δt_1 (s)	Δt_2 (s)
Horizontal	160	170	160	120
Vertical	110	135	180	135
Diagonal	180	170	110	120

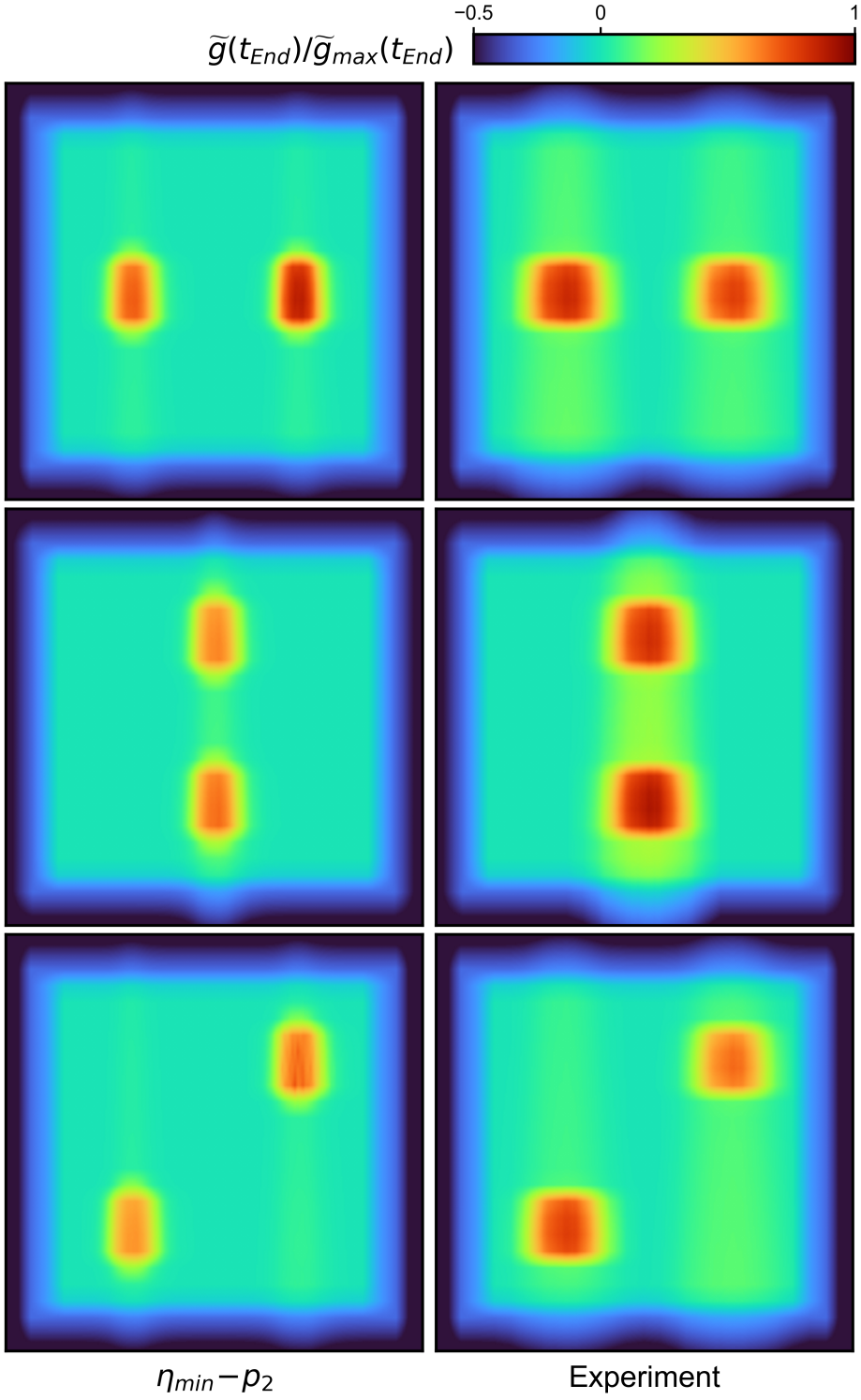


Figure 7.30: *Simulations of normalized integrated total gene expression, $\widetilde{g}(t_{End})/\widetilde{g}_{max}(t_{End})$, in two voxels in all arrangements subjected to separate gene expression illumination procedure as shown in Figure 7.29. Left, simulations of normalized $\widetilde{g}(t_{End})$ for all three arrangements with intensities as detailed in Figure 7.28 and illumination durations as shown in Table 7.7. Right, simulations of normalized $\widetilde{g}(t_{End})$ of all three experiments. The intensities and illumination durations are the same as detailed in Figure 7.29 and Table 7.8. Both simulations are normalized to maximum possible $\widetilde{g}(t_{End})$ within a thickness of 1 mm. The halo effect in the simulations was added qualitatively as a visual aid.*

Experiments' Results

Figures 7.31, 7.32 and 7.33 show the normalized contrasted fluorescence of the three experiments, C_F. Due to the increased radiant exposure when compared to the illumination for $\eta_{min} - p_2$, the voxels are indeed wider as predicted. However, this is especially the case for the two experiments with voxels in horizontal and vertical arrangement. While the green light scattering is the probable cause of the widening beyond the prediction of the model, it would be expected that the same should hold for the diagonal arrangement. From these singular experiments it is not clear what causes these discrepancies. The two likely causes are the inaccurate determination of the background gene expression or an increased maximum contrast, $r_{a'/b'}$. The increased maximum contrast could be due to some unknown variation of the samples, similar to the one seen in one of the groups of steady-state experiments shown in Figure 5.10. On the other hand, the background gene expression estimation could have been underestimated due to either an increased halo influence or the slices were thinner than 1 mm, or both. However, slices would have needed to be almost half the intended thickness to account for the apparent significant increase in gene expression, which is well beyond the estimated error in slice thickness.

Regardless of the unexpectedly high gene expression, all experiments show excellent localization with high contrast. The voxels are also of the same approximate size in all experiments, with a slight exception in horizontal arrangement. Table 7.9 shows the values of normalized integrated total gene expression at the points of interest for all the simulations and experiments for all arrangements. For voxels in diagonal arrangement the predicted values match the experiment quite well. For voxels in the horizontal and vertical arrangement the values at each point of interest are almost doubled. As previously mentioned, the cause likely lies with background gene expression, both in its determination and its actual magnitude.

The main discrepancy between the experiment and simulation is the uneven gene expression between the voxels in horizontal arrangement. A similar effect was observed in voxels in horizontal arrangement subjected to concurrent gene expression illumination. In the latter a plausible explanation was an increased green radiant exposure in one of the voxels, increasing the contribution of the scattered light. However, this is not the case for separate gene expression illumination, this in turn also suggest this effect could also be present in the experiment with concurrent gene expression illumination. If anything, total gene expression should be lower at p_1, as with concurrent gene expression illumination τ does play a role in uneven gene expression distribution, which is nicely reflected in the simulation of $\eta_{min} - p_2$. Some contribution to this effect could come from η_R not being constant along the path of red light; however, it is not too prominent, as otherwise it should also be noticeable with voxels in diagonal arrangement.

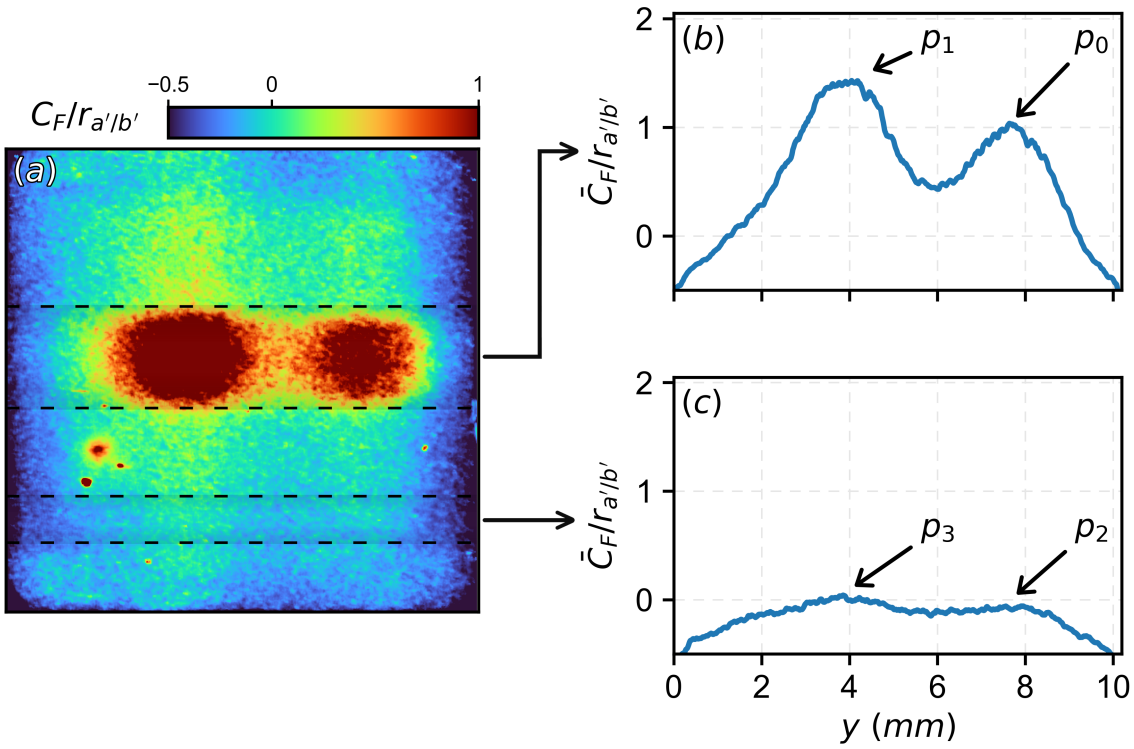


Figure 7.31: *Measurement of an experiment of two voxels in horizontal arrangement subjected to separate gene expression illumination procedure shown in Figure 7.29.* (*a*) *Summed image of normalized fluorescence with two bands of interest indicated by the dashed lines. Additional light shading was added to the dashed lines to better highlight the bands.* (*b*) *and* (*c*) *Normalized fluorescence averaged in the bands of interest around points* p_1 *and* p_0*, and* p_3 *and* p_2 *respectively. The value of* $r_{a'/b'}$ *used was* 3.5 .

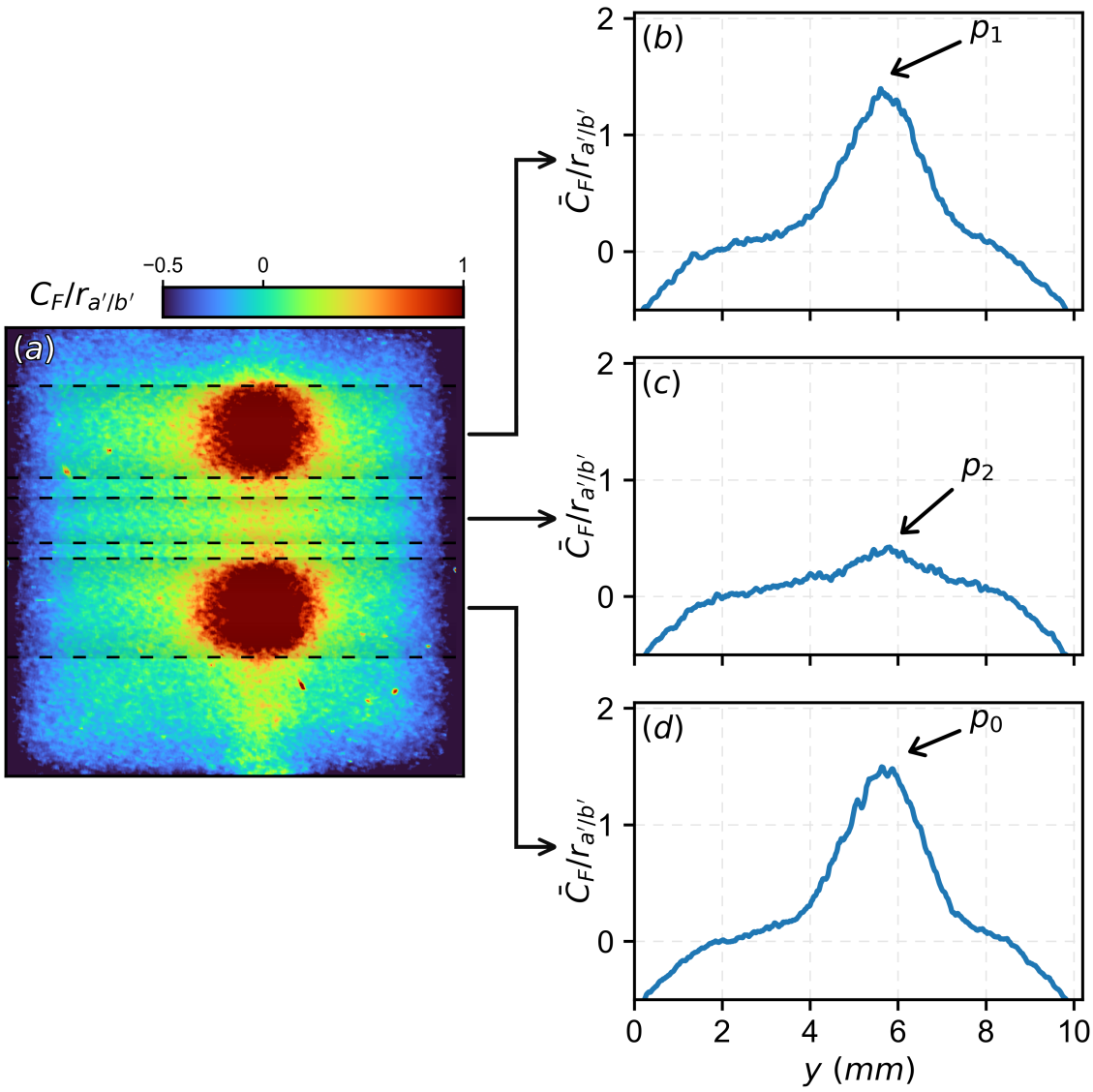


Figure 7.32: *Measurement of an experiment of two voxels in vertical arrangement subjected to separate gene expression illumination procedure shown in Figure 7.29.* (*a*) *Summed image of normalized fluorescence with three bands of interest indicated by the dashed lines. Additional light shading was added to the dashed lines to better highlight the bands.* (*b*), (*c*) *and* (*d*) *Normalized fluorescence averaged in the bands of interest around points* p_1, p_2 *and* p_0 *respectively. The value of* $r_{a'/b'}$ *used was* 3.5 .

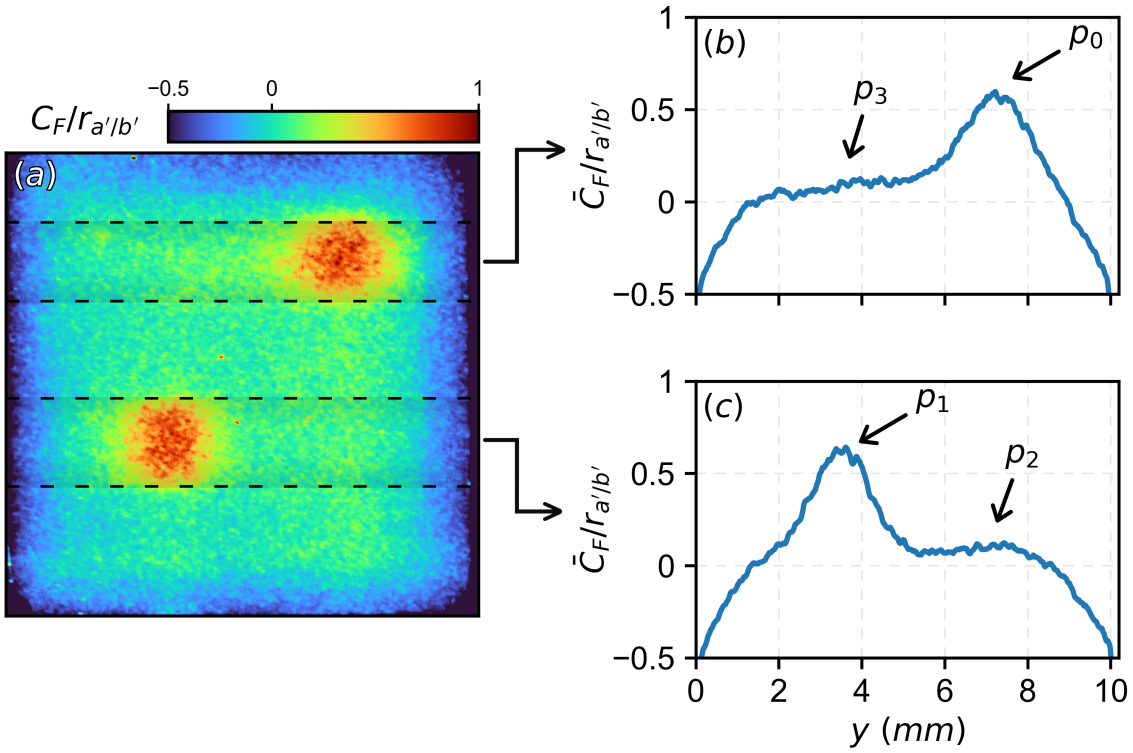


Figure 7.33: *Measurement of an experiment of two voxels in diagonal arrangement subjected to separate gene expression illumination procedure shown in Figure 7.29.* (*a*) *Summed image of normalized fluorescence with two bands of interest indicated by the dashed lines. Additional light shading was added to the dashed lines to better highlight the bands.* (*b*) *and* (*c*) *Normalized fluorescence averaged in the bands of interest around points* p_3 *and* p_0*, and* p_1 *and* p_2 *respectively. The value of* $r_{a'/b'}$ *used was* 3.5 .

Table 7.9: *Normalized integrated total gene expression at points of interest determined from two simulations, $\eta_{min} - p_2$ and Experiment, and from the summed fluorescence images of the experiments for all three arrangements of two voxels. p_0/p_1 and $p_{0,1}/p_{2,3}$ refer to ratios between the normalized integrated total gene expressions at respective points. The majority contributor to the error estimates of the measured values is the background gene expression.*

	$\tilde{g}(t_{End})/\tilde{g}_{max}(t_{End})$		
	$\eta_{min} - p_2$	Experiment	$\bar{C}_F/r_{a'/b'}$
Horizontal Arrangement			
p_0	0.86	0.73	1.0 ± 0.9
p_1	0.68	0.80	1.4 ± 1.2
p_2	0.05	0.12	0.0 ± 0.6
p_3	0.06	0.15	0.0 ± 0.6
p_0/p_1	1.26	0.91	0.7 ± 0.5
p_0/p_3	–	5.39	> 10
p_1/p_3	12.0	–	–
Vertical Arrangement			
p_0	0.64	0.87	1.5 ± 1.2
p_1	0.59	0.78	1.4 ± 1.1
p_2	0.09	0.22	0.4 ± 0.6
p_0/p_1	1.08	1.11	1.1 ± 0.6
p_1/p_2	6.56	3.62	3 ± 5
Diagonal Arrangement			
p_0	0.65	0.64	0.64 ± 0.20
p_1	0.57	0.74	0.60 ± 0.19
p_2	0.06	0.12	0.11 ± 0.10
p_3	0.04	0.08	0.10 ± 0.10
p_0/p_1	1.15	0.82	1.07 ± 0.23
p_0/p_2	–	5.12	–
p_1/p_2	9.16	–	5 ± 4

7.4.1 Discussion

The separate gene expression illumination procedure seems to be a good solution to gene expression in two voxels. Due to its simplicity is can also easily be generalized to multiple voxels by simply allocating each voxel a fixed interval during which its gene expression will occur. With two voxels the maximum possible total gene expression is split in two and each additional voxel takes its own additional share of total gene expression further reducing the contrast. One way to mitigate this effect is to increase the duration of the experiment. However, while the increased duration would increase the available total gene expression, it becomes increasingly difficult to maintain the voxels due to increased scattering and overall attenuation. Equations (7.38) and (7.39) seemingly allow for any attenuation as long as there is sufficient radiant exposure; however, this also leads to potentially very high light intensities, if the illumination times are to be kept short. The limiting factor is now the survivability of cells in high light intensity conditions. The other, more noticeable, effect is the increased scattering, which would significantly misshape the incident light, homogenizing the intensity profile as the light travels further into the build volume.

7.5 Conclusion

All three approaches to illumination have yielded two localized voxels with varying levels of contrast. When it comes to horizontal arrangement, illumination for concurrent gene expression provides the best performance, as it can maintain a high gene expression rate throughout the experiment (Figure 7.34). Illumination durations given by (7.18) are very similar to illumination durations for separate gene expression given by (7.38) and (7.38). The difference is to what degree a voxel is illuminated with green light given the voxel's position with respect to incident red light. This arises from the red light leakage unevenly affecting each voxel due to different attenuation factors. Accounting for this correction, illumination can be expanded to any number of voxels on the same horizontal line, and furthermore, illumination of all these voxels can be considered as a single step equivalent to a single voxel illumination, provided the total time is short enough.

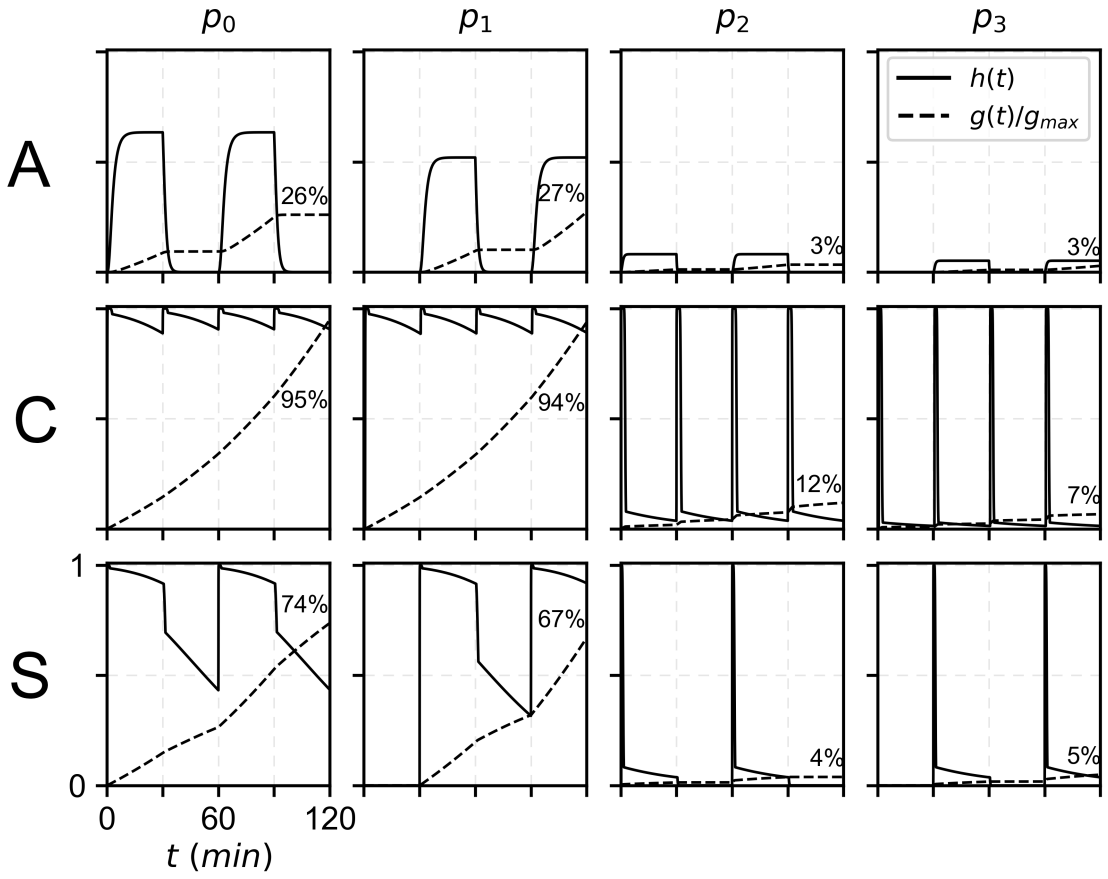


Figure 7.34: *Response of the normalized gene expression rate, $h(t)$, and normalized total gene expression, $g(t)/g_{max}$, in horizontally arranged voxels to all three illuminations – alternating illumination, **A**, concurrent gene expression illumination, **C**, and separate gene expression illumination **S**. The graphs are consolidated from Figures 7.2, 7.15 and 7.28.*

For two voxels in vertical arrangement, the best performance is given by separate gene expression illumination (Figure 7.35). Alternating illumination can be competitive provided that green light intensity is increased for each voxel accordingly to account for light attenuation. However, because separate gene expression illumination is based on the deactivation procedure, the available range of η is greater and can be saturated more given the same $\eta_{low} = \eta_{min}$. If the green intensity profile is non-constant, this increased range allows for a wider voxel without much increase in gene expression in the suppressed region. Illumination for concurrent gene expression underperforms in vertical arrangement and provides no clear benefit over the other two illumination procedures.

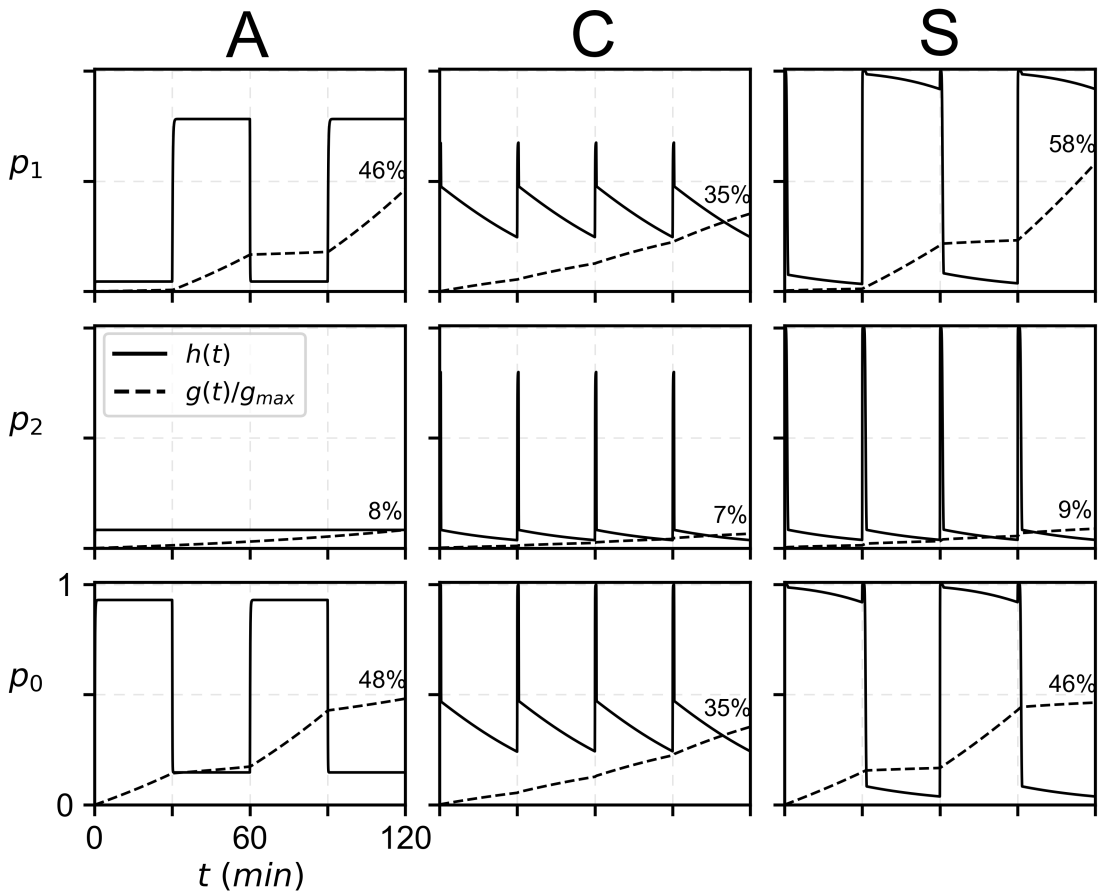


Figure 7.35: *Response of the normalized gene expression rate, $h(t)$, and normalized total gene expression, $g(t)/g_{max}$, in horizontally arranged voxels to all three illuminations – alternating illumination, **A**, concurrent gene expression illumination, **C**, and separate gene expression illumination **S**. The graphs are consolidated from Figures 7.7, 7.19 and 7.28.*

Illumination for separate gene expression is also the best candidate for two voxels in diagonal arrangement (Figure 7.36). Alternating illumination could be improved but it has the same shortcomings as with two voxels in vertical arrangement. On the other hand, illumination for concurrent gene expression offers similar performance – higher gene expression at p_0 and p_1 but also higher gene expression at p_2 and p_3. However, the homogeneity of the voxels is quite susceptible to non-constant green light intensity profiles. Furthermore, determining the radiant exposure requires numerically solving a system of equations, which gets even more complicated with the addition of more voxels.

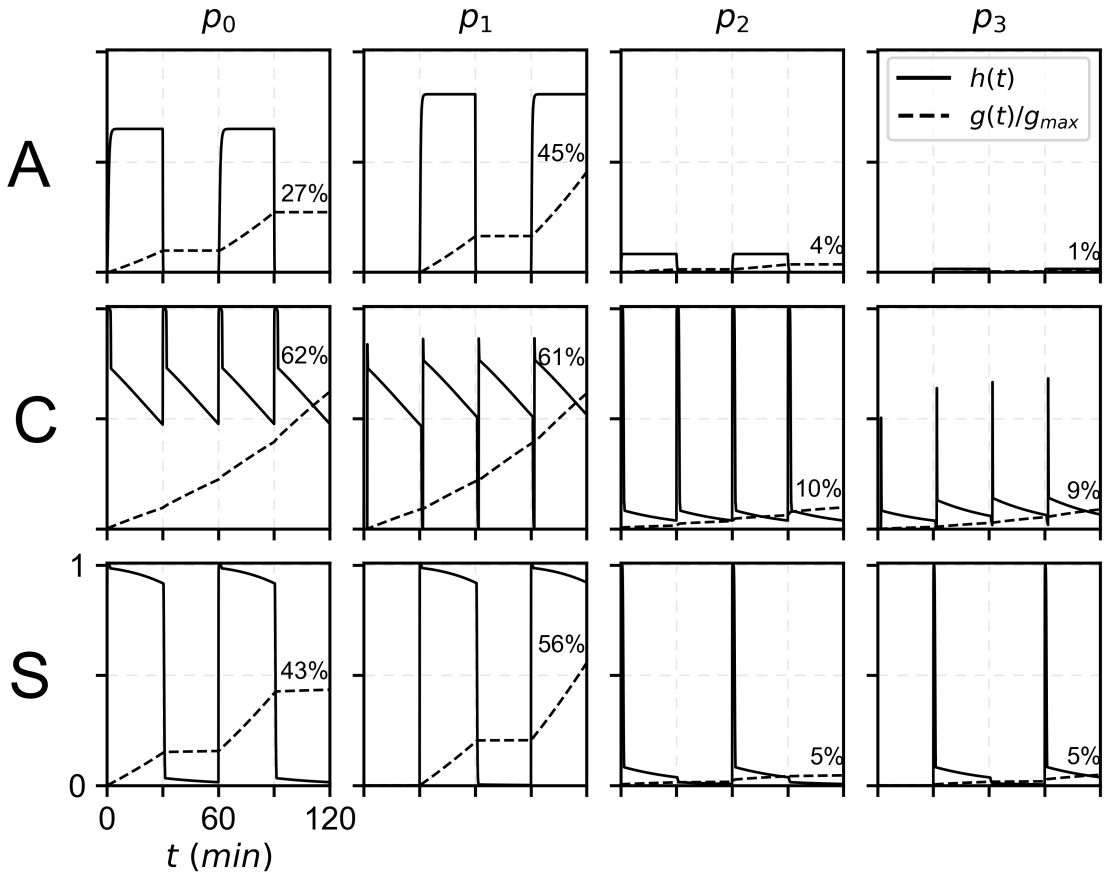


Figure 7.36: *Response of the normalized gene expression rate, $h(t)$, and normalized total gene expression, $g(t)/g_{max}$, in horizontally arranged voxels to all three illuminations – alternating illumination, **A**, concurrent gene expression illumination, **C**, and separate gene expression illumination **S**. The graphs are consolidated from Figures 7.11, 7.23 and 7.28.*

Considering these three approaches, separate gene expression illumination should be used for voxels in vertical and diagonal arrangement while the concurrent gene expression illumination should be used for voxels in horizontal arrangement. The overall illumination procedure can be further optimized by considering any voxels in horizontal arrangement as a single entity that replaces a single voxel in the illumination procedure. This entirely removes the concept of voxels in horizontal arrangement. Furthermore, given the nature of separate gene expression illumination, it is quite irrelevant whether or not the voxels are in vertical or diagonal arrangement, as gene expression can be achieved in each voxel quite independently. The main criteria that then remains, with regards to voxel arrangements, is how the voxels are arranged in time and for how long gene expression is allowed to occur in each.

Chapter 8

Gene Expression in 3D Geometry

Gene Expression in 3D Geometry introduces the concept of spatial and temporal slicing. Illumination procedures determined in Chapter 7 along with geometry of incident light influence spatial slicing while cell population growth determines the temporal slicing. Spatiotemporal slicing was applied to a double helix to generate an illumination procedure, which would result in a 3D object. Due to the concentration of produced material being low the double helix was reconstructed from the resulting gene expression.

8.1 Spatial and Temporal Slicing

The basic building block in this 3D printing method is a voxel. Consequently, any object to be printed must thus be segmented into voxels. Segmentation of an object into its basic building blocks, which are 3D printing technique specific, is known as slicing. In 3D printing context, besides segmentation, slicing also refers to generation of instructions for each individual basic building block. Given the illumination procedures investigated in the previous chapter, the base building block for this 3D printing method can be expanded to a set of one or more voxels, which are arranged parallel to the incident red light – horizontal arrangement. The illumination procedure for voxel sets should thus follow the illumination for separate gene expression while the individual voxels within the voxel set should follow illumination for concurrent gene expression.

Slicing an object along the Z-axis of the build volume, which is perpendicular to the direction of both red and green incident light, generates a secondary building block, a Z-slice. The thickness of said Z-slices, which are parallel to the XY plane, is in the most general sense determined by the intensity profile of one of the incident beams whose span in the Z direction is the greatest. This is a requirement when the individual Z-slices are to be independent of each other. However, the intensity profiles are not necessarily very binary and therefore some light can leak beyond the prescribed Z-slice boundary. This is then also further affected by light scattering. The benefit of having Z-slices that are independent or near independent of each other, is that the order in which they are illuminated does not matter when it comes to the spatial dimension. Said property is in a direct contrast to the majority of existing 3D printing techniques where building an object layer by layer can only be achieved in a continuous sequence in a fixed direction.

Each Z-slice can be further broken down into a number of bands whose width is governed by the gap in the red light intensity profile. Each band is then occupied by a single voxel set, which can be discontinuous or not. Figure 8.1(a) shows a Z-slice segmented into five bands of which one is empty and one contains a discontinuous voxel set. Note that individual voxels are not required to conform to a grid. Furthermore, as shown in Figure 8.1(b), bands do not have to be evenly spaced and can even overlap, as long as voxel sets do not. However, overlapping the bands should be avoided unless the overlapped and not directly illuminated voxel set is inactive during illumination.

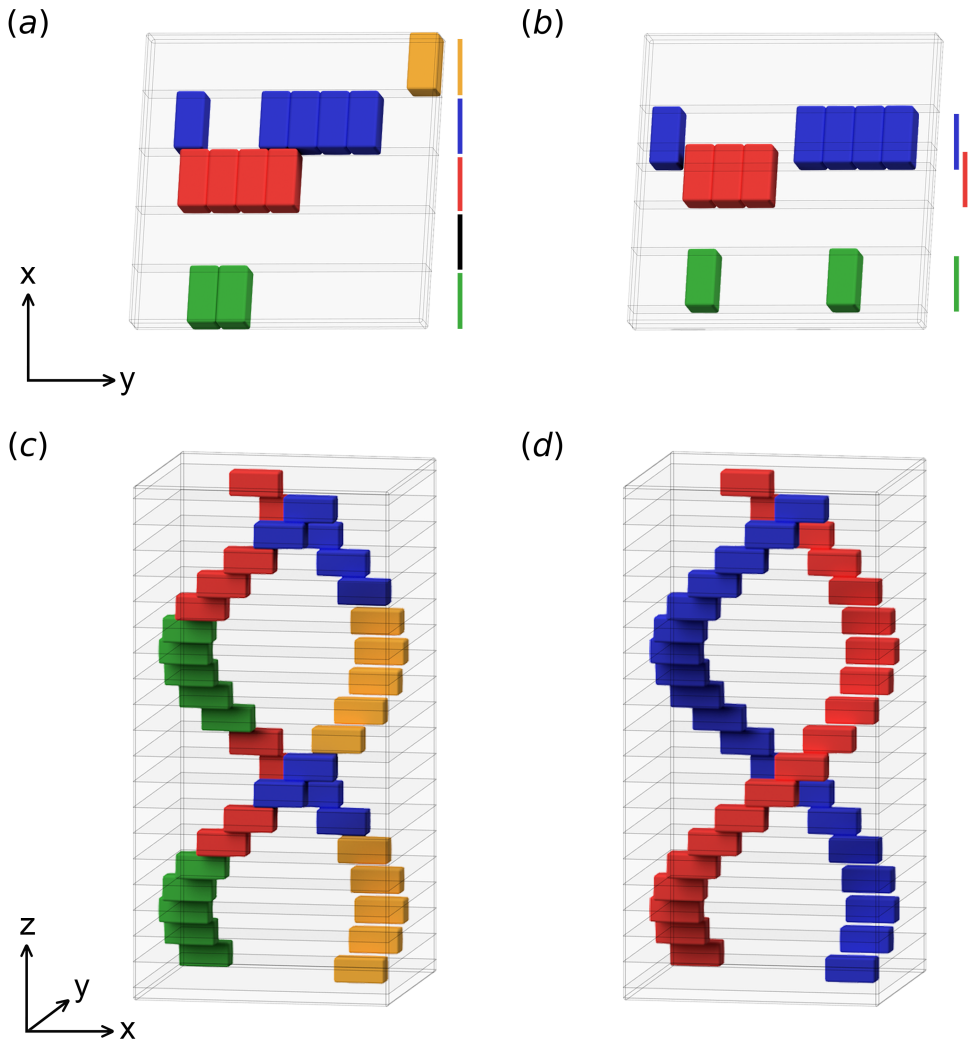


Figure 8.1: *Schematic of spatial slicing. Individual voxels are represented by a rectangular cuboid.* (*a*) *Z-slice fully segmented into five non-overlapping bands with four voxel sets.* (*b*) *Z-slice partially segmented into three bands, some with overlap, with three voxel sets.* (*c*) *Double helix example object segmented into* 19 *Z-slices and four colour-coded X-slices. The distribution of voxel sets per X-slice is as even as possible. Segmentation was done in a way to keep X-slices as planar as possible while maintaining object fidelity.* (*d*) *Double helix example object segmented into* 19 *Z-slices and two colour-coded X-slices.*

Grouping one band from each Z-slice results in X-slices, which are parallel to the incident red light and perpendicular to the incident green light. However, as all bands in any given Z-slice are not necessarily occupied by a voxel set, due to geometry or segmentation of the object, X-slices can also be discontinuous. Furthermore, the grouped bands are not required to be collinear in the Z-direction. Any band can be arbitrarily chosen within a given Z-slice to form part of one X-slice. Figure 8.1(*c*) shows an example object segmented into four discontinuous colour-coded X-slices. With this segmentation the X-slices most resemble a vertical planar layer; however,

due to the small resolution of an individual voxel and an arbitrary limit of four X-slices, the fidelity of the object can only be maintained by including bands which are not entirely within the same plane. Foregoing any restriction of band position certain geometries can be segmented into fewer X-slices. This is the case with a double helix as shown in Figure 8.1(d).

While the spatial resolution is conditioned by the light intensity profiles, the temporal resolution is determined by the time allocated to each voxel set during which gene expression is to occur. Due to the geometry of the intensity profiles, it is not necessary to split the print duration into an amount of temporal slices which equals the amount of voxel sets. It is sufficient to split the duration of the print into segments that correspond to each X-slice. This follows from the independence of Z-slices, which under separate gene expression illumination allows for one active voxel set for each Z-slice. Because the amount of total gene expression is limited by the duration of the print, it is best to minimize the amount of X-slices in order to maximize the amount of total gene expression available for each X-slice and thus its contrast.

Although the order in which Z-slices and X-slices are illuminated is not important with regards to the spatial distribution, it can be important with regards to the temporal distribution. Splitting the duration of the print into equally long temporal slices will cause X-slices that are illuminated later in the print to exhibit greater gene expression when compared to X-slices illuminated earlier in the print. This is due to cell growth and the resulting larger cell population later in the print. Two ways to mitigate this effect are either to split the print into unequally long temporal slices or to split the print into a number of temporal slices, which is a multiple of the number of X-slices. Each X-slice is then illuminated multiple times. The first option, shown in Figure 8.2(a), can allocate an exactly even amount of maximum available total gene expression, provided that the population growth curve is known. On the other hand, the second option, shown in Figure 8.2(b), can achieve an approximately even distribution but can be less susceptible to the variability of the population growth, as the entire object is illuminated in a shorter time span. More repeated illuminations the better the approximation. Additionally, if the duration of illumination of the entire X-slice is comparable to the duration of the last temporal slice, the second option is less susceptible to final voxel sets having less time to express genes due to the end of print. However, proper time allocation can be achieved by sacrificing some print time at the end to introduce another temporal slice in which voxel sets are only deactivated after sufficiently long active period.

The order of illumination of Z-slices within each X-slice also becomes restricted if the duration of illumination of the entire X-slice is comparable to the duration of temporal slices. In such a case the order of illumination of Z-slices should be the same for all X-slices. This ensures that the first and last voxel set in the X-slice have the same allocated time of growth before the next voxel set in the respective Z-slice is illuminated, as when that occurs the previous voxel set is deactivated.

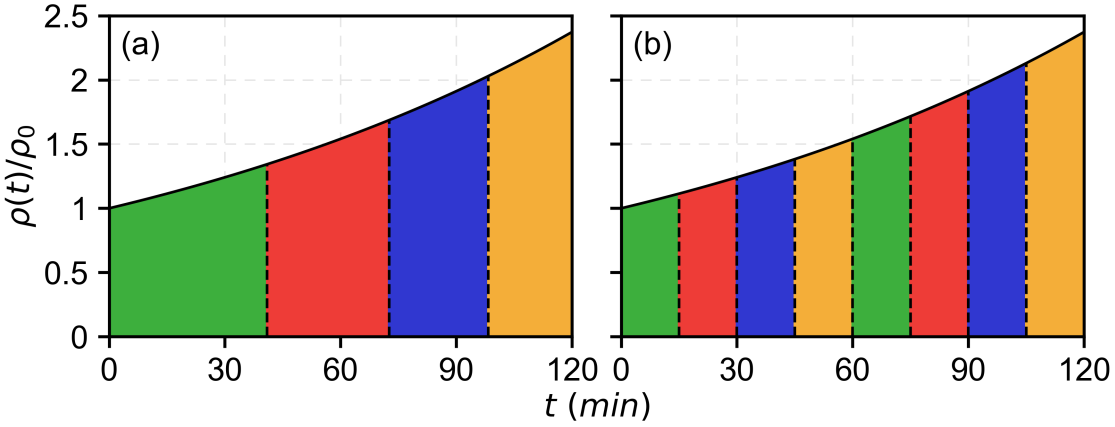


Figure 8.2: *Normalized exponentially growing cell density segmented into temporal slices. Each colored segment of the graph corresponds to a temporal slice whose colour refers to its corresponding X-slice. (a) Segmentation of the print time into four unevenly long temporal slices with an even area under the cell density graph. (a) Segmentation of the print time into eight 15 minute long temporal slices with two temporal slices per X-slice. Allocation of temporal slices to X-slices can be mirrored after the first half of print to achieve an even more even distribution.*

The intervals of uneven temporal slices can be determined using the following sequence:

$$\int_{t_n}^{t_{n+1}} \rho(t)\,dt = \frac{1}{N}\int_{0}^{t_{End}} \rho(t)\,dt\,,$$
$$\rho(t_{n+1}) = \frac{1}{N}\left(\rho(t_{End}) - \rho(0)\right) + \rho(t_n)\,, \tag{8.1}$$

where $\rho(t)$ is the density of cells and N is the number of temporal slices. In the case of exponential growth, the formula for the boundaries of temporal slices is:

$$t_n = \frac{1}{k_{growth}} \ln\left(1 + \frac{n}{N}\left(e^{k_{growth}t_{End}} - 1\right)\right). \tag{8.2}$$

Sequence (8.1) assumes constant gene expression rate between temporal slices. If varying expression rates were also to be accounted for, total gene expression density, $g(t)$, should be used instead of $\rho(t)$.

8.2 Double Helix

A double helix was chosen as a test print due to its nontrivial geometry and the ability to slice it into only two X-slices. The main feature of the geometry is that the resulting X-slices move from front to back of the build volume with respect to the incident green and red light. One X-slice thus cumulatively obscures the other in every way along the height of the double helix.

8.2.1 Illumination

The four geometrical properties of the double helix are its twist radius, height, twist rotation and the angle between the individual helices. The illumination procedure was determined for a double helix with these values set to 3 mm, 22 mm, 2π rad and π rad respectively. The double helix was segmented into 22 Z-slices with each helix being its own X-slice. As such, the spatial slicing is almost identical to the one shown in Figure 8.1(d). Note that the thickness of Z-slices is thus 1 mm, whereas the span of the red light intensity is 2.3 mm. To account for this, the relative position of the green beam with regards to the red beam was adjusted. This was done by repositioning the green beam towards the top of the red beam's intensity profile. With such a configuration, the red intensity profile is effectively split into two $\approx$1 mm regions, one that overlaps the green intensity profile and one that does not (Figure 8.3). This geometry was exploited to reduce the required illumination time at each individual voxel. Since illumination for separate gene expression follows the deactivation procedure (Chapter 7), illumination of each voxel consists of two steps. With the given overlap of the green and red light these two steps can occur at the same time but for two different voxels. While the second voxels is being activated by both the green beam and the top of the red beam, the first voxel is being deactivated by the bottom part of the red beam. However, due to voxels following a curve, deactivation of a voxel occurs at a slightly different position compared to it's activation. Fortunately, given the helix parameters and voxel size, the discrepancy is not significant. Accordingly, this geometry also requires that the voxels are illuminated in a fixed sequence from bottom to top.

Due to imperfect knowledge of the growth curve the three hour print time was segmented into eight 15 minute temporal slices after the first hour. Temporal slices follow the pattern shown in Figure 8.2(b) except that temporal slices alternate between only two X-slices. Both X-slices consist of 22 Z-slices in which there is a corresponding voxel set of a single voxel. Each voxel can thus be allocated 40 s of illumination, for both activation and deactivation. Given that activation occurs with the presence of red light, green light intensity was set very high in order to achieve a large η_{high}, more precisely k_1 was set to equal $5 \cdot k_2$. Due to the large η_{high}, 7.39 still

approximately holds and was used to determine the red light intensity. Target η at the surface of the build volume was set to = 0.1, which is approximately achieved with red light intensity of 27.6 W/m^2 after deactivation. The corresponding peak green light intensity was thus set to 75 W/m^2.

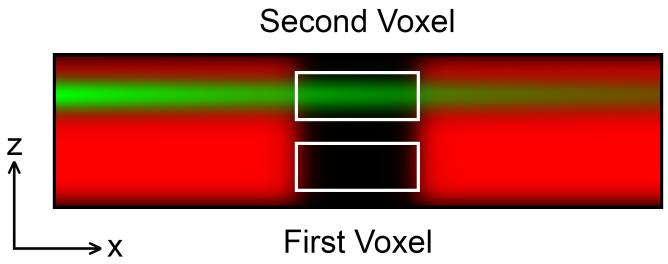


Figure 8.3: *Schematic representation of the red and green light intensity profiles overlap used during the double helix print. White rectangles indicate the approximate positions of the two affected voxels.*

In order to maintain the same intensity at each voxel, the incident intensities were varied to accommodate for the different attenuation factors. Figure 8.4 shows incident light intensities over time normalized to the respective intensity required at all voxels. Intensities are shown for a single illumination of the entire double helix. The illumination of an individual helix is just short of 15 minutes to accommodate for time spent moving between voxels.

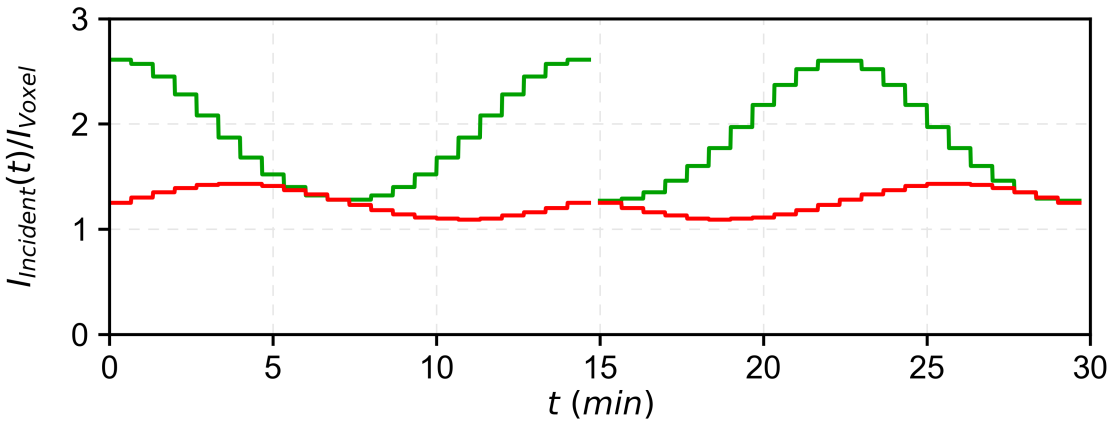


Figure 8.4: *Incident intensities used during the print of a double helix normalized to the respective intensity required at all voxels. The graphs' colour corresponds to the colour of incident light. Attenuation coefficients used were* μ_G = 120 m^{-1} *for green and* μ_R = 45 m^{-1} *for red light.*

Figure 8.5 shows the simulation of the double helix print. The bar at the top of the helix is there due to a lack of a deactivation step. Following illumination shown in Figure 8.4, the top and last two voxels in each helix only get exposed to both green and red light illumination and never only red light illumination. This results in the local volume that is illuminated by the green beam, to be constantly active throughout the print, resulting in significant gene expression.

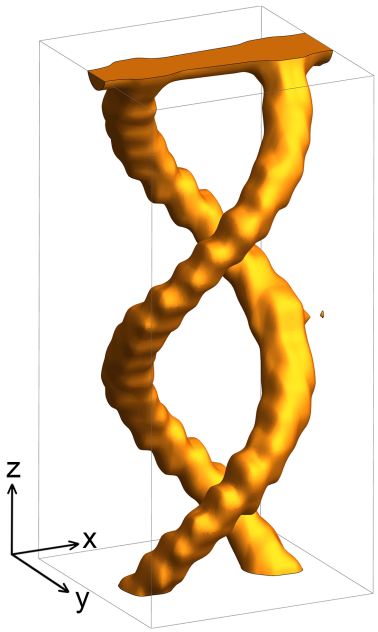


Figure 8.5: *Simulation of gene expression in the double helix print. Each voxel is illuminated with intensities according to Figure 8.4 four times over two hours. Shown is the volume with total gene expression above* 25% *of the maximum.*

8.2.2 Print Results

Figure 8.6 shows the fluorescence image of slices containing the double helix. There are 20 physical slices due to them being slightly thicker than 1 mm on average and due to the misalignment of the physical slices with the Z-slices. The misalignment resulted in the bottom most Z-slice to be cut in two and the remaining bit exhibited too little fluorescence to be included as a part of the double helix.

Double helix was reconstructed from the fluorescent image by extracting all slices as slices of interest. Following that, a threshold was manually determined for each slice. The variability of the individual thresholds between slices was $\pm 6\%$ from the average threshold value. Values above the threshold were assigned white and values below were assigned black. The largest two connected white areas were selected to remain. Any black islands within the two white areas were painted white. An example resulting image is shown in Figure 8.7(a). The binary images were then further smoothed (Figure 8.7(b)). Lastly, all images were stacked on top of each other with a spacing of 1 mm. White areas were then thickened to 1 mm, which resulted in a 3D object shown in Figure 8.7(c).

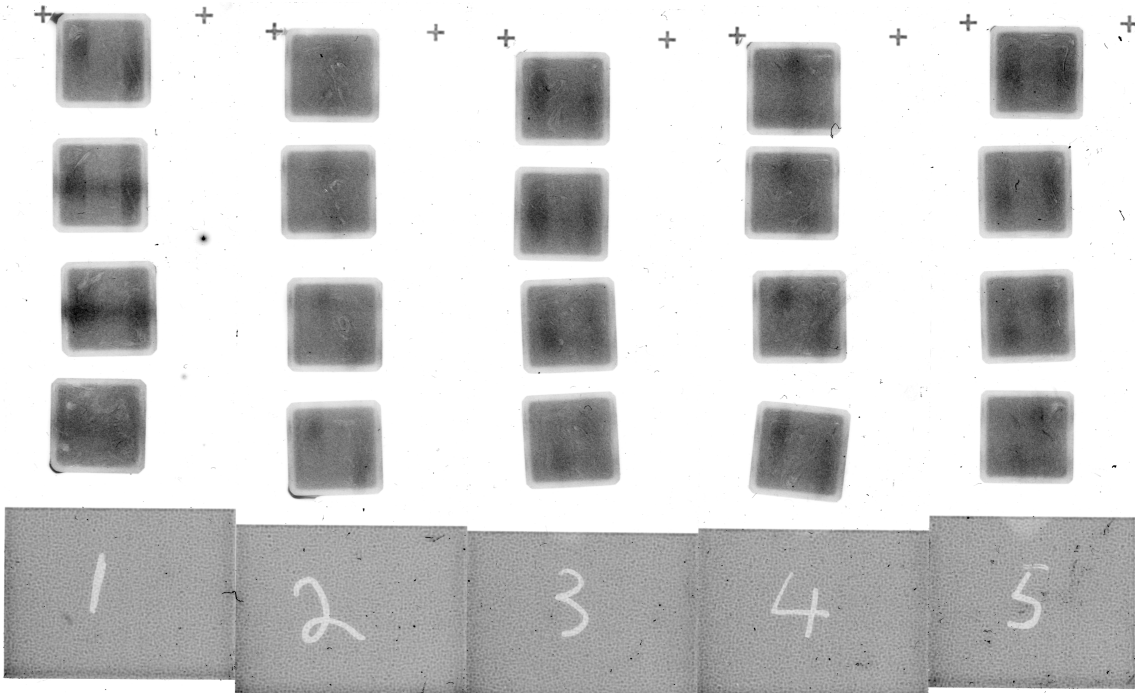


Figure 8.6: *Fluorescence image of physical slices from the double helix print. The leftmost bottom slice corresponds to the top of the double helix and the rightmost top slice corresponds to the bottom of the double helix. Numbers on the microscope slides indicate the position of the slices in build volume. The color range of the image that corresponds to pixel values was adjusted for better visualisation.*

The reconstructed object resembles a double helix quite well. Certain parts of the double helix, where voxels appear wider than expected, are likely due to green light scattering and misalignment of physical slices to Z-slices. If a physical slice cuts two Z-slices in half, it also cuts two neighbouring voxels in half. This results in an apparently wider voxel with lower intensity in the fluorescent image, as the two halves of two voxels appear side by side. On the other hand, there are some narrow parts. These are likely also due to two reasons. The first is that the narrowing occurs mostly on one helix, which is the helix that was illuminated second. This means that at the end of the print there was less time allocated for gene expression to occur in this helix. The second is that these narrowings are in areas of the helix where the distance between two consecutive voxels is greatest in the X direction. This means that position of red light deactivating the previous voxel is offset by the greatest possible amount. Due to there being red and green light present during activation, η will also be lower outside the voxel. The larger red light offset thus results in red light gap being positioned somewhat over areas outside the intended voxel where η is lower to begin with. These narrowings are present in the simulation but are much more subtle. Overall, it was expected for the entire object to have a slightly worse contrast due to light scattering between the Z-slices, which were considered to be independent when the illumination procedure was determined.

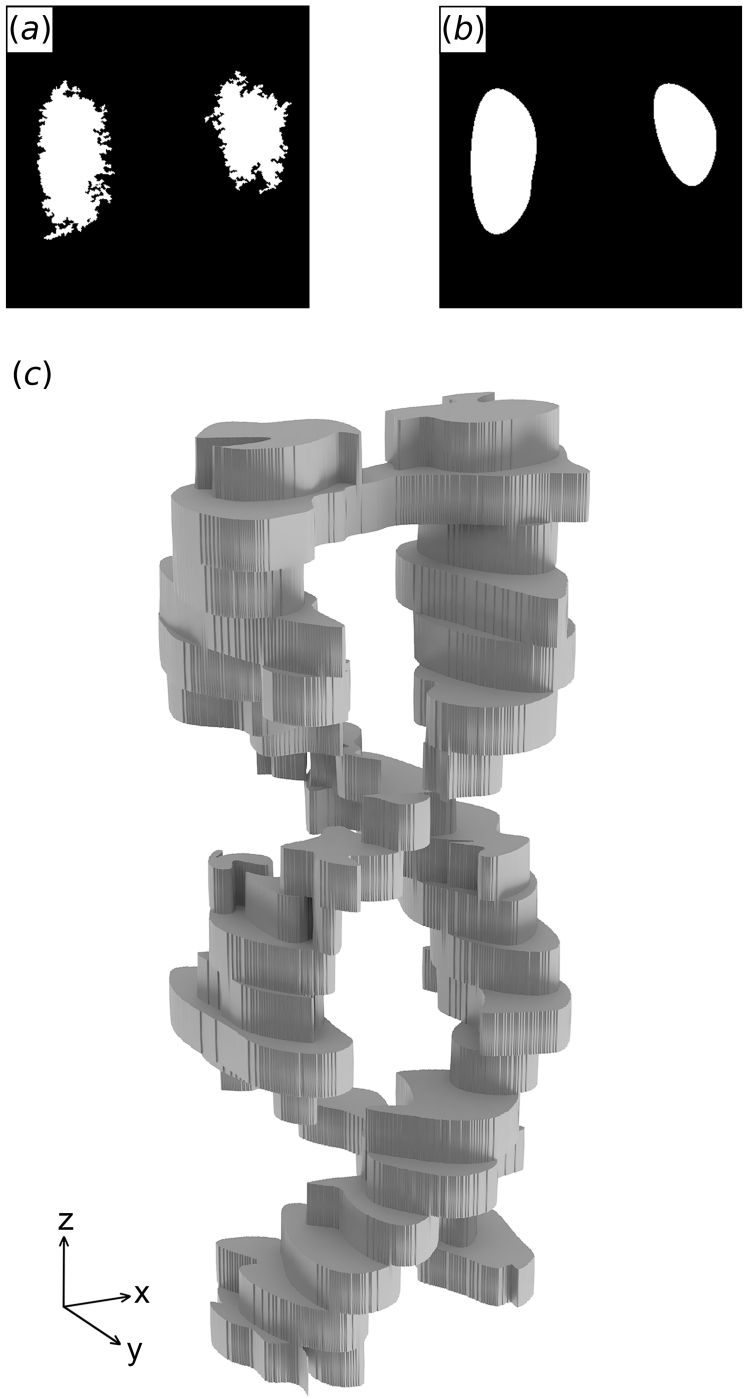


Figure 8.7: *Reconstruction of a double helix from the fluorescence image of the physical slices.* (*a*) *Binary image of one of the imaged slices.* (*b*) *Smoothed binary image of the slice shown in* (*a*). (*c*) *3D reconstruction obtained from a stack of smoothed binary images with a thickness of* 1 *mm.*

8.3 Conclusion

As shown by the results of the double helix print it is possible for gene expression to occur in 3D geometry. While the double helix is very amenable to spatial and temporal slicing, it does offer significant geometrical complexity to showcase the ability of the method to induce gene expression in bespoke geometry. However, it can be quite restrictive to try and print 3D objects that would require more X-slices due to the relatively low contrast and limited amount of time that can be allocated for illumination of each X-slice. The presence of light scattering is also expected to have an increasingly more negative effect on the fidelity of the print the larger the object. The print of the double helix further confirmed that it is possible to induce gene expression in voxels that are shadowed by previously activated voxels. However, this is of course not expected to be the case if gene expression were to induce a change in opacity with regards to green and red light. Furthermore, any local change in the refractive index due to gene expression can also be detrimental to the fidelity of the print, if red or green beam are required to pass through areas of varying refractive index.

Chapter 9

Conclusions and Future Work

9.1 Conclusions

Work presented in this thesis resulted in a successful development of a novel 3D printing method that can utilize engineered hydrogel suspended *E. coli* to deposit biological material in an arbitrary 3D geometry. The first objective, of no object requiring printable support, is fulfilled by default by having the build volume filled with hydrogel, which provides the necessary support. The second objective is achieved by employing the CcaSR two-component signal transduction system, which can be activated by green light and deactivated by red light. With proper distribution of light illumination, localized gene expression is demonstrated within a voxel and with the capabilities of the translation system said voxel can be positioned in an arbitrary location within the build volume. The third objective is achieved partially through the fulfilment of the first objective, as this allows the object's parts to be 3D-printed in an arbitrary order, and partially by the spatial distribution of the illuminating light. While the spatial distribution of light does allow for object generation that is nonplanar, it also provides its own restrictions related to the geometry of the incoming light. The last objective is also achieved by default due to the setup of the method. As long as the cells populating the build volume are properly bioengineered to produce various materials there is nothing inherent in the investigated method that would prevent multi-material production. Due to the method employing light to activate production, multi-material prints can be achieved by *simply* engineering the cells to produce a given material in response to a given colour of light. From the optical perspective it is then also relatively simple to introduce more colours into the existing optical paths and achieve the same level of control for multiple materials.

The results of steady-state experiments, presented in Chapter 5, indicated the importance of stray light on the extent and shape of gene expression. Both red and green light have a noticeable effect on gene expression even at relatively low

intensities. With green light this manifests as unwanted gene expression, which is quite noticeable when the effect of green light illumination only competes with the effect of cell growth. Because dark conversion rate of active photoreceptors is negligible and growth is relatively slow, activation caused by weak stray green light accumulates significantly over time. It has been shown that with the system used a good way to counteract this unwanted gene expression caused by stray green light is the presence of red light with its own stray and scattered components. However, this same red light can significantly interfere with gene expression in the voxel. A best fit estimate was performed on the ratio between gene expression in the voxel and gene expression in the suppressed region versus green light intensity in the presence of red light illumination in order to estimate the relative amount of red light present in the voxel. It was found to be significant and it's effect could not be ignored when predicting gene expression and determining illumination procedures.

Two sets of steady-state experiments further showed that gene expression during incubation is negligible and to some degree showed the expected result that gene expression is correlated to the growth of the cell population. From steady-state experiments it has also been observed that any photoreceptors that have been activated before the experiment will contribute to overall gene expression. This is again due to the persistence of the active state of photoreceptors. Lastly, the ratios of gene expression in voxels and suppressed regions to background gene expression of steady-state experiments were used to perform a best fit estimates. The results of the best fit estimates yielded the maximum signal to noise ratio.

In Chapter 6 the deactivation procedure was introduced where the voxels is illuminated by green light followed by illumination of red light. It was shown through mathematical derivation of the procedure that it behaves fundamentally different to steady-state approach. The steady-state approach relies on the ratio of red to green light intensity to determine the ratio of gene expression rate in the voxel and the suppressed region. Whereas with the deactivation procedure the ratio of gene expression rates in the presence of red light leakage is mainly determined by the gene expression rate in the suppressed region, which can be chosen arbitrarily regardless of light intensities. It has also been shown that the deactivation procedure is a better approach for the estimated red light leakage present in this system.

Intensities of light should be as high as possible for both steady-state approach and the deactivation procedure. This way transient effects are as short as possible and thus have a lesser impact average ratio of gene expression rates. To some extent green light intensity also has to be high in order to sufficiently counteract the dilution of active photoreceptors due to cell population growth.

The results from single illumination experiments, where samples were subjected to the deactivation procedure right after the incubation period, presented in Chapter 6, further confirmed that persistent illumination is not required for gene expression to occur in a significant fashion and that well localized voxels can be printed using this procedure. Due to the dilution effect resulting from growth, further experiments were run where illumination following the deactivation procedure was applied periodically instead of subjecting the samples to only a single illumination. With these experiments gene expression rate was refreshed to optimal values at four different periods. As expected the results showed the same total gene expression for all four periods.

By running experiments where illumination was not constant, the effects of individual magnitudes of the forward and reverse photoconversion rates became apparent. Green and red light intensities determined by employing the photoconversion rates measured by Olson et al. [67] were too high in order to achieve the desired results. For this reason two sets of simulations were run for all experiments presented in Chapter 6. One set used the reported photoconversion values and the other set used photoconversion values that are five times greater. The factor of five was estimated by observing the influence of red light leakage on gene expression in the voxel. By qualitatively comparing the results of simulations with the measurements of experiments it was concluded that indeed the actual photoconversion rates are more likely to be five times greater than reported.

In Chapter 7 three illumination approaches were investigated for three different arrangements of two voxels in a plane. Solutions of the optogenetic model were derived for each arrangement and illumination procedure given two conditions: equal gene expression within both voxels and effectively minimal gene expression without. Alternating illumination was used as the simplest approach. Due to constant illumination when illuminating a given voxel, it behaves similarly to steady-state illumination provided that the light intensities are high enough. While the illumination procedure performed well in terms of generating two separate voxels it has two unnecessary restrictions: constant and concurrent intensities. Illumination procedure for concurrent gene expression turned out to be somewhat more effective that alternating illumination on average; however, calculating the required radiant exposure was much more complex. The major performance improvement over the alternating illumination was for voxels in horizontal arrangement due to low interaction of red light with both of the voxels. Illumination for separate gene expression is similar to alternating illumination without the unnecessary restrictions. As such, it is effectively an illumination procedure that utilized the deactivation procedure at individual voxels. Given its simplicity and performance it was deemed superior to concurrent gene expression illumination in vertical and diagonal arrangements.

Due to the determination of illumination procedures relying only on the fraction of active-state photoreceptors, all experiments were also simulated to further verify the ability of the model to predict gene expression and to see whether transient effects unexpectedly affect experiments. By comparing simulations with experiments, both qualitatively and quantitatively, it was shown that the model is quite accurate in predicting the outcome of experiments. Some discrepancies can be seen, which could be attributed to light scattering and/or an unknown change in the ratio between maximum and background gene expression.

Finally, in Chapter 8 spatial and two types of temporal slicing of 3D objects were introduced. Due to the build volume being filled by hydrogel and thus providing support for potential part of a 3D object, spatial slicing can occur in an arbitrary order, the only restrictions come from the geometry of illuminating light and the fact that red light while being used to define one voxel will deactivate other previously activated voxels in the same plane. This deactivation is also one reason for temporal slicing, as voxels need to be given time to produce material before they are deactivated. The second reason is due to the growing population of cells during print. For a fixed gene expression rate the amount of material produced will vary over the course of the print. Temporal slicing is thus done in such a way to alleviate these effects and attempts to achieve a homogeneous total gene expression in all voxels. To test the spatial and temporal slicing a double helix was successfully printed using separate gene expression illumination. Due to its relative geometrical complexity it showcased the ability of the method to generate an arbitrary object using nonconventional spatiotemporal slicing, hydrogel suspended bacteria and red and green light illumination.

Overall, the bottom up investigation in this thesis, from localized gene expression to 3D object generation, has provided a substantial insight into individual aspects of the 3D printing method. Such as, knowledge of light distribution is important and stray and scattered light may not be readily neglected and should be minimized as much as possible. Persistence of CcaSR photoreceptors results in significant negative influence of the preactivated photoreceptors. Gene expression does not require persistent illumination and contrast may be improved by exploiting the transient effects of photoreceptor activation and deactivation. The geometry of light illumination plays a major role in determining various illumination procedures for more complex object geometries. The evolving cell population requires slicing of objects to include temporal considerations. Knowing these limitations, further systems can be devised which attempt to mitigate or solve the issues and result in prints with a better contrast, resolution, print time, larger build volumes, different materials and higher object density.

9.2 Future work

The work presented in the thesis has demonstrated the viability of the proposed 3D printing method to selectively express genes in bacteria in a 3D volume. However, the amount of produced material during the presented experiments is not sufficient to generate a solid object based on the produced material alone. While the specific amounts were not measured in this work, it is clear from the medium formulation that the available mass for material production, that is not water, is only ≈2%. Additionally, the experiments concluded well before the stationary phase of cell growth is reached leaving plenty of food. Therefore, even if all the food is consumed for exclusively desired material production, the object would still be mostly water by mass. Circumventing this issue requires research into ways of maintaining the cell population state and continually providing food or material to be converted into the 3D object. Preferably the cell population would be kept in the exponential phase to maximize material production; however, sufficient material production could presumably be achieved in the stationary phase. With such a system in place and depending on the stability of the cell population, temporal slicing would likely not be necessary. While material production would no longer vary due to the change in cell population, there would be an ever increasing presence of the printed object. The effect of the 3D object on the ability of cells to produce even more material would need to be investigated but more importantly the issue of maintaining a high level of active-photoreceptors would also need solving. When an object is generated it would in most cases have properties that are by design different to that of the supporting environment such as the hydrogel. If optical properties differ significantly, spatial slicing presented in this work would no longer suffice, as it does not consider object occlusion. The more the object manifests during print the more the spatial slicing would need to be adapted. Certain geometries might even prevent the use of the proposed spatial slicing, as the homogeneity or fidelity of the 3D object might be affected later in the print.

Increasing the total build volume in the axes parallel to incident light beams or increasing the cell density would require research into hydrogels or its additives in order to minimize the hydrogel turbidity. This step is crucial to minimize the blurring effects of scattering or more generally the attenuation in order to maintain a reasonable distribution of light intensity at all depths of the build volume. Beyond adapting the hydrogel or perhaps even the cells, the issue of turbidity could potentially be reduced by changing the geometry of the incoming light. By having a specially shaped beam of deactivating light overlap the beam of activating light, the build volume would only be limited in one dimension by the incident light and could be shaped akin to a panel. A different option can include focusing the activating

light reducing the effects arising from excessive attenuation and potentially reducing the required intensities of deactivating light.

Further investigations and improvements should also be attempted on the photoreceptors system. In this work the dynamic range of gene expression was significantly lower than what was previously reported for the same system. It is hypothesized that this is due to the difference of the metabolic pathway; however, it is unclear what other factors might affect gene expression in this way. The photosensing system in general should probably be modified in a way to maintain a constant active signal or a signal that maintains a constant response which can no longer be deactivated after a short time after activation. With such a photosensing system the proposed method could be utilized during the incubation period with a single illumination pattern leaving the cells in the build volume to grow the object without any further intervention with light.

To utilize the full potential of microbial cell factories, the sensing system should also be improved in a way that is responds to multiple colours of light, with each colour corresponding to a different desired metabolic pathway. Such an adaptation is rather crucial in order to achieve multi-material or composite material 3D objects. Notably the sensing and metabolic pathways can be distributed to different strains of cells. For composite materials two different metabolic pathways, within the same or different cells, could even correspond to the same colour of light. Whether or not such adaptations are all compatible with other aspects of the printing method is the big question.

Bibliography

[1] S. S. Paul, H. Trabelsi, Y. Yaseen, U. Basu, H. A. Altaii and D. Dhali, *Chapter 2 - Advances in long DNA synthesis*, in *Microbial Cell Factories Engineering for Production of Biomolecules*, edited by V. Singh (Academic Press, 2021) pp. 21–36.

[2] C. P. Foong, M. Higuchi-Takeuchi, A. D. Malay, N. A. Oktaviani, C. Thagun and K. Numata, *A marine photosynthetic microbial cell factory as a platform for spider silk production*, Communications Biology **3**, 357 (2020).

[3] D. Lahiri, M. Nag, B. Dutta, A. Dey, T. Sarkar, S. Pati, H. A. Edinur, Z. Abdul Kari, N. H. Mohd Noor and R. R. Ray, *Bacterial Cellulose: Production, Characterization, and Application as Antimicrobial Agent.*, International journal of molecular sciences **22** (2021).

[4] J. Lee, H. J. Park, M. Moon, J.-S. Lee and K. Min, *Recent progress and challenges in microbial polyhydroxybutyrate (PHB) production from CO2 as a sustainable feedstock: A state-of-the-art review*, Bioresource Technology **339**, 125616 (2021).

[5] L. Liang, C. Heveran, R. Liu, R. T. Gill, A. Nagarajan, J. Cameron, M. Hubler, W. V. I. I. I. Srubar and S. M. Cook, *Rational Control of Calcium Carbonate Precipitation by Engineered Escherichia coli*, ACS Synth. Biol. **7**, 2497 (2018).

[6] E. M. Spiesz, D. T. Schmieden, A. M. Grande, K. Liang, J. Schwiedrzik, F. Natalio, J. Michler, S. J. Garcia, M.-E. Aubin-Tam and A. S. Meyer, *Bacterially Produced, Nacre-Inspired Composite Materials*, Small **15**, 1805312 (2019).

[7] K. Kaur, V. Dattajirao, V. Shrivastava and U. Bhardwaj, *Isolation and Characterization of Chitosan-Producing Bacteria from Beaches of Chennai, India.*, Enzyme research **2012**, 421683 (2012).

[8] K. Persson, W. Russell, M. Mörgelin and H. Herwald, *The Conversion of Fibrinogen to Fibrin at the Surface of Curliated Escherichia coli Bacteria Leads to the Generation of Proinflammatory Fibrinopeptides*, Journal of Biological Chemistry **278**, 31884 (2003).

[9] E. N. Hayta, M. J. Ertelt, M. Kretschmer and O. Lieleg, *Bacterial Materials: Applications of Natural and Modified Biofilms*, Advanced Materials Interfaces **8**, 2101024 (2021).

[10] S. V. Murphy and A. Atala, *3D bioprinting of tissues and organs*, Nature Biotechnology **32**, 773 (2014).

[11] Y. Ze, R. Wang, H. Deng, Z. Zhou, X. Chen, L. Huang and Y. Yao, *Three-dimensional bioprinting: A cutting-edge tool for designing and fabricating engineered living materials*, Biomaterials Advances **140**, 213053 (2022).

[12] M. Hospodiuk, M. Dey, D. Sosnoski and I. T. Ozbolat, *The bioink: A comprehensive review on bioprintable materials*, Biotechnology Advances **35**, 217 (2017).

[13] B. A. E. Lehner, D. T. Schmieden and A. S. Meyer, *A Straightforward Approach for 3D Bacterial Printing*, ACS Synth. Biol. **6**, 1124 (2017).

[14] M. Schaffner, P. A. Rühs, F. Coulter, S. Kilcher and A. R. Studart, *3D printing of bacteria into functional complex materials*, Science Advances **3**, eaao6804 (2017).

[15] F. Moser, E. Tham, L. M. González, T. K. Lu and C. A. Voigt, *Light-Controlled, High-Resolution Patterning of Living Engineered Bacteria Onto Textiles, Ceramics, and Plastic*, Advanced Functional Materials **29**, 1901788 (2019).

[16] K. Dubbin, Z. Dong, D. M. Park, J. Alvarado, J. Su, E. Wasson, C. Robertson, J. Jackson, A. Bose, M. L. Moya, Y. Jiao and W. F. Hynes, *Projection Microstereolithographic Microbial Bioprinting for Engineered Biofilms*, Nano Lett. **21**, 1352 (2021).

[17] N. Gohil, G. Bhattacharjee and V. Singh, *Chapter 1 - An introduction to microbial cell factories for production of biomolecules*, in *Microbial Cell Factories Engineering for Production of Biomolecules*, edited by V. Singh (Academic Press, 2021) pp. 1–19.

[18] C. Engler, R. Kandzia and S. Marillonnet, *A One Pot, One Step, Precision Cloning Method with High Throughput Capability*, PLOS ONE **3**, 1 (2008).

[19] D. G. Gibson, L. Young, R.-Y. Chuang, J. C. Venter, C. A. Hutchison and H. O. Smith, *Enzymatic assembly of DNA molecules up to several hundred kilobases*, Nature Methods **6**, 343 (2009).

[20] A. L. Demain and J. L. Adrio, *Contributions of Microorganisms to Industrial Biology*, Molecular Biotechnology **38**, 41 (2008).

[21] M. N. Baeshen and A. M. Al-Hejin, *Production of Biopharmaceuticals in E. coli: Current Scenario and Future Perspectives*, Journal of Microbiology and Biotechnology **25**, 953 (2015).

[22] J. van Dijl and M. Hecker, *Bacillus subtilis: from soil bacterium to super-secreting cell factory*, Microbial Cell Factories **12**, 3 (2013).

[23] B. Yilmaz, A. Al Rashid, Y. A. Mou, Z. Evis and M. Koç, *Bioprinting: A review of processes, materials and applications*, Bioprinting **23**, e00148 (2021).

[24] C. M. Heveran, S. L. Williams, J. Qiu, J. Artier, M. H. Hubler, S. M. Cook, J. C. Cameron and W. V. Srubar, *Biomineralization and Successive Regeneration of Engineered Living Building Materials*, Matter **2**, 481 (2020).

[25] J. Qiu, J. Artier, S. Cook, W. V. Srubar, J. C. Cameron and M. H. Hubler, *Engineering living building materials for enhanced bacterial viability and mechanical properties*, iScience **24**, 102083 (2021).

[26] R. Mitra, T. Xu, H. Xiang and J. Han, *Current developments on polyhydroxyalkanoates synthesis by using halophiles as a promising cell factory*, Microbial Cell Factories **19**, 86 (2020).

[27] C. Gilbert and T. Ellis, *Biological Engineered Living Materials: Growing Functional Materials with Genetically Programmable Properties*, ACS Synth. Biol. **8**, 1 (2019).

[28] O. Jeon, Y. B. Lee, H. Jeong, S. J. Lee, D. Wells and E. Alsberg, *Individual cell-only bioink and photocurable supporting medium for 3D printing and generation of engineered tissues with complex geometries*, Mater. Horiz. **6**, 1625 (2019).

[29] C. M. Smith, J. J. Christian, W. L. Warren and S. K. Williams, *Characterizing Environmental Factors that Impact the Viability of Tissue-Engineered Constructs Fabricated by a Direct-Write Bioassembly Tool*, Tissue Engineering **13**, 373 (2007), pMID: 17518570.

[30] S. Derakhshanfar, R. Mbeleck, K. Xu, X. Zhang, W. Zhong and M. Xing, *3D bioprinting for biomedical devices and tissue engineering: A review of recent trends and advances*, Bioactive Materials **3**, 144 (2018).

[31] J. Li, M. Chen, X. Fan and H. Zhou, *Recent advances in bioprinting techniques: approaches, applications and future prospects*, Journal of Translational Medicine **14**, 271 (2016).

[32] J. Malda, J. Visser, F. P. Melchels, T. Jüngst, W. E. Hennink, W. J. A. Dhert, J. Groll and D. W. Hutmacher, *25th Anniversary Article: Engineering Hydrogels for Biofabrication*, Advanced Materials **25**, 5011 (2013).

[33] C. C. Chang, E. D. Boland, S. K. Williams and J. B. Hoying, *Direct-write bioprinting three-dimensional biohybrid systems for future regenerative therapies*, Journal of Biomedical Materials Research Part B: Applied Biomaterials **98B**, 160 (2011).

[34] M. L. Bedell, A. M. Navara, Y. Du, S. Zhang and A. G. Mikos, *Polymeric Systems for Bioprinting*, Chem. Rev. **120**, 10744 (2020).

[35] S. Khalil and W. Sun, *Biopolymer deposition for freeform fabrication of hydrogel tissue constructs*, Materials Science and Engineering: C **27**, 469 (2007), next Generation Biomaterials.

[36] C. M. Smith, A. L. Stone, R. L. Parkhill, R. L. Stewart, M. W. Simpkins, A. M. Kachurin, W. L. Warren and S. K. Williams, *Three-Dimensional BioAssembly Tool for Generating Viable Tissue-Engineered Constructs*, Tissue Engineering **10**, 1566 (2004), pMID: 15588416.

[37] K. Hölzl, S. Lin, L. Tytgat, S. V. Vlierberghe, L. Gu and A. Ovsianikov, *Bioink properties before, during and after 3D bioprinting*, Biofabrication **8**, 032002 (2016).

[38] J. Gopinathan and I. Noh, *Recent trends in bioinks for 3D printing*, Biomaterials Research **22**, 11 (2018).

[39] A. GhavamiNejad, N. Ashammakhi, X. Y. Wu and A. Khademhosseini, *Crosslinking Strategies for 3D Bioprinting of Polymeric Hydrogels.*, Small (Weinheim an der Bergstrasse, Germany) **16**, e2002931 (2020).

[40] T. Boland, T. Xu, B. Damon and X. Cui, *Application of inkjet printing to tissue engineering*, Biotechnology Journal **1**, 910 (2006).

[41] X. Cui, D. Dean, Z. M. Ruggeri and T. Boland, *Cell damage evaluation of thermal inkjet printed Chinese hamster ovary cells*, Biotechnology and Bioengineering **106**, 963 (2010).

[42] R. E. Saunders, J. E. Gough and B. Derby, *Delivery of human fibroblast cells by piezoelectric drop-on-demand inkjet printing*, Biomaterials **29**, 193 (2008).

[43] S. V. Murphy, A. Skardal and A. Atala, *Evaluation of hydrogels for bio-printing applications*, Journal of Biomedical Materials Research Part A **101A**, 272 (2013).

[44] B. Guillotin, M. Ali, A. Ducom, S. Catros, V. Keriquel, A. Souquet, M. Remy, J.-C. Fricain and F. Guillemot, *Chapter 6 - Laser-Assisted Bioprinting for Tissue Engineering*, in *Biofabrication*, edited by G. Forgacs and W. Sun (William Andrew Publishing, Boston, 2013) pp. 95–118.

[45] R. Trombetta, J. A. Inzana, E. M. Schwarz, S. L. Kates and H. A. Awad, *3D Printing of Calcium Phosphate Ceramics for Bone Tissue Engineering and Drug Delivery*, Annals of Biomedical Engineering **45**, 23 (2017).

[46] Z. Wang, R. Abdulla, B. Parker, R. Samanipour, S. Ghosh and K. Kim, *A simple and high-resolution stereolithography-based 3D bioprinting system using visible light crosslinkable bioinks*, Biofabrication **7**, 045009 (2015).

[47] F. P. Melchels, J. Feijen and D. W. Grijpma, *A review on stereolithography and its applications in biomedical engineering*, Biomaterials **31**, 6121 (2010).

[48] M. Furutani, T. Ide, S. Kinoshita, R. Horiguchi, I. Mori, K. Sakai and K. Arimitsu, *Initiator-free photopolymerization of common acrylate monomers with 254 nm light*, Polymer International **68**, 79 (2019).

[49] J. R. Tumbleston, D. Shirvanyants, N. Ermoshkin, R. Janusziewicz, A. R. Johnson, D. Kelly, K. Chen, R. Pinschmidt, J. P. Rolland, A. Ermoshkin, E. T. Samulski and J. M. DeSimone, *Continuous liquid interface production of 3D objects*, Science **347**, 1349 (2015).

[50] M. P. de Beer, H. L. van der Laan, M. A. Cole, R. J. Whelan, M. A. Burns and T. F. Scott, *Rapid, continuous additive manufacturing by volumetric polymerization inhibition patterning*, Science Advances **5**, eaau8723 (2019).

[51] S. K. Lee and D. Neckers, *Two-photon radical-photoinitiator system based on iodinated benzospiropyrans*, Chemistry of Materials **3**, 858 (1991).

[52] M. Regehly, Y. Garmshausen, M. Reuter, N. F. König, E. Israel, D. P. Kelly, C.-Y. Chou, K. Koch, B. Asfari and S. Hecht, *Xolography for linear volumetric 3D printing*, Nature **588**, 620 (2020).

[53] V. Hahn, P. Rietz, F. Hermann, P. Müller, C. Barner-Kowollik, T. Schlöder, W. Wenzel, E. Blasco and M. Wegener, *Light-sheet 3D microprinting via two-colour two-step absorption*, Nature Photonics **16**, 784 (2022).

[54] T. F. Scott, B. A. Kowalski, A. C. Sullivan, C. N. Bowman and R. R. McLeod, *Two-Color Single-Photon Photoinitiation and Photoinhibition for Subdiffraction Photolithography*, Science **324**, 913 (2009).

[55] F. Li, S. C. Thickett, F. Maya, E. H. Doeven, R. M. Guijt and M. C. Breadmore, *Rapid Additive Manufacturing of 3D Geometric Structures via Dual-Wavelength Polymerization*, ACS Macro Lett. **9**, 1409 (2020).

[56] H. van der Laan, M. A. Burns and T. F. Scott, *Volumetric Photopolymerization Confinement through Dual-Wavelength Photoinitiation and Photoinhibition*, ACS Macro Lett. **8**, 899 (2019).

[57] B. E. Kelly, I. Bhattacharya, H. Heidari, M. Shusteff, C. M. Spadaccini and H. K. Taylor, *Volumetric additive manufacturing via tomographic reconstruction*, Science **363**, 1075 (2019).

[58] P. N. Bernal, P. Delrot, D. Loterie, Y. Li, J. Malda, C. Moser and R. Levato, *Volumetric Bioprinting of Complex Living-Tissue Constructs within Seconds*, Advanced Materials **31**, 1904209 (2019).

[59] P. N. Bernal, M. Bouwmeester, J. Madrid-Wolff, M. Falandt, S. Florczak, N. G. Rodriguez, Y. Li, G. Größbacher, R.-A. Samsom, M. van Wolferen, L. J. W. van der Laan, P. Delrot, D. Loterie, J. Malda, C. Moser, B. Spee and R. Levato, *Volumetric Bioprinting of Organoids and Optically Tuned Hydrogels to Build Liver-Like Metabolic Biofactories*, Advanced Materials **34**, 2110054 (2022).

[60] K.-C. Yeh, S.-H. Wu, J. T. Murphy and J. C. Lagarias, *A Cyanobacterial Phytochrome Two-Component Light Sensory System*, Science **277**, 1505 (1997).

[61] M. Ikeuchi and T. Ishizuka, *Cyanobacteriochromes: a new superfamily of tetrapyrrole-binding photoreceptors in cyanobacteria*, Photochemical and Photobiological Sciences **7**, 1159 (2008).

[62] K. Fushimi and R. Narikawa, *Cyanobacteriochromes: photoreceptors covering the entire UV-to-visible spectrum*, Current Opinion in Structural Biology **57**, 39 (2019).

[63] A. Levskaya, A. A. Chevalier, J. J. Tabor, Z. B. Simpson, L. A. Lavery, M. Levy, E. A. Davidson, A. Scouras, A. D. Ellington, E. M. Marcotte and C. A. Voigt, *Engineering Escherichia coli to see light*, Nature **438**, 441 (2005).

[64] Y. Hirose, T. Shimada, R. Narikawa, M. Katayama and M. Ikeuchi, *Cyanobacteriochrome CcaS is the green light receptor that induces the expression of phycobilisome linker protein*, Proceedings of the National Academy of Sciences **105**, 9528 (2008).

[65] J. Fernandez-Rodriguez, F. Moser, M. Song and C. A. Voigt, *Engineering RGB color vision into Escherichia coli*, Nature Chemical Biology **13**, 706 (2017).

[66] E. J. Olson, L. A. Hartsough, B. P. Landry, R. Shroff and J. J. Tabor, *Characterizing bacterial gene circuit dynamics with optically programmed gene expression signals*, Nature Methods **11**, 449 (2014).

[67] E. J. Olson, C. N. Tzouanas and J. J. Tabor, *A photoconversion model for full spectral programming and multiplexing of optogenetic systems*, Molecular Systems Biology **13**, 926 (2017).

[68] N. T. Ong and J. J. Tabor, *A Miniaturized Escherichia coli Green Light Sensor with High Dynamic Range.*, Chembiochem : a European journal of chemical biology **19**, 1255 (2018).

[69] N. C. Rockwell, S. S. Martin and J. C. Lagarias, *Red/Green Cyanobacteriochromes: Sensors of Color and Power*, Biochemistry **51**, 9667 (2012).

[70] M. Nakajima, S. Ferri, M. Rögner and K. Sode, *Construction of a Miniaturized Chromatic Acclimation Sensor from Cyanobacteria with Reversed Response to a Light Signal*, Scientific Reports **6**, 37595 (2016).

[71] G. M. Taylor, P. M. Mordaka and J. T. Heap, *Start-Stop Assembly: a functionally scarless DNA assembly system optimized for metabolic engineering*, Nucleic Acids Research **47**, e17 (2018).

[72] J. Beal, N. G. Farny, T. Haddock-Angelli *et al.*, *Robust estimation of bacterial cell count from optical density*, Communications Biology **3**, 640 (2020).

[73] C. Prats, A. Giró, J. Ferrer, D. López and J. Vives-Rego, *Analysis and IbM simulation of the stages in bacterial lag phase: Basis for an updated definition*, Journal of Theoretical Biology **252**, 56 (2008).

[74] N. Sultanova, S. Kasarova and I. Nikolov, *Dispersion Properties of Optical Polymers*, ACTA PHYSICA POLONICA A **116**, 585 (2009).

[75] G. M. Hale and M. R. Querry, *Optical Constants of Water in the 200-nm to 200-μm Wavelength Region*, Appl. Opt. **12**, 555 (1973).

[76] D. A. Cross and P. Latimer, *Angular Dependence of Scattering from Escherichia coli Cells*, Appl. Opt. **11**, 1225 (1972).